



HAL
open science

The South Atlantic Ocean circulation and its variability at different scales

Gastón Manta

► **To cite this version:**

Gastón Manta. The South Atlantic Ocean circulation and its variability at different scales. Meteorology. Université Paris sciences et lettres, 2022. English. NNT : 2022UPSLE044 . tel-04597595

HAL Id: tel-04597595

<https://theses.hal.science/tel-04597595>

Submitted on 3 Jun 2024

HAL is a multi-disciplinary open access archive for the deposit and dissemination of scientific research documents, whether they are published or not. The documents may come from teaching and research institutions in France or abroad, or from public or private research centers.

L'archive ouverte pluridisciplinaire **HAL**, est destinée au dépôt et à la diffusion de documents scientifiques de niveau recherche, publiés ou non, émanant des établissements d'enseignement et de recherche français ou étrangers, des laboratoires publics ou privés.



THÈSE DE DOCTORAT
DE L'UNIVERSITÉ PSL

Préparée à l'Ecole Normale Supérieure

**The South Atlantic Ocean circulation and its variability at
different scales**

Soutenue par

Gaston Manta

Le 3 juin 2022

École doctorale n°129

Sciences de l'environnement
d'Ile-de-France

Spécialité

Météorologie, Océanographie,
Sciences de l'environnement

Préparée au

Laboratoire de Météorologie
Dynamique



Composition du jury :

| | |
|--|------------------------------|
| Laurent BOPP Directeur de recherche, Ecole Normale Supérieure (LMD) | <i>Président du jury</i> |
| Alonso HERNANDEZ GUERRA Full professor, Universidad de Las Palmas de Gran Canaria (IOCAG) | <i>Rapporteur</i> |
| Sophie CRAVATTE Directeur de recherche, Université de Toulouse,(LEGOS) | <i>Rapporteur</i> |
| Gilles REVERDIN Directeur de recherche, Sorbonne Université (LO-CEAN) | <i>Examineur</i> |
| Martin SARACENO Associate professor, Universidad de Buenos Aires (CIMA) | <i>Examineur</i> |
| Herlé MERCIER Directeur de recherche, Université de Bretagne Occidentale (LOPS) | <i>Examineur</i> |
| Sabrina SPEICH Full professor, Ecole Normale Supérieure (LMD) | <i>Directrice de thèse</i> |
| Marcelo BARREIRO Full professor, Universidad de la República (DCAFO), Uruguay | <i>Co-encadrant de thèse</i> |

Abstract

The ocean, like the atmosphere, is a key component of the climate system redistributing heat from lower to higher latitudes. Also, it has absorbed the majority of the anthropogenic heat through its large heat capacity. The Atlantic Meridional Overturning Circulation (AMOC) is the main mechanism in how the ocean redistributes heat and other properties across this basin. The AMOC has historically received special attention in its northern basin due to its large contribution to the global circulation and influence over the climate in Europe and North America. Over the last decade, the efforts to observe the global ocean and in particular the South Atlantic have increased, as this basin has the unique characteristic to export heat to the northern hemisphere across the equator and it connects the AMOC with the other ocean basins.

This Ph.D. thesis aims to understand new insights from the South Atlantic Ocean circulation from a physical oceanography perspective, using the exponentially growing number of observations provided by the deployment of Argo floats, ship-based hydrography, and satellite observations. The study uses different new analyses applied to the ocean and to a recently released atmospheric reanalysis. The Ph.D. work has focused on three different aspects of the South Atlantic Circulation. In the first part, it has aimed to assess the meridional volume, freshwater, and heat (MHT) transports at 34.5°S in the South Atlantic in the first GO-SHIP hydrographic transect at this latitude that took place in January 2017. An upper and an abyssal overturning cell are identified with a strength of 15.64 ± 1.39 Sv and 2.4 ± 1.6 Sv, respectively. The net northward MHT is 0.27 ± 0.10 PW, increasing by 0.12 PW when we remove the observed mesoscale eddies with a climatology derived from the Argo floats data set. We attribute this change to an anomalous predominance of cold-core eddies during the cruise period. The zonal changes in water masses properties and velocity denote the imprint of exchange pathways with both the Southern and the Indian oceans.

During the second part of the Ph.D., the analysis focused on the Brazil-Malvinas Confluence, which is the region where opposing and intense western boundary currents, major contributors of the AMOC, meet along the Southwestern Atlantic slope. Based on shipborne observations combined with satellite data and an eddy tracking algorithm, we analyze the cross-shelf exchanges during May 2016. Two types of shelf water export were observed triggered by mesoscale dynamics: one was the export of shallow Rio de la Plata Plume waters driven off-shelf by the retroflexion of the Brazil Current. An additional type of off-shelf transport consisted of a subsurface layer of Subantarctic Shelf Waters that subducted at the Confluence. We show that geostrophic currents derived from satellite altimetry over the slope can be useful to track this subsurface off-shelf export as they

are significantly correlated with absolute velocity measurements at this depth. Moreover, Argo temperature and salinity profiles show evidence of these two types of shelf water export, suggesting this is a relatively frequent phenomenon.

The last part of the study consisted of studying the natural coupled variability of ocean and atmosphere by applying the Multivariate Singular Spectrum Analysis (MSSA) to the ERA5 dataset. We identified prominent interannual oscillations of 12.8 and 5.3 year periods, characterized by a basinwide southwest-northeast anticlockwise propagation pattern. The novelty of these results relies on that MSSA allows characterizing the spatio-temporal evolution of the variability mode. The results of the Ph.D. work have been summarized in three papers prepared for international A-rated scientific journals. Two of them have already been published.

Keywords : Heat transport, mesoscale eddies, shelf water export, coupled variability

Résumé

L'océan, comme l'atmosphère, est un élément clé du système climatique qui redistribue la chaleur des basses vers les hautes latitudes. Il a également absorbé la majorité de la chaleur anthropique grâce à sa grande capacité thermique. La circulation méridienne de retournement de l'Atlantique (AMOC) est le principal mécanisme par lequel l'océan redistribue la chaleur et d'autres propriétés dans ce bassin. Historiquement, l'AMOC a fait l'objet d'une attention particulière dans son bassin nord en raison de sa grande contribution à la circulation mondiale et de son influence sur le climat en Europe et en Amérique du Nord. Au cours de la dernière décennie, les efforts d'observation de l'océan global et en particulier de l'Atlantique Sud ont augmenté, car ce bassin a la caractéristique unique d'exporter de la chaleur vers l'hémisphère Nord à travers l'équateur et connecte l'AMOC avec les autres bassins océaniques. Ce doctorat vise à améliorer la compréhension de la circulation dans l'océan Atlantique Sud du point de vue de l'océanographie physique, en utilisant le nombre croissant d'observations fournies par les flotteurs Argo, des mesures hydrographiques et des observations satellitaires. Le travail s'est concentré sur trois aspects différents de la circulation de l'Atlantique Sud. Dans la première partie, il s'agissait d'évaluer les transports méridiens de volume, d'eau douce et de chaleur (MHT) à 34.5°S dans l'Atlantique Sud lors du premier transect hydrographique GO-SHIP à cette latitude, en janvier 2017. Une cellule de retournement supérieure et une cellule de retournement abyssale sont identifiées avec une force de 15.64 ± 1.39 Sv et 2.4 ± 1.6 Sv, respectivement. La MHT nette vers le nord-est de 0.27 ± 0.10 PW, augmentant de 0.12 PW lorsque nous retirons les tourbillons de méso-échelle observés avec une climatologie dérivée de l'ensemble de données des flotteurs Argo. Nous attribuons cette différence à une prédominance anormale des tourbillons de cœur froid pendant la période de la campagne. Au cours de la deuxième partie du doctorat, l'analyse s'est concentrée sur la confluence Brésil-Malouines, qui est la région où des courants de bord ouest opposés et intenses, contributeurs majeurs du AMOC, se rencontrent et génèrent l'une des régions les plus énergétiques de l'océan mondial. Sur la base d'observations embarquées combinées à des données satellitaires et à un algorithme de suivi des tourbillons, nous analysons les échanges trans-plateau au cours du mois de mai 2016. Deux types d'exportation d'eau du plateau ont été observés, déclenchés par la dynamique de méso-échelle: l'exportation des eaux peu profondes du panache du Rio de la Plata, entraînées hors du plateau par la réflexion du courant du Brésil, et le transport vers le large d'une couche d'eaux du plateau subantarctique situé sous la surface, qui s'est subductée à la confluence. Nous montrons que les courants géostrophiques dérivés de l'altimétrie par satellite au-dessus du talus peuvent être utiles pour suivre cette exportation hors plateau en subsurface.

De plus, les profils de température et de salinité Argo montrent des preuves de ces deux types d'exportation d'eau du plateau, suggérant qu'il s'agit d'un phénomène relativement fréquent. La dernière partie de l'étude a consisté à étudier la variabilité naturelle couplée de l'océan et de l'atmosphère en appliquant l'analyse multivariée du spectre singulier (MSSA) au jeu de données ERA5. Nous avons identifié des oscillations interannuelles importantes de périodes de 12 et 5 ans, caractérisées par un modèle de propagation sud-ouest-nord-est dans le sens inverse des aiguilles d'une montre. La nouveauté de ces résultats repose sur le fait que la méthode MSSA permet de caractériser l'évolution spatio-temporelle du mode de variabilité. Les résultats de ces travaux ont été résumés dans trois articles préparés pour des revues scientifiques internationales de rang A, dont deux d'entre eux ont déjà été publiés.

Mots clés : Transport de chaleur, tourbillons à mésoéchelle, exportation de l'eau du plateau, variabilité couplée

Acknowledgements

Thank you very much Sabrina; you are an excellent person and advisor and provided me with the best working conditions. Thank you very much Marcelo; A 3rd thesis together speaks for itself. Thank you very much Johannes Karstensen, Alberto Piola, and Michael Ghil; world-class co-advisors in chapters 2,3, and 4, respectively. Thank you very much to the jury and to the PhD committee, Rosemary Morrow, Brian King (I tried not to include every figure I did in the 3 years), and Andrea Doglioli. Thank you very much ANII-Campus France for providing me with the grant (POS_CFRA_2017_1_146868).

Thank you very much Corentin Subirade; you were the best office mate and now my new brother of life. Thank you very much Rémi, Yanxu, Artemis, Pierre, Sabrina's "students' football team" and all the people at ENS; you were very nice to me since day 1. Thank you very much Romina, Camila and all the DCAFO in Uruguay; looking forward to having the opportunity to return.

Thank you very much Jaime, Pato, Gonza, and all the South American crew; you made me feel at home. Thank you very much Théa, Stéphane, Guénaëlle, and all the Bourg la Reine's crew; you made me feel at home. Thank you very much France; you are a beautiful country with a fantastic social security system. And thank you very much Paris; so much culture and lockdowns definitely changed me.

Thank you very much family and friends present from the beginning, specially Mamá, Papá, Laura, and Luis for coming to the defense; you are my ultras. And of course, thank you very much Anita; you are the coauthor of my life.

Preface: Too big to see it

The accelerated consequences of climate change have resulted in what is often called a climate crisis. The global surface temperature has been rising since the late 1800s as a function of cumulative anthropogenic CO₂ emissions. A warmer climate is a system with higher energy and therefore prone to extreme events. Most of the energy has been captured by the ocean; a warmer ocean expands its volume and, also due to the melting of ice caps, the sea level increases. The majority of the consequences are negative for humanity and biodiversity. Meanwhile, ocean observations are being created at exponential acceleration, and both the generation of knowledge and specific actions to stop the climate crisis need to increase at the same rate. Although this thesis won't change the course of history, actions based on knowledge will. There is no Planet B.

Contents

| | |
|--|------------|
| Abstract | i |
| Résumé | iii |
| Acknowledgements | v |
| Preface: Too big to see it | vi |
| Glossary | ix |
| 1 General Introduction | 1 |
| 1 The ocean in the climate system and the Meridional Overturning Circulation | 2 |
| 2 The large scale circulation, the South Atlantic, and its variability modes | 4 |
| 3 The ocean observing system and mesoscale eddies | 8 |
| 4 General objectives | 15 |
| 2 The South Atlantic Meridional Overturning Circulation and Mesoscale Eddies in the First GO-SHIP Section at 34.5°S | 17 |
| 1 Introduction | 19 |
| 2 Data | 22 |
| 3 Methods | 23 |
| 4 Results | 25 |
| 5 Conclusions | 38 |
| 6 Data Availability Statement | 39 |
| 7 References | 39 |
| 3 Shelf Water Export at the Brazil-Malvinas Confluence Evidenced From Combined in situ and Satellite Observations | 43 |
| 1 Introduction | 45 |
| 2 Data | 45 |
| 3 Materials and Methods | 47 |
| 4 Results | 48 |
| 5 Summary and Conclusion | 57 |
| 6 Data Availability Statement | 59 |
| 7 References | 60 |
| 4 The South Atlantic Dipole From Multichannel Singular Spectrum Analysis | 64 |

Contents

| | | |
|----------|---|-----------|
| 1 | Abstract | 66 |
| 2 | Introduction | 66 |
| 3 | Data and Methods | 68 |
| | 3.1 Data | 68 |
| | 3.2 Multichannel Singular Spectrum Analysis (M-SSA) | 69 |
| | 3.3 Monte Carlo M-SSA | 69 |
| 4 | Results | 70 |
| | 4.1 Spatiotemporal evolution of the oscillatory modes | 71 |
| 5 | Summary and conclusion | 74 |
| 5 | General conclusions and perspectives | 76 |
| | 1 Perspectives | 81 |
| | General Bibliography | 84 |
| | Appendix 1: Supplementary figures for Chapter 2 | 91 |
| | Appendix 2: Supplementary figures for Chapter 3 | 99 |

Glossary

This section aims to help those readers non-familiar with the field and/or region of study, in which some acronyms are usually taken for granted. Acronyms are mostly restricted to the long terms repeated several times and are introduced throughout the text.

((S)A)MOC *((South) Atlantic) Meridional Overturning Circulation: it refers to the oceanic circulation crossing latitudes but also to the intensity in Sverdrups ($1Sv = 10^6 m^3 s^{-1}$)*

ADCP *Acoustic Doppler Current Profiler: measure water velocity. There can be ones mounted in the Vessel-Ship (VADCP-SADCP), and other ones lowered (LADCP) in the CTD-rosette*

ADT *Absolute Dynamic Topography: satellite field, estimate surface currents and allows to detect eddies*

AEs, CEs *Anticyclonic and Cyclonic mesoscale eddies: Warm and cold-core, respectively*

BMC *Brazil Malvinas Confluence: the region where Brazil and Malvinas Currents meet*

CTD *Conductivity-Temperature-Depth: is the main instrument in oceanography, measures conductivity and temperature while it is lowered into the water, obtaining a vertical profile*

EEZ *Exclusive economic zone: is an area of the ocean, generally extending 200 nautical miles from the coast in which a nation has jurisdiction over living and nonliving resources*

GO-SHIP *Global Ocean Ship-based Hydrographic Investigations Program: Oceanic sections doing full-water profiling with high resolution and data quality standards*

M-SSA *Multivariate Singular Spectrum Analysis: A statistical technique to find oscillations (usually through time) in the data combining different variables*

MHT *Meridional Heat Transport: Heat transport across an oceanic section in PW ($10^{15}W$)*

Oceanic Front *Were two distinct water masses meet, usually associated with ocean currents. Most of the relevant oceanographic processes occur along fronts, especially related to primary production increasing, plankton accumulation, and high density of fishery resources*

STF *Subtropical Front, STSF* *Subtropical Shelf Front, SAF* *Subantarctic Front*

RdIP *Rio de la Plata: refers to the estuary, usually its huge discharges, while (RD)PPW refers to the low salinity water mass in which the discharges are mixed, covering a much larger area*

SSS *Sea surface Salinity: usually referred to the satellite field*

SST *Sea Surface Temperature: usually referred to the satellite field*

T-S (diagram) *Temperature-Salinity (diagram). These are the main variables to identify water masses at a given pressure, usually measured from the CTD. The T-S diagram is the graphical representation of the profiles*

TOEddies *Tracking Ocean Eddies: Satellite mesoscale eddy tracking algorithm used here*

TSG *Thermosalinograph: measures near-surface temperature and salinity as the ship moves*

Water Mass *A body of water with a common formation history. After sinking and losing contact with the atmosphere conserves its density, temperature and salinity properties and therefore is traceable through the deep ocean. It is often called like the region where it is formed (sinks) and the depth level it reaches (intermediate, deep, bottom). It also refers to a body of water in contact with the atmosphere, and in this case it usually has a large T-S range.*

AABW *Antarctic Bottom Water, AAIW Antarctic Intermediate Water, STSW Subtropical Shelf Water, TW Tropical Water, UCDW Upper Circumpolar Deep Water, SACW South Atlantic Central Water, SASW Subantarctic Shelf Water, NADW North Atlantic Deep Water, LCDW Lower Circumpolar Deep Water, RDPPW Rio de la Plata Plume Water*

WBC *Western Boundary Current: intense currents found on the western slope of oceanic basins*

Chapter 1

General Introduction

This chapter begins with a brief introduction to basic concepts of physical oceanography and the oceanic meridional overturning circulation. Then, the large scale circulation in the South Atlantic is described, followed by the introduction of the concept of mesoscale dynamics and mesoscale eddies. Finally, a brief review of the history and main components of the global ocean observing system is presented, leading to the outline of the general objectives of the thesis.

1 The ocean in the climate system and the Meridional Overturning Circulation

The ocean, like the atmosphere, is a key component of the climate system. They both redistribute the net surplus in radiative heating at the top of the atmosphere in the tropical region toward the high latitudes which have a radiative deficit (Wunsch, 2005; Czaja et al., 2006; Fig.1.1a). While in the atmosphere, the poleward energy flux is mainly achieved by the Hadley cell in the tropics and the transients in the extratropics (Trenberth et al., 2003), in the ocean is carried out by the large-scale circulation and mesoscale eddies both in the tropics and extratropics (Wunsch, 1999; Jayne et al., 2002; Ferrari et al., 2011). The ocean has also absorbed nearly 90% of the anthropogenic heat (Levitus et al., 2012; Von Schuckmann et al., 2020; Fig.1.1b) and 30% of the carbon (Khatiwala et al., 2013; Friedlingstein et al., 2021) due to its large heat capacity and the carbonate system, respectively. Without the ocean, the increase of temperature in the atmosphere would be several times higher than the observed since the preindustrial conditions.

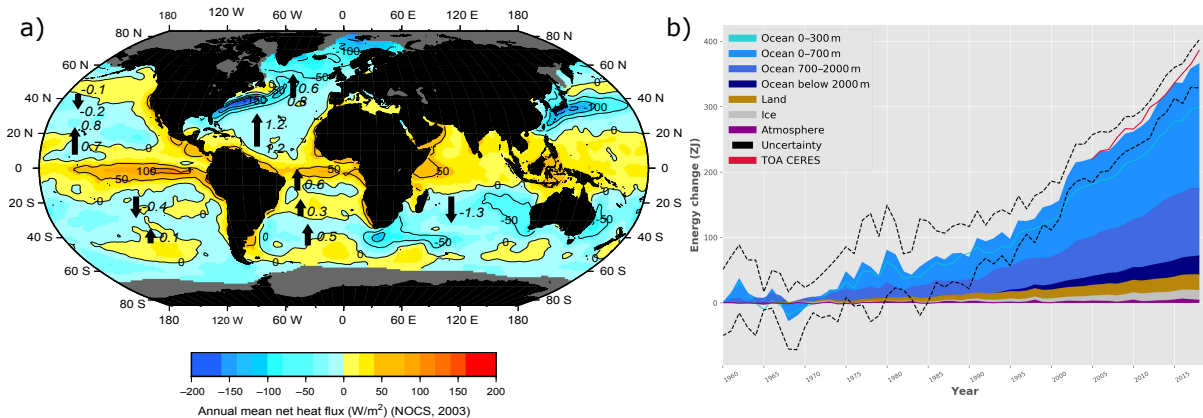


Figure 1.1: a) Annual average net heat flux (W/m^2). Positive: heat gain by the sea. Negative: heat loss by the sea. Data are from the NOCS climatology (Grist et al., 2003). Superimposed numbers and arrows are the meridional heat transports (PW). Positive transports are northward. Taken from Talley, 2011. b) Change in the heat content of the different components of the climate system. Taken from Von Schuckmann et al., 2020.

The Meridional Overturning Circulation (MOC) is a major mechanism in how the ocean redistributes heat (Talley, 2003). The MOC connects the overturning cells confined within ocean basins and helps to promote the balance of the net buoyancy loss in the northern North Atlantic and around Antarctica. While the excess heat from the tropics is transported by the upper ocean to higher latitudes in each basin through the western boundary currents as a response to the wind-driven circulation, the density-driven part

of the MOC originates from sinking waters at high latitudes. It consists of two global-scale meridional overturning cells. The “upper-cell”, responsible for most of the volume transport, is linked to the formation of North Atlantic Deep Water (NADW) in the subpolar North Atlantic and Nordic Seas, but also to the upwelling of deep waters in the Southern Ocean. The “lower” or “abyssal” cell is linked to the dense water formation around Antarctica and to the abyssal upwelling due to the interaction of the flow with the bottom topography (Talley, 2003; Lumpkin et al., 2007; McDougall et al., 2017).

The Atlantic component of the MOC (AMOC) in the northern basin, historically has received special attention, because it is known to have a large contribution to the global MOC and an influence on the climate of Europe and North America (Srokosz et al., 2015). Over the last decade, the efforts to observe the global ocean and in particular the South Atlantic have increased, as this basin is the only one with a net heat transport from high latitudes to the equator, because the upper 1200 m layer flows northward to compensate for the southward export of colder NADW (Garzoli et al., 2013; Buckley et al., 2016; Fig.1.2). Paleoclimatic records show abrupt climatic changes in the past linked with changes in the AMOC. In particular, a cooling of the North Atlantic countries has been proposed when the AMOC weakened (Peterson et al., 2000; Ganopolski et al., 2001; Stott et al., 2002).

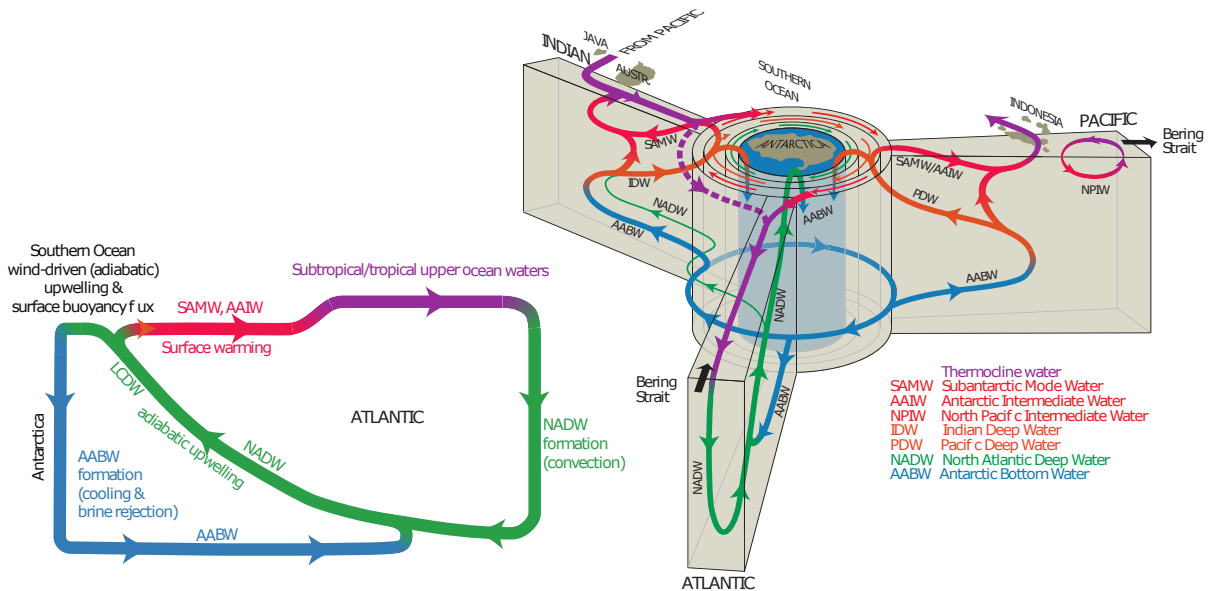


Figure 1.2: Schematic figure of the Meridional Overturning Circulation. The lower left panel shows a simplified version of the two overturning cells in the Atlantic. Modified from Talley, 2013.

The term AMOC is not only referred to the meridional circulation but also to a measure of the intensity of the circulation as the zonally and vertically accumulated

flow at each latitude, connecting the northward flowing of surface warm waters and the southward flowing of deeper cold waters across all latitudes. Therefore, it is positively and nearly linearly correlated with the MHT (e.g. Garzoli et al., 2013; Dong et al., 2015). How the AMOC and the MHT are measured and calculated is defined in Chapter 2. The AMOC displays variability at all time scales, not only due to the slow density-driven movements (years-decades) of the sinking waters in higher latitudes as historically conceived but also at high frequencies (days-weeks) due to deep ocean mesoscale activity and propagating waves, among other mechanisms (e.g. Kersale et al., 2020; Kersalé et al., 2021). Therefore, the AMOC is an important element of the oceanic circulation both in the North and South Atlantic that need to be considered not only in a steady state but also as time-varying (Frajka-Williams et al., 2019).

2 The large scale circulation, the South Atlantic, and its variability modes

The large scale atmospheric and ocean circulations are influenced by the rotation of the Earth, are stratified, and their horizontal extension is much larger than the vertical, and so are the magnitude of the velocities in these axes. While in the vertical axis (z) the pressure gradients tend to be balanced by gravity throughout the hydrostatic balance (Eq. 1.1), in the horizontal axes (x,y) the pressure gradients tend to be balanced by the Earth's rotation, the Coriolis effect, in what is called the geostrophic balance (Eq. 1.2):

$$\rho g = \frac{\partial p}{\partial z} \quad (1.1)$$

$$(u_g, v_g) = \left(\frac{-1}{\rho f} \frac{\partial p}{\partial y}, \frac{1}{\rho f} \frac{\partial p}{\partial x} \right) \quad (1.2)$$

Where p is pressure, ρ density, u_g, v_g , are zonal and meridional geostrophic velocities, and f the Coriolis parameter, $f = 2\Omega\sin(\varphi)$, with Ω the rotation rate of the earth and φ is the latitude. On the large scale (days, approximately 50 and 500 km for ocean and atmosphere respectively), away from the Equator and the frontiers, the ocean and atmosphere movements are very close to the geostrophic balance, and therefore a pressure field can provide information on the horizontal circulation. The flow follows the isobars with the high pressure towards the left (right) in the Southern (Northern) Hemisphere due to the change of sign of the Coriolis parameter (Fig.1.3).

Several analyses can be done in order to understand to what extent geostrophic balance appropriately explains the oceanic circulation, as it is clear that small-scale fast

2. The large scale circulation, the South Atlantic, and its variability modes

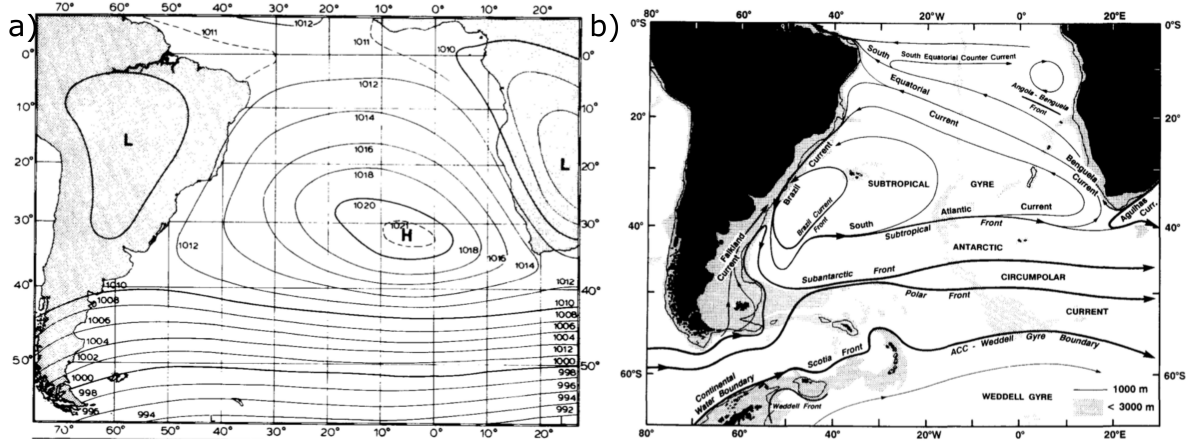


Figure 1.3: a) Mean atmospheric sea level pressure for January. b) Schematic circulation of oceanic surface currents in the South Atlantic. Taken from Peterson et al., 1991.

movements in the ocean are not balanced by Earth’s rotation. The adimensional Rossby Number (Ro) compares the ratio between rotation and advection terms in the momentum balance of the Navier-Stokes equations:

$$Ro = \frac{U}{Lf} \quad (1.3)$$

where U and L are the typical velocity and length scales, respectively, and f is the Coriolis parameter. When $Ro \ll 1$, the main balance in the momentum equation reduces to the balance between Coriolis and the pressure gradient force, and therefore the flow is considered geostrophic. This analysis can be taken further by introducing the first baroclinic Rossby deformation radius (Rd), which is an intrinsic scale of the ocean that accounts for the effects of ocean stratification and Earth rotation:

$$Rd = \frac{NH}{f} \quad (1.4)$$

where N is the Brunt–Väisälä frequency, which is a measure of stratification, H is a vertical scale of the ocean stratification, and f is the Coriolis parameter. Rd gives an approximation of the minimum horizontal scale in which the ocean structures will satisfy the geostrophic balance. Typical values for the ocean are $N = 3 \cdot 10^{-3} \text{ s}^{-1}$, $H=1\text{km}$, and $f = 10^{-4} \text{ s}^{-1}$, and therefore $Rd \approx 30\text{km}$. Rd increases towards lower latitudes as oceanic stratification increases and the Coriolis parameter decreases, and also decreases in the shallow continental shelves following ocean depth (Fig.1.4).

The large-scale circulation in the subtropical South Atlantic is dominated by high-pressure circulation in the lower atmosphere and upper ocean (also referred to as “sub-tropical gyre”; Fig.1.3). The atmospheric high-pressure circulation, the semipermanent

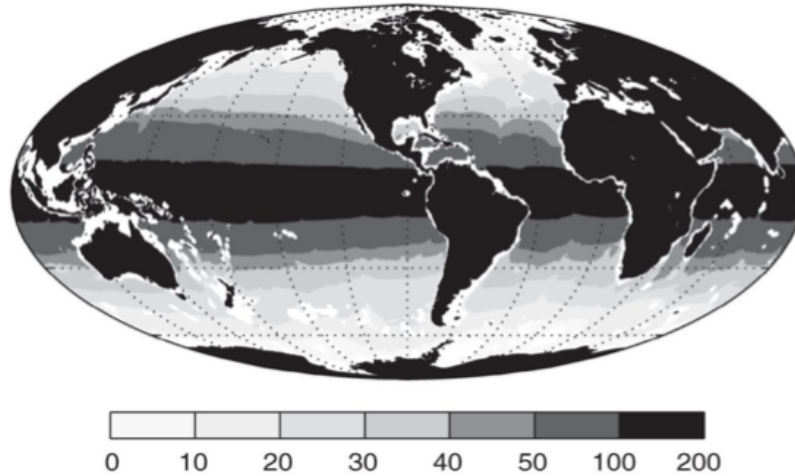


Figure 1.4: Internal Rossby radius of deformation (km).

anticyclone, is strongly associated with the subsidence of the polar branch of the Hadley cell at about 30°S , with the trades and westerlies blowing at the surface in the equatorial and poleward side of the gyre, respectively. The ocean subtropical gyre is essentially wind-driven. At the large scale, it can be described by geostrophic currents in response to the sea level increase due to the convergent Ekman transport towards the center of the gyre. The subtropical atmosphere and ocean circulation are coupled. Changes in the position and strength of the atmospheric anticyclone will determine changes in the ocean gyre, adding predictability to the system, not only at the annual but also at intraseasonal and interannual time scales (Venegas et al., 1997; Rodrigues et al., 2015).

The atmospheric and oceanic circulation in the South Atlantic are not only locally but also remotely forced. The El Niño Southern Oscillation (ENSO) occurring in the Tropical Pacific is the main driver of interannual variability in the South Atlantic (e.g. Venegas et al., 1997; Barreiro et al., 2004 ; Rodrigues et al., 2015). For example, ENSO events trigger the Pacific–South American wave train that causes a weakening and meridional shift of the South Atlantic anticyclone, and as a consequence low-level wind and SST anomalies are observed in the region (Rodrigues et al., 2015). The Southern Annular Mode (SAM), or Antarctic Oscillation (AAO), describes latitudinal shifts of the westerlies and also displaces the Atlantic anticyclone, in addition to inducing remote effects in the low-latitudes of the South Atlantic. For example, the northward advection of cold waters over the Southwestern Atlantic shelf is negatively correlated with the SAM on interannual scales. The SAM induces along-shore wind stress anomalies that induce an Ekman transport that in turn generates the cross-shore pressure gradient that modulates the along-shore transport variability (Lago et al., 2021).

The main difference in the structure of the atmospheric and oceanic subtropical circulation is that the atmospheric circulation is relatively symmetric along a zonal axis, whereas the ocean gyre is not. The poleward flow of the ocean is indeed restricted to an intense narrow current flowing along the continental slope in the west of the basin, named Western Boundary Current (WBC). The South Brazil Current is the WBC of the South Atlantic subtropical gyre. WBCs are topographically steered and follow the isobaths over the slope. Moreover, they are majorly responsible for the total ocean heat transport due to both the intense speeds and the thermohaline differences with the surrounding ocean (Talley, 2011).

A distinguishable characteristic of the South Atlantic is the fact that it is intimately connected with other three WBCs in other oceanic basins: the Agulhas, the Malvinas and the Deep Western Boundary Current. The density-driven Deep Western Boundary Current is formed by buoyancy loss in the Labrador and Greenland Seas in the North Atlantic and is composed of sinking North Atlantic Deep Water (NADW) flowing southward at about 2000 to 3800 m of depth until the Southern Ocean (Smethie Jr et al., 2000; Fig.1.3). The Malvinas and Agulhas Current are, as the South Brazil, wind-driven. These two currents irrupt into the South Atlantic steered by the geometry of the continents and their dynamical nonlinearities, materializing the cold and warm water route of the AMOC, respectively (Gordon, 1986; Speich et al., 2001; R uhs et al., 2019).

In the Eastern South Atlantic, the Agulhas Current, the South Indian subtropical gyre WBC, leaks into the Atlantic as the African Continent extends only up to 35 S whereas the zero wind curl is located poleward of this latitude. The Agulhas Current Leakage sheds among the biggest and long-lived anticyclonic eddies, named Agulhas Rings. These eddies are known to transport heat and salt from the Indian Ocean into the South Atlantic (McDonagh et al., 1999). On the western end of the South Atlantic, the South American continent extends southward until 55 S. There, the interaction between the bottom topography and the Antarctic Circumpolar Current nonlinearities act upon deflecting a branch of this current northward, along the continental slope. This branch is then called Malvinas Current. It penetrates the South Atlantic ocean as far as converging with the South Brazil Current into the Brazil-Malvinas Confluence (Olson et al., 1988; Peterson et al., 1991).

The Brazil-Malvinas Confluence is precisely the region where these opposing and intense WBCs meet along the Southwestern Atlantic slope at about 38 S. As for other confluence regions in the world ocean, the Brazil-Malvinas Confluence is very energetic.

It is characterized by high eddy kinetic energy and mesoscale activity. It is a region of intense mixing and water mass transformation. In such a dynamic regime, cross-shelf exchanges occur (e.g. Guerrero et al., 2014). Therefore, the Brazil-Malvinas Confluence is a region of particular interest in the basin (Olson et al., 1988; Fig.1.5).

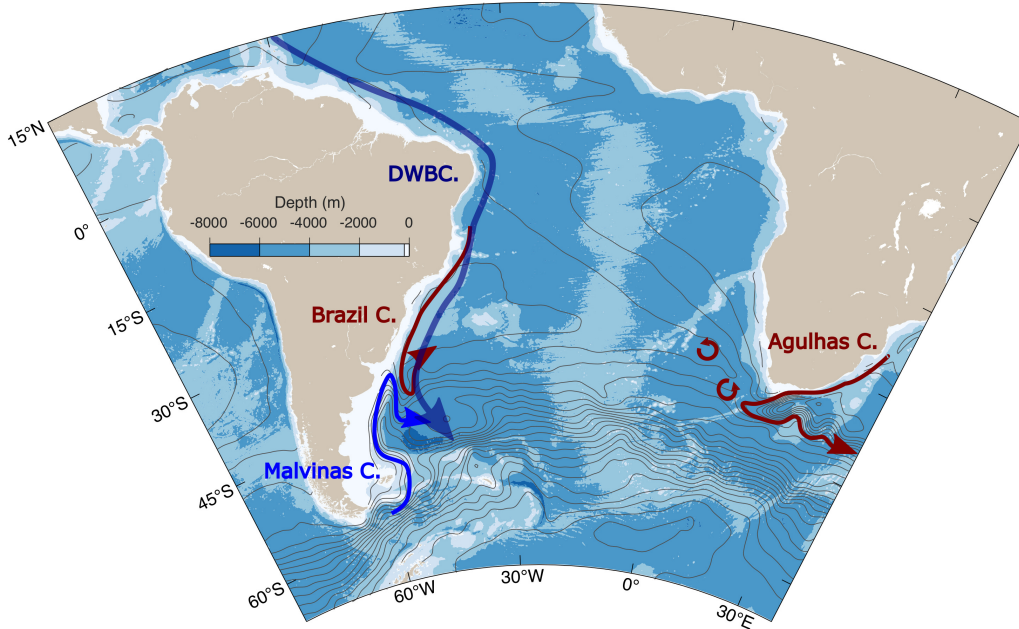


Figure 1.5: Schematic figure of the South Atlantic Western Boundary Currents. The South Brazil Current, Agulhas Current and Agulhas rings shed into the Atlantic, Malvinas Current, and the Deep Western Boundary Current. In shades, it is shown the bathymetry and gray lines show mean dynamic topography.

3 The ocean observing system and mesoscale eddies

Mesoscale eddies are ubiquitous structures in the ocean and one of the major sources of ocean variability (Stammer, 1997; Wunsch, 1999; Chelton et al., 2011). These round-shaped structures of 20-200 kilometers in diameter spin faster than they translate, and as a consequence they trap water in their core, advecting ocean properties like heat, salt, mass, and other biogeochemical properties across the World Ocean (Chelton et al., 1990; Chelton et al., 2011). The eddies are defined as mesoscale when their radius is larger or equal to R_d , and therefore are thought to be in near geostrophic balance, while oceanic structures smaller than R_d are defined as submesoscale (McWilliams, 2019). In the Southern Hemisphere, warm-core mesoscale eddies that produce an increase in sea level height and spin anticlockwise are called anticyclonic eddies, while those who have cold-core, produce a depression in sea level height and spin clockwise are called cyclonic eddies. Below the surface, anticyclonic eddies generate mass convergence, downwelling vertical movements and therefore a depression of the isopycnals, while cyclonic eddies

generate mass divergence, upwelling movements and a rising of the isopycnals. The former movement can upwell nutrient-rich waters into the euphotic layer, and therefore increase primary productivity at depth (Cornec et al., 2021; Fig.1.6).

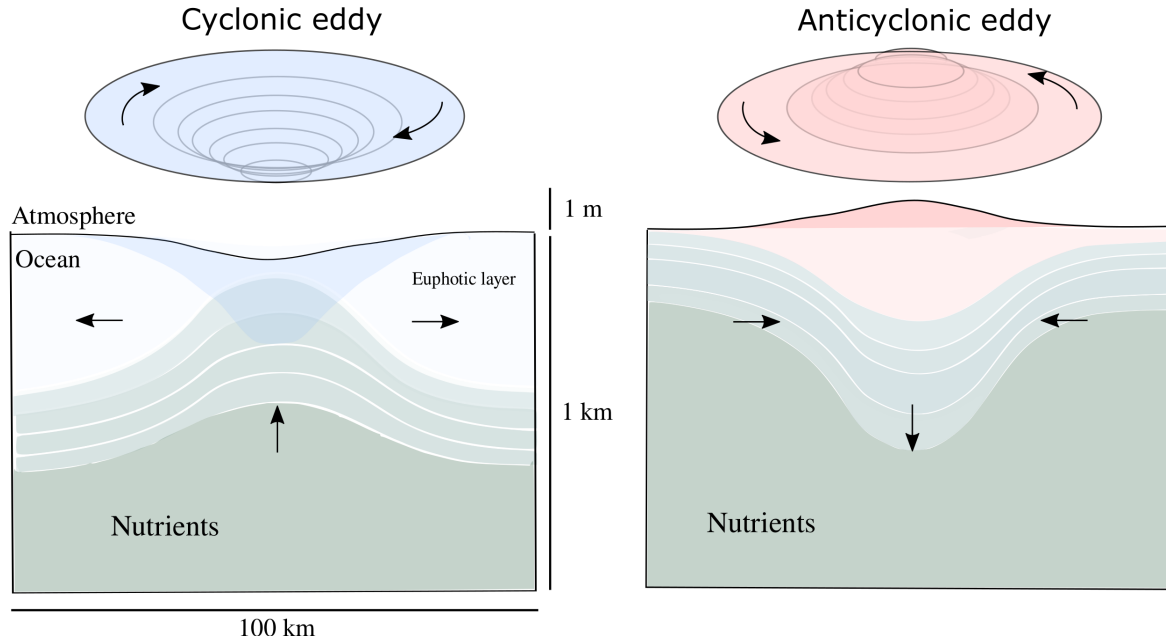


Figure 1.6: Schematic figure of mesoscale eddies in the Southern Hemisphere. Modified from Ioannou, 2019.

The existence of mesoscale eddies was already known from theory and sparse in situ observations (e.g. Fuglister et al., 1951), in particular from dedicated field experiments (e.g. The POLYMODE program; Collins et al., 1989). However, it was not until the introduction of satellite observations in the late 1970s that it was possible to see a snapshot of the surface global ocean revealing the ubiquitous presence of mesoscale eddies. A new era of observations was then introduced (Abdalla et al., 2021). Since the beginning of the infrared imagery of Earth's surface, very useful information was gathered including aspects of the oceanic circulation. For example, intense gradients over the slope and round-shaped patches of contrasting temperature revealed the presence of WBCs and mesoscale eddies, respectively (Olson et al., 1988; Fig.1.7).

Since the introduction of satellite altimetry in 1992, it was possible to estimate the near-surface geostrophic velocity of the ocean (Stammer et al., 2017). Satellite altimetry can measure the sea level height with a precision of millimeters (Chelton et al., 2011; Chelton et al., 2007; Hernandez et al., 1995), and by using the sea level height field, it is possible to adapt Equation 1 to estimate the surface geostrophic velocity:

$$(u_g, v_g) = \left(\frac{-g}{f} \frac{\partial \eta}{\partial y}, \frac{g}{f} \frac{\partial \eta}{\partial x} \right) \quad (1.5)$$

Were u_g, v_g are zonal and meridional geostrophic velocities, g and f gravity and Coriolis parameter respectively, and the sea level height (Stewart, 2008).

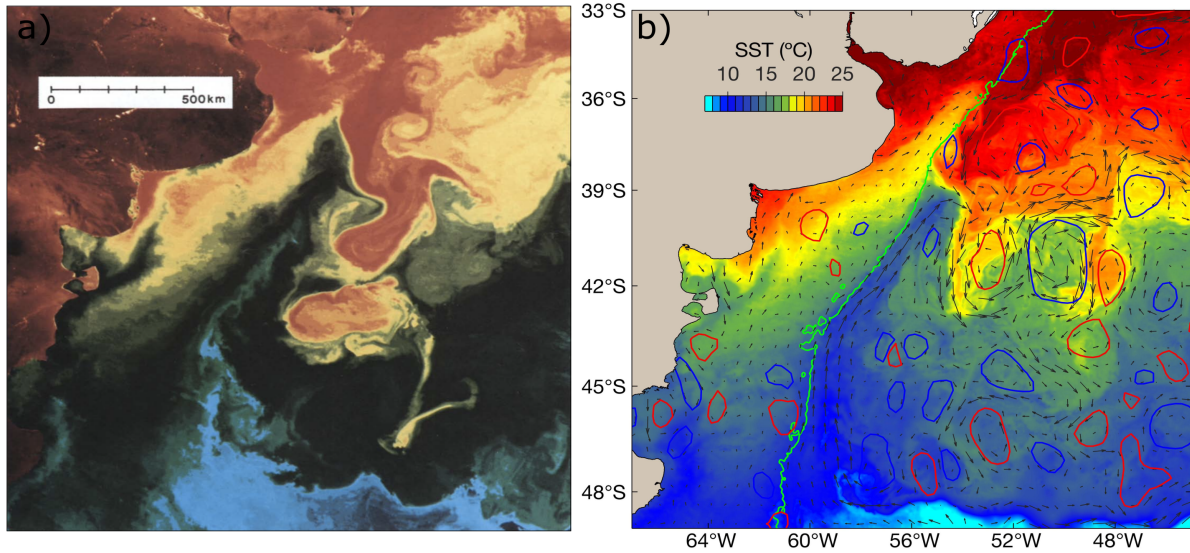


Figure 1.7: a) Overview of the surface temperature in the Brazil-Malvinas Confluence region during February 1985. Warm waters ($>20^{\circ}\text{C}$) are coded in red, temperature decreases grading through yellow and green with blues being the coldest ($<7^{\circ}\text{C}$). This time frame corresponds to a southward extension of the Brazil Current and the formation of a large anticyclonic warm eddy. Taken from Olson et al., 1988. b) Sea surface temperature in the Brazil-Malvinas Confluence as in a) but for a given day in February 2017. The vectors show altimetry-derived geostrophic velocities, and the red and blue contours anticyclonic and cyclonic eddies from an eddy tracking algorithm, respectively. The green line delimits the shelf-break at the 200m isobath.

In this way, it was now possible to have an estimation of the difference in the geostrophic velocity between two points. Nevertheless, satellite altimetry has several limitations such as: it is not possible to have a precise knowledge of the long term mean geostrophic circulation because a detailed mapping of the geoid is needed and this is still missing, and also satellite precision has changed over the time (Stammer et al., 2017); observations are done only at nadir, and therefore the measure is made only along the satellite track leading to an effective resolution lower than R_d in some regions depending on the frequency and distances of the satellite passages (Morrow et al., 2019; Fig.1.8). Moreover, ageostrophic movements in the ocean cannot be neglected. In spite of this, satellite altimetry is still a very good first-order approximation to the near-surface absolute velocity for the large-scale ocean circulation ($Ro \ll 1$), as decades of comparisons with in-situ observations have

demonstrated and therefore, at this scale ($Ro \ll 1$), sea surface isolines are equivalent to streamlines (Abdalla et al., 2021).

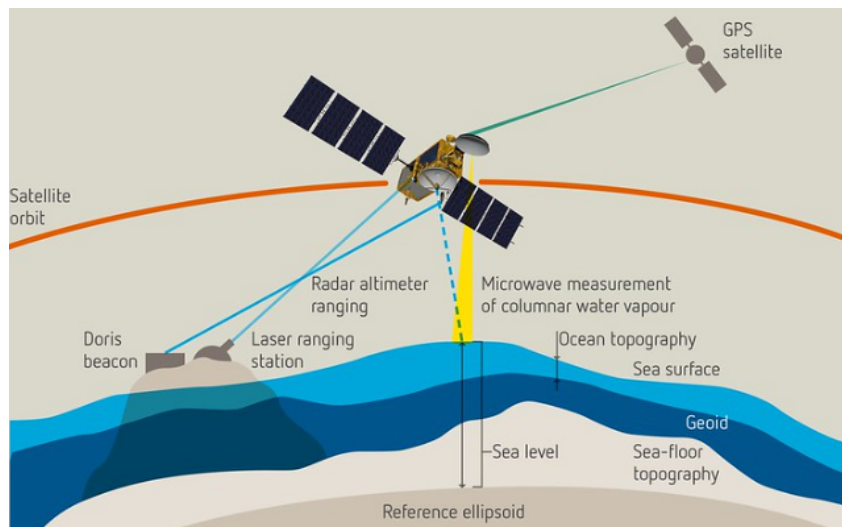


Figure 1.8: Schematic figure of satellite altimetry measurements. Taken from <https://www.eumetsat.int/>

Satellite altimetry also allows to identify and track mesoscale eddies by finding a sea-level relative extreme enclosed by streamlines of sea level of a similar size to the R_d . Many of the observed eddies behave as coherent structures over time. They also move at a velocity that is less than a distance equivalent to their diameter each day. As a consequence, the eddies areas (that can be visualized as closed streamlines or sea-surface contours) overlap through consecutive days. This allows the use of gridded maps of observations (SST or Sea Surface height, for example) to detect and track ocean eddies that are visible from such fields. Recently, objective eddy detection and tracking algorithms have been developed (Chaigneau et al., 2008; Chaigneau et al., 2011; Chelton et al., 2011; Pegliasco et al., 2015). In this study we will make an extensively use of a recent algorithm, TOEddies that not only detects eddies but also identifies the eddy splitting and merging events they undergo and colocalize the eddies with in situ vertical profiles achieved by Argo profiling floats and research cruises (Laxenaire et al., 2018; Laxenaire et al., 2019; Laxenaire et al., 2020).

As the ocean observing system expands, so is our capacity to study it. Nowadays, a common practice to monitor and study the ocean is to combine satellite observations, which give spatial and temporal information about the ocean, though these are restricted to the surface layers and to a few variables only (sea surface temperature, sea surface salinity, ocean color, sea level and derived geostrophic currents) with autonomous platforms in the ocean taking measurements at one point in the ocean but adding information

on the vertical and/or the same as satellite plus other variables. For example, a common complementary dataset for satellite eddy tracking algorithms is the colocalized Argo profiles, allowing to study the 3-D evolution of eddies in a completely autonomous way (Laxenaire et al., 2019; Laxenaire et al., 2020; Cornec et al., 2021). Argo floats are autonomous vertical profiling floats drifting in the ocean usually at 1000 m of depth and making a profile of temperature and salinity from 2000 m up to the surface every 10 days (Fig.1.9). The Argo International Program began in 2000 and has increased exponentially over the last decade due to its huge success, being a major contributor to what has been called a ‘Data Tsunami’ in oceanography (Brett et al., 2020).

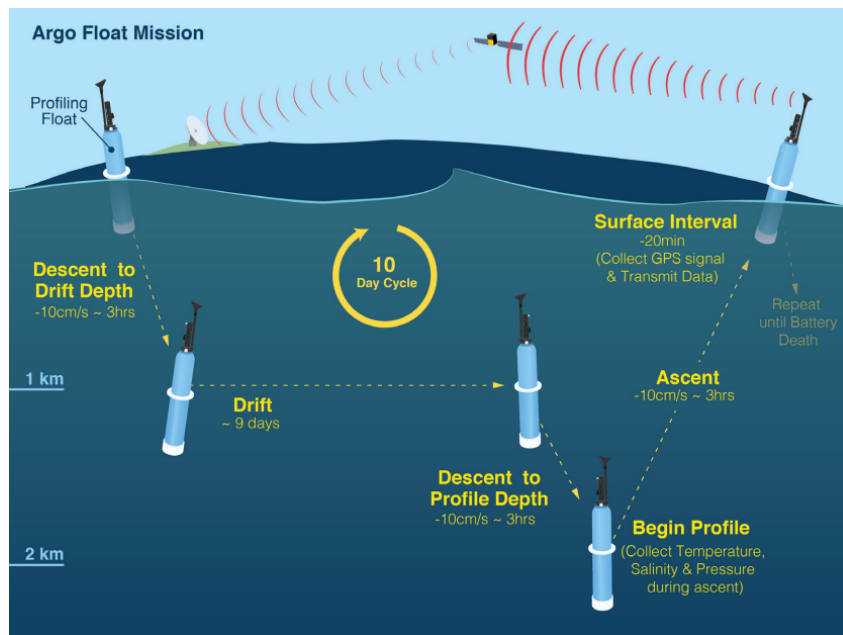


Figure 1.9: a) Argo cycle scheme. Taken from Jayne et al., 2017.

Several other platforms have contributed to the ‘Data Tsunami’ of the Global Ocean Observation System (GOOS), most of them autonomous, reducing operational costs and making a revolutionary contribution to oceanography. The Argo program now contains more than 2 million profiles and about 4000 active floats (e.g. Wong et al., 2020), and it is expanding towards Biogeochemical (BGC)Argo, measuring other variables like oxygen, fluorescence and nutrients, and the Deep Argo program, with floats profiling down to 6000m (Roemmich et al., 2019). The Animal Borne Ocean Sensors (AniBOS) network has allowed obtaining crucial CTD profiles in high latitudes over the last decade, especially in polar regions where part of the ocean is covered by ice and therefore difficult to access (e.g. McMahon et al., 2021). Gliders allow monitoring of oceanic sections quasi permanently at a low operational cost (e.g. Rudnick et al., 2017). Saldrones allow to study the ocean-atmosphere interface much more precisely than large ships, that mix the water

3. The ocean observing system and mesoscale eddies

column, and where instruments can be several meters apart (e.g. Gentemann et al., 2020; Fig.1.10).

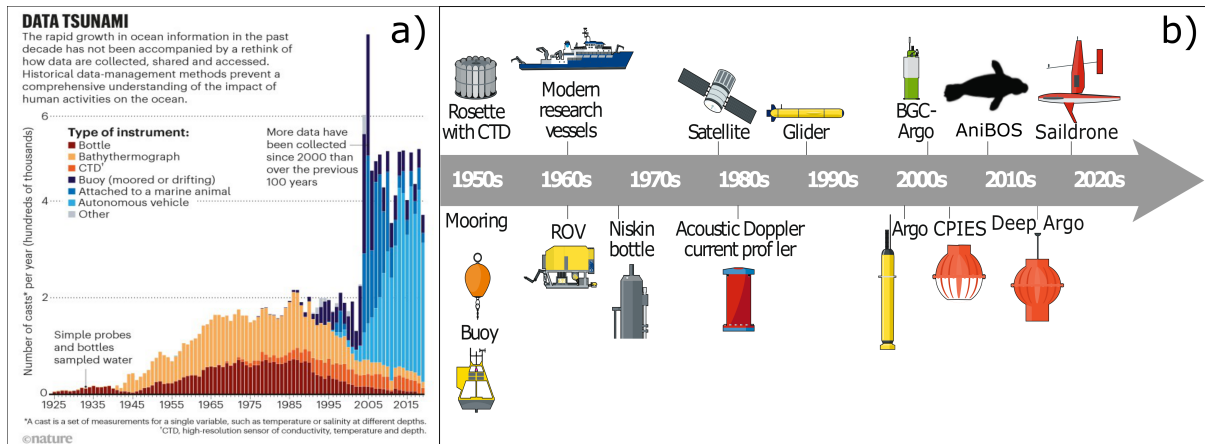


Figure 1.10: a) Timeline of oceanic casts. Taken from Brett et al., 2020. b) Timeline of oceanic platforms. Modified from Chai et al., 2020. In this diagram, the dates of the introduction of each instrument are a very raw approximation.

Also, the number of moorings has increased exponentially over the last decade. In the ocean bottom, Current and Pressure-recording Inverted Echo Sounders (CPIES) allow to estimate the volume transport through the water column. By displaying an array of CPIES over a latitudinal line in an ocean basin separated by a distance similar to R_d , and combined with in situ ocean density profiles and satellite observations, it is possible to obtain a time series of the estimated MOC at that latitude (Meinen et al., 2018). Most of the CPIES have been concentrated along the boundaries because it is where most of the transport takes place, and it is also closer to ports, reducing operational costs, as a ship is needed to display the moorings but also to obtain the data.

Over a decade of continuous observations of the AMOC has revealed an astonishing and unexpected variability of the deep ocean currents, which were believed to be almost steady in short-term periods, varying through the slow density fields in scales of decades or even longer. The CPIES showed large seasonal and intraseasonal oscillations, both for the North Atlantic at 26°N and 53°N (e.g. Srokosz et al., 2015) and in the South Atlantic at 34.5°S (e.g. Kersale et al., 2020; Chidichimo et al., 2021). This finding was even more valuable considering that the deployment of such basin-wide arrays of moorings (e.g. Rapid Climate Change (RAPID) at 26°N and South Atlantic Meridional Overturning Circulation – Basin-wide Array (SAMBAR) at 34.5°S) were done after the publication of several articles in the early 2000s that concluded that the AMOC could be slowing down very fast due to anthropogenic warming and could eventually derive in

an abrupt climate change, alerting the whole scientific community (e.g. Vellinga et al., 2002). For example, Bryden et al., 2005) projected a decreasing trend of the AMOC of about 30% over the last 50 years based on five ship-based observations. Since then, a large international effort has been made to monitor the AMOC and expand the Global Observing System in general, and almost every boundary current is being monitored (Frajka-Williams et al., 2019; Fig.1.11).

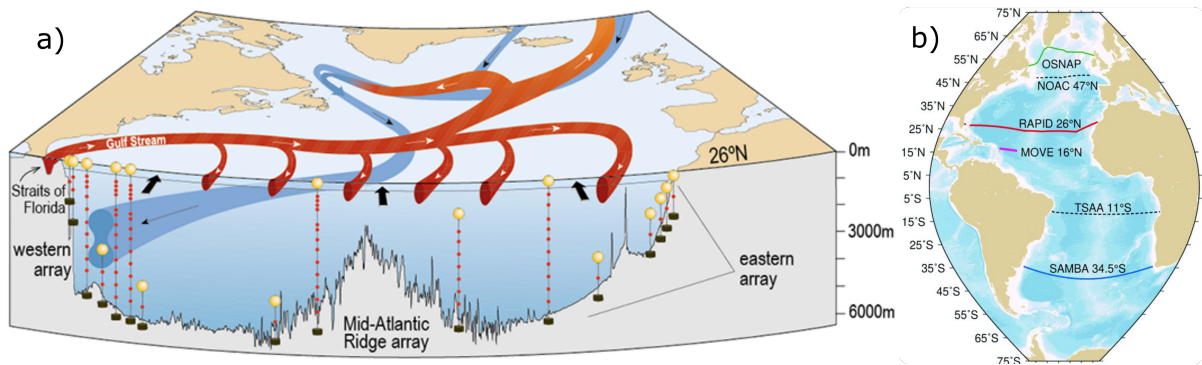


Figure 1.11: a) Schematic figure of the RAPID mooring array in the North Atlantic. b) Location of other mooring arrays in the Atlantic Ocean, with their respective names. Taken from <https://rapid.ac.uk/>

The South Atlantic Meridional overturning circulation Basin-wide Array at 34.5°S (SAMBA) is the longest time series of the AMOC and MHT in the South Atlantic with about one decade of data. It is located in the southernmost latitude with coasts on both sides in the South Atlantic, and therefore prone to inter-oceanic exchanges, particularly next to Africa. It is also a region of high eddy-kinetic energy in both boundaries. Large variability has been observed along this array, especially in the intraseasonal time scale, when compared to the North Atlantic (Meinen et al., 2013; Meinen et al., 2018; Kersalé et al., 2021; Fig.1.12). Even though obtaining a time series of the AMOC is a large and fundamental step towards understanding deep ocean variability, this mooring array still has limitations. For example, only density anomalies can be computed from in-situ observations at 34.5°S (Relative contribution in Fig.1.12), and therefore to estimate the total transport a time-mean reference velocity from a model needs to be added (Reference contribution in Fig.1.12), in addition to Ekman transport estimated from wind satellite (Ekman contribution in Figure 12) (Meinen et al., 2018; Kersalé et al., 2021). Therefore, the understanding of the AMOC's structure and variability needs the use of a multi-platform approach.

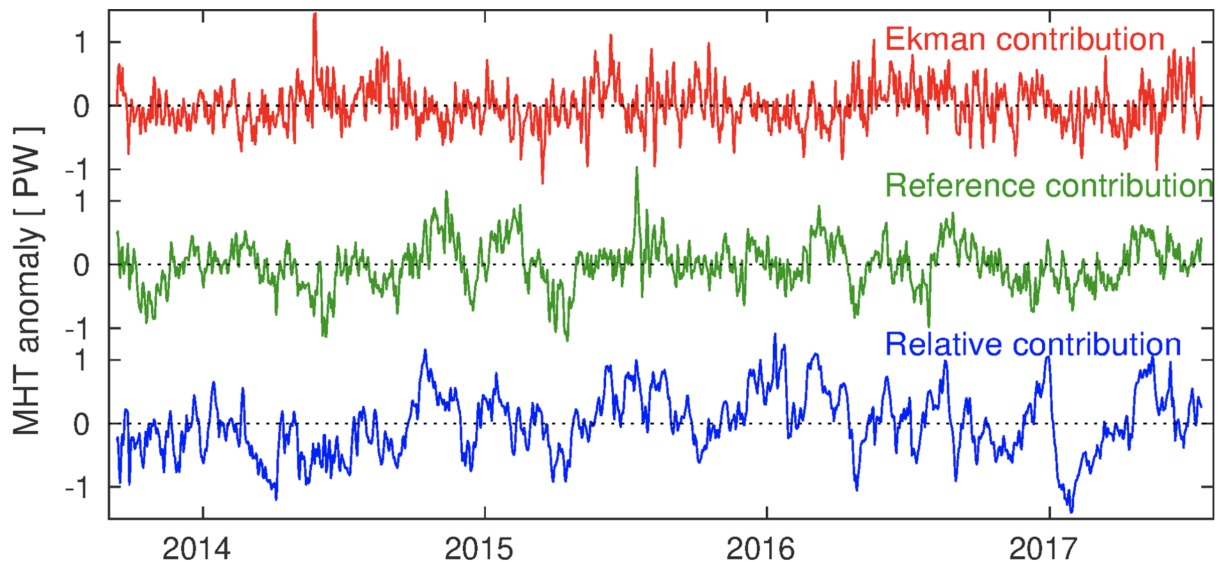


Figure 1.12: Meridional Heat Transport (MHT) anomaly over the SAMBA line at 34.5°S in the Atlantic. Ekman contribution is estimated from satellite, reference contribution from ECCO2 model (Menemenlis et al., 2005), and relative contribution from moorings (PIES). Reproduced from Kersalé et al., 2021.

4 General objectives

The last decade has seen the realization of theoretical advances and assessments from observations and numerical modeling on ocean circulation, mesoscale dynamics and variability. These provide a better understanding of various phenomena, such as the global ocean circulation, lateral and vertical mixing, and mechanisms for advection of water masses. This is of great importance for apprehending the role of the ocean circulation on climate and marine ecosystems. This thesis has focussed on such processes in the South Atlantic ocean. This is one of the most turbulent regions of the world ocean and it is also central to the AMOC. In particular, the work has tried to answer to the following questions:

1 - What is the amplitude of the mean AMOC in the South Atlantic and what is the role of mesoscale eddies?

This thesis tried to answer this question, by assessing the meridional transports of volume, heat and freshwater across the SAMBA line, a zonal section at 34.5°S in the South Atlantic where mooring arrays are deployed and a GO-SHIP cruise has been achieved in early 2017. The assessments will then be discussed by comparing the results with previously published work using a more classical geostrophic constraint in the larger South Atlantic area and direct estimates of MOC variability from the 34.5°S mooring data. This part of the PhD work has been published in *Journal of Geophysical Research*:

Oceans (Manta et al., 2021) and is presented in Chapter 2.

2 - What is the role of mesoscale eddies in western boundary currents variability and cross-shelf exchanges?

In this framework, the PhD work has focused on the dynamics of the South Brazilian Current and its confluence with the Malvinas Current which represents a hotspot of eddy kinetic energy in the South Atlantic. This area is important as it undergoes strong air-sea interactions and regulates regional marine ecosystems. The approach undertaken takes advantage of a very high-resolution oceanographic cruise, Argo profiling floats and satellite data. This work has been formalized as a paper and published in *Frontiers in Marine Sciences* (Manta et al., 2022). The main outcomes are discussed in Chapter 3 of this manuscript.

3 - To finalize the assessment on the South Atlantic ocean circulation, the PhD study attempts to address the main modes of the basin's coupled ocean-atmosphere variability.

Indeed, the South Atlantic AMOC as well as the South Brazil – Malvinas current system show variability at different time scales. In order to separate the ocean internal variability from that due to the coupled ocean-atmosphere modes, the PhD work has been finalized by a careful analysis of the latter that allows consolidating the previous results as well as studies previously published on this topic. This part of the PhD work is presented and discussed in Chapter 4 of this manuscript. Finally, Chapter 5 provides the conclusions of the PhD study and discusses possible perspectives to be examined in the future.

Chapter 2

The South Atlantic Meridional Overturning Circulation and Mesoscale Eddies in the First GO-SHIP Section at 34.5°S

In this chapter we analyzed the data from the first GO-SHIP Section at 34.5°S, which took place in January 2017. We described the water masses properties along the section, estimated the transports, and studied the impact of satellite-detected mesoscale eddies along the section. We found considerable zonal differences in the water masses properties and transport. We estimated the heat transport and compared it with other GO-SHIP sections carried out in the past at lower latitudes in the South Atlantic. We found an equatorial net heat transport at 34.5°S that increases towards lower latitudes, consistent with previous research. By combining the section data with satellite observations, an eddy tracking algorithm and Argo floats profiles, we estimated the contribution of mesoscale eddies to the transports. The study provides evidence that they have indeed a significant contribution. We also showed that one month, which is an average period in which a ship working 24 hours per day takes to go from one boundary to the other of the basin carrying out full-depth CTD stations every 50 km across an ocean basin, it cannot be considered as a synoptic situation, as also revealed by recent publications using data retrieved from moorings (e.g. Kersalé et al., 2020). Despite the expansion of the Global Ocean Observing System is revealing limitations of the GO-SHIP sections (e.g. that oceanic meridional transports are highly variable at relatively short time periods and therefore one section per decade might be aliased by such variability), these sections remain not only a useful dataset per se but also a reference for all other observations and modeling due to their high resolution and quality standards of the data.

Key Points:

- Overturning maximum is 15.64 ± 1.39 Sv; Meridional heat and freshwater transport are 0.27 ± 0.10 PW and 0.23 ± 0.02 Sv, respectively
- Excluding the mesoscale eddies from the section increased the meridional heat transport by 0.12 PW
- The distribution of water masses and currents reflects the favorable position of the section for observing

Supporting Information:

- Supporting Information S1

Correspondence to:

G. Manta,
gaston.manta@lmd.ens.fr





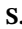













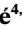
Citation:

Manta, G., Speich, S., Karstensen, J., Hummels, R., Kersalé, M., Laxenaire, R., et al. (2021). The South Atlantic meridional overturning circulation and mesoscale eddies in the first GO-SHIP section at 34.5°S. *Journal of Geophysical Research: Oceans*, 126, e2020JC016962. <https://doi.org/10.1029/2020JC016962>

Received 7 NOV 2020

Accepted 21 DEC 2020

The South Atlantic Meridional Overturning Circulation and Mesoscale Eddies in the First GO-SHIP Section at 34.5°S

G. Manta^{1,2} , S. Speich¹ , J. Karstensen³ , R. Hummels³ , M. Kersalé^{4,5} , R. Laxenaire⁶ , A. Piola^{7,8,9,10} , M. P. Chidichimo^{7,9,10} , O. T. Sato¹¹ , L. Cotrim da Cunha¹² , I. Ansoorge¹³ , T. Lamont^{13,14,15} , M.A. van den Berg¹⁴ , U. Schuster¹⁶ , T. Tanhua³ , R. Kerr¹⁷ , R. Guerrero¹⁸ , E. Campos^{11,19} , and C. S. Meinen⁵ 

¹Laboratoire de Météorologie Dynamique, LMD-IPSL, École Polytechnique, ENS, CNRS, Paris, France, ²Departamento de Ciencias de la Atmósfera, Facultad de Ciencias, Universidad de la República, Montevideo, Uruguay, ³GEOMAR Helmholtz Centre for Ocean Research Kiel, Kiel, Germany, ⁴Cooperative Institute for Marine and Atmospheric Studies, University of Miami, Miami, FL, USA, ⁵NOAA Atlantic Oceanographic and Meteorological Laboratory, Miami, FL, USA, ⁶Center for Ocean-Atmospheric Prediction Studies, Florida State University, Tallahassee, FL, USA, ⁷Departamento de Oceanografía, Servicio de Hidrografía Naval (SHN), Buenos Aires, Argentina, ⁸Departamento de Ciencias de la Atmósfera y los Océanos, Universidad de Buenos Aires, Buenos Aires, Argentina, ⁹Consejo Nacional de Investigaciones Científicas y Técnicas, Buenos Aires, Argentina, ¹⁰Instituto Franco-Argentino Sobre Estudios de Clima y Sus Impactos, CNRS-CONICET-UBA, Buenos Aires, Argentina, ¹¹Oceanographic Institute, University of São Paulo, São Paulo, Brazil, ¹²Faculdade de Oceanografia, BrOA, Universidade do Estado do Rio de Janeiro, Rio de Janeiro, Brazil, ¹³Oceanography Department, University of Cape Town, Cape Town, South Africa, ¹⁴Department of Environment, Forestry and Fisheries, Oceans & Coasts Research Branch, Cape Town, South Africa, ¹⁵Bayworld Centre for Research and Education, Cape Town, South Africa, ¹⁶College of Life and Environmental Sciences, University of Exeter, Exeter, UK, ¹⁷Laboratório de Estudos dos Oceanos e Clima, Instituto de Oceanografia, Universidade Federal do Rio Grande—FURG, Rio Grande, Brazil, ¹⁸Departamento de Ciencias Marinas, Facultad de Ciencias Exactas y Naturales, Universidad Nacional de Mar del Plata, Funes, Argentina, ¹⁹Department of Biology, Chemistry and Environmental Sciences, College of Arts and Sciences, American University of Sharjah, Sharjah, United Arab Emirates

Abstract The variability of the Atlantic meridional overturning circulation (AMOC) has considerable impacts on the global climate system. Past studies have shown that changes in the South Atlantic control the stability of the AMOC and drive an important part of its variability. That is why significant resources have been invested in a South (S)AMOC observing system. In January 2017, the *R/V Maria S. Merian* conducted the first GO-SHIP hydrographic transect along the SAMOC-Basin Wide Array (SAMBA) line at 34.5°S in the South Atlantic. This paper presents estimates of meridional volume, freshwater (MFT), and heat (MHT) transports through the line using the slow varying geostrophic density field and direct velocity observations. An upper and an abyssal overturning cell are identified with a strength of 15.64 ± 1.39 Sv and 2.4 ± 1.6 Sv, respectively. The net northward MHT is 0.27 ± 0.10 PW, increasing by 0.12 PW when we remove the observed mesoscale eddies with a climatology derived from the Argo floats data set. We attribute this change to an anomalous predominance of cold core eddies during the cruise period. The highest velocities are observed in the western boundary, within the Brazil and the Deep Western Boundary currents. These currents appear as a continuous deep jet located 150 km off the slope squeezed between two cyclonic eddies. The zonal changes in water masses properties and velocity denote the imprint of exchange pathways with both the Southern and the Indian oceans.

Plain Language Summary The Atlantic meridional overturning circulation (AMOC) is a crucial element of the global ocean circulation and climate. It connects the Southern Ocean to the northern North Atlantic, and is responsible for the interhemispheric northward transport of heat and freshwater. The South Atlantic is a crossroad for water masses from the Southern, the Indian and the North Atlantic oceans. This paper analyzes the first full-ocean-depth trans-basin measurements of the southernmost enclosed section of the Atlantic between South Africa and Brazil along 34.5°S. Our results confirm a northward transport of heat at this latitude. We also found a complex water mass structure and dynamics, characterized by intense boundary currents and mesoscale eddies. It is the sum of these elements that is not only crucial for the Atlantic but also for the global ocean circulation and climate.

1. Introduction

The meridional overturning circulation (MOC) is a global-wide circulation pattern that connects the overturning cells confined within ocean basins and helps to promote the balance of the net buoyancy loss in the northern North Atlantic and around Antarctica. While the excess heat from the tropics is transported by the upper ocean to higher latitudes in each basin through the western boundary currents as a response to the wind-driven circulation, the density-driven part of the MOC originates from sinking waters at high latitudes. It consists of two global-scale meridional overturning cells. The “upper-cell,” responsible for most of the volume transport; it is linked to the formation of North Atlantic Deep Water (NADW) in the subpolar North Atlantic and Nordic Seas, but also to the upwelling of deep waters in the Southern Ocean. The “lower” or “abyssal” cell is linked to the dense water formation around Antarctica and to the abyssal upwelling due to the interaction of the flow with the bottom topography (Lumpkin & Speer, 2007; T. J. McDougall & Ferrari, 2017; Talley, 2003). The MOC plays a crucial role in the global climate system, with a maximum northward heat transport of 1.3 PW (1.3×10^{15} W) in the subtropical North Atlantic, accounting for 25% of the global combined atmosphere-ocean meridional heat flux (Buckley & Marshall, 2016; Frajka-Williams et al., 2019; Hsiung, 1985; Johns et al., 2011; Talley, 2003).

As the Atlantic Ocean plays a key role in the global system, that segment of the MOC is usually referred to as the Atlantic meridional overturning circulation (AMOC; e.g., Talley, 2003). The South Atlantic is the only basin with a net heat transport from the pole to the equator as the upper 1200 m layer flows northward to compensate for the southward export of colder NADW (Buckley & Marshall, 2016; S. L. Garzoli et al., 2013). Another distinguishing characteristic of the AMOC in the North and South Atlantic is a large disparity in the strength of the abyssal overturning cell between hemispheres. While the abyssal cell transport is roughly 45% the size of the transport associated with upper overturning cell at 34.5°S in the Southwestern Atlantic (7.8 Sv vs. 17.3 Sv respectively; 1 Sv = 10^6 m³ s⁻¹; Kersalé et al., 2020), in the North Atlantic at 26.5°N the abyssal cell is very weak, only about 1 Sv (Frajka-Williams et al., 2011; Lumpkin & Speer, 2007).

The South Atlantic basin exhibits a wide range of interoceanic convergences and mixing of different waters in the upper limb of the upper overturning cell. The landmass configuration in conjunction with the wind-driven circulation leads to an inflow of cold and fresh waters from the Pacific through the Drake Passage via the so-called “cold water route” as well as warmer and saltier Indian Ocean waters via the Agulhas Current leakage around South Africa, which is usually referred to as the “warm water route” (A. L. Gordon, 1985; Rintoul, 1991; Speich et al., 2007, 2001). Large anticyclonic eddies, referred to as Agulhas Rings (Lutjeharms & Gordon, 1987; Ou et al., 1986), filaments, and coastal jets (Lutjeharms et al., 1992) also play roles in the Indian to Atlantic transfer.

The transport of water from the Indian and South Pacific oceans into the South Atlantic has substantial implications for the overturning circulation of the Atlantic Ocean as a whole (A. L. Gordon, 1985). Weijer et al. (1999) and Biastoch et al. (2008) have demonstrated that these interbasin fluxes of heat and salt are important for maintaining the stability of the AMOC. Moreover, coupled general circulation models show a strong sensitivity in the response of the AMOC to the magnitude and direction of the salt transport through the southern boundary of the Atlantic basin (e.g., Cimadoribus et al., 2012; Drijfhout et al., 2011).

Agulhas Rings play a fundamental role in the transport of warm and salty Indian water into the South Atlantic. Recent studies have shown these eddies have a particularly long lifetime, which can exceed 4 years, and that they can cross the South Atlantic basin and reach the Brazilian coast (Arhan et al., 1999; Guerra et al., 2018; Laxenaire et al., 2018). As they move in the South Atlantic, the core water masses are modified by local air-sea interactions (S. L. Garzoli & Matano, 2011; Laxenaire et al., 2019). This complex circulation within the South Atlantic represents a strong motivation to study the AMOC in the South Atlantic.

Broader understanding of the importance of AMOC variability in the South Atlantic led to the development of an international initiative to study the AMOC in the South Atlantic—the South Atlantic meridional overturning circulation initiative (SAMOC; e.g., Ansorge et al., 2014; Speich et al., 2009). Over the last few decades, several efforts have been made to measure the AMOC strength in the South Atlantic. Snapshot trans-basin ship sections were conducted as part of the World Ocean Circulation Experiment (WOCE) in the 1980s and 1990s, and some of these sections were later repeated as part of the Global Ocean Ship-based Hydrographic Investigation Program (GO-SHIP; e.g., Sloyan et al., 2019; Talley et al., 2016). These sections

Table 1
Summary of Previous Estimates of South Atlantic Upper Overturning Circulation ($AMOC_{max}$), Total Meridional Heat (MHT) and Freshwater Transport (MFT), at 34.5°S and Nearby Latitudes

| Source | Section-latitude | $AMOC_{max}$ (Sv) | MHT (PW) | MFT (Sv) | Date (mm/yy) | Data |
|--------------------------------|------------------|-------------------|-----------------|---------------|--------------|--------------------|
| Hernández-Guerra et al. (2019) | A10-30°S | 11.7–17.7 | Not provided | Not provided | 11/03–9/11 | GO-SHIP |
| Bryden et al. (2011) | 24°S | 21.5–16.5 | 0.7–0.4 | 0.04–0.17 | 2/83–2/09 | GO-SHIP |
| McDonagh and King (2005) | A10-30°S | Not provided | 0.22 ± 0.08 | 0.5 ± 0.1 | 12/92 | GO-SHIP |
| McDonagh and King (2005) | A11-45°S | Not provided | 0.43 ± 0.08 | 0.7 ± 0.1 | 12/92 | GO-SHIP |
| Holfort and Siedler (2001) | A10-30°S | Not provided | 0.29 | Not provided | 12/92 | GO-SHIP |
| Holfort and Siedler (2001) | A11-45°S | Not provided | 0.37 | Not provided | 12/92 | GO-SHIP |
| S. L. Garzoli et al. (2013) | AX18–35.1°S | 18.1 ± 2.3 | 0.54 ± 0.14 | Not provided | 02–11 | XBTs, Argo and WOD |
| Majumder et al. (2016) | 34.5°S | 20.66 ± 4.13 | 0.66 ± 0.21 | Not provided | 00–14 | Argo & Altimetry |
| Dong et al. (2015) | 34.5°S | 19.5 ± 3.48 | 0.49 ± 0.22 | Not provided | 93–06 | Altimetry |
| Kersalé et al. (2020) | 34.5°S | 17.3 ± 5.0 | Not provided | Not provided | 09/13–07/17 | PIES |
| C. S. Meinen et al. (2018) | 34.5°S | 14.7 ± 8.3 | Not provided | Not provided | 03/09 12/10 | CPIES & model |
| Perez et al. (2011) | 34.5°S | 15.6 ± 3.1 | 0.42 ± 0.18 | Not provided | 86–98 | Model |

Note. The reference citation, date, and data used are also shown. Note that different studies used different error estimate methods.

are surveyed with high accuracy, full depth, coast to coast measurements with a spatial resolution of near the internal Rossby deformation radius (around 40 km for the deep ocean at 34.5°S; Talley et al., 2016). The data provide a quasi-synoptic picture of an oceanic section, although conducting a trans-basin section/cruise at these latitudes takes roughly a month. Assuming the ocean to be in hydrostatic and geostrophic balance, the meridional flow can be estimated considering boundary conditions such as a mass balance (Wunsch, 1996). At least four GO-SHIP sections along the A10 transect nominally along 30°S have been conducted since 1993 (e.g., Hernández-Guerra et al., 2019). Likewise, another four GO-SHIP sections have been occupied along 24°S (e.g., Bryden et al., 2011) and one along 45°S (Holfort & Siedler, 2001) over the same time period.

Repeated expendable bathythermograph (XBT) transects collected via ships of opportunity have also been used to estimate quasi-quarterly meridional transports of volume and heat over the past 2 decades; XBT probes measure the temperature in the upper 800 m or so, with these data being combined with data from deeper reaching profile data (e.g., Argo profiles), with satellite altimetry data, and/or with deep ocean historical climatologies in order to calculate AMOC and MHT (Dong et al., 2009, 2015; Garzoli & Baringer, 2007; S. L. Garzoli et al., 2013; Majumder et al., 2016). A summary of historical oceanic flux calculations from GO-SHIP sections and XBTs transects in the South Atlantic are shown in (Table 1).

Another approach to measuring the AMOC is via basin-wide arrays. These arrays typically involve a mix of geostrophic/density end point moorings and direct velocity observing systems, such as the RAPID-MOCHA-WBTS array deployed at 26.5°N (e.g., Cunningham et al., 2007) and the OSNAP array within the Subpolar North Atlantic (Lozier et al., 2017). Using auxiliary data (e.g., hydrographic information for the interior ocean) additional properties such as the MHT can be estimated from these trans-basin arrays as well (e.g., Johns et al., 2011). The arrays provide high resolution (daily) observations and a key finding has been that the AMOC transport shows surprisingly large variability on intraseasonal to interannual timescales (e.g., Cunningham et al., 2007; Kanzow et al., 2010; Lozier et al., 2019; Srokosz & Bryden, 2015).

Basin-wide AMOC arrays in the South Atlantic include the international South Atlantic MOC Basin-wide Array (SAMBA; e.g., Anson et al., 2014; Speich et al., 2009) at 34.5°S and an array at 11°S (e.g., Herrford et al., 2020). The SAMBA line of moorings began in a pilot mode in 2009, with a much better resolved array put in place beginning in 2013. SAMBA consists primarily of pressure-equipped inverted echo sounders (PIES) and current-and-pressure-equipped inverted echo sounders (CPIES), with four additional tall dynamic height/current meter moorings added on the South African continental margin in 2014 (e.g., Kersalé et al., 2018, 2020, 2019; C. S. Meinen et al., 2013; 2018). Hydrographic observations collected during the

mooring maintenance cruises provide regional snapshots of the flow patterns and water mass regimes in the boundary regions. For example, the location and strength of two branches of the lower limb of the AMOC at 34.5°S, each carrying significant flows of recently ventilated North Atlantic Deep Water, have been identified using shipboard hydrographic observations as well as moored observations on both the western (e.g., Valla et al., 2018, 2019) and eastern boundaries (e.g., Kersalé et al., 2018, 2019).

The strength of the AMOC (henceforth referred to as $AMOC_{max}$) at each latitude is defined as the vertical maximum of the stream function and is always located in the upper-cell (Buckley & Marshall, 2016). Different observational estimates of the $AMOC_{max}$ at 34.5°S or in close proximity vary from 17.9 Sv to 18.1 Sv (XBTs; Dong et al., 2009; S. L. Garzoli et al., 2013), 11.7–21.5 Sv (trans-basin hydrographic cruises; Hernández-Guerra et al., 2019), and 19.5–20.7 Sv (Argo- and satellite-derived MOC; Majumder et al., 2016). Using the shallowest PIES mooring at each margin of the SAMBA section together with Ekman transport estimates from gridded observation-based winds (Cross-Calibrated Multi-Platform) and a time-mean reference velocity estimate at one specific depth from different ocean models, the $AMOC_{max}$ upper-cell transport over a period of ~ 6 years has been estimated to be about 14.7 ± 8.3 Sv (temporal standard deviation; C. S. Meinen et al., 2018). More recently, estimates that include the full array of SAMBA PIES and CPIES between September 2013 and July 2017 provide an $AMOC_{max}$ time-mean upper-cell transport value of 17.3 Sv and a temporal standard deviation of 13 Sv after applying a 30-day low-pass filter (Kersalé et al., 2020). Kersalé et al. (2020) also estimated a time-mean value of 7.8 ± 6.2 Sv transport of the $AMOC_{max}$ abyssal-cell.

It should be noted that estimates like the latter in the South Atlantic are far fewer in number, coming solely from hydrographic sections between latitudes ranging from 24°S to 32°S. It should also be noted that the methods applied to the SAMBA mooring array rely on a time-mean reference velocity from numerical models at one specific depth. In addition, as no measurements exist inshore of 1,350 dbar on both boundaries, estimates in those shelf areas are also based on model velocities. As such, only the variability of $AMOC_{max}$ from the SAMBA PIES/CPIES array is a complete robust observational assessment (Kersalé et al., 2020).

Previous estimates of the $AMOC_{max}$ variability at this latitude from blended altimetry and XBT sections data (e.g., Dong et al., 2015) or Argo float data (e.g., Majumder et al., 2016) have revealed substantial seasonal to interannual variability, where the Ekman as well as the geostrophic transport contribution play a role both showing annual cycles, which are out of phase. The SAMBA-SAMOC observations have also demonstrated a significant high-frequency variability (Kersalé et al., 2020; C. S. Meinen et al., 2018). Both baroclinic (density) and barotropic (bottom pressure) variations at the eastern boundary at 34.5°S show significant or even dominant contributions to the overall AMOC variability at 34.5°S. These findings are different to the ones at 26.5°N, where previous work has shown that the baroclinic (density) component in the eastern boundary contributes primarily on the seasonal time scale (e.g., Chidichimo et al., 2010). At interannual time scales, large (~3 Sv) changes in the $AMOC_{max}$ have been observed both at 26.5°N and 34.5°S (e.g., C. S. Meinen et al., 2018; Smeed et al., 2018). A recent study which used the entire SAMBA moored array has shown that the amplitude of the $AMOC_{max}$ variability at 34.5°S is even larger than previously estimated with a standard deviation of 15.5 Sv for the upper-cell and 6.2 Sv for the abyssal-cell (Kersalé et al., 2020). The strongest variability occurs on timescales between 30 and 90 days tightly linked to the passage of eddies across the section (Kersalé et al., 2019). At the boundaries, not only the upper layers but also the deep and abyssal flows are highly variable with the standard deviation exceeding the time mean C. S. Meinen et al., 2017; Kersalé et al., 2019; Valla et al., 2019).

In addition to the volume transport, the meridional heat (MHT) and freshwater (MFT) transports associated with the $AMOC_{max}$ are of interest (Table 1), as variations in these flows can have significant impacts on the global climate system (e.g., Lopez et al., 2016). While the $AMOC_{max}$ is logically broken up into upper and abyssal cells, which seem to vary independently (Kersalé et al., 2020), the MHT and MFT estimates are really only meaningful as full-depth calculations. Full-depth MFT have been estimated for latitudes neighboring 34.5°S (Bryden et al., 2011; McDonagh & King, 2005). At 34.5°S MFT estimates have derived combining upper ocean measurements from XBTs and Argo floats merged with deep hydrographic climatologies (Dong et al., 2015; S. L. Garzoli et al., 2013; Majumder et al., 2016) or by analysis of model simulations (Perez et al., 2011; Table 1).

A first set of full-depth trans-basin hydrographic observations along 34.5°S were collected in early 2017 (Figure 1). Here we present the observed hydrographic structure, the derived volume transport or $AMOC_{max}$,

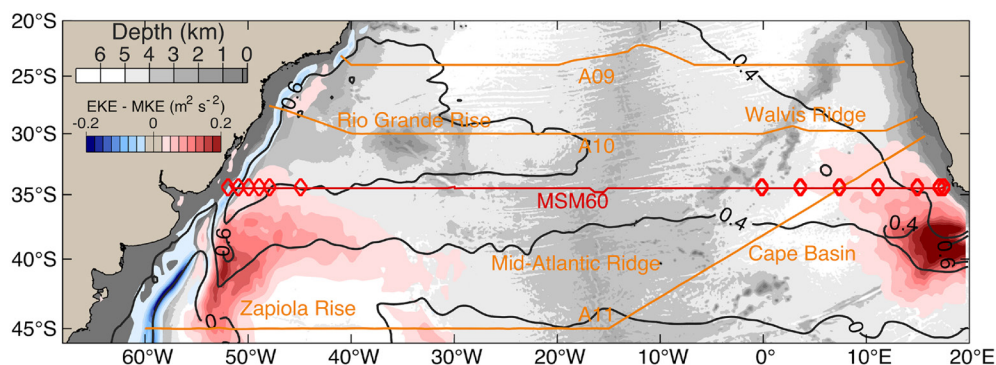


Figure 1. South Atlantic region with the bathymetry from ETOPO2 (Smith & Sandwell, 1997) shaded in gray. In red and blue shades is shown the long-term eddy kinetic energy (EKE) -mean kinetic energy (MKE) computed from Duacs/AVISO surface geostrophic velocity fields. The long-term mean dynamic topography also from Duacs/AVISO is shown as black contours to depict the mean basin circulation. The major bathymetric features are labeled in orange text. GO-SHIP sections are shown as orange lines and the MSM60 cruise track in red. Red diamonds over 34.5°S line show the location of moorings deployed (taken from C. S. Meinen et al., 2017; Kersalé et al., 2019).

MHT, and MFT and compare the results with other estimates, including those from the moored instruments in SAMBA. Moreover, the variability linked to the presence of eddies and its impact on oceanic fluxes along the section is also analyzed.

2. Data

2.1. Ship Observations

We used the hydrographic data collected during the expedition of the German Research Vessel *Maria S. Merian* conducted on January 4 to 31, 2017 (MSM60). In total, 128 full water depth stations (down to 5,450 m) were carried out. These stations were located nominally every 50 km with an increase in horizontal resolution over the continental margins. The rosette system included a pumped Sea-Bird SBE 9plus conductivity-temperature-depth (CTD) system, equipped with double sensor packages for temperature, conductivity (salinity) and oxygen, and lowered acoustic doppler current profilers (LADCP; two Teledyne 300 kHz instruments), and 22 sampling bottles with 10 liter capacity. Water samples were collected for oxygen, salinity, and other chemical properties. Salinity samples were analyzed with Optimare salinometer, Oxygen samples were analyzed on board using the Winkler method, and both were used to calibrate the observations from the CTD. The sampling and calibration for the data reported here followed the respective GO-SHIP recommendations (Hood et al., 2010; Sloyan et al., 2019). Underway measurements included two ship-mounted acoustic doppler current profilers (SADCPs) of 75 and 38 kHz. See further details on the data collection and quality control in Karstensen et al. (2019).

Moreover, ship observations from GO-SHIP sections A09 at 24°S (King & Hamersley, 2010) and A10 at 30°S (M. Baringer & Macdonald, 2013) are used for reference. The data was obtained from the CLIVAR and Carbon Hydrographic Data Office websites. We will applied the same analysis (described in Section 3) to all hydrographic data in order to compare the differences of the AMOC at different latitudes under the same assumptions.

2.2. Satellite Observations

For the analysis the following three satellite data sets were used: (1) 6-h multi-sensor blended winds with a 0.25° horizontal resolution (Bentamy & Fillon, 2012) distributed by the Copernicus Marine Environment Monitoring Service (CMEMS); (2) daily sea surface temperature (SST) at 1 km horizontal resolution from the Group for High Resolution Sea Surface Temperature with its product version four Multiscale Ultrahigh Resolution L4 analysis (Chin et al., 2017); (3) daily Ssalto/Duacs Multimission Altimeter derived absolute dynamic topography (ADT) and derived surface geostrophic velocity fields at a 0.25° horizontal grid and distributed by CMEMS. This data set considers all data recorded by the 12 available altimetric missions

(Duacs/AVISO+, 2015). Note, in the updated version released in April 2014, improved data processing provides a better description of mesoscale activity than previously distributed products (Capet et al., 2014; Pujol et al., 2016).

2.3. Eddy Detection and Colocalized Argo Profiles

The Duacs/AVISO+ (2015) altimetry data set is used as input for the ocean eddy detection and tracking algorithm (TOEddies) and derived database developed by Laxenaire et al. (2018). The TOEddies algorithm is a two-step process: it identifies the occurrences of eddies before deriving their trajectories under the assumption that mesoscale eddies satisfy the geostrophic balance and therefore, enclosed streamlines of ADT should coincide with the location of a mesoscale eddy. The novelty of this algorithm is that it defines and tracks eddies from ADT fields (and not from the sea level anomalies or derived geostrophic velocities) and it considers the complex network of trajectories arising from eddy splitting and merging. A detailed description of the TOEddies can be found in Laxenaire et al. (2018). The TOEddies database is used here for the detection of the mesoscale eddies crossed during the cruise and for the derivation of their trajectories.

The TOEddies database also provides Argo profiles (Argo, 2020) colocalized with eddies and categorized as being “outside” or “inside” anticyclonic (AEs) or cyclonic eddies (CEs). Using this database, we built a summer climatology of the upper 1700 dbar from 648 Argo profiles in close proximity to the 34.5°S section (between 33.5°S and 35.5°S). We used that climatology to substitute the temperature and salinity MSM60 cruise data in the upper 1700 dbar in order to estimate the impact of mesoscale eddies on the AMOC volume, heat and freshwater transport during the cruise. Another climatology was created with TOEddies, in this case to evaluate the expected proportion of AEs and CEs at 34.5°S and the deviations from the mean conditions during the MSM60 cruise. To do so, a daily presence/absence matrix for eddies was created using the entire TOEddies atlas time span (1993–2018) for each longitude grid point at 34.375°S which is one of the closest latitude grid point to the cruise track (the same pattern was observed at 34.625°S). From the matrix, for each grid point of the section, the average monthly percentage of time occupied by an eddy was calculated.

3. Methods

3.1. Data Gridding and Derived Variables

In order to combine the SADCP data (upper 1000 m) with the CTD and LADCP data, the latter was linearly interpolated to an equidistant grid of 1 dbar/0.05 longitude (approximately 4.6 km) between 58°W and 18°E. Given the high-resolution velocity sampling from the SADCP a change in the velocity fine structure occurs at 1,000 m depth because below only discrete LADCP casts are available. A land/bottom mask was created from the ship multibeam echosounder (EM122) data. This approach enabled us to use all measurements while minimizing the impact of bottom triangles (Figure S1).

For all calculations, we used the Gibbs-SeaWater Oceanographic Toolbox containing the thermodynamic equation of seawater 2010 (TEOS-10) subroutines (T. J. McDougall & Barker, 2011). We computed absolute salinity (S_A) and conservative temperature (Θ) from the CTD pressure, temperature and salinity to obtain better estimations of the transport in the South Atlantic Ocean, as the differences of total AMOC transport can reach to 6% when compared with estimates derived from the previous definition of the thermodynamic equation of seawater (Almeida et al., 2018). However, to obtain the neutral density (γ^n) field we also determined potential temperature (θ) and practical salinity (S_p) because currently γ^n is not available as a function of Θ and S_A in TEOS-10 (T. J. McDougall & Barker, 2011; see Figure S2 for differences between Θ and θ and between S_A and S_p along the section). We also derived a composite of daily satellite data for SST and ADT as the ship progressed westward.

3.2. Calculation of the Total Velocity Field: Volume, Heat and Freshwater Transport

Given the large high-frequency variability of the ocean currents observed at 34.5°S (Kersalé et al., 2020; C. S. Meinen et al., 2018) and the non-synoptic nature of the ship survey, we used two approaches to estimate the total velocity field. First, we assumed the combined LADCP and SADCP field (Method 1). Second, from the CTD measurements and following the methodology of Bryden and Imawaki (2001), we used the slow

varying density field to compute the time-averaged mean geostrophic circulation adding also Ekman fluxes. Following M. O. Baringer & Garzoli (2007), Buckley and Marshall (2016) and Holliday et al. (2018), the total meridional velocity field (v) is composed of:

$$v = v_{\text{ageos}} + v_{\text{geos}} + v_{\text{ref}}, \quad (1)$$

where v_{ageos} is the Ekman velocity, v_{geos} the geostrophic velocity, and v_{ref} the barotropic flow.

The zonal integral of v_{ageos} is the Ekman transport calculated as:

$$T_{\text{ek}} = - \int_{x_{\text{West}}}^{x_{\text{East}}} \frac{\tau_x}{f\rho} dx, \quad (2)$$

where τ_x is the zonal component of the local wind stress, f is the Coriolis parameter, and ρ is the density of seawater. To compute the oceanic fluxes, we assumed that the Ekman transport is confined and equally distributed in the top 50 dbar of the water column.

The geostrophic velocity (v_{geos}) was estimated from the hydrography and selecting a certain reference level of no-motion but also explicitly adding a barotropic velocity (v_{ref}). The total meridional velocity field is of central importance for all further calculations and therefore different approaches to estimate the level of no motion and the barotropic velocity were applied to quantify the uncertainties. Note, the uncertainties range given in Section 4 are estimated by applying the different approaches outlined below.

Most importantly we used different levels of no-motion following previous studies. The first two levels of no-motion chosen were the neutral density surface $\gamma^n = 28.10 \text{ kg m}^{-3}$ (Method 2) and 3,400 dbar (Method 3), which is the mean pressure level of the $\gamma^n = 28.10 \text{ kg m}^{-3}$. This choice was motivated by earlier studies which identified that level as the interface between southward flowing NADW and northward flowing Lower Circumpolar Deep Water (LCDW; e.g., Hernandez- Guerra & Talley, 2016; Hernández-Guerra et al., 2019; McDonagh & King, 2005). For these two methods, we derived a zero net mass transport through the section with a simple barotropic adjustment by adding a small barotropic meridional velocity across the entire section (e.g., M. O. Baringer & Garzoli, 2007).

The third geostrophic approach (Method 4) was to assume the level of no motion at the bottom and then adjust the velocities by adding the near-bottom (within 20 dbar of the bottom) LADCP measurements (e.g., McDonagh et al., 2010). This approach was motivated by the fact that close to the seafloor the LADCP bottom-track mode provides accurate near-bottom absolute velocities (Visbeck, 2002). Again, a small barotropic meridional velocity across the entire section was added to achieve the mass balance. Then, the error estimate from the geostrophic field was computed as the standard deviation of the oceanic fluxes derived from the mass balance total velocity field (v) using the three levels of no motion ($\gamma^n = 28.10 \text{ kg m}^{-3}$, 3,400 dbar, and bottom).

Not surprisingly, the meridional transport calculations were sensitive to the method used for computing the total velocity field, as shown in the results section. However, the selection of $\gamma^n = 28.10 \text{ kg m}^{-3}$ and equally distributing the mass imbalance as a velocity correction across the section (Method 2) gave a solution that allowed to compare with previous assessments using a similar approach in the South Atlantic, in particular A09 and A10 (Dong et al., 2009; Ganachaud & Wunsch, 2003; S. L. Garzoli et al., 2013; Hernández-Guerra et al., 2019; McDonagh & King, 2005).

A sensitivity analysis was also performed to quantify the effect of mesoscale eddies in the transports and AMOC_{max}. To do so, we replaced the upper 1,700 dbars hydrography with a summer (December-January-February) climatology constructed from the 648 non-eddy Argo profiles available between 33.5°S and 35.5°S based on the TOEddies database (Method 5).

Another common approach to estimate the volume transport across coast to coast trans-basin sections is to use inverse methods. These methods use mass conservation for every vertical layer after predefining several constraints like boundary currents, mean transport and flow through deep channels (Wunsch, 1996). Hernández-Guerra et al. (2019) demonstrated that inversions at 30°S using different models and constraints can lead to very diverse solutions. In this first realization of a GO-SHIP section along the SAMBA line, we choose to assess the transport by a simpler direct approach.

After securing the conservation of mass condition through the section, we obtained the $AMOC_{max}$, MHT, and MFT following Buckley and Marshall (2016) and are expressed in units of Sv, PW, and Sv, respectively. First, we defined a stream function for the zonally integrated meridional volume transport in pressure coordinates:

$$\Psi(y, z) = \int_{x_{West}}^{x_{East}} \int_{p_{max}}^{p_{min}} v \, dx dp, \quad (3)$$

where v is the estimated total meridional velocity component field (see above), x and p are the coordinates in the zonal and vertical domain. Then, we determined the $AMOC_{max}$ of the upper cell by the maximum value and depth of the stream function over the water column. On the other hand, the $AMOC_{max}$ of the abyssal cell was computed as the net volume transport of AABW.

The meridional heat transport (MHT), was computed as:

$$MHT = Cp\rho_0 \int_{x_{West}}^{x_{East}} \int_{p_{max}}^{p_{min}} v\Theta \, dx dp, \quad (4)$$

with Θ the conservative temperature, ρ_0 the section mean potential density and Cp a reference value for the heat capacity of seawater = $3850 \text{ J kg}^{-1} \text{ C}^{-1}$. Finally, the freshwater transport (MFT) was calculated as:

$$MFT = \int_{x_{West}}^{x_{East}} \int_{p_{max}}^{p_{min}} v \left(1 - \frac{S_A}{S_0} \right) dx dp, \quad (5)$$

where S_A is absolute salinity and S_0 is the section-averaged absolute salinity. The MFT is approximately $-S_0$ times the salinity transport, with exact equality holding if there is no net mass transport across the section. While the $AMOC_{max}$ used here reflects the intensity of the upper meridional overturning cell only, both MHT and MFT are an estimate of the full-depth oceanic fluxes.

4. Results

4.1. Surface Conditions and Direct Velocity Measurements

The MSM60 underway measurements of SST from the Thermosalinograph (TSG) are in good agreement with satellite observations despite the fact that the TSG temperature sensor is located at 5 m depth (Figure 2a). During the cruise, SST varied from 18.65°C to 25.17°C , increasing westward as expected from both, the climatology and the fact that the cruise was conducted over one month in early austral summer (January) and were we expect SST to increase. From satellite SST data we found that within the area between 25°W and 55°W an increase of SST by up to 4°C is seen (not shown here).

The velocity fields derived from the ADCPs were intense ($>0.5 \text{ m s}^{-1}$) in the Brazil Current (BC henceforth) near 50°W and during the crossing of mesoscale eddies. MSM60 crossed 13 cyclonic (named C1–C13, Figures 2a) and 12 anticyclonic (A1–A12, Figure 2a) mesoscale eddies, although not all were crossed at their center as revealed in comparison with the TOEddies database. From the 128 CTD profiles taken during the cruise, 27 (21%) were located within cyclonic eddies and 12 (9%) within anticyclonic eddies. This represents an anomalous predominance of cyclonic eddies (CEs) over anticyclonic eddies (AEs) at the time of the cruise. By analyzing the 26 years of TOEddies database, both the annual and summer means display an expected 19% and 14% of the section occupied with AEs and CEs, respectively. During the month of the cruise in January 2017, the mean percentage of the section occupied by eddies was 14% for AEs and 21% for CEs, locating January 2017 in the 96th percentile in the proportion of CEs with respect to AEs for the 312 analyzed months.

Four long-lived Agulhas rings (A1, A2, A3, and A12) were crossed but only one (A3) was intercepted close to its core and sampled with CTD profiles. A12, was a long-lived Agulhas ring more than 4 years old that crossed the entire basin (Figure S3). The SADCs also documented two large cyclonic eddies, one centered at 14°E in the Cape Basin (C1) and another one in the west just east of the BC at 47.4°W (C12). The

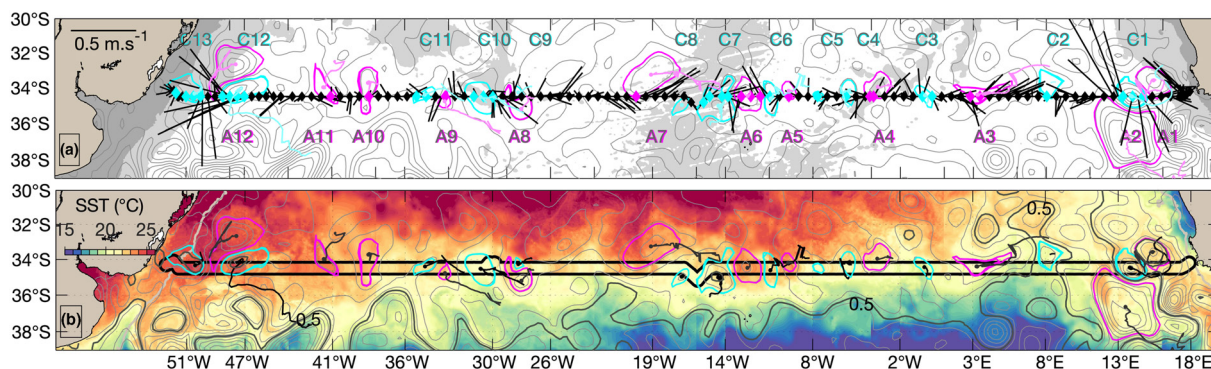


Figure 2. Maps of the South Atlantic with the MSM60 cruise track between 4 and 31 January 2017 from Cape Town, South Africa, to Montevideo, Uruguay. (a) Highlighting the averaged velocity in the upper 100 dbar measured by the 38 kHz SADCPC (black sticks) and each of the 128 CTD station locations (black diamonds). The anticyclonic and cyclonic eddies crossed, together with the correspondent CTD profile inside those eddies are colored in magenta and cyan, respectively. The eddy “tails” show the eddy trajectories during the preceding 120 days (or less for eddies with shorter lifespan). ADT composite, computed by taking each day of the cruise track cut by longitude is shown in gray contours. The daily progress of the cruise is displayed as one tick corresponding to one day in the x axis of panel (a) corresponding 18°E to the 4th of January. Bathymetry from 0 to 200 m and 200–3,500 m is shaded in dark and light gray, respectively. (b) SST (shaded) and ADT (gray contours) composite. In between the black lines are plotted the MSM60 TSG temperature measurements at 5 m of depth in the same color scale as SST. In magenta and cyan are the contours of the anticyclonic and cyclonic eddies that intercepted the cruise track. The precedent 120 days (or less for eddies with shorter lifespan) trajectory for each eddy is displayed as a black line. ADT, absolute dynamic topography; CTD, conductivity-temperature-depth; SADCPC, ship-mounted acoustic doppler current profilers; SST, sea surface temperature; TSG, thermosalinograph.

reconstructed trajectory of C1 showed the eddy originated from an instability along the Benguela upwelling system front (Figure 2). This is also confirmed by the low dissolved oxygen concentration within the eddy (Figure 4c).

On the eastern margin, the Benguela Current appears as a relatively wide and weak equatorward eastern boundary current, but interacting with the intense cyclonic eddy (C1, Figures 2b and 3a). Near 5°E, an intrusion of surface subantarctic waters has been observed due to the presence of an intense dipole (Kersalé et al., 2018) associated with satellite-derived ADT lower than 0.5 m at 34.5°S (Figure 1). In this area, during the MSM60 cruise, the ADT was particularly low relative to the time-mean ADT, with the 0.5 m contour reaching 32°S (Figure 2b). This same area was up to 2°C colder compared to its surrounding (Figure 2a). Subtropical waters are generally separated from subantarctic waters by the Subtropical Front (STF; Belkin & Gordon, 1996; Orsi et al., 1995). In the South Atlantic, the STF coincides with ADT ranging between 0.4 m and 0.5 m (e.g., Artana et al., 2019). ADTs lower than 0.5 m along the section correspond to cold, fresh, highly oxygenated water of subantarctic origin (Figure 2). This is the case of the vertical structure of the cyclonic eddy C2 that was crossed at 6°E, (Figure 4). The Θ - S_A diagram shows that the properties of the water in the eddy are characteristics of the Subantarctic Zone (SAZ) and they form an intrusion of cold and fresh water between the 26.2 and 26.4 kg m^{-3} isopycnals in comparison with surrounding waters within the same density (Figure 5a). Though the water mass properties clearly point to the subantarctic origin of these waters, it was not possible to track eddy C2 back to the SAZ as its trajectory is short and complex (it is embedded in a subantarctic intrusion where frequent eddy splitting and merging occurs and only short-lived coherent structures are observed). Nevertheless, other long-lived coherent eddies that have intercepted the SAMBA section during the MSM60 cruise originate in the SAZ (e.g., C12). All these eddies are characterized by ADT lower than 0.5 m (Figure 2).

4.2. Water Masses and Layering

For water mass definitions we followed Valla et al., (2019) and Hernández-Guerra et al. (2019) and separated the water column along the SAMBA section in seven main water masses (see Table 2). Surface Water (SW) is considered a layer in constant transformation due to air-sea fluxes and as such cannot be considered as a water mass in a proper sense. SW is defined by $\gamma^t < 26.35 \text{ kg m}^{-3}$, it has a mean pressure of 70 dbar and includes the upper part of South Atlantic Central Water (SACW). SACW is formed by subduction in the subtropical gyre and extends to about 750 dbar or $\gamma^t = 27.10 \text{ kg m}^{-3}$ which includes the permanent thermocline layer (A. L. Gordon, 1981, 1986). SACW has the largest temperature and salinity range (17–7°C

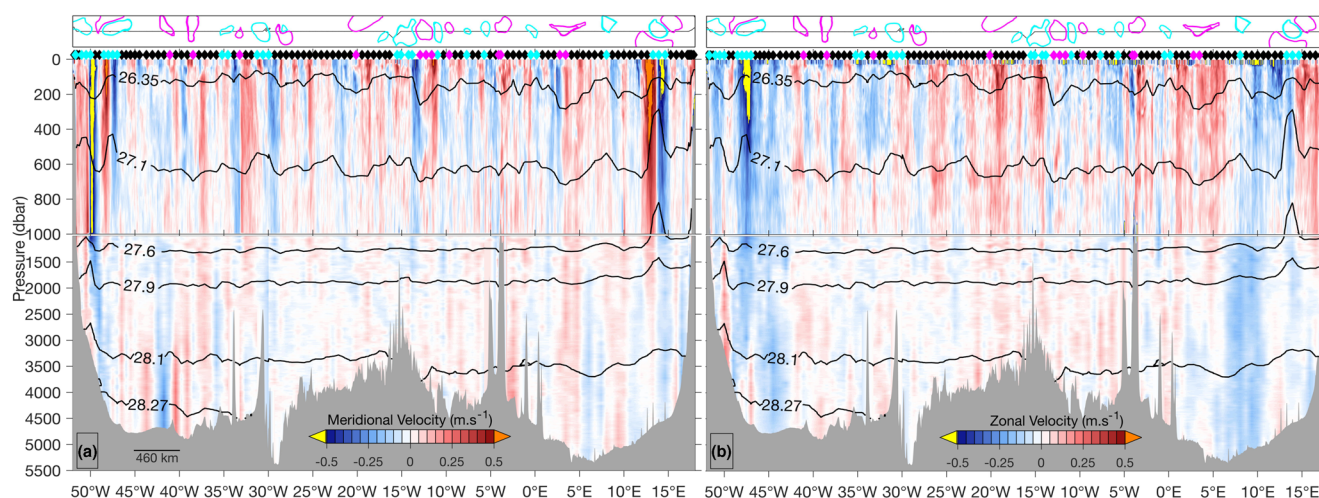


Figure 3. Direct velocity measurements along 34.5°S. The upper 1,000 dbar are vertically stretched and show spatially higher resolution SADCPC measurements. The deep velocity section is derived from 128 LADCP profiles. (a) Meridional Velocity (m s^{-1}) and (b) Zonal Velocity (m s^{-1}). Values above 0.5 m s^{-1} and below -0.5 m s^{-1} are colored in orange and yellow for better visualization, respectively. Details inside those areas are shown in Figures 10 and 11. Neutral density layers (γ^n , kg m^{-3}) bounding each water mass are shown in black. LADCP, lowered acoustic doppler current profilers; SADCPC, ship-mounted acoustic doppler current profilers.

and $34.6\text{--}36.1 \text{ g kg}^{-1}$) leading to a considerable stratification, which is even stronger toward the east of the basin (Figures 4d and 5a).

Below the thermocline, between 750 and 1,140 dbar ($27.10 \text{ kg m}^{-3} < \gamma^n < 27.58 \text{ kg m}^{-3}$), lies the highly oxygenated, low-salinity ($<34.5 \text{ g kg}^{-1}$) Antarctic Intermediate Water AAIW. The AAIW found in the Atlantic Ocean has contrasting properties across the basin (McCarthy et al., 2011; Piola & Georgi, 1982; Rusciano et al., 2012). Atlantic AAIW originates from two different source waters (see Rusciano et al., 2012 for a detailed discussion): Subantarctic Mode Water (SAMW) that is transformed in a fresh variety of AAIW in the southwest South Atlantic (Piola & Gordon, 1989; Suga & Talley, 1995) continuing eastwards along the southern edge of the South Atlantic Current and along the Atlantic portion of the SAF (A-AAIW hereafter, characterized by $S_p \leq 34.2$; $S_A \leq 34.4$; Boebel et al., 1999; McCartney, 1977; Rusciano et al., 2012; Tsuchiya et al., 1994). A-AAIW extends from the western continental slope to 25°W and it is characterized by dissolved oxygen concentration above $250 \mu\text{mol kg}^{-1}$ (Figure 4c). The other source is AAIW of Indian origin (I-AAIW, $S_p \geq 34.3$; $S_A \geq 34.45$) that enters the South Atlantic through the Agulhas/Benguela Current system (A. L. Gordon et al., 1987; A. L. Gordon et al., 1992; Rusciano et al., 2012; Stramma & England, 1999). I-AAIW lies in the easternmost sector of the section, east of 12°E in the Cape Basin and is characterized by oxygen concentrations lower than $200 \mu\text{mol kg}^{-1}$. A third variety is sometimes called Indo-Atlantic AAIW (IA-AAIW, $34.2 < S_p < 34.3$; $34.4 < S_A < 34.45$), which is created by isopycnal mixing of A-AAIW and I-AAIW in the Cape Basin and covers a depth range of 800–1,000 m depth (Capuano et al., 2018; A. L. Gordon et al., 1987; Rusciano et al., 2012). Consequently IA-AAIW is found between A-AAIW and I-AAIW, from the Mid-Atlantic Ridge to $\sim 12^\circ\text{E}$ (Figures 4c and 5b).

Below the AAIW layer, between 1,140 and 1,600 dbar ($27.60 < \gamma^n < 27.90 \text{ kg m}^{-3}$), we observe Upper Circumpolar Deep Waters (UCDW) through a minimum in dissolved oxygen (ca. $180 \mu\text{mol kg}^{-1}$). UCDW is more zonally homogenous in terms of thermohaline and oxygen properties from west to east in comparison with AAIW (Figures 4c and 5b). This is probably due to the fact that UCDW enters the western South Atlantic mostly through the Drake Passage (Callahan, 1972) and the South Atlantic Current (Stramma & England, 1999), but despite a small recirculation in the southeast Indian Ocean, there is no major evidence of UCDW sources in the Indian Ocean unlike for AAIW (Stramma & England, 1999).

Between 1,600 and 3,400 dbar ($27.90 < \gamma^n < 28.10 \text{ kg m}^{-3}$) two varieties of NADW are observed (Figure 4). W-NADW is found in the western part of the section. This water mass is more saline ($34.9 < S_A < 35.15$) and better oxygenated ($230 < O_2 < 245 \mu\text{mol kg}^{-1}$; Figure 4) than the NADW in the eastern part of the section (E-NADW, $34.9 < S_A < 35$ and $200 < O_2 < 227 \mu\text{mol kg}^{-1}$; Arhan et al., 2003). The contrast between the

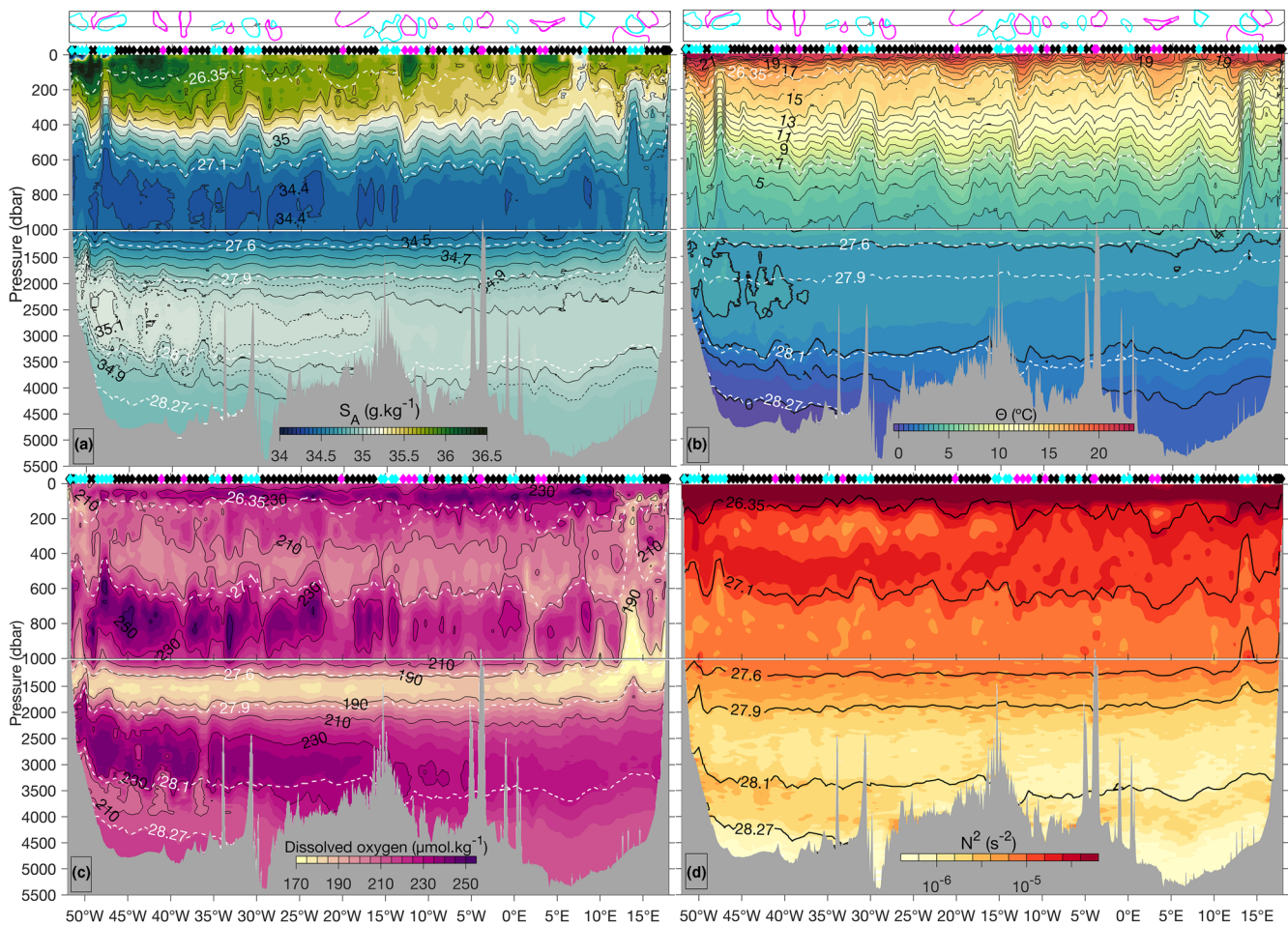


Figure 4. Water properties observed during the MSM60 cruise. (a) Conservative temperature (Θ , $^{\circ}\text{C}$), (b) Absolute salinity (S_A (g kg^{-1})), (c) Dissolved oxygen ($\mu\text{mol kg}^{-1}$), and (d) Brunt-Väisälä frequency (N^2 (s^{-2})). The neutral density layers (γ^n (kg m^{-3})) bounding each water mass are shown in white dotted lines in (a), (b), (c), and in black lines (d), respectively. A map showing the location of anticyclonic and cyclonic eddies crossed during the cruise in magenta and cyan respectively is shown on top of panels a and (b). The diamonds indicate the location of the 128 CTD profiles, colored in black, magenta and cyan depending if they were occupied outside, or within an anticyclonic or a cyclonic eddy, respectively. The upper 1,000 dbars are vertically stretched. CTD, conductivity-temperature-depth.

two NADW blends stems from W-NADW being more directly transported southward by the Deep Western Boundary Current from its formation region in the Labrador Sea and the Greenland-Scotland Ridges system (Reid et al., 1977; Table S1). The core of E-NADW is more difficult to identify, as it is even more eroded, characterized by homogeneous thermohaline properties with respect to its surroundings ($35 < S_A < 35.05$; $34.80 < S_p < 34.85$; $220 < O_2 < 227 \mu\text{mol kg}^{-1}$; Figure 4a). According to Arhan et al., (2003), the E-NADW transport is southward ($11 \pm 4 \text{ Sv}$) at 35°S and its flow can be traced upstream across the Cape Basin to passages across the Walvis Ridge south of 28°S , and then back to the deep western boundary current of the Atlantic Ocean near the tropics as proposed by Reid (1989).

Along its southward path, NADW penetrates toward the Southern Ocean and transforms into Circumpolar Deep Waters, which in the South Atlantic is split into two layers by the southward flowing NADW: UCDW and Lower Circumpolar Deep Water (LCDW; Lumpkin & Speer, 2007; Reid et al., 1977). LCDW is located below NADW and above Antarctic Bottom Waters (AABW) at $28.1 < \gamma^n < 28.27 \text{ kg m}^{-3}$. Data from the MSM60 section suggest that the observed LCDW undergoes mixing with NADW and AABW with considerable zonal differences in thermohaline characteristics and flow direction, being the water mass layer that exhibits the largest differences between the western and the eastern sides of the section. Zonal differences in LCDW thermohaline and oxygen properties are observed along the SAMBA line (Figure 5 and S5). The LCDW property diversity coincides with very specific domains separated by the steep topographic features,

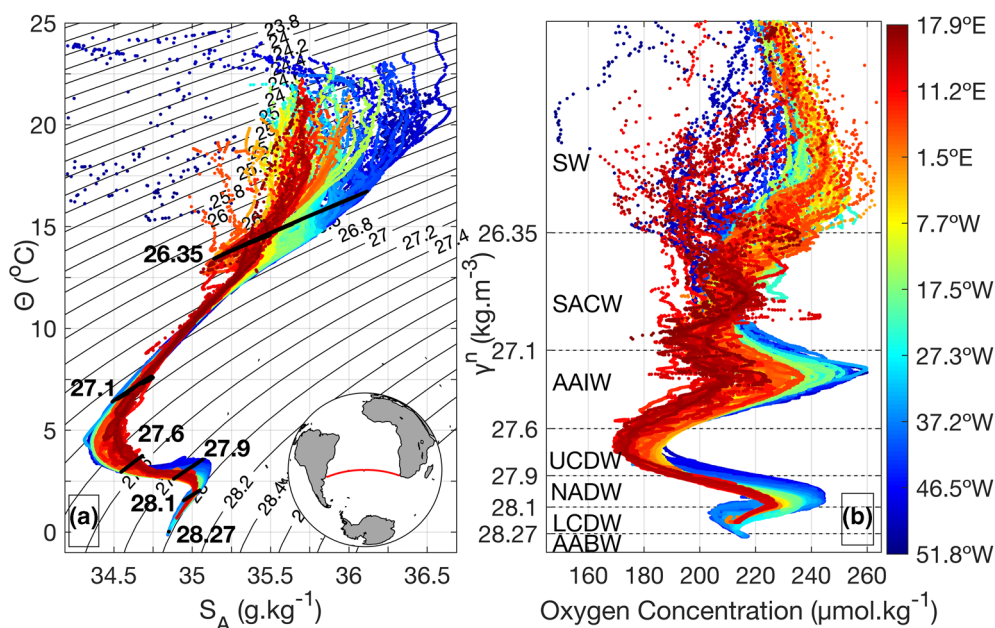


Figure 5. (a) Θ - S_A diagram for the CTD profiles collected during the MSM60 cruise. $S_A < 34 \text{ g kg}^{-1}$ has been clipped for better visualization. Bold black lines and numbers represent the neutral density levels between water masses (shown in b). See Figure S4 for Θ - S_P diagram. The cruise track is shown in the insert. (b) Dissolved oxygen concentration ($\mu\text{mol kg}^{-1}$) as a function of neutral density (kg m^{-3}). Water mass acronyms and selected neutral density boundaries are indicated by dashed lines. For references to the water mass see Table 2. CTD, conductivity-temperature-depth.

such as the Rio Grande Rise at 31°W , the Mid-Atlantic Ridge at 16°W , and Walvis Ridge at 4°W (Figure 1). West of 31°W , W-LCDW is clearly identified as a layer of about 1,000 dbar of thickness lying between 3,000 and 4,000 dbar (Figure 4). There, it flows northward synchronically with AABW, and it differs from the latter mainly in its dissolved oxygen concentration, ranging between 202 and $214 \mu\text{mol kg}^{-1}$ in W-LCDW and $214\text{--}218 \mu\text{mol kg}^{-1}$ in AABW, respectively (Figures 4c and 7b; Valla et al., 2018). W-LCDW is the less oxygenated variety of LCDW ($<214 \mu\text{mol kg}^{-1}$) and its properties can be traced back as a mixing between AABW and NADW (Reid, 1989). East of 31°W , the LCDW isopycnal layer, as we have defined it, flows southward and it extends vertically down to the seafloor (Figures 6b and 7b). As there is no AABW east to

30°W , LCDW is mainly influenced by the NADW, with slight differences in thermohaline properties across topographic features. Between the Rio Grande Rise and the Mid Atlantic Ridge, there is still an influence of W-LDCW, with relatively low oxygen, salinity and temperature, especially in the deep channel at 30°W (Figure 4). The warmest, relatively saltiest, and highly oxygenated variety of LCDW is observed between the Mid-Atlantic Ridge and the Walvis Ridge, possibly due to the influence of still relatively pristine NADW. The fact that this portion of the section is shallower than the Cape Basin, topography prevents the flow of the densest (coldest) variety of LCDW. Finally, the most eroded variety of E-LCDW is observed in the Cape Basin, east of 3°W . That water mass presents notably homogeneous thermohaline composition and therefore it is difficult to trace its origin based solely on the thermohaline and dissolved oxygen properties. It has been argued that the origin of E-LCDW can be traced to older (e.g., relatively less salty and oxygenated) varieties of NADW and AABW (Arhan et al., 2003; Gladyshev et al., 2008; Reid, 1989; Stramma & England, 1999).

Finally, in the western basin, younger AABW, the densest and coldest water mass ($\gamma_n > 28.27 \text{ kg m}^{-3}$) extends from 3,420 dbar to the seafloor and at 34.5°S is confined to the Argentine Basin west of 33°W . This water

Table 2
Neutral Density Ranges (γ^n) and Mean Pressure, Conservative Temperature (Θ), Absolute Salinity (S_A), Practical Salinity (S_P), and Oxygen Concentration ($\mu\text{mol kg}^{-1}$) per Water Mass Across 34.5°S in the Atlantic

| Water Mass | $\gamma^n \text{ (kg m}^{-3}\text{)}$ | Pres. (dbar) | $\Theta \text{ (}^\circ\text{C)}$ | $S_A \text{ (g kg}^{-1}\text{)}$ | $S_P \text{ (psu)}$ | $\text{O}_2 \text{ (}\mu\text{mol kg}^{-1}\text{)}$ |
|------------|---------------------------------------|--------------|-----------------------------------|----------------------------------|---------------------|---|
| SW | <26.35 | 79 | 17.85 | 35.74 | 35.57 | 228.13 |
| SACW | 26.35–27.10 | 377 | 11.63 | 35.22 | 35.05 | 211.34 |
| AAIW | 27.10–27.60 | 921 | 4.34 | 34.48 | 34.31 | 216.66 |
| UCDW | 27.60–27.90 | 1549 | 2.88 | 34.76 | 34.59 | 185.59 |
| NADW | 27.90–28.10 | 2,637 | 2.47 | 35.02 | 34.85 | 223.39 |
| LCDW | 28.10–28.27 | 4,432 | 1.07 | 34.92 | 34.77 | 216.09 |
| AABW | >28.27 | 4,544 | -0.07 | 34.85 | 34.67 | 215.87 |

Note. Acronyms correspond to Surface Water (SW), South Atlantic Central Water (SACW), Antarctic Intermediate Water (AAIW), Upper Circumpolar Deep Water (UCDW), North Atlantic Deep Water (NADW), Lower Circumpolar Deep Water (LCDW) and Antarctic Bottom Water (AABW).

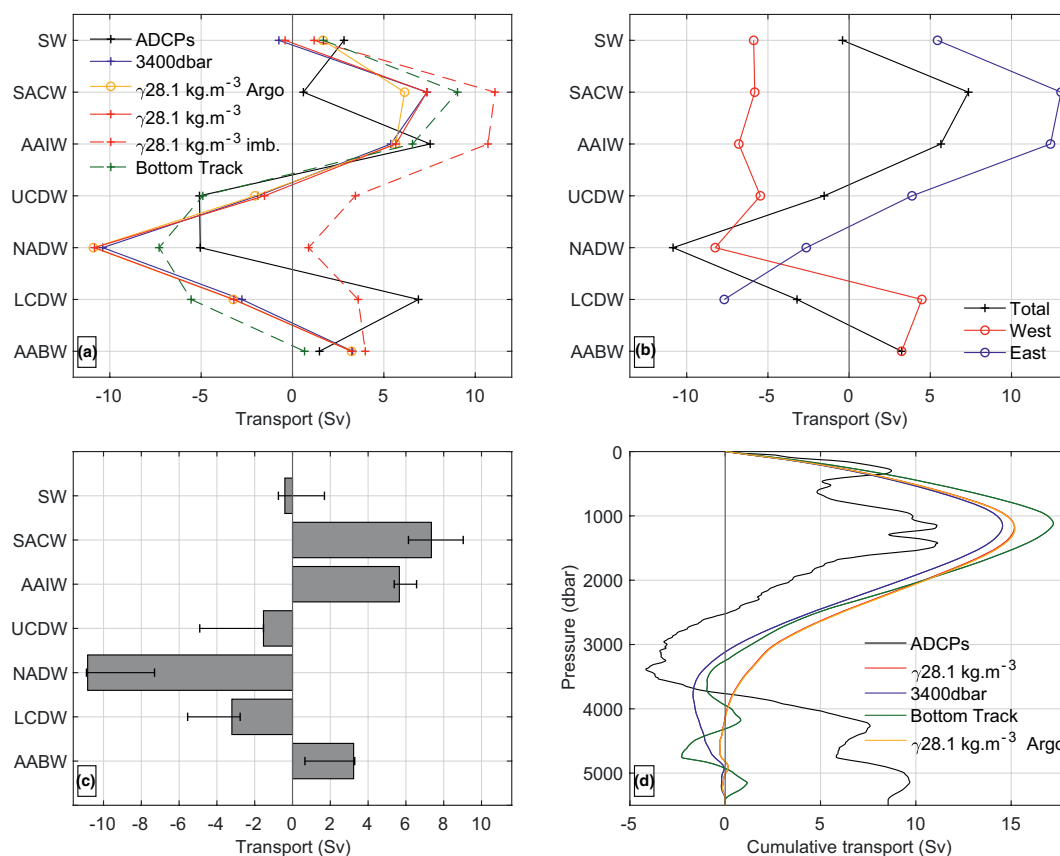


Figure 6. MSM60 meridional volume transport at 34.5°S in the South Atlantic. (a) Transport by isopycnal layers referring to specific water masses. Each color represents a different method: direct observations from ADCPs are shown in black (Method 1), while the rest are based on the geostrophic approaches and are shown in red, blue, green and yellow for Methods 2, 3, 4, and 5, respectively. The dashed red line represents the volume transport estimate obtained with no barotropic adjustment from Method 2. (b) West (red), East (blue) and total (black) transport by water mass from Method 2. The South Atlantic was separated in West and East at 17°W, close to the Mid-Atlantic Ridge. (c) Volume transport by water mass. Gray bars show the calculation from Method 2. The error bars represent the minimum and maximum estimates from all the mass balanced methods used to estimate the total velocity using the original data. (d) Cumulative volume transport by pressure level for the different methods.

mass is formed in the surroundings of Antarctica, mainly in the Weddell Sea (Orsi et al., 1999) and therefore it is highly oxygenated ($O_2 > 225 \mu\text{mol kg}^{-1}$) and characterized by particularly low temperature ($\theta < 0^\circ\text{C}$). The $\gamma = 28.27 \text{ kg m}^{-3}$, which is commonly used to separate LCDW from AABW, closely follows the 0°C isotherm, also used as the upper bound for AABW (Georgi, 1981; Valla et al., 2019; Figure 4a).

The MSM60 data show that besides the common layering, substantial differences between the western and the eastern basins can be identified (Figure 5, S5, and S6 and Table S1). These differences reflect the contrasting origins and trajectories of water masses converging in the South Atlantic at 34.5°S (A. L. Gordon et al., 1992; Speich et al., 2001; 2007) that ultimately affects the large-scale transport of heat, freshwater and biogeochemical components such as nutrients and carbon.

4.3. Volume, Heat and Freshwater Transports

We estimated an Ekman transport of -0.42 Sv across the entire transect using the satellite wind measurements. The zonally integrated Ekman transport at 34.5°S computed for the period 2009–2018 from satellite data shows a pronounced annual cycle. Austral winter values are the highest, with a maximum of 8.24 Sv in June, due to the equatorward migration of the semi-permanent anticyclone in the atmosphere, whereas

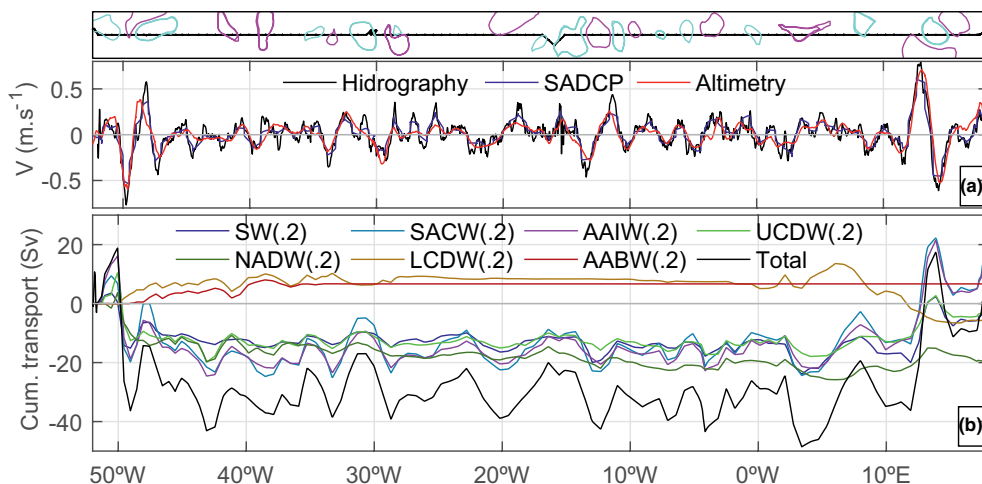


Figure 7. (a) Averaged upper 100 dbar surface velocity derived from hydrography applying the geostrophic equilibrium and mass-balanced adjusted, and SADCPC are shown in black and blue, respectively. Surface geostrophic velocities from altimetry are shown in red. (b) Cumulative vertically integrated meridional transport across 34.5°S from west to east. The individual water masses have been multiplied by 2 for better visualization. SADCPC, ship-mounted acoustic doppler current profilers.

in austral summer the Ekman transport is the lowest. Hence, the observed Ekman transport during the MSM60 cruise was close to its climatological value for January of 0.27 Sv (Figure S8).

The volume transport from ADCPs measurements (Method 1) generates an initial imbalance of 8.54 Sv, which is not surprising given that it took 28 days to cross the entire section and large transport variability at shorter time scales (15.5 Sv daily standard deviation in the upper cell) revealed from daily trans-basin transport estimates (Kersalé et al., 2020). Another possible source of error may be linked to a too coarse sampling of the narrow and intense western boundary current below 1,000 dbar and where only data at discrete CTD (LADCP) stations is available. Applying Method 2, this initial imbalance increases to 34.64 Sv when we calculate the geostrophic transport relative to a level of no motion at $\gamma^{\theta} = 28.10 \text{ kg m}^{-3}$. As discussed in Section 3.2, transport estimates are particularly sensitive to the choice of such level (Figure 6 and Table 3). However, this level allowed us to compare the results with previous studies in the region (Dong et al., 2009; Ganachaud & Wunsch, 2003; S. L. Garzoli et al., 2013; Hernández-Guerra et al., 2019; McDonagh & King, 2005). In particular, this initial volume transport imbalance is similar to the 36 Sv obtained by Hernández-Guerra et al. (2019) using geostrophic velocities and the same level of no motion at 30°S.

The zonally integrated volume transport shows the two overturning cells expected at this latitude, with an upper cell with northward transport in the SACW and AAIW layers approximately down to 1,300 dbar and deeper southward transport of NADW. That is the cell that usually is referred in the literature as the AMOC

Table 3
Overturning Maximum (AMOC), Meridional Heat Transport (MHT) and Freshwater Transport (MFT) in the South Atlantic at 34.5°S Calculations Using Different Approximations

| Method | 1 | 2 | 3 | 4 | 5 |
|--------------------|-------|-----------------------|--------------|-----------------------------|-----------------------|
| Data set | ADCPs | CTDs | CTDs | CTDs | Argo/CTDs |
| Level of no-motion | - | $\gamma^{\theta}28.1$ | 3,400 dbar | Bottom | $\gamma^{\theta}28.1$ |
| Barotropic adj. | - | Mass balance | Mass balance | LADCP bottom + Mass balance | Mass balance |
| AMOC (Sv) | 11.14 | 15.18 | 14.55 | 17.21 | 15.20 |
| MHT (PW) | 0.26 | 0.23 | 0.19 | 0.38 | 0.35 |
| MFT (Sv) | 0.16 | 0.21 | 0.24 | 0.25 | 0.10 |

Note. CTD, conductivity-temperature-depth; LADCP, lowered acoustic doppler current profilers.

or the upper overturning cell in contrast to the abyssal overturning cell (e.g., Kersalé et al., 2020). The upper cell is, in our present climate state, more intense than the abyssal cell (Figure 6a). Between 1,300 dbar and 3,400 dbar, the volume transport is mostly southward and associated with NADW, while below 4,800 dbar it switches to a northward flow associated with AABW. Between 3,400 dbar and 4,800 dbar, within the LCDW, northward transport is observed in the west and southward transport is observed in the east, denoting zonal differences (Figure 7b). Indeed, the only inconsistency found in the transport sign between ADCPs and geostrophy was in the eastern LCDW, where ADCPs displayed a mean northward transport. This water mass has been identified by a specific isopycnal layer. However, as we discussed in the previous sections, the LCDW is indeed present near the western boundary at 34.5°S whereas it consists of modified LCDW through mixing with AABW at the eastern end of the basin. This might explain the variability in the direction of the volume transport in this layer.

The $AMOC_{max}$ amounts to 15.64 ± 1.39 Sv considering the original data and the three levels of no motion with mass balance. The maximum northward transport of the cell is achieved between the surface and $1,156 \pm 17$ dbar (Figure 6d), with estimates ranging between 14.55 Sv and 17.21 Sv depending on the method and data used to compute the total meridional velocity, and 11.14 Sv for the ADCPs, that is not mass balanced (Table 3). These AMOC transports are lower than previous estimates based on different methods and datasets (S. L. Garzoli et al., 2013; Dong et al., 2009; 2014; Table 1). Nevertheless, the MSM60 based estimates fall within the 17.3 ± 5.0 Sv time mean upper cell transport from Kersalé et al. (2020) using PIES, which also presented a very large peak-to-peak variability in the 2013–2017 period, and a very large transport anomaly (~ -20 Sv) in January 2017 (Figure S7). Overall, the recent studies from moored arrays have suggested that the transport variability across 34.5°S is very high, even within a month. This strong basin-wide variability is mostly caused by fluctuations at the western and eastern boundaries (Kersalé et al., 2020, 2019; C. S. Meinen et al., 2017, 2018).

The MHT estimate during MSM60 is 0.27 ± 0.10 PW when derived from the mass balanced geostrophic approximation using three different levels of no-motion and 0.26 PW using ADCPs data. These values are also lower than the estimates of 0.55 ± 0.14 PW by Dong et al (2009) at 35°S. The low $AMOC_{max}$ and MHT values could be partially explained by the intense (heat) transport observed for the southward flowing BC during the MSM60 cruise and the low $AMOC_{max}$ state reported by Kersalé et al., (2020) for the same period. Moreover, the predominance of cyclonic eddies with large negative temperature anomalies along the section (e.g., C1 and C12) could also explain both the low MHT and the increase of 0.16 PW in MHT when replacing the upper 1,700 dbar with the non-eddy Argo climatology (Table 3). As eddies are not perfectly symmetric and were not crossed at the center, they have a net contribution to the MHT. While the contribution to the MHT between 1,701 dbar and the bottom is -0.17 PW for both datasets (as they are essentially the same), the upper 1,700 dbars contribution to the MHT are 0.40 and 0.55 PW for the original and Argo climatology datasets, respectively. No substantial increase in the $AMOC_{max}$ was observed for the above-mentioned datasets, where eddies under this eulerian approach seem to have a small contribution (Table 3).

Freshwater transport is on average 0.23 ± 0.02 Sv when derived from the mass balanced geostrophic approximation using three different levels of no-motion ranging from 0.10 to 0.25 Sv according to the method and data set used (Table 3).

In order to assess how the volume transport is distributed not only in the vertical but also zonally across the section, we computed the vertically integrated transport and the cumulative sum transport for each water mass across the SAMBA section, from west to east (Figures 6b and 7b). In addition, we compared the averaged upper 100 dbar geostrophic velocity derived from hydrography with Method 2 to SADCPC velocity and the surface geostrophic velocity derived from satellite altimetry ADT. They compare well, in terms of spatial variability and amplitude and this gives confidence on in situ velocity estimates (Figure 7a). The vertical integrated transport per longitude across the SAMBA section confirms, as discussed in previous studies (e.g., C. S. Meinen et al., 2018), that the eastern and western boundaries play a dominant role in setting the AMOC. The western boundary shows a northward flow from the shelf to the mid-slope at 50 °W, and then an intense southward flow associated with both, the BC and the Deep Western Boundary current. On the other hand, the eastern boundary is characterized by jets of alternating direction. The interior transport is also structured in alternating south-north currents, but of lower amplitude (Figure 7b).

The zonal cumulative sum of transport per water mass for SW, SACW, AAIW and UCDW layers displays a similar pattern. The largest transports are attributed to SACW and AAIW. The transport fluctuations of

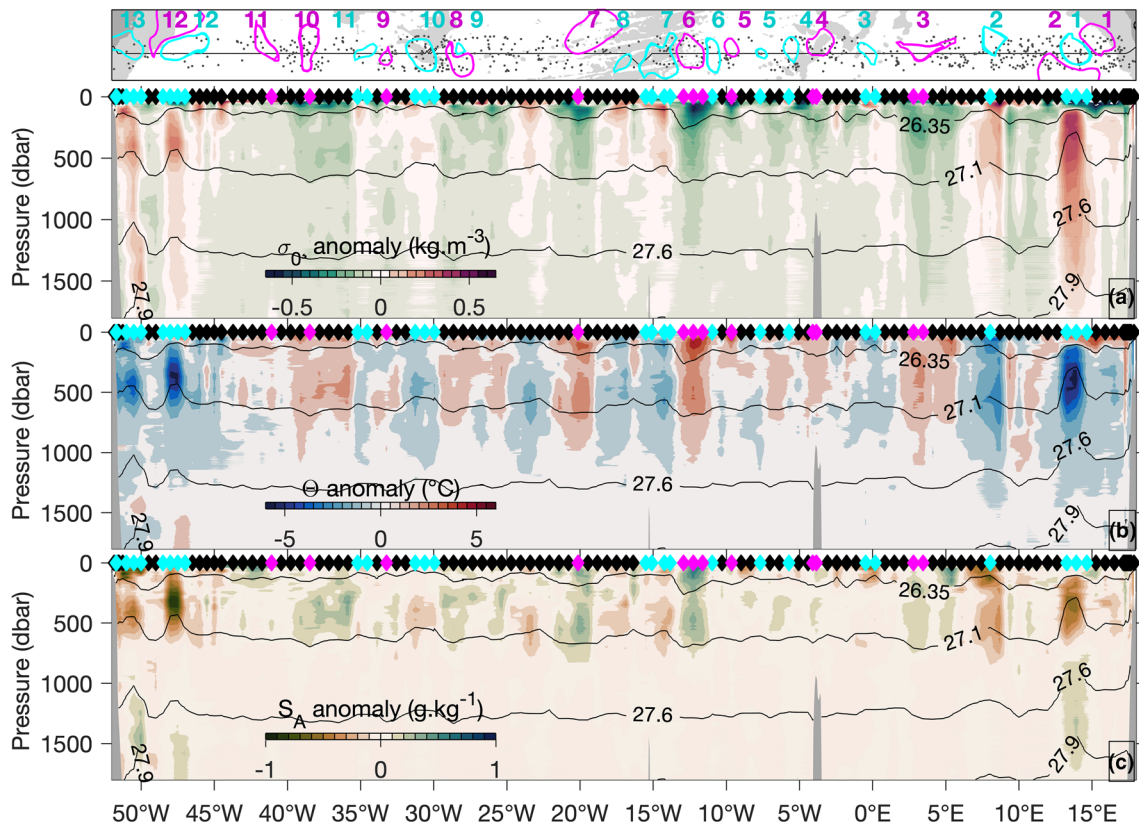


Figure 8. (a) Potential density (σ_0 , kg m^{-3}), (b) Conservative temperature (Θ , $^{\circ}\text{C}$), and (c) Absolute salinity (S_A , g kg^{-1}) anomalies from MSM60 cruise at 34.5°S in the South Atlantic relative to a summer climatology constructed from non-eddy Argo profiles using the TOEddies database (Laxenaire et al., 2018). Diamonds in the top axis of each panel represent the MSM60 CTD stations colored in black, magenta or cyan depending if the station is outside or within anticyclonic or cyclonic eddies, respectively. The upper panel in (a) shows a map with the cruise track in black, the contours of the anticyclonic and cyclonic eddies with their corresponding number in magenta and cyan respectively, and the gray dots indicate the location of Argo profiles used for producing the climatology. CTD, conductivity-temperature-depth; TOEddies, the ocean eddy detection and tracking algorithm.

these water masses are associated with boundary currents and mesoscale activity. Below, deep and bottom water masses display a more uniform behavior, very likely because they are less influenced by intense mesoscale dynamics. NADW has a negative transport almost across the entire section (from the western continental slope to 3°E) with the strongest transport concentrated at the western boundary. LCDW flows in the opposite direction. Its northward transport is observed across the section, from the western margin to 3°E , although in the middle of the Atlantic, between 30°W and 3°E , LCDW transport is near 0. Between 3°E and 6°E LCDW and NADW transports are directed northward and southward, respectively. From 6°E to 12°E they switch direction. This is probably due to a deep and bottom water recirculation described by various authors in previous studies (Arhan et al., 1999; Gladyshev et al., 2008; Kersalé et al., 2019; Reid, 1989). East of 12°E , transport in both water masses is southward. Finally, recently ventilated AABW transport is mostly northward and is confined between 48°W and 33°W (Figure 7b).

4.4. Vertical Structure of Mesoscale Eddies and Western Boundary Currents

The summer climatology created from non-eddy Argo float profiles in the upper 1,700 dbar allowed to estimate both the contribution of mesoscale eddies to oceanic transport of properties and the anomalies associated with these structures in the water column. Anomalies up to 0.65 kg m^{-3} , 5.5°C , and 0.95 g kg^{-1} in density, conservative temperature and absolute salinity, respectively, are observed in the upper 1,000 dbar associated with mesoscale eddies, with cold and fresh anomalies observed for CEs and warm and salty anomalies for AEs as expected (Figure 8 and S9).

During MSM60, at least four stations were occupied close to the center of mesoscale eddies, two cyclonic (C1 and C12) and two anticyclonic (A3 and A6). C1, the most intense mesoscale structure crossed through its center, displays anomalies that are about twice as large as in the other profiles and extends as deep as 1,600 dbar. Most of the eddies show more intense anomalies between about 100 and 700 dbar, suggesting that they are subsurface intensified. Their identification based on surface properties only (weak ADT, SST) can lead to an underestimation of the anomalies. For example, though C12 presents a positive SST anomaly (3.89°C), while the vertical structure shows intense negative conservative temperature, absolute salinity and positive density anomalies between 100 and 1,200 m depth, clearly indicating that this is a cyclonic cold core eddy. Similarly, A3 and A6 do not show significant SST or salinity anomalies, though their core is warmer and saltier than the surrounding waters (Figure 8).

One clear asymmetry between AEs and CEs is that the absolute maxima in density anomalies are observed immediately above $\gamma^n = 26.35 \text{ kg m}^{-3}$ for AEs (surface intensified negative density anomalies) and immediately below $\gamma^n = 26.35 \text{ kg m}^{-3}$ for cyclonic eddies (subsurface intensified positive density anomalies). The maximum (absolute value) in conservative temperature and absolute salinity anomalies follow the same pattern. Below the thermocline, where stratification is weaker, the vertical displacement of the isopycnals in A3 and A6 is larger than in the upper layers. The intense and deep-reaching eddies like C1 show an inversion in salinity anomalies below 800 dbar essentially impacted by AAIW (Figure 8c).

The vertical structure of three mesoscale eddies (A3, A6, and C12) crossed very close to the center and sampled with at least three CTD profiles exhibit very different characteristics. The easternmost eddy C1 was crossed near the eastern boundary, Anticyclone A6 was crossed east of the Mid-Atlantic Ridge and the westernmost eddy C10 was located west of the Mid-Atlantic Ridge. Differences in sea-level height between the center of the eddy and the maximum velocity contour are 5, 15, and 25 cm for C10, A6 and C1 respectively (Figures 9a–9c). The SADC and geostrophic (Method 2) meridional velocities are in good agreement (Figures 9d–9j). Every contour of 5 cm in the ADT gradient for a typical radius of 40 km provides 0.15 m s^{-1} surface geostrophic velocities at this latitude, which is also the color interval in Figure 9d–i. The most intense eddy, C1, shows currents of 0.8 m s^{-1} with a stronger northward flow. These three eddies seem to be subsurface intensified and separated from the surface. This is particularly true for C1 whose maximum velocity core lies at 100 dbar. As the ADT gradient decreases, subsurface density anomalies decrease, currents within the eddy tend to get shallower, weaker, and the core region with velocities close to 0 wider (Figure 9d–l).

In the western boundary, the BC appears as a narrow jet (50 km) between 50°W and 49.55°W associated with a large tilt in the isopycnals. The continuous SADC measurements allowed us to sample the core of the BC at 49.85°W with southward mean velocities of about 0.8 m s^{-1} in the upper 500 dbars. This is nearly 150 km offshore than the usual location of the BC at 51.5°W according to Valla et al., (2018). The BC was surrounded by two cyclonic eddies, C12 and C13. C12 was centered north of 34.5°S and registered the maximum zonal velocity of the section (0.8 m s^{-1}). TOEddies tracked C12 from the Zapiola gyre, with a mean translation speed of about 8 km per day, nearly double that of the other CEs crossed (Figure 2b). SADC, ship-mounted acoustic doppler current profilers.

The volume transport between 50°W and 49.55°W associated with western boundary currents (BC and Deep Western Boundary Current) was particularly intense, with a maximum transport of -35.60 Sv between surface and 2,827 dbar from ADCPs (Method 1), and -46.19 Sv from surface to 2,842 dbar from geostrophy (Method 2), respectively. Identifying the limit between the BC and the Deep Western Boundary Current can be difficult as both currents flow southward near the slope. In the upper 1,000 dbars, both methods display a strong jet with a mean meridional velocity about -0.5 m s^{-1} . Below 1,000 dbar, the southward jet displays a progressively offshore shift in the downward direction, as observed by Valla et al. (2018; Figure 10).

The BC volume transport from surface to 500 dbar, a common reported value, during MSM60 is -13.97 – -15.87 Sv from Method 1 and 2, respectively. In the upper 800 dbars, both methods display a volume transport of -20.86 – -23.46 , respectively. Our estimates agree to the -19.4 Sv at 35°S reported by S. L. Garzoli et al., (2013) from 17 XBTs transects in the upper 800 m, and also with Schmid & Majumder (2018; and references therein) who estimate a volume transport of $-17.3 \pm 3.5 \text{ Sv}$ combining Argo floats and sea surface

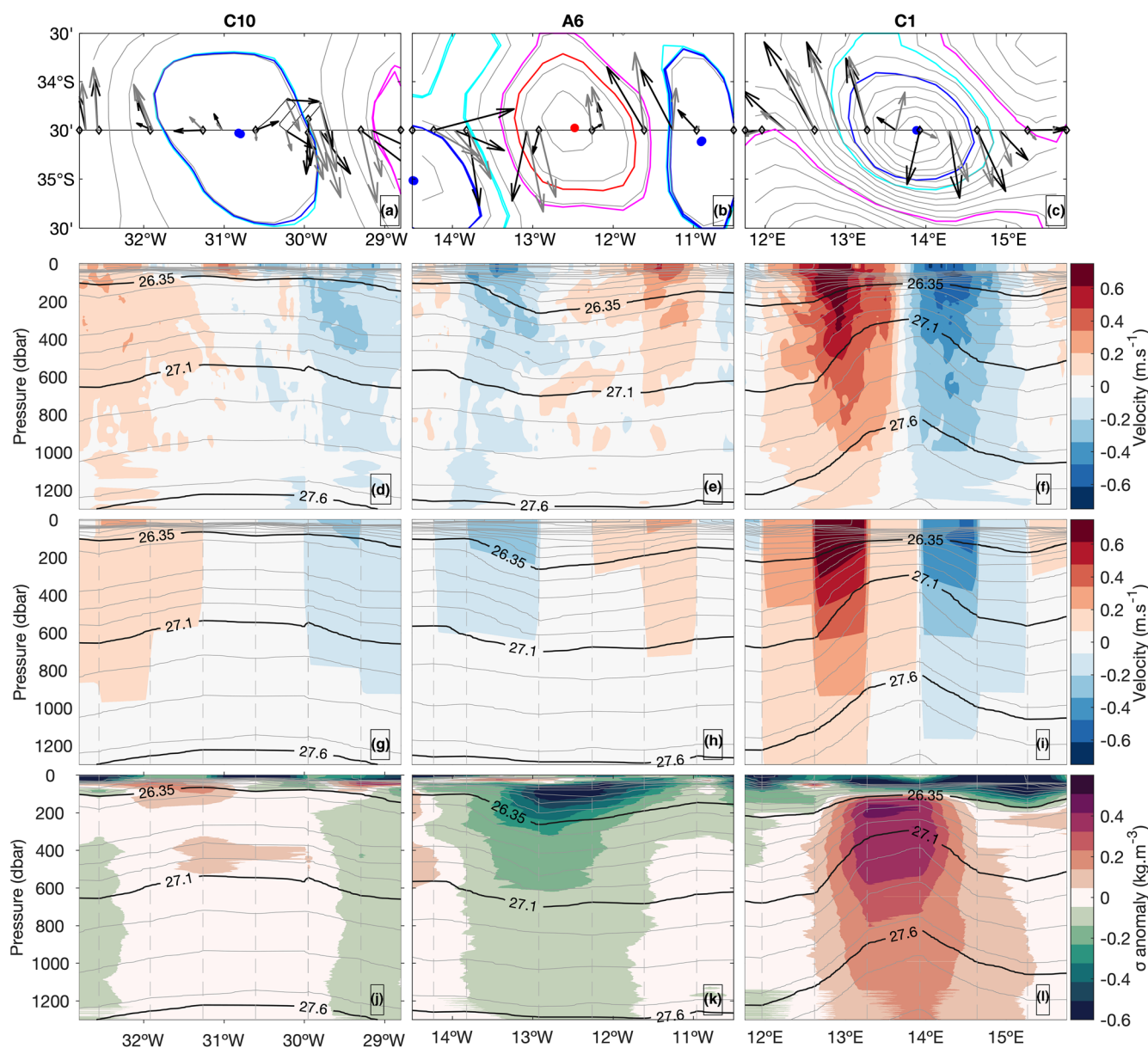


Figure 9. Three mesoscale eddies crossed through their center during MSM60. Each column corresponds to a specific eddy and each row to one property. (a–c) Absolute Dynamic Topography (ADT) observed from satellite altimetry (gray contours, 5 cm contour interval). The black line shows the cruise track over 34.5°S and the black diamonds the CTD profiles location. Black and gray arrows represent the ocean current velocity vectors calculated from altimetry and geostrophy (averaged over the upper 100 m), respectively. Cyan (magenta) and blue (red) contours represent the outermost and maximum velocity contours of the cyclonic (anticyclonic) eddies, respectively. The dot represents the eddy centroid. (d–f) SADCPC velocity. Black contours show neutral density isolines. (g–i) Geostrophic velocity calculated relative to $\gamma = 28.1 \text{ kg m}^{-3}$ and then mass balanced. Black contours show neutral density isolines. The dashed line shows the CTD profile positions. (j–l) Vertical profiles of potential density anomaly (kg m^{-3}) calculated relative to the summer non-eddy Argo climatology.

height, also in the upper 800 m. The reason for our higher ($\sim 4 \text{ Sv}$) values could be related not only to the temporal variability of the BC but also with the high-resolution data used here, allowing to sample the sharp gradients associated with the boundary current.

4.5. Comparison with Nearby GO-SHIP Transects

Given the sensitivity of the transport estimates to the method used, a final analysis was undertaken to compare our results with nearby GO-SHIP sections A09 at 24°S (King & Hamersley, 2010), A10 at 30°S (M.

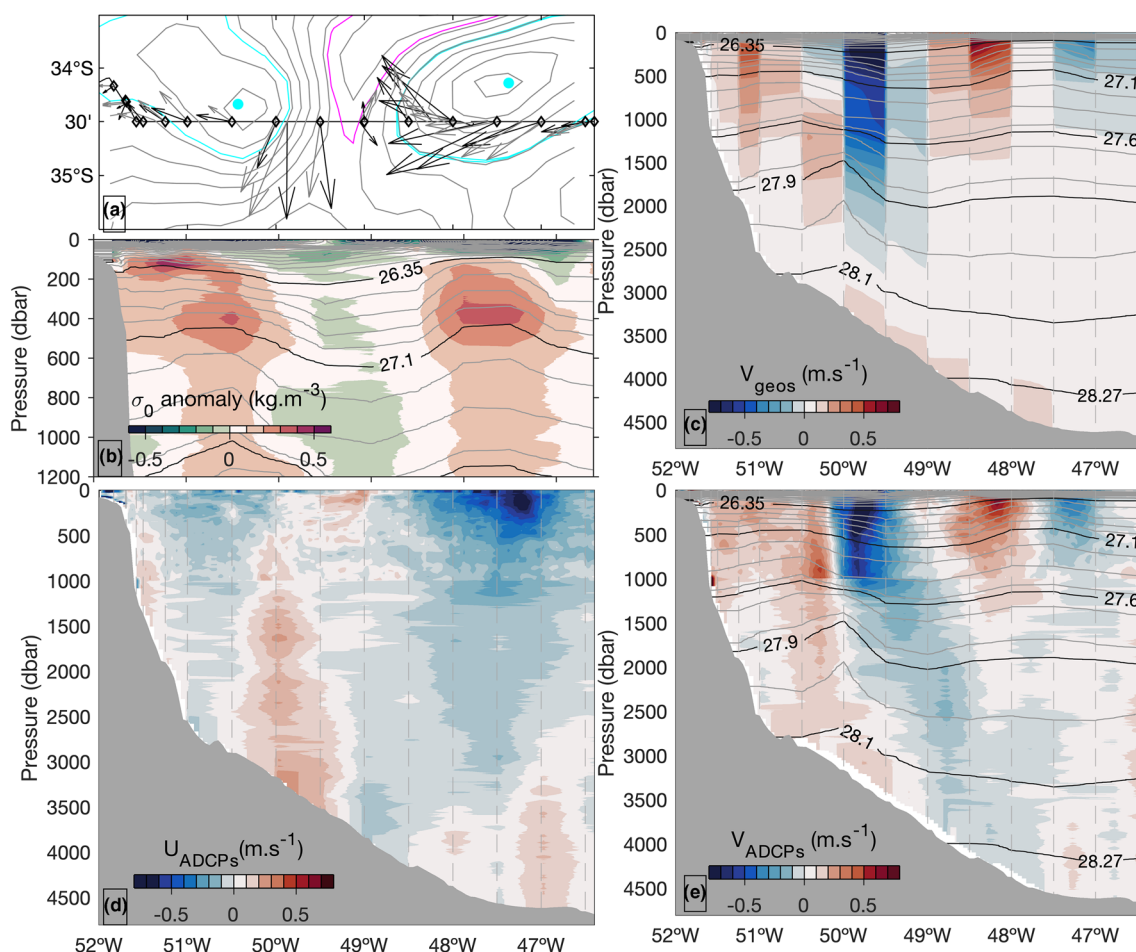


Figure 10. South Atlantic western boundary velocity structure at 34.5°S during the MSM60 cruise. (a) Horizontal map of the satellite derived absolute dynamic topography with isolines every 5 cm in gray. The black line shows the cruise track over 34.5°S. Black and gray arrows represent the ocean current velocity vectors calculated from altimetry and geostrophy (averaged over the upper 100 m), respectively. Cyan and magenta contours represent the maximum velocity contours of the cyclonic and anticyclonic eddies, respectively. (b) Vertical profile of potential density anomaly (kg m^{-3}) relative to a non-eddy Argo climatology for summer. (c) Geostrophic velocity (method 1). Black contours show neutral density isolines. (d) Zonal and (e) Meridional Velocity from ADCPs. The abrupt change in the horizontal resolution at 1000 dbar is due to the change from the SADCP observations gridded every 0.05° to the LADCP observations restricted to the CTD profiles approximately every 0.5° . CTD, conductivity-temperature-depth; LADCP, lowered acoustic doppler current profilers; SADCP, ship-mounted acoustic doppler current profilers.

Baringer & Macdonald, 2013) and MSM60 at 34.5°S (Table 4). Following the same approach as Method 2, all data were gridded into a 0.05° by 1 dbar across the main latitude of each section. Then, we computed the geostrophic velocity relative to $\gamma^n = 28.1 \text{ kg m}^{-3}$ as level of no motion, added the Ekman transport in the upper 50 dbar and then added a uniform barotropic velocity in order to achieve mass balance. It is important to underline that the zonal distance between grid point is different due to latitudinal variations, with 0.05° representing 5058, 4812 and 4,579 m for 24°S, 30°S and 34.5°S, respectively.

Overall, the results are consistent with previous studies (e.g., Ganachaud & Wunsch, 2003). The computed AMOC volume transports are 24.47, 20.43 and 15.18 Sv, and MHT values are 1.08, 0.65 and 0.23 PW at 24°S, 30°S and 34.5°S, respectively (Table 4). Both, the northward heat transport across all three sections and the AMOC strength increase northward from 34.5°S. The increase rate is nearly linear between 34.5°S and 24°S, being 0.09 PW and 0.08 PW, 1.17 Sv and 1.50 Sv per degree latitude from

Table 4
Volume Transport, Meridional Heat Transport (MHT) and Freshwater Transport (MFT) Estimates of the Meridional Overturning Circulation Through the Different trans-Atlantic Sections in This Study Applying the Same Methodology: $\gamma^n = 28.1 \text{ kg m}^{-3}$ as Level of No Motion and Equally Distributing the Imbalance Assumed as the Barotropic Flow

| Section | Date | AMOC (Sv-dbar) | MHT (PW) | MFT (Sv) |
|--------------|--------|----------------|----------|----------|
| A09 24°S | Mar/09 | 24.47–1275 | 1.08 | −0.23 |
| A10 30°S | Oct/11 | 20.43–1208 | 0.65 | −0.02 |
| MSM60 34.5°S | Jan/17 | 15.18–1175 | 0.23 | 0.21 |

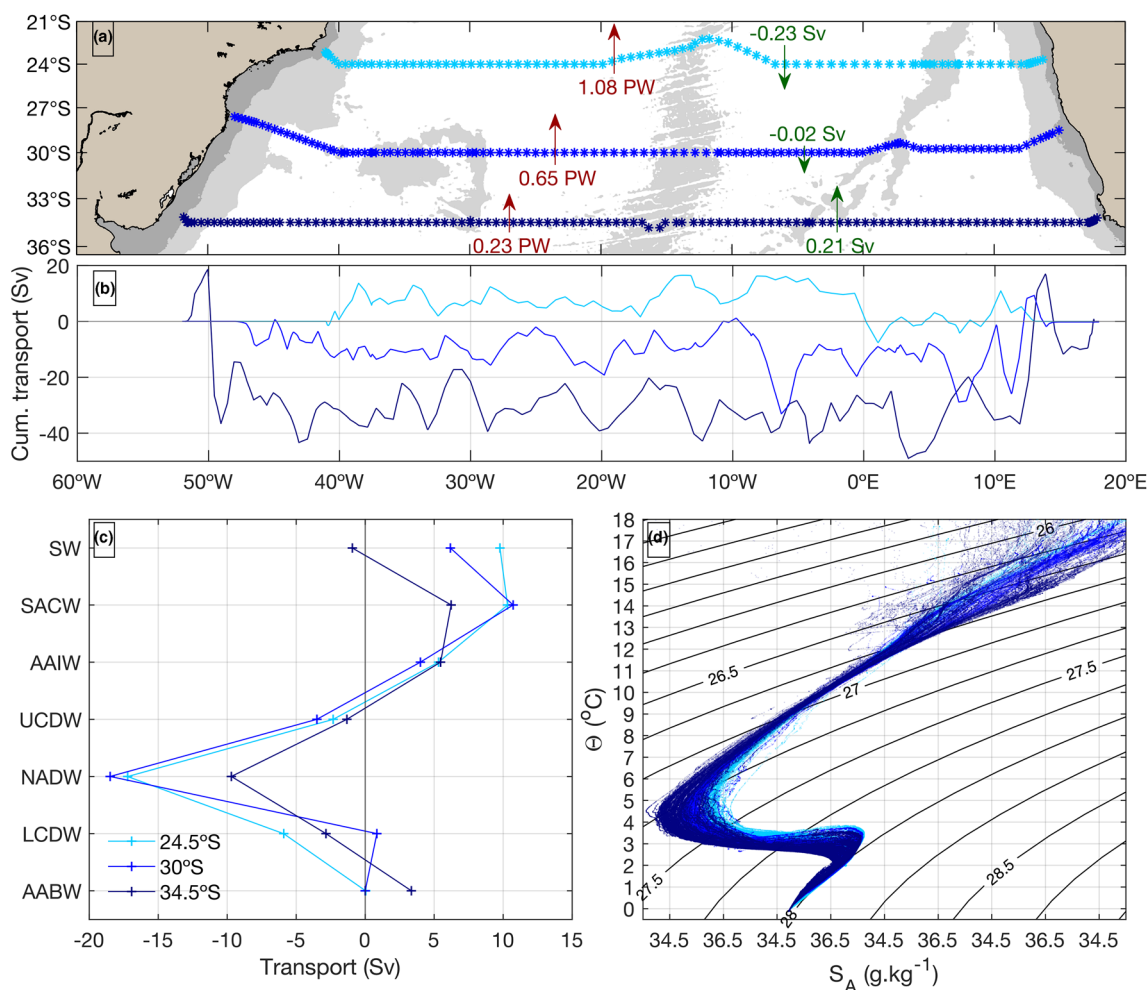


Figure 11. Transport and water masses comparison in the South Atlantic from 3 GO-SHIP sections (A9, A10, and MSM60; see Table 3 for details). (a) CTD positions for A9 (light blue), A10 (blue), and MSM60 (dark blue). The arrows show the net heat (red) and freshwater (green) transports per section. The gray shading represents water depths less than 200 and 3,500 m in the ETOPO2 data set (Smith & Sandwell, 1997). Colors for each section are the same in all panels. (b) Cumulative vertically integrated meridional transport from west to east for the three sections. (c) Transport by water mass layer (see Table 2 for references) (d) Θ - S_A diagram.

34.5°S to 30°S and from 30°S to 24°S, respectively. The latitudinal MHT changes in the upper limb of the SAMOC at 34.5°S relative to the A10 and A09 fluxes are mainly due to the northward transport increase in the upper layers (SW to SACW). SW transport is particularly intense and northward at 24°S (9.9 Sv), less intense at 30°S (6.1 Sv), and negative at 34.5°S (−0.4 Sv). SACW transport is close to 10 Sv at 24°S and 30°S and 7.35 Sv at 34.5°S. NADW is also about 6 Sv larger at lower latitudes than at 34.5°S (Figures 11c and Table 4).

The lower value of MHT at 34.5°S compared to the other two northern sections is partially explained by the intense southward transport of the BC during MSM60 (Peterson & Stramma, 1991; Figure 11b). Moreover, mesoscale eddies also play a role in the upper limb transport. At 34.5°S, mesoscale activity is more energetic than at 30°S and 24°S (Laxenaire et al., 2018). Freshwater transport estimates show a convergence toward the center of the South Atlantic gyre, as expected from the method used (Buckley & Marshall, 2016), with negative values of −0.23 Sv and −0.02 Sv at 24°S and 30°S, while at 34.5°S freshwater transport is 0.21 Sv (Table 4, Figure 11a). The implied freshwater convergence obtained between these latitudes (24°–34.5°S) is quite large as the evaporation needed to achieve that balance should be about three times larger than the annual mean (A. L. Gordon & Piola, 1983). The high sensitivity of the method, and the salt export through the Bering Strait ($27.6 \cdot 10^6 \text{ kg s}^{-1}$, Coachman & Aagaard, 1988), not considered here could explain the large value obtained.

The abyssal overturning cell appears clearly only at 34.5°S, although it is known that AABW flows northward through the Vema Channel at 30°S. However, as only one CTD station was carried out in the Vema Channel during A10 it was not possible to estimate the geostrophic transport there. NADW transport decreases from near -18 Sv at 24°S to -10.84 Sv at 34.5°S. At 24°S there is no AABW nor abyssal overturning cell. The northward limit of the abyssal cell seems to be close to 30°S, confining the AABW flow to the deep Vema and Hunter Channels as suggested also by previous studies (e.g., Hogg et al., 1982; Valla et al., 2019). Finally, although all the sections compared were done in austral spring or summer, observations and models show that the annual cycle in meridional heat transport can account for more than 30% of the variance and should also be considered for comparisons (e.g., Dong et al., 2014). This also emphasizes the need for more regular observations which are able to capture and account for the variations in the annual cycle.

5. Conclusions

This study provides a first description of the water mass structure, currents and meridional volume, heat, and freshwater transport along 34.5°S in the South Atlantic Ocean. The meridional circulation of the upper, deep and abyssal layers is described from direct observations for the first time and complements the efforts by the SAMOC international initiative to determine and monitor the meridional circulation at this latitude, which is a hot spot for the entire AMOC. We also describe and discuss the mesoscale eddy structures encountered during the cruise. Such mesoscale features explain most of the transbasin variability observed in the upper 1,000 dbar.

At 34.5°S we find the abyssal overturning cell is weaker (2.4 ± 1.6 Sv) than the upper cell (15.64 ± 1.39 Sv) and it consists of northward flow of AABW confined to the western basin. Across the section, a net meridional heat transport of 0.27 ± 0.10 PW is observed from geostrophic approximations and 0.26 PW from direct velocity observations (corrected for the mass imbalance over the section). These heat transport estimates are lower than previously reported (~ 0.5 PW, Dong et al., 2015) and could be explained by the relatively low intensity of the upper overturning cell during the cruise compared with the mean reported from moorings (Kersalé et al., 2020) and the anomalous predominance of cold core eddies. In comparisons with neighboring transbasin sections, applying the same analysis methods, we find that the AMOC volume transport and MHT increased toward the equator (0.65 PW at 30°S and 1.08 PW at 24°S). This agrees with previous results indicating this unique characteristic of the equatorial MHT in the South Atlantic, and can be explained by the intensified northward transport and warm waters in the upper layers being compensated by southward flow of relatively cold NADW at depth. The decrease in strength of the upper overturning cell is, among other phenomena, associated with the intensification of the warm Brazil Current (BC) flowing southward between 24°S and 34.5°S, and to a minor extent mesoscale activity, leading to a weakening of the AMOC with increasing latitude (from 24.47 Sv at 24°S to 15.18 Sv at 34.5°S).

One unique value of transbasin sections is having access to hydrographic properties and the flow field at the same time. From the 34.5°S section we identify the existence of more recently ventilated water masses on the western side of the basin and older waters in the east. The major differences in oxygen and thermohaline composition were observed within the AAIW, NADW, and LCDW layers. AAIW is directly injected from the Brazil-Malvinas Confluence region in the west while in the east is supplied mostly from the Indian Ocean and therefore is saltier, warmer and less oxygenated. NADW flows southward and reaches 34.5°S along both boundaries. Because of the indirect path, the eastern NADW branch is less salty and less oxygenated. LCDW is warmer and saltier in the eastern part of the section and also the transport changes sign across the basin, flowing northward in the western part and southward in the eastern part.

Highest velocities are observed in the BC while transient, mesoscale eddies with high but alternating velocities are evident in the upper 500 m of the section. The eddies also carry water mass anomalies that originate from the Indian Ocean and subantarctic waters originated from the Pacific before they dissolve near the Brazil-Malvinas confluence. We find that the eddies have only a small impact on the upper overturning cell but the MHT almost doubled when the eddies (predominantly cold core eddies) were removed. It should also be noted that during the cruise we observed an anomalous predominance of CEs over AEs.

Whereas our results confirm previous findings that the South Atlantic circulation sets preferential paths for inter-oceanic exchanges and actively participates in the transformation of water masses, particularly in

regions of high mesoscale activity (e.g., S. L. Garzoli & Matano, 2011; Speich et al., 2007), they also show the need of high-resolution observations, especially near the boundaries, to correctly resolve the meridional transports.

Data Availability Statement

The data from the MSM60 cruise are available at: https://doi.org/10.2312/cr_msm60. ADT data were downloaded from <http://marine.copernicus.eu/>, SST from <https://podaac.jpl.nasa.gov/>, eddy tracking from https://vesg.ipsl.upmc.fr/thredds/catalog/IPSLFS/rlaxe/catalog.html?data_set=DatasetScanIPSLFS/rlaxe/Database_South_Atl.zip. GO-SHIP datasets were downloaded from <http://cchdo.ucsd.edu>.

Acknowledgments

The authors declare to have no conflict of interest and deeply acknowledge all the people on board MSM60, the SAMOC-SAMBAR team, and all the open access datasets. This work was supported by the European Union's Horizon 2020 research and innovation program under grant agreements no. 633211 (AtlantOS) and no. 817578 (TRIATLAS), the TOEddies CNES-TO-SCA research grant. In addition, this work was further supported under the South African NRF grants UID 110733 and 118901. G. Manta received funding from bourse ANII-Campus France (POS_CFRA_2017_1_146868). M. Kersalé was supported in part under the auspices of the Cooperative Institute for Marine and Atmospheric Studies (CIMAS), a Cooperative Institute of the University of Miami and the National Oceanic and Atmospheric Administration (NOAA), cooperative agreement NA20OAR4320472. M. Kersalé and C. S. Meinen also acknowledge additional support from the NOAA Atlantic Oceanographic and Meteorological Laboratory. R. Hummels acknowledges support from the German Federal Ministry of Education and Research as part of the cooperative project RACE (03F0605 B, 03F0824 C) and the European Union's Horizon 2020 research and innovation program under grant agreement 817578 TRIATLAS project. SAMBAR Project is funded by the Sao Paulo State Research Foundation (FAPESP, grants 2011/50552-4 and 2017/09659-6). T. Lamont, M.A. van den Berg, and I. Ansonge received funding from the South African National Research Foundation (no. 110733) as well as the Department of Environment, Forestry and Fisheries. The authors also acknowledge the mesoscale calculation server CICLAD (<http://ciclad-web.ipsl.jussieu.fr>) dedicated to Institut Pierre Simon Laplace modeling and data analyses effort for technical and computational support.

References

- Almeida, L., de Azevedo, J. L. L., Kerr, R., Araujo, M., & Mata, M. M. (2018). Impact of the new equation of state of seawater (TEOS-10) on the estimates of water mass mixture and meridional transport in the Atlantic Ocean. *Progress in Oceanography*, 162, 13–24. <https://doi.org/10.1016/j.pocean.2018.02.008>
- Ansonge, I. J., Baringer, M. O., Campos, E. J., Dong, S., Fine, R. A., Garzoli, S. L., & Roberts, M. J. (2014). Basin-wide oceanographic array bridges the South Atlantic. *Eos, Transactions American Geophysical Union*, 95(6), 53–54. <https://doi.org/10.1002/2014EO060001>
- Argo. (2020). Argo float data and metadata from Global Data Assembly Centre (Argo GDAC). *SEANOE*. <https://doi.org/10.17882/42182>
- Arhan, M., Mercier, H., & Lutjeharms, J. R. E. (1999). The disparate evolution of three Agulhas rings in the South Atlantic Ocean. *Journal of Geophysical Research*, 104(C9), 20987–21005. <https://doi.org/10.1029/1998JC900047>
- Arhan, M., Mercier, H., & Park, Y. H. (2003). On the deep water circulation of the eastern South Atlantic Ocean. *Deep Sea Research Part I: Oceanographic Research Papers*, 50(7), 889–916. [https://doi.org/10.1016/S0967-0637\(03\)00072-4](https://doi.org/10.1016/S0967-0637(03)00072-4)
- Artana, C., Provost, C., Lellouche, J.-M., Rio, M.-H., Ferrari, R., & Sennéchaël, N. (2019). The Malvinas Current at the confluence with the Brazil Current: Inferences from 25 years of Mercator ocean reanalysis. *Journal of Geophysical Research: Oceans*, 124, 7178–7200. <https://doi.org/10.1029/2019JC015289>
- Baringer, M. O., & Garzoli, S. L. (2007). Meridional heat transport determined with expendable bathythermographs—Part I: Error estimates from model and hydrographic data. *Deep Sea Research Part I: Oceanographic Research Papers*, 54(8), 1390–1401. <https://doi.org/10.1016/j.dsr.2007.03.011>
- Baringer, M., & Macdonald, A. (2013). *A10 Cruise Summary Information*. Downloaded from <https://cchdo.ucsd.edu/cruise/33RO20110926>
- Belkin, I. M., & Gordon, A. L. (1996). Southern Ocean fronts from the Greenwich meridian to Tasmania. *Journal of Geophysical Research: Oceans*, 101(C2), 3675–3696. <https://doi.org/10.1029/95JC02750>
- Bentamy, A., & Fillon, D. C. (2012). Gridded surface wind fields from Metop/ASCAT measurements. *International Journal of Remote Sensing*, 33(6), 1729–1754. <https://doi.org/10.1080/01431161.2011.600348>
- Bjostoch, A., Böning, C. W., & Lutjeharms, J. R. E. (2008). Agulhas leakage dynamics affects decadal variability in Atlantic overturning circulation. *Nature*, 456(7221), 489–492. <https://doi.org/10.1038/nature07426>
- Boebel, O., Davis, R. E., Ollitrault, M., Peterson, R. G., Richardson, P. L., Schmid, C., & Zenk, W. (1999). The intermediate depth circulation of the western South Atlantic. *Geophysical Research Letters*, 26(21), 3329–3332. <https://doi.org/10.1029/1999GL002355>
- Bryden, H. L., & Imawaki, S. (2001). *Ocean heat transport*. In: *International Geophysics* (77 pp. 455–474). Academic Press. [https://doi.org/10.1016/S0074-6142\(01\)80134-0](https://doi.org/10.1016/S0074-6142(01)80134-0)
- Bryden, H. L., King, B. A., & McCarthy, G. D. (2011). South Atlantic overturning circulation at 24°S. *Journal of Marine Research*, 69(1), 38–55. <https://doi.org/10.3389/fmars.2019.00260>
- Buckley, M. W., & Marshall, J. (2016). Observations, inferences, and mechanisms of the Atlantic Meridional Overturning Circulation: A review. *Reviews of Geophysics*, 54, 5–63. <https://doi.org/10.1002/2015RG000493>
- Callahan, J. E. (1972). The structure and circulation of deep water in the Antarctic. Deep sea research and oceanographic abstracts (Vol. 19, No. 8, pp. 563–575). Elsevier.
- Capet, A., Mason, E., Rossi, V., Troupin, C., Faugère, Y., Pujol, I., & Pascual, A. (2014). Implications of refined altimetry on estimates of mesoscale activity and eddy-driven offshore transport in the eastern boundary upwelling systems. *Geophysical Research Letters*, 41(21), 7602–7610. <https://doi.org/10.1002/2014GL061770>
- Capuano, T. A., Speich, S., Carton, X., & Laxenaire, R. (2018). Indo-Atlantic exchange, Mesoscale dynamics, and Antarctic intermediate water. *Journal of Geophysical Research: Oceans*, 123(5), 3286–3306. <https://doi.org/10.1002/2017JC013521>
- Chidichimo, M. P., Kanzow, T., Cunningham, S. A., & Marotzke, J. (2010). The contribution of eastern boundary density variations to the North Atlantic meridional overturning circulation at 26, 5°N. *Ocean Science*, 6, 475–490. <https://doi.org/10.5194/os-6-475-2010>
- Chin, T. M., Vazquez-Cuervo, J., & Armstrong, E. M. (2017). A multi-scale high-resolution analysis of global sea surface temperature. *Remote Sensing of Environment*, 200, 154–169. <https://doi.org/10.1016/j.rse.2017.07.029>
- Cimatoribus, A. A., Drijfhout, S. S., Den Toom, M., & Dijkstra, H. A. (2012). Sensitivity of the Atlantic meridional overturning circulation to South Atlantic freshwater anomalies. *Climate Dynamics*, 39(9–10), 2291–2306. <https://doi.org/10.1007/s00382-012-1292-5>
- Coachman, L. K., & Aagaard, K. (1988). Transports through Bering Strait: Annual and interannual variability. *Journal of Geophysical Research: Oceans*, 93(C12), 15535–15539. <https://doi.org/10.1029/JC093iC12p15535>
- Cunningham, S. A., Kanzow, T., Rayner, D., Baringer, M. O., Johns, W. E., Marotzke, J., & Meinen, C. S. (2007). Temporal variability of the Atlantic meridional overturning circulation at 26.5°N. *Science*, 317(5840), 935–938. <https://doi.org/10.1126/science.1141304>
- Dong, S., Baringer, M. O., Goni, G. J., Meinen, C. S., & Garzoli, S. L. (2014). Seasonal variations in the South Atlantic meridional overturning circulation from observations and numerical models. *Geophysical Research Letters*, 41, 4611–4618. <https://doi.org/10.1002/2014GL060428>
- Dong, S., Garzoli, S., Baringer, M., Meinen, C., & Goni, G. (2009). Interannual variations in the Atlantic meridional overturning circulation and its relationship with the net northward heat transport in the South Atlantic. *Geophysical Research Letters*, 36(20), L20606. <https://doi.org/10.1029/2009GL039356>

- Dong, S., Goni, G., & Bringas, F. (2015). Temporal variability of the South Atlantic meridional overturning circulation between 20°S and 35°S. *Geophysical Research Letters*, 42(18), 7655–7662. <https://doi.org/10.1002/2015GL065603>
- Drijfhout, S. S., Weber, S. L., & van der Swaluw, E. (2011). The stability of the MOC as diagnosed from model projections for pre-industrial, present and future climates. *Climate Dynamics*, 37(7–8), 1575–1586. <https://doi.org/10.1007/s00382-010-0930-z>
- Duacs/AVISO+ (2015). SSALTO/DUACS user handbook:(M) SLA and (M) ADT near-real time and delayed time products (vol. 6, pp. 74). CLS-DOS-NT-06-034.
- Frajka-Williams, E., Cunningham, S. A., Bryden, H., & King, B. A. (2011). Variability of Antarctic Bottom Water at 24.5°N in the Atlantic. *Journal of Geophysical Research*, 116, C11026. <https://doi.org/10.1029/2011jc007168>
- Frajka-Williams, E., Anson, I. J., Baehr, J., Bryden, H. L., Chidichimo, M. P., Cunningham, S. A., & Holliday, N. P. (2019). Atlantic meridional overturning circulation: Observed transports and variability. *Frontiers in Marine Science*, 6, 260. <https://doi.org/10.3389/fmars.2019.00260>
- Ganachaud, A., & Wunsch, C. (2003). Large-scale ocean heat and freshwater transports during the World Ocean Circulation Experiment. *Journal of Climate*, 16(4), 696–705. [https://doi.org/10.1175/1520-0442\(2003\)016<0696:LSOHAF>2.0.CO;2](https://doi.org/10.1175/1520-0442(2003)016<0696:LSOHAF>2.0.CO;2)
- Garzoli, S. L., & Baringer, M. O. (2007). Meridional heat transport determined with expandable bathythermographs—Part II: South Atlantic transport. *Deep Sea Research Part I: Oceanographic Research Papers*, 54(8), 1402–1420. <https://doi.org/10.1016/j.dsr.2007.04.013>
- Garzoli, S. L., Baringer, M. O., Dong, S., Perez, R. C., & Yao, Q. (2013). South Atlantic meridional fluxes. *Deep-Sea Research Part I*, 71, 21–32. <https://doi.org/10.1016/j.dsr.2012.09>
- Garzoli, S. L., & Matano, R. (2011). The South Atlantic and the Atlantic meridional overturning circulation. *Deep Sea Research Part II: Topical Studies in Oceanography*, 58(17–18), 1837–1847. <https://doi.org/10.1016/j.dsr2.2010.10.063>
- Georgi, D. T. (1981). On the relationship between the large-scale property variations and fine structure in the circumpolar deep water. *Journal of Geophysical Research*, 86(C7), 6556–6566. <https://doi.org/10.1029/JC086iC07p06556>
- Gladyshev, S., Arhan, M., Sokov, A., & Speich, S. (2008). A hydrographic section from South Africa to the southern limit of the Antarctic circumpolar current at the Greenwich meridian. *Deep Sea Research Part I: Oceanographic Research Papers*, 55(10), 1284–1303. <https://doi.org/10.1016/j.dsr.2008.05.009>
- Gordon, A. L. (1981). South Atlantic thermocline ventilation. *Deep Sea Research Part I*, 28, 1239–1264. [https://doi.org/10.1016/0198-0149\(81\)90033-9](https://doi.org/10.1016/0198-0149(81)90033-9)
- Gordon, A. L. (1985). Indian-Atlantic transfer of thermocline water at the Agulhas retroflection. *Science*, 227(4690), 1030–1033. <https://doi.org/10.1126/science.227.4690.1030>
- Gordon, A. L. (1986). Interocean exchange of thermocline water. *Journal of Geophysical Research*, 91(C4), 5037–5046. <https://doi.org/10.1029/JC091iC04p05037>
- Gordon, A. L., Lutjeharms, J. R., & Gründlingh, M. L. (1987). Stratification and circulation at the Agulhas retroflection. *Deep Sea Research Part A: Oceanographic Research Papers*, 34(4), 565–599. [https://doi.org/10.1016/0198-0149\(87\)90006-9](https://doi.org/10.1016/0198-0149(87)90006-9)
- Gordon, A. L., & Piola, A. R. (1983). Atlantic Ocean upper layer salinity budget. *Journal of Physical Oceanography*, 13(7), 1293–1300. [https://doi.org/10.1175/1520-0485\(1983\)013<1293:AOULSB>2.0.CO;2](https://doi.org/10.1175/1520-0485(1983)013<1293:AOULSB>2.0.CO;2)
- Gordon, A. L., Weiss, R. F., Smethie, W. M., Jr, & Warner, M. J. (1992). Thermocline and intermediate water communication between the South Atlantic and Indian Oceans. *Journal of Geophysical Research*, 97(C5), 7223–7240. <https://doi.org/10.1029/92JC00485>
- Guerra, L. A. A., Paiva, A. M., & Chassignet, E. P. (2018). On the translation of Agulhas rings to the western South Atlantic Ocean. *Deep Sea Research Part I: Oceanographic Research Papers*, 139, 104–113. <https://doi.org/10.1016/j.dsr.2018.08.005>
- Hernández-Guerra, A., & Talley, L. D. (2016). Meridional overturning transports at 30°S in the Indian and Pacific Oceans in 2002–2003 and 2009. *Progress in Oceanography*, 146, 89–120. <https://doi.org/10.1016/j.pocean.2016.06.005>
- Hernández-Guerra, A., Talley, L. D., Pelegrí, J. L., Vélez-Belchi, P., Baringer, M. O., Macdonald, A. M., & McDonagh, E. L. (2019). The upper, deep, abyssal and overturning circulation in the Atlantic Ocean at 30°S in 2003 and 2011. *Progress in Oceanography*, 176, 102136. <https://doi.org/10.1016/j.pocean.2019.102136>
- Herrford, J., Brandt, P., Kanzow, T., Hummels, R., Araujo, M., & Durgadoo, J. V. (2020). Seasonal variability of the Atlantic meridional overturning circulation at 11°S inferred from bottom pressure measurements. *Ocean Science Discussions*, In review, 1–37. <https://doi.org/10.5194/os-2020-55>
- Hogg, N., Biscaye, P., Gardner, W., & Schmitz, W. J., Jr (1982). On the transport and modification of Antarctic Bottom Water in the Vema Channel. *Journal of Marine Research*, 40(23), 1–263.
- Holfort, J., & Siedler, G. (2001). The meridional oceanic transports of heat and nutrients in the South Atlantic. *Journal of Physical Oceanography*, 31(1), 5–29. [https://doi.org/10.1175/1520-0485\(2001\)031<0005:TMOTOH>2.0.CO;2](https://doi.org/10.1175/1520-0485(2001)031<0005:TMOTOH>2.0.CO;2)
- Holliday, N. P., Bacon, S., Cunningham, S. A., Gary, S. F., Karstensen, J., King, B. A., & McDonagh, E. L. (2018). Subpolar North Atlantic overturning and gyre-scale circulation in the summers of 2014 and 2016. *Journal of Geophysical Research: Oceans*, 123(7), 4538–4559. <https://doi.org/10.1029/2018JC013841>
- E. M. Hood, C. L. Sabine, & B. M. Sloyan (Eds.), (2010). *The GO-SHIP repeat hydrography manual: A collection of expert reports and guidelines*. IOCCP report number 14, ICPO publication series number 134. Retrieved From <http://www.go-ship.org/HydroMan.html>
- Hsiung, J. (1985). Estimates of global oceanic meridional heat transport. *Journal of Physical Oceanography*, 15(11), 1405–1413. [https://doi.org/10.1175/1520-0485\(1985\)015<1405:EOGOMH>2.0.CO;2](https://doi.org/10.1175/1520-0485(1985)015<1405:EOGOMH>2.0.CO;2)
- Johns, W. E., Baringer, M. O., Beal, L. M., Cunningham, S. A., Kanzow, T., Bryden, H. L., & Curry, R. (2011). Continuous, array-based estimates of Atlantic Ocean heat transport at 26.5°N. *Journal of Climate*, 24(10), 2429–2449. <https://doi.org/10.1175/2010JCLI3997.1>
- Kanzow, T., Cunningham, S. A., Johns, W. E., Hirschi, J. J., Marotzke, J., Baringer, M. O., & Bryden, H. L. (2010). Seasonal variability of the Atlantic meridional overturning circulation at 26.5°N. *Journal of Climate*, 23(21), 5678–5698. <https://doi.org/10.1175/2010JCLI3389.1>
- Karstensen, J., Speich, S., Asdar, S., Berbel, G. B. B., Branlard, L., Carvalho, A., et al. (2019). *Seamount observatory and SAMOC overturning, cruise No. MSM60, January 04 – February 01, 2017*. Cape Town (South Africa)-Montevideo (Uruguay): MARIA S. MERIAN-Berichte, Gutachterpanel Forschungsschiffe. https://doi.org/10.2312/cr_msm60
- Kersalé, M., Lamont, T., Speich, S., Terre, T., Laxenaire, R., Roberts, M. J., & Anson, I. J. (2018). Moored observations of mesoscale features in the Cape Basin: characteristics and local impacts on water mass distributions. *Ocean Science*, 14, 923–945. <https://doi.org/10.5194/os-14-923-2018>
- Kersalé, M., Meinen, C. S., Perez, R. C., Le Hénaff, M., Valla, D., Lamont, T., & Garzoli, S. (2020). Highly variable upper and abyssal overturning cells in the South Atlantic. *Science Advances*, 6(32), eaba7573. <https://doi.org/10.1126/sciadv.aba7573>
- Kersalé, M., Perez, R. C., Speich, S., Meinen, C. S., Lamont, T., Le Hénaff, M., & Schmid, C. (2019). Shallow and deep eastern boundary currents in the South Atlantic at 34.5°S: Mean structure and variability. *Journal of Geophysical Research: Oceans*, 124(3), 1634–1659. <https://doi.org/10.1029/2018JC014554>

- B. A. King, & D. R. C. Hamersley (Eds.). (2010). *RSS James Cook cruise JC032, 07 Mar–21 Apr 2009: Hydrographic sections across the Brazil current and at 24°S in the Atlantic* (48, pp. 173). National Oceanography Centre Southampton Cruise Report.
- Laxenaire, R., Speich, S., Blanke, B., Chaigneau, A., Pegliasco, C., & Stegner, A. (2018). Anticyclonic eddies connecting the western boundaries of Indian and Atlantic oceans. *Journal of Geophysical Research: Oceans*, 123(11), 7651–7677. <https://doi.org/10.1029/2018JC014270>
- Laxenaire, R., Speich, S., & Stegner, A. (2019). Evolution of the thermohaline structure of one Agulhas ring reconstructed from Satellite altimetry and Argo floats. *Journal of Geophysical Research: Oceans*, 124, 8969–9003. <https://doi.org/10.1029/2018JC014426>
- Lopez, H., Dong, S., Lee, S. K., & Goni, G. (2016). Decadal modulations of interhemispheric global atmospheric circulations and monsoons by the South Atlantic meridional overturning circulation. *Journal of Climate*, 29(5), 1831–1851. <https://doi.org/10.1175/JCLI-D-15-0491.1>
- Lozier, M. S., Bacon, S., Bower, A. S., Cunningham, S. A., De Jong, M. F., De Steur, L., & Heimbach, P. (2017). Overturning in the subpolar north Atlantic program: A new international ocean observing system. *Bulletin of the American Meteorological Society*, 98(4), 737–752. <https://doi.org/10.1175/BAMS-D-16-0057.1>
- Lozier, M. S., Li, F., Bacon, S., Bahr, F., Bower, A. S., Cunningham, S. A., & Gary, S. F. (2019). A Sea change in our view of overturning in the subpolar North Atlantic. *Science*, 363(6426), 516–521. <https://doi.org/10.1126/science.aau6592>
- Lumpkin, R., & Speer, K. (2007). Global ocean meridional overturning. *Journal of Physical Oceanography*, 37(10), 2550–2562. <https://doi.org/10.1175/JPO3130.1>
- Lutjeharms, J. R. E., De Ruijter, W. P. M., & Peterson, R. G. (1992). Interbasin exchange and the Agulhas retroflection; the development of some oceanographic concepts. *Deep Sea Research Part A: Oceanographic Research Papers*, 39(10), 1791–1807. [https://doi.org/10.1016/0198-0149\(92\)90029-S](https://doi.org/10.1016/0198-0149(92)90029-S)
- Lutjeharms, J. R. E., & Gordon, A. L. (1987). Shedding of an Agulhas ring observed at sea. *Nature*, 325(6100), 138–140.
- Majumder, S., Schmid, C., & Halliwell, G. (2016). An observations and model-based analysis of meridional transports in the South Atlantic. *Journal of Geophysical Research: Oceans*, 121(8), 5622–5638. <https://doi.org/10.1002/2016JC011693>
- McCarthy, G., McDonagh, E., & King, B. (2011). Decadal variability of thermocline and intermediate waters at 24 S in the South Atlantic. *Journal of Physical Oceanography*, 41(1), 157–165. <https://doi.org/10.1175/2010JPO4467.1>
- McCartney, M. S. (1977). Subantarctic mode water. In a Voyage of discovery. *Deep Sea Research* (vol. 24, pp. 103–119).
- McDonagh, E. L., & King, B. A. (2005). Oceanic fluxes in the South Atlantic. *Journal of Physical Oceanography*, 35(1), 109–122. <https://doi.org/10.1175/JPO-2666.1>
- McDonagh, E. L., McLeod, P., King, B. A., Bryden, H. L., & Valdés, S. T. (2010). Circulation, heat, and freshwater transport at 36 N in the Atlantic. *Journal of Physical Oceanography*, 40(12), 2661–2678. <https://doi.org/10.1175/2010JPO4176.1>
- McDougall, T. J. & P. M. Barker, (2011): *Getting started with TEOS-10 and the Gibbs Seawater (GSW) Oceanographic Toolbox* (pp. 28). SCOR/IAPSO WG127, ISBN 978-0-646-55621-5.
- McDougall, T. J., & Ferrari, R. (2017). Abyssal upwelling and downwelling driven by near-boundary mixing. *Journal of Physical Oceanography*, 47(2), 261–283. <https://doi.org/10.1175/JPO-D-16-0082.1>
- Meinen, C. S., Garzoli, S. L., Perez, R. C., Campos, E., Piola, A. R., Chidichimo, M. P., Dong, S., et al. (2017). Characteristics and causes of deep western boundary current transport variability at 34.5°S during 2009–2014. *Ocean Science*, 13, 175–194. <https://doi.org/10.5194/os-13-175-2017>
- Meinen, C. S., Speich, S., Perez, R. C., Dong, S., Piola, A. R., Garzoli, S. L., & Campos, E. J. (2013). Temporal variability of the meridional overturning circulation at 34.5°S: Results from two pilot boundary arrays in the South Atlantic. *Journal of Geophysical Research: Oceans*, 118(12), 6461–6478. <https://doi.org/10.1002/2013JC009228>
- Meinen, C. S., Speich, S., Piola, A. R., Anson, I., Campos, E., Kersalé, M., & Perez, R. C. (2018). Meridional overturning circulation transport variability at 34.5 S during 2009–2017: Baroclinic and barotropic flows and the dueling influence of the boundaries. *Geophysical Research Letters*, 45(9), 4180–4188. <https://doi.org/10.1029/2018GL077408>
- Orsi, A. H., Johnson, G. C., & Bullister, J. L. (1999). Circulation, mixing, and production of Antarctic bottom water. *Progress in Oceanography*, 43(1), 55–109. [https://doi.org/10.1016/S0079-6611\(99\)00004-X](https://doi.org/10.1016/S0079-6611(99)00004-X)
- Orsi, A. H., Whitworth, T., III, & Nowlin, W. D., Jr (1995). On the meridional extent and fronts of the Antarctic circumpolar current. *Deep Sea Research Part I: Oceanographic Research Papers*, 42(5), 641–673. [https://doi.org/10.1016/0967-0637\(95\)00021-W](https://doi.org/10.1016/0967-0637(95)00021-W)
- Ou, H. W., & De Ruijter, W. P., (1986). Separation of an inertial boundary current from a curved coastline. *Journal of Physical Oceanography*, 16(2), 280–289. [https://doi.org/10.1175/1520-0485\(1986\)016<0280:SOAIBC>2.0.CO;2](https://doi.org/10.1175/1520-0485(1986)016<0280:SOAIBC>2.0.CO;2)
- Perez, R. C., Garzoli, S. L., Meinen, C. S., & Matano, R. P. (2011). Geostrophic velocity measurement techniques for the meridional overturning circulation and meridional heat transport in the South Atlantic. *Journal of Atmospheric and Oceanic Technology*, 28(11), 1504–1521. <https://doi.org/10.1175/JTECH-D-11-00058.1>
- Peterson, R. G., & Stramma, L. (1991). Upper-level circulation in the South Atlantic Ocean. *Progress in Oceanography*, 26(1), 1–73. [https://doi.org/10.1016/0079-6611\(91\)90006-8](https://doi.org/10.1016/0079-6611(91)90006-8)
- Piola, A. R., & Georgi, D. T. (1982). Circumpolar properties of Antarctic intermediate water and Subantarctic mode water. *Deep Sea Research Part A: Oceanographic Research Papers*, 29(6), 687–711. [https://doi.org/10.1016/0198-0149\(82\)90002-4](https://doi.org/10.1016/0198-0149(82)90002-4)
- Piola, A. R., & Gordon, A. L. (1989). Intermediate waters in the southwest South Atlantic. *Deep-Sea Research*, 36(1), 1–16. [https://doi.org/10.1016/0198-0149\(89\)90015-0](https://doi.org/10.1016/0198-0149(89)90015-0)
- Pujol, M.-I., Faugère, Y., Taburet, G., Dupuy, S., Pelloquin, C., Ablain, M., & Picot, N. (2016). DUACS DT2014: the new multi-mission altimeter data set reprocessed over 20 years. *Ocean Science*, 12(5), 1067–1090. <https://doi.org/10.5194/os-12-1067-2016>
- Reid, J. L. (1989). On the total geostrophic circulation of the South Atlantic Ocean: Flow patterns, tracers, and transports. *Progress in Oceanography*, 23(3), 149–244. [https://doi.org/10.1016/0079-6611\(89\)90001-3](https://doi.org/10.1016/0079-6611(89)90001-3)
- Reid, J. L., Nowlin, W. D., & Patzert, W. C. (1977). On the characteristics and circulation of the southwestern Atlantic Ocean. *Journal of Physical Oceanography*, 7, 62–91. [https://doi.org/10.1175/1520-0485\(1977\)007<0062:OTCACO>2.0.CO;2](https://doi.org/10.1175/1520-0485(1977)007<0062:OTCACO>2.0.CO;2)
- Rintoul, S. R. (1991). South Atlantic interbasin exchange. *Journal of Geophysical Research: Oceans*, 96(C2), 2675–2692. <https://doi.org/10.1029/90JC02422>
- Rusciano, E., Speich, S., & Ollitruault, M. (2012). Interocean exchanges and the spreading of Antarctic intermediate water south of Africa. *Journal of Geophysical Research: Oceans*, 117(C10). <https://doi.org/10.1029/2012JC008266>
- Schmid, C., & Majumder, S. (2018). Transport variability of the Brazil Current from observations and a data assimilation model. *Ocean Science*, 14(3), 417–436. <https://doi.org/10.5194/os-14-417-2018>
- Sloyan, B. M., Wanninkhof, R., Kramp, M., Johnson, G. C., Talley, L., Tanhua, T., & Katsumata, K. (2019). The global ocean ship-base hydrographic investigations program (GO-SHIP): A platform for integrated multidisciplinary ocean science. *Frontiers in Marine Science*, 6, 445. <https://doi.org/10.3389/fmars.2019.00445>

- Smeed, D. A., Josey, S. A., Beaulieu, C., Johns, W. E., Moat, B. I., Frajka-Williams, E., et al. (2018). "The North Atlantic Ocean is in a state of reduced overturning." *Geophysical Research Letters*, *45*(3), 1527–1533. <https://doi.org/10.1002/2017GL076350>
- Smith, W., & Sandwell, D. (1997). Global sea floor topography from satellite altimetry and ship depth soundings. *Science*, *277*(5334), 1956–1962. <https://doi.org/10.1126/science.277.5334.1956>
- Speich, S., Blanke, B., & Cai, W. (2007). Atlantic meridional overturning circulation and the Southern Hemisphere supergyre. *Geophysical Research Letters*, *34*(23). <https://doi.org/10.1029/2007GL031583>
- Speich, S., Blanke, B., & Madec, G. (2001). Warm and cold water routes of an OGCM thermohaline conveyor belt. *Geophysical Research Letters*, *28*(2), 311–314. <https://doi.org/10.1029/2000GL011748>
- Speich, S., Garzoli, S. L., Piola, A., Baehr, J., Baringer, M., Barreiro, M., & Chereskin, T. (2009). A monitoring system for the South Atlantic as a component of the MOC (pp. 21–25). *Proceedings of OceanObs09: Sustained ocean observations and information for society (Annex), Venice, Italy*.
- Srokosz, M. A., & Bryden, H. L. (2015). Observing the Atlantic Meridional Overturning Circulation yields a decade of inevitable surprises. *Science*, *348*(6241), 1255575. <https://doi.org/10.1126/science.1255575>
- Stramma, L., & England, M. (1999). On the water masses and mean circulation of the South Atlantic Ocean. *Journal of Geophysical Research*, *104*(C9), 20863–20883. <https://doi.org/10.1029/1999JC000139>
- Suga, T., & Talley, L. D. (1995). Antarctic Intermediate Water circulation in the tropical and subtropical South Atlantic. *Journal of Geophysical Research*, *100*(C7), 13441–13453. <https://doi.org/10.1029/95JC00858>
- Talley, L. D. (2003). Shallow, intermediate, and deep overturning components of the global heat budget. *Journal of Physical Oceanography*, *33*(3), 530–560. [https://doi.org/10.1175/1520-0485\(2003\)033<0530:SIADOC>2.0.CO;2](https://doi.org/10.1175/1520-0485(2003)033<0530:SIADOC>2.0.CO;2)
- Talley, L. D., Feely, R. A., Sloyan, B. M., Wanninkhof, R., Baringer, M. O., Bullister, J. L., & Gruber, N. (2016). Changes in ocean heat, carbon content, and ventilation: A review of the first decade of GO-SHIP global repeat hydrography. *Annual Review of Marine Science*, *8*, 185–215. <https://doi.org/10.1146/annurev-marine-052915-100829>
- Tsuchiya, M., Talley, L. D., & McCartney, M. S. (1994). Water-mass distributions in the western South Atlantic; A section from South Georgia Island (54°S) northward across the equator. *Journal of Marine Research*, *52*(1), 55–81. <https://doi.org/10.1357/0022240943076759>
- Valla, D., Piola, A. R., Meinen, C. S., & Campos, E. (2018). Strong mixing and recirculation in the northwestern Argentine Basin. *Journal of Geophysical Research: Oceans*, *123*, 4624–4648. <https://doi.org/10.1029/2018JC013907>
- Valla, D., Piola, A. R., Meinen, C. S., & Campos, E. (2019). Abyssal transport variations in the southwest South Atlantic: First insights from a long-term observation array at 34.5°S. *Geophysical Research Letters*, *46*, 6699–6705. <https://doi.org/10.1029/2019GL082740>
- Visbeck, M. (2002). Deep velocity profiling using lowered acoustic Doppler current profilers: Bottom track and inverse solutions. *Journal of Atmospheric and Oceanic Technology*, *19*(5), 794–807. [https://doi.org/10.1175/1520-0426\(2002\)019<0794:DVPULA>2.0.CO;2](https://doi.org/10.1175/1520-0426(2002)019<0794:DVPULA>2.0.CO;2)
- Weijer, W., de Ruijter, W. P., Dijkstra, H. A., & Van Leeuwen, P. J., (1999). Impact of interbasin exchange on the Atlantic overturning circulation. *Journal of Physical Oceanography*, *29*(9), 2266–2284. [https://doi.org/10.1175/1520-0485\(1999\)029<2266:IOIEOT>2.0.CO;2](https://doi.org/10.1175/1520-0485(1999)029<2266:IOIEOT>2.0.CO;2)
- Wunsch, C. (1996). *The ocean circulation inverse problem*. Cambridge University Press. <https://doi.org/10.1017/CBO9780511629570>

Chapter 3

Shelf Water Export at the Brazil-Malvinas Confluence Evidenced From Combined in situ and Satellite Observations

In this chapter, we processed the data from an unprecedented high-resolution oceanographic cruise carried out in the Uruguayan economic Exclusive Zone in the Southwestern Atlantic. This has enabled the description of the circulation and water masses in the study area. By using correspondences between the in-situ and satellite data, it has also been possible to expand an index positioning latitudinally the Brazil-Malvinas Confluence. This index confirmed that the Brazil-Malvinas Confluence was located in the study area during the oceanographic cruise. The analyses carried out show that the presence of the Brazil-Malvinas Confluence in the region induced an intense shelf water export into the open ocean. The study revealed that the export happened at the surface of the ocean but also at depth and involved two different sources of shelf water. By combining the in situ data from the oceanographic cruise with satellite data, and an eddy tracking algorithm it has been possible to show that mesoscale eddies are the major drivers of these events. Up to our knowledge, although modeling outputs suggested it, the subsurface shelf water export was not yet characterized by underway in situ observations of hydrography and currents. The two types of shelf water export pathways may contribute to balancing the mass convergence associated with along-shore flows. It might also have an important impact on the regional biogeochemical budgets as well as for marine ecosystems. For example, the Argentine hake (*Merluccius hubbsi*), which is the main fish resource of Uruguay and Argentina, spawns in the exported subsurface water mass (Subantarctic Shelf Waters). This could negatively affect the survival of the larvae by advecting them too far in the open ocean from their nursery zone. On the other hand, the nutrient-rich shelf waters not only fertilize the oligotrophic deep ocean but also advects waters with large biomass, which could lead to a region of concentration of highly valuable big pelagic fish, like tuna or swordfish. Eventually, we showed evidence from Argo floats that these two types of shelf water export happen frequently and that geostrophic currents from altimetry and surface chlorophyll can be good proxies to identify these events.



Shelf Water Export at the Brazil-Malvinas Confluence Evidenced From Combined *in situ* and Satellite Observations

Gaston Manta^{1,2*}, Sabrina Speich¹, Marcelo Barreiro², Romina Trinchin², Camila de Mello², Rémi Laxenaire^{1,3} and Alberto R. Piola^{4,5,6,7}

¹ Laboratoire de Météorologie Dynamique, LMD-IPSL, UMR 8539, École Polytechnique, ENS, CNRS, Paris, France,

² Departamento de Ciencias de la Atmósfera, Facultad de Ciencias, Universidad de la República, Montevideo, Uruguay,

³ Laboratoire de L'Atmosphère et des Cyclones (LACy), UMR 8105 CNRS, Météo-France, Université de La Réunion, Paris,

France, ⁴ Facultad de Ciencias Exactas y Naturales, Universidad de Buenos Aires, Buenos Aires, Argentina, ⁵ Consejo

Nacional de Investigaciones Científicas y Técnicas (CONICET), Buenos Aires, Argentina, ⁶ Departamento Oceanografía,

Servicio Hidrografía Naval, Buenos Aires, Argentina, ⁷ Unidad Mixta Internacional: Instituto Franco-Argentino Sobre Estudios del Clima y sus Impactos, Buenos Aires, Argentina

OPEN ACCESS

Edited by:

William Savidge,
University of Georgia, United States

Reviewed by:

Tamaryn Morris,
South African Weather Service,
South Africa
Anna Rubio,
Technology Center Expert in Marine
and Food Innovation (AZTI), Spain

*Correspondence:

Gaston Manta
gaston.manta@lmd.ipsl.fr

Specialty section:

This article was submitted to
Coastal Ocean Processes,
a section of the journal
Frontiers in Marine Science

Received: 18 January 2022

Accepted: 07 February 2022

Published: 21 March 2022

Citation:

Manta G, Speich S, Barreiro M, Trinchin R, de Mello C, Laxenaire R and Piola AR (2022) Shelf Water Export at the Brazil-Malvinas Confluence Evidenced From Combined *in situ* and Satellite Observations. *Front. Mar. Sci.* 9:857594. doi: 10.3389/fmars.2022.857594

The Brazil-Malvinas Confluence (BMC) is the region where opposing and intense western boundary currents meet along the Southwestern Atlantic slope at about 38°S, generating one of the most energetic mesoscale regions of the global ocean. Based on shipborne observations acquired within the Uruguayan Economic Exclusive Zone (EEZ), combined with satellite data and an eddy tracking algorithm, we analyze the cross-shelf exchanges during May 2016, when the BMC was in an anomalous northern position. Two types of shelf water export were observed triggered by mesoscale dynamics: one was the export of shallow Rio de la Plata Plume waters driven off-shelf by the retroreflection of the Brazil Current. This export formed a 70 km wide, 20 m deep filament that propagated offshore at 0.3 m s⁻¹, with a transport of 0.42 Sv. It lasted about 10 days before being mixed with ambient Confluence waters by strong winds. An additional type of off-shelf transport consisted of a subsurface layer of Subantarctic Shelf Waters (SASW) about 60 m thick that subducted at the BMC reaching 130 m deep and transporting 0.91 ± 0.91 Sv. We show that geostrophic currents derived from satellite altimetry over the slope can be useful to track this subsurface off-shelf export as they are significantly correlated with absolute velocity measurements at this depth. Argo temperature and salinity profiles show evidence of these two types of shelf water export occurring between the BMC front and the separation of the Brazil Current from the shelf-break, suggesting this is a relatively frequent phenomenon, in agreement with previous observations.

Keywords: subsurface shelf water export, cross-shelf exchanges, mesoscale eddies, satellite altimetry, Argo floats, western boundary currents

INTRODUCTION

Western boundary currents (WBCs) and adjacent continental shelves display two distinct circulation regimes separated by a strong vorticity barrier and therefore exhibit distinct water-mass properties and ecosystem composition (Roughan et al., 2011; Franco et al., 2018). Nevertheless, at the separation of WBCs from the shelf-break, the instabilities of the currents generate meanders and eddies that induce strong interactions between the shelf and the deep ocean generating intense cross-shelf exchanges (Arruda and da Silveira, 2019; Ismail and Ribbe, 2019; Malan et al., 2020; Roughan et al., 2022). These cross-shelf exchanges have important consequences for marine life, as they provide nutrients to the oligotrophic deep ocean and offshore advection of larvae from species that live on the shelf (Franco et al., 2017, 2018). Historically, these systems have been difficult to model accurately, due to a combination of numerical constraints such as small-scale highly energetic dynamics over steep and complex topography, and also due to the lack of observations to compare with, making the sampling of these sporadic events very valuable.

In the South Atlantic, the WBCs are the poleward flowing warm and salty south Brazil Current (BC), which is a relatively weak western boundary current associated with the subtropical gyre, and the cold and relatively fresh northward-flowing Malvinas Current (MC), which is a branch of the Antarctic Circumpolar Current (Gordon, 1989). While the BC extends down to about 500 m, the MC presents a predominantly barotropic structure and extends to the bottom (e.g., Vivier and Provost, 1999). Both currents converge along the South American slope at about 38°S at the so-called Brazil-Malvinas Confluence (BMC), generating one of the most energetic mesoscale regions of the global ocean (Chelton et al., 1990). On average, the BC begins to separate from the shelf break at 36.5°S, and the main core of the MC retroflects at about 38.8°S where the 200 and 1,000 m isobaths diverge at Ewing terrace. At that point, the MC is no longer constrained by the topographic steering and retroflects, while a shallow branch of the MC continues northward over the shelf-break (Matano et al., 2010). Between 36.5 and 38.8°S, the ocean area over the slope is characterized by high eddy kinetic energy with changes in current speed and direction (Figure 1A). Satellite-derived salinity, *in situ* observations, and modeling studies suggest that this region is also where most of the cross-shelf exchanges in the Southwestern Atlantic take place (Guerrero et al., 2014; Matano et al., 2014; Franco et al., 2018; Berden et al., 2020; Orúe-Echevarría et al., 2021).

The Uruguayan Economic Exclusive Zone (EEZ) is located in the northwestern edge of the Argentine Basin covering the slope between 34.6 and 37.3°S. The EEZ spans an area of about $140 \times 10^3 \text{ km}^2$ (Figure 1) and includes part of the region of high kinetic energy and intense cross-shelf exchanges (e.g., Guerrero et al., 2014; Matano et al., 2014; Franco et al., 2018; Berden et al., 2020). The water column over the slope region is characterized by at least six water masses from various sources, a micro-tidal regime, and large seasonal variability. Sea surface temperature (SST) variability presents a seasonal amplitude of 12°C and the wind stress curl reverses seasonally (Piola et al., 2018). Most prominent in the shelf circulation is the northward flow of

Subantarctic Shelf Water (SASW) originating from the Patagonia continental shelf (Piola et al., 2000). The northeastward flow of SASW is dynamically controlled by the along-shore wind stress variability (Lago et al., 2021) and in the outer shelf by variations of the intensity of the MC (Matano et al., 2010; Artana et al., 2019). Numerical simulations indicate that in early summer and early winter about 1 Sv of SASW is exported offshore close to the BMC (Franco et al., 2018), while the mid-shelf portion of SASW continues flowing northeastward up to near 32°S. There, SASW meets the subtropical shelf waters (STSW), forming a density compensated front referred to as the Subtropical Shelf Front (Piola et al., 2000). This frontal system extends from the inner shelf at 32°S to the outer shelf near 38.5°S, at the initiation of the BMC (Figure 1B; Gordon, 1989; Piola et al., 2000).

A distinct characteristic of the regional shelf circulation is the influence of the discharge of the Rio de la Plata (RdIP) estuary, which drains the second largest hydrological basin in South America (Framiñan et al., 1999; Piola et al., 2005). With a mean outflow of about $25,000 \text{ m}^3 \text{ s}^{-1}$, the RdIP significantly dilutes and supplies nutrients to the neighboring shelf waters (Piola et al., 2000). The RdIP buoyant plume, associated with absolute salinities lower than 33.65 g kg^{-1} , presents a strong seasonal variability, with northeastward spreading in austral fall-winter, and southward retraction in summer (Piola et al., 2000). These waters spread over the entire Uruguayan shelf and are often exported to the deep ocean (e.g., Provost et al., 1996; Guerrero et al., 2014). Large interannual variability has also been observed mainly driven by a positive relationship between El Niño Southern Oscillation (ENSO) and precipitation in the RdIP basin during spring, summer and fall (e.g., Grimm et al., 2000; Barreiro, 2010).

The Uruguayan EEZ, although known to be highly variable, is poorly sampled, with historically no national oceanographic research vessel capable of performing full-depth CTD profiles nor underway velocity measurements. During April and May 2016, the Spanish R/V Sarmiento de Gamboa conducted 82 full-depth CTD stations in the Uruguayan EEZ, covering along-slope transects, thus providing ideal measurements to study cross-shelf exchanges. Here we analyze the cruise data, together with other *in situ* and satellite observations and an eddy tracking algorithm, to provide a full water column description of the water masses and circulation, with particular focus on the intense mesoscale variability and cross-shelf exchanges.

DATA

We analyzed the hydrographic data collected by the Spanish R/V Sarmiento de Gamboa cruise conducted between 9 April and 10 May 2016 (henceforth “the cruise”). The sampling consisted of 12 along-shelf transects, separated by approximately 25 km, and a nominal distance between stations of 50 km. The sections were occupied from the deep ocean toward the coast. In this way, an almost regular grid was created over $\sim 320 \text{ km}$ along-slope and 370 km across-slope polygon. In total, 82 full-depth stations (between 18 and 4,147 m) were occupied using a Sea Bird Electronics (SBE) 32 Carousel Water Sampler rosette and a SBE

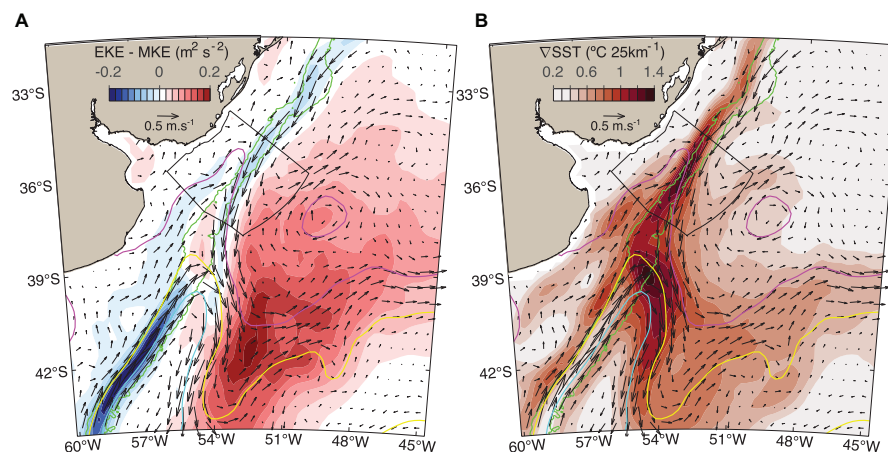


FIGURE 1 | Long-term mean conditions in the Southwestern Atlantic Ocean derived from satellite observations. Both panels show the mean surface geostrophic currents displayed as black arrows, the green lines show the 500 and 2,500 m isobaths, and the 0 m (cyan), 0.25 m (yellow), and 0.5 m (magenta) Absolute Dynamic Topography contours which indicate the retroflection of the main core of the Malvinas Current, the mean confluence position and the separation of the Brazil Current from the shelf-break, respectively. The black polygon delimits the Uruguayan Exclusive Economic Zone (EEZ). Background colors show the long-term daily mean of **(A)** eddy kinetic energy (EKE) minus mean kinetic energy (MKE) and **(B)** SST gradient.

911 plus Conductivity, Temperature and Depth (CTD) profiler, fitted with a SBE43 oxygen sensor and an ECO-AFL/FL Wet Labs Fluorometer. The CTD was fitted with dual temperature and conductivity sensors. Water samples for salinity, dissolved oxygen, nutrients and chlorophyll-a determination were taken in all odd-numbered transects at 5 m depth, and at additional depths depending on the maximum station depth. Two additional water samples were collected within the euphotic depth for chlorophyll-a, and for nutrients at 100, 500, 1,000, and 1,500 m, and near the bottom when the station depth allowed it. At stations shallower than 100 m, a mid-depth sample was collected. The CTD sensors were laboratory calibrated in April 2015. In addition, salinity and dissolved oxygen were calibrated based on the water samples collected during the cruise.

Additionally, underway measurements of temperature, salinity and fluorescence were sampled at 1 min intervals using a Sea-Bird SEACAT SBE 21 Thermosalinograph (TSG) and a Turner 10 fluorescence system. Temperature and salinity from the TSG were calibrated with the nearest CTD measurements. Wind measurements, air temperature, and humidity were also collected underway at about 10 m above the sea surface with a Geonica Meteodata automatic weather station. A hull-mounted Teledyne RD Ocean Surveyor Acoustic Doppler Current Profiler (ADCP) operating at a frequency of 75 and 150 kHz recorded underway ocean currents with 16 m and 8 m depth bins, starting at 10 m and reaching up to 700 and 400 m depth, respectively. The ADCP was operated at 75 kHz over the deep ocean and at 150 kHz over the shelf, recording one profile approximately every 1 min.

Turbidity from water samples was determined on board with a Multiparameter Senso Direct 150 Lovibond. *In situ* chlorophyll-a was also determined on board by acetone extraction and fluorometer reading following Yentsch and Menzel (1963). Fluorescence values from the TSG were calibrated using 32

measurements of chlorophyll-a from water samples collected at 5 m depth by empirically computing a scale factor to minimize the root square mean error. Fluorescence values from the CTD were previously adjusted with a “dark offset” calculation for each profile, by subtracting the mean value of the aphotic zone in values deeper than 200 m to each profile. The adjusted chlorophyll-a data compare well and are significantly correlated (**Supplementary Figure 1**), although absolute values of chlorophyll-a are out of the scope of this study, which focuses on identifying low and high-productivity regions. Water samples for nutrients were fixed on board and measured at the Institute of Marine Sciences (ICM-CSIC) in Barcelona, Spain. At the laboratory nitrate, nitrite, and phosphate concentration were determined using a Seal Analytical MT19 Auto Analyzer with the colorimetric technique and an automated system by continuous flow analysis applying the methodology of Grasshoff et al. (2009).

To complement the cruise hydrographic data we used all Argo profiles available for the Southwestern Atlantic between 32–42°S and 58–49°W (Argo, 2021). Moreover, to gather more information on the regional dynamics, we use satellite data sets with daily resolution: (I) SST with 0.25° horizontal resolution from the National Oceanic and Atmospheric Administration Optimum Interpolation Sea Surface Temperature for analyzing the long-term characteristics between 1993 and 2019 (OI SST V2; Reynolds et al., 2007), (II) The Multi-scale Ultra-high Resolution (MUR) SST analysis (Chin et al., 2017). This data set has a horizontal resolution 0.01°, making it more useful to identify (sub) mesoscale structures. These data are only available since 2002 and were therefore only used to study the variability of SST within the period of the cruise; (III) Surface chlorophyll-a concentration L4 (gridded and gap-filled) product from Marine Copernicus (CMEMS) with 4 km resolution (Garnesson et al., 2019) within the period of the cruise; (IV) L4 Sea Surface Salinity (SSS) v03.21 from the European Space Agency Sea Surface

Salinity Climate Change Initiative consortium at 50 km and a weekly resolution, spatially sampled on a 25 km EASE (Equal-Area Scalable Earth) grid and 1 day of time sampling. This dataset combines the satellite measurements from SMOS, SMAP, and Aquarius covering the period January 2010–September 2020 (see Boutin et al., 2021); (V) Ssalto/Duacs Multimission Altimeter derived absolute dynamic topography (ADT) and derived surface geostrophic velocity fields at a 0.25° horizontal grid for the period 1993–2019 distributed by CMEMS (Capet et al., 2014; Pujol et al., 2016). This latter dataset is also used as input for the Tracked Ocean Eddies (TOEddies) automatic detection algorithm developed by Chaigneau et al. (2011), Pegliasco et al. (2015) and Laxenaire et al. (2018, 2019, 2020). The TOEddies algorithm detects eddies as ADT extrema, corresponding to the center of an eddy, within closed ADT contours. By restricting the detection to eddies large enough to be in geostrophic equilibrium, these ADT contours correspond to streamlines and the largest closed contour is identified as the eddy boundary. Eddies are then tracked over time by computing their surface overlap over time taking advantage of their large size relative to their daily displacement. A detailed description of TOEddies can be found in Laxenaire et al. (2018).

Furthermore, we used ETOPO1 bathymetry with 1 min (about 2 km) horizontal resolution (Amante and Eakins, 2009). Finally, we also accounted for the daily discharges of the Rio de la Plata between 1988 and 2019 from Borús et al. (2017) and ERA5 reanalysis (Hersbach et al., 2020) hourly surface winds and sea level pressure from 1993 to 2019 in the Southwestern Atlantic (32–42°S 60–45°W) with 0.25° horizontal resolution to study the climatological context during the period of the cruise. **Table 1** summarizes the datasets used.

MATERIALS AND METHODS

CTD profiles were generated in 1 dbar bin average. All the gridded fields were linearly interpolated and previously smoothed with a 5 dbar centered moving average to remove spiciness from the plots. ADCP data was processed with Cascade V7.2 (Le Bot et al., 2011) with tide correction and a 16 m vertical resolution. Along and across slope velocities were computed by assuming a 40° inclination of the slope with respect to the zonal axis. Conservative temperature (Θ , °C) and absolute salinity (S_A , g kg⁻¹) were calculated from observations from the Thermodynamic Equation of SeaWater 2010 (McDougall and Barker, 2011) and used for the water mass characterization. Water masses in the deep ocean were classified based on neutral density (γ_n) ranges and thermohaline properties following Valla et al. (2018). Mixing of SACW and TW with shelf waters leads to substantial freshening over a wide neutral density range and are labeled as “others.” On the shelf (stations shallower than 200 m depth) thermohaline properties were used to identify shelf water masses following Berden et al. (2020; specified in **Table 2**). The data were sorted as shelf (0–200 m) and the slope (500–2,500 m) based on interpolated ETOPO1 bathymetry (Amante and Eakins, 2009), and retaining only the values within the desired ranges. In the case of Argo floats, we also filtered duplicated

TABLE 1 | Datasets and main characteristics related to this study.

| Dataset | Main characteristic |
|--|--|
| In situ observations of the cruise | |
| Termosalinograph (TSG) | Underway continuous surface measurements of temperature, salinity and fluorescence |
| Hull-mounted acoustic doppler current profiler (ADCP) | Underway continuous measurements of water velocity between 28 and 500 m of depth |
| Conductivity-temperature-Depth (CTD) | 82 full water depth profiles of temperature, salinity, pressure, oxygen and fluorescence |
| Water samples | Discrete samples taken from the rosette of the CTD at 32 of the 82 stations at 5 m depth |
| Other in situ observations | |
| Argo profiles | Temperature, salinity and pressure profiles between surface and at least 1,000 m |
| Rio de la Plata (RdIP) discharges | Daily time series between 1988 and 2019 |
| Satellite observations | |
| Absolute dynamic topography (ADT) and derived geostrophic currents | Estimate the surface geostrophic flow, identify the Brazil-Malvinas Confluence, the separation of Brazil Current from the shelf break and the retroflection of Malvinas Current. Spatio-temporal resolution: Daily, 25 km. |
| TOEddies | Identify the surface extension of mesoscale eddies. Spatio-temporal resolution: Daily, 25 km. |
| Sea surface temperature (SST) | Combined with ADT, provides information about the surface water mass distribution and circulation. Spatio-temporal resolution: Daily, 1–25 km. |
| Sea surface salinity (SSS) | Tracking low salinity surface shelf waters in the deep ocean. Spatio-temporal resolution: Weekly, 50 km. |
| Chlorophyll-a | Study spatial evolution of highly productive waters that might be related to shelf water export. Spatio-temporal resolution: Daily, 4 km. |
| Other datasets | |
| ERA 5 reanalysis | Understand the mean and the anomalous conditions of the winds during the period of the cruise in the entire basin. Spatio-temporal resolution: Hourly, 25 km. |
| ETOPO 1 bathymetry | Bottom depth. Horizontal resolution: 2 km |

profiles and retained only those with good quality (flagged as 1 or 2), and the co-localized values between 1,000 and 2,500 m. To study the vertical distribution of the shelf waters with Argo floats, we interpolated the irregular sampling to a regular 10 m interval, which is the coarser resolution of the Argo profiles, in order to get the same number of observations per profile. For all the observations, we colocalized each measurement to obtain the closest satellite measurement in space and time to compare.

Using satellite altimetry, we followed the criteria proposed by Lumpkin and Garzoli (2011) to detect the location of the confluence over the slope “as the latitude where the surface current vectors interpolated to the 1,000 m isobath change direction from southward (Brazil Current) to northward (Malvinas Current) in 77 day low-passed velocity fields.” However, we modified it as follows. Instead of interpolating the meridional velocity to a

TABLE 2 | Water masses mean characteristics in the Uruguayan Economic Exclusive Zone.

| Water mass | RDPPW | SASW | STSW ^a | TW | SACW | AAIW | UCDW | NADW | LCDW | AABW | |
|---|---------------|----------------------|-------------------|---------------|-----------|-------------|-------------|-------------|-------------|-------------|-----------|
| γ^{θ} (kg m ⁻³) | $S_A < 33.65$ | $33.65 < S_A < 34.6$ | $\Theta < 17$ | $S_A > 33.65$ | < 26.35 | 26.35–27.10 | 27.10–27.60 | 27.60–27.90 | 27.90–28.10 | 28.10–28.27 | > 28.27 |
| Pressure (dbar) | 19 | 70 | 84 | 103 | 332 | 821 | 1,560 | 2,431 | 3,349 | 3,847 | |
| Θ (°C) | 17.78 | 10.87 | 14.67 | 19.72 | 11.12 | 4.05 | 2.98 | 2.60 | 0.87 | -0.06 | |
| S_A (g kg ⁻¹) | 30.77 | 33.84 | 34.81 | 36.38 | 35.14 | 34.42 | 34.78 | 35.02 | 34.9 | 34.85 | |
| S_P (psu) | 30.63 | 33.68 | 34.64 | 36.21 | 34.97 | 34.25 | 34.61 | 34.85 | 34.73 | 34.67 | |

Columns show the name of the water mass, and the associated neutral density ranges (γ^{θ} , kg m⁻³) in the deep ocean. The remaining lines show the characteristics of each water mass averaged over all stations: pressure (dbar), conservative temperature (Θ , °C), absolute salinity (S_A , g kg⁻¹), and practical salinity (S_P , psu). Acronyms correspond to RDPPW, Rio de la Plata Plume Water; SASW, Subantarctic Shelf Water; STSW, Subtropical Shelf Water; TW, Tropical Water; SACW, South Atlantic Central Water; AAIW, Antarctic Intermediate Water; UCDW, Upper Circumpolar Deep Water; NADW, North Atlantic Deep Water; LCDW, Lower Circumpolar Deep Water; and AABW, Antarctic Bottom Water.

^aSTSW was restricted to the shelf.

unique latitudinal point over the 1,000 m isobath, we localized the change in the meridional currents averaged between the 500 and 2,500 m isobaths over the slope. Though no substantial differences are found in the results, our indicator is less sensitive to slight zonal displacements of the currents.

Following earlier work (e.g., Barré et al., 2011; Ferrari et al., 2017) we used three specific ADT contours as (i) a proxy for the position of the BMC (ADT 0.25 m; correlated with $R^2 = 0.94$; $p < 0.001$), (ii) the retroflexion of MC (ADT 0 m), and (iii) the separation of BC from the shelf-break (ADT 0.5 m). Note that ADT is not a useful tool to study long-term variations because both, steric height and shift in the currents have induced variations (e.g., Fang and Zhang, 2015; Ruiz-Etcheverry and Saraceno, 2020), but it can be a useful tool to identify fronts in the past decade.

RESULTS

Results are divided into four subsections. First, we describe the interannual contextualization of the period of the cruise and show that 2016 was a period of strong anomalous circulation conditions. Secondly, we analyze the oceanic variability during the period of the cruise. Then, we present a general description of the *in situ* observations, followed by the characterization of the shelf water export to the adjacent deep ocean and its relationship with the position of the BMC and mesoscale activity. Finally, based on extended Argo profiles and satellite observations, we explore the frequency of the shelf water distribution over the slope and the utility of altimetry to identify the shelf water export events.

Interannual Contextualization of the Period of the Cruise

To put the observations collected during the 2016 cruise into a long-term context we calculated the BMC index (BMCi) for the period 1993–2020. The BMCi is an indicator of the meridional fluctuations of the confluence. The seasonal amplitude of the BMCi is about 1° latitude (Lumpkin and Garzoli, 2011), reaching the southernmost and northernmost locations at the end of the summer and winter, respectively. A striking feature found in the BMCi is the trend of about 1° during the study period, or about

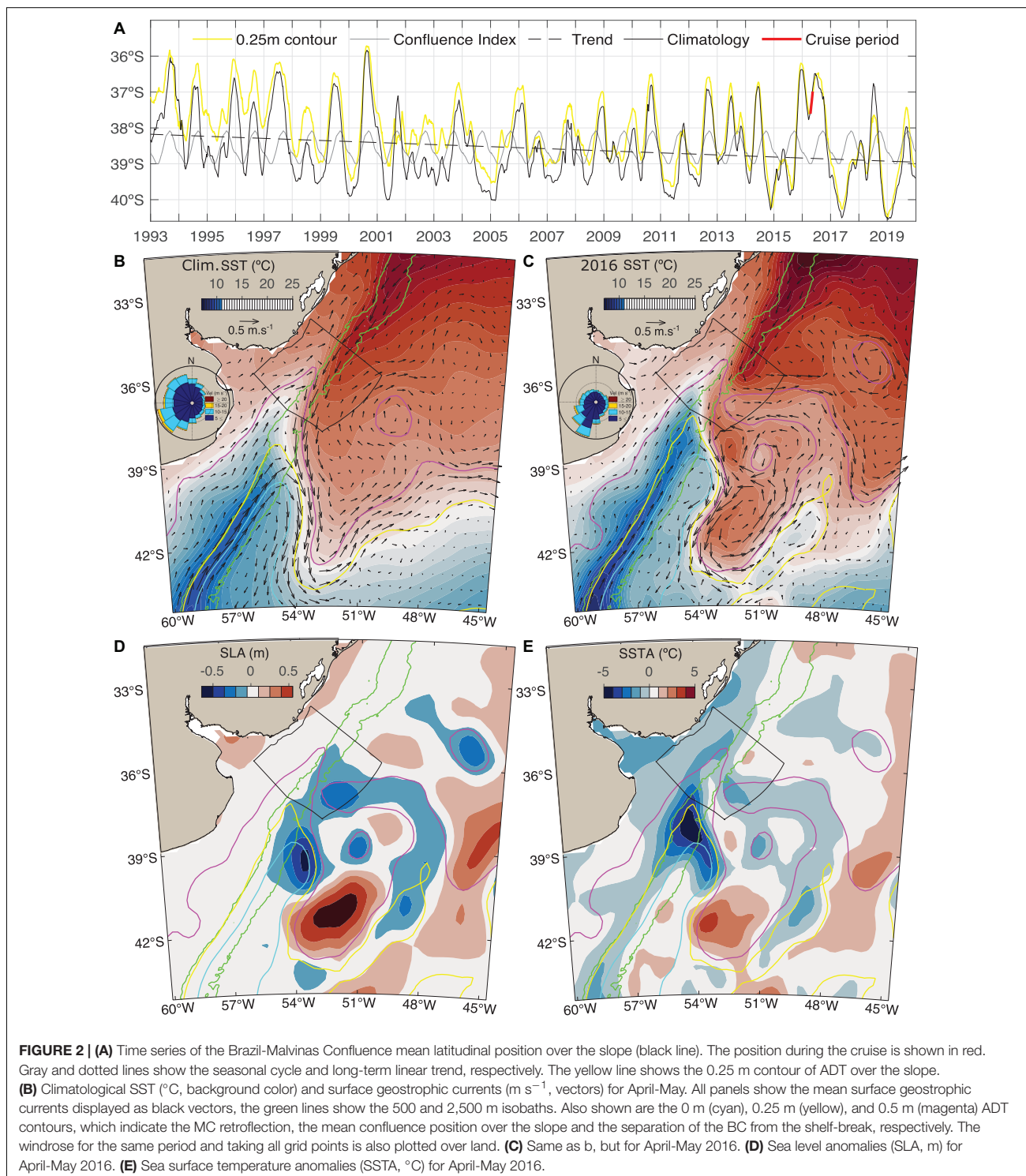
0.3° decade⁻¹. This trend represents a meridional shift from a mean position at about 38–39°S. This trend has been reported earlier both for the BMC and the separation of the BC from the shelf-break (e.g., Goni et al., 2011; Ruiz-Etcheverry and Saraceno, 2020; Bodnariuk et al., 2021) and is less than half of the trend reported by Lumpkin and Garzoli (2011) during the period 1992–2007. The reduction in linear trend when considering the past decade appears to be associated with larger amplitude meridional fluctuations observed after 2010 compared with the preceding decade (Figure 2A).

During 2016, the BMC was in an anomalous northern position that lasted from the beginning of January until September, being in a record northern position relative to the climatology during the majority of the summer and at the end of autumn (Figure 2A). During the cruise, the BMC was located on average at the 82th percentile of its latitude distribution (increasing toward lower latitude), 92th after removing the seasonal cycle. The anomalous northward position of the BMC coincided with intense SST and ADT anomalies of about 5°C and 0.5 m when comparing inshore and offshore positions at the 2,500 m isobath (Figures 2B,C). It is also remarkable that the negative anomalies of SST and ADT, associated with the recirculation of the MC, with negative SST and ADT anomalies from 40°S 52°W up to the Uruguayan slope at 37°S 54°W (Figures 2C–E). In the entire Southwestern Atlantic basin, ERA5 data shows persistent anomalous southwesterly winds during April and May 2016, particularly during May (Wind roses in Figures 2B,C).

Likewise, mean RdlP discharges were above 95th percentile during the first half of 2016, probably related to extreme discharges associated with the ENSO “Godzilla” event that peaked during the previous summer (Schiermeier, 2015). In particular, the previous 30-day running-mean discharge, a gross estimation of the available RDPPW over the shelf, was 56,670 m³ s⁻¹, more than twice the climatological mean of 25,000 m³ s⁻¹, corresponding to the 98th percentile in a 32-year daily time series from Borús (2017; Supplementary Figure 2).

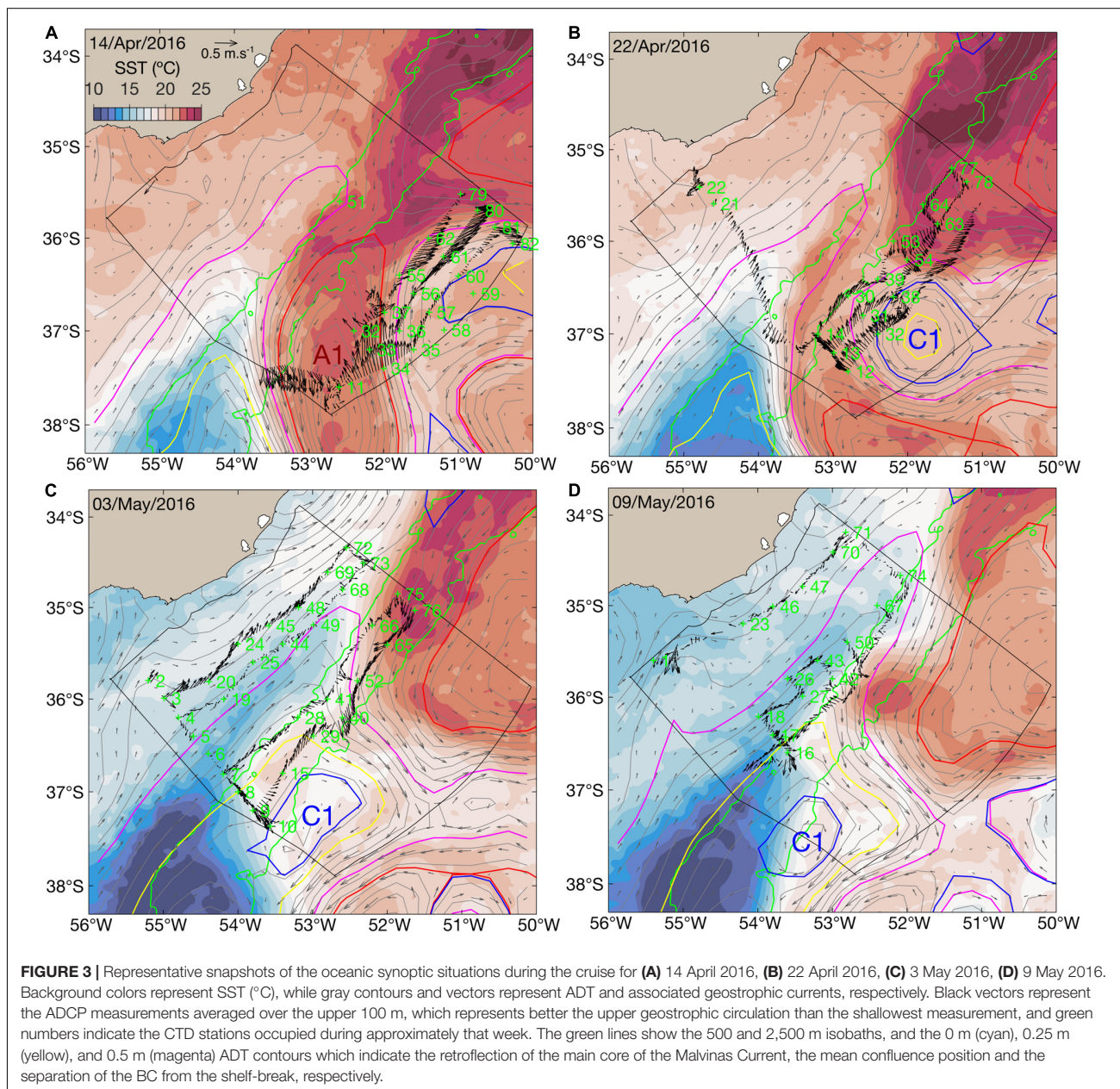
Variability Within the Period of the Cruise and Shelf Water Export

The period of the cruise was characterized by changing atmospheric and oceanic synoptic conditions. Intensification of a



low-pressure system in the South Atlantic generated strong winds (up to 23.5 m s^{-1} on 25 April) and forced the vessel to return to the port of Montevideo between 26 and 29 April. The persistent southwesterly winds induced a drop in the air temperature and

a large oceanic heat loss (not shown). Moreover, there was advection of cold waters under intense northeastward currents on the shelf that persisted until the end of the cruise and even longer (Proença et al., 2017). Thus, unplanned, this resulted in an 18-day



sampling of the deep ocean stations (from 9 to 26 April) and a 12-day sampling of the shelf and slope stations (from 29 April to 10 May) separated by a 2 day stop in between. Henceforth we dubbed these spatio-temporal grouping of stations as the first “half” and second “half” of the cruise, respectively.

Each half of the cruise can also be split into two parts based on the mesoscale dynamical state of the ocean, lasting about a week each. During the first 10 days of the cruise, the open-ocean area south of 36°S was mostly occupied by a large anticyclonic eddy (A1) that detached from BC and moved southward (**Figure 3A**). Subsurface salinities up to 37 g kg^{-1} were measured within A1 and the BC, and the most intense currents were observed

at the periphery of A1, with speeds larger than 1 m s^{-1} and reaching depths as deep as 300 dbar. As a consequence of the eddy shedding, the BC retroflexion was located north of 36°S . During the following 8 days, a cyclonic eddy (C1) entered the region from the east and occupied part of the area where A1 was located the previous week, with the retroflexion of the BC displacing slightly southward (**Figure 3B**; see also **Supplementary Video 1**). The second half of the cruise was characterized by the southward displacement of C1 out of the study area followed by a southward extension of BC reaching 37°S (**Figure 3C**). This period can also be divided into two different mesoscale dynamical regimes: from 29 April to 3 May C1 persisted as a coherent structure

(Figure 3C), whereas, from 4 to 9 May, C1 displaced toward the MC (Figure 3D).

***In situ* Observations in the Uruguayan Economic Exclusive Zone During April–May 2016**

Underway surface temperature and salinity were both extremely variable in space and time during the cruise. Extreme temperature values were associated with variability from WBCs over the slope, with coldest waters (10°C) south of the Uruguayan EEZ related to the MC, and warmest waters (25°C) associated with the mesoscale activity of the BC (Figure 4B). The SST over the shelf cooled about 6°C between the beginning and the end of the cruise (Figures 4A,D). The air temperature was lower than SST during most of the cruise, up to 8°C cooler than the SST over the BC and 5°C in some parts of the shelf (Figure 4B). Surface salinity varied from 0.5 g kg⁻¹ close to the RdLP and 37.0 g kg⁻¹ in the deep ocean, with also large variations through time. The position at [35.3°S, 55°W] near station 1 close to the RdLP mouth was crossed three times 9 and 26 April, and 10 May, and the TSG salinity and temperature observations were 26.1, 26.7, and 8.5 g kg⁻¹, and 21.0, 18.9, and 14.6°C, respectively (Figure 4A). Due to the extreme discharges of the RdLP, MODIS Aqua image during 9 May shows the muddy RdLP water more than 100 km away from its climatological position off Montevideo (not shown; Maciel et al., 2021). This was also reflected in the anomalous low salinity water ($S_A < 2 \text{ g kg}^{-1}$) observed at station 1 conducted on 9 May inshore of the RdLP turbidity front. At this station, turbidity concentration was at least one order of magnitude higher than at other stations (Figure 4C). Nitrate and phosphate were maximum also at this station, 23.42 and 2.77 $\mu\text{mol kg}^{-1}$, respectively. Overall, nutrients were high over the shelf and in the cold waters over the southern portion of the slope, with maximum values close to the RdLP and in the southern shelf break covered by MC, and low over the deep ocean stations (Figure 4F).

Surface chlorophyll-a was mostly positively correlated with the nutrient distribution, decreasing toward the deep ocean. Maximum values were measured near the coast immediately offshore from the turbidity front ($10 < S_A < 25 \text{ g kg}^{-1}$), although they did not peak at station 1 in the RdLP waters, where nutrient values were maximum, due to the effect on light attenuation in muddy waters (e.g., Carreto et al., 2003; Kruk et al., 2015; Martínez and Ortega, 2015). High surface fluorescence and chlorophyll-a were also observed in the southernmost area of the Uruguayan EEZ, at stations 7 and 9 over the outer shelf and slope, over the Ewing Terrace and Rio de la Plata canyon under the influence of the MC retroflection at about 37°S 54°W. These stations showed the coldest surface waters and high concentration of nutrients (Figures 4D–F), and also the highest integrated fluorescence in the CTD profile (3.15 mg m^{-3}) in the upper 50 m (Figure 4D), as these stations were occupied at the end of a chlorophyll bloom that took place 10–25 April according to satellite observations (Supplementary Video 1). The intense front observed in this region, and the mixing with shelf waters probably triggered this bloom. In contrast, a band of high nutrient low chlorophyll was formed in the outer shelf

from 26 April until the end of the cruise, probably due to the fully mixed water column by strong southwesterly winds (wind rose from ship measurements in Figure 4B) and intense northeastward currents.

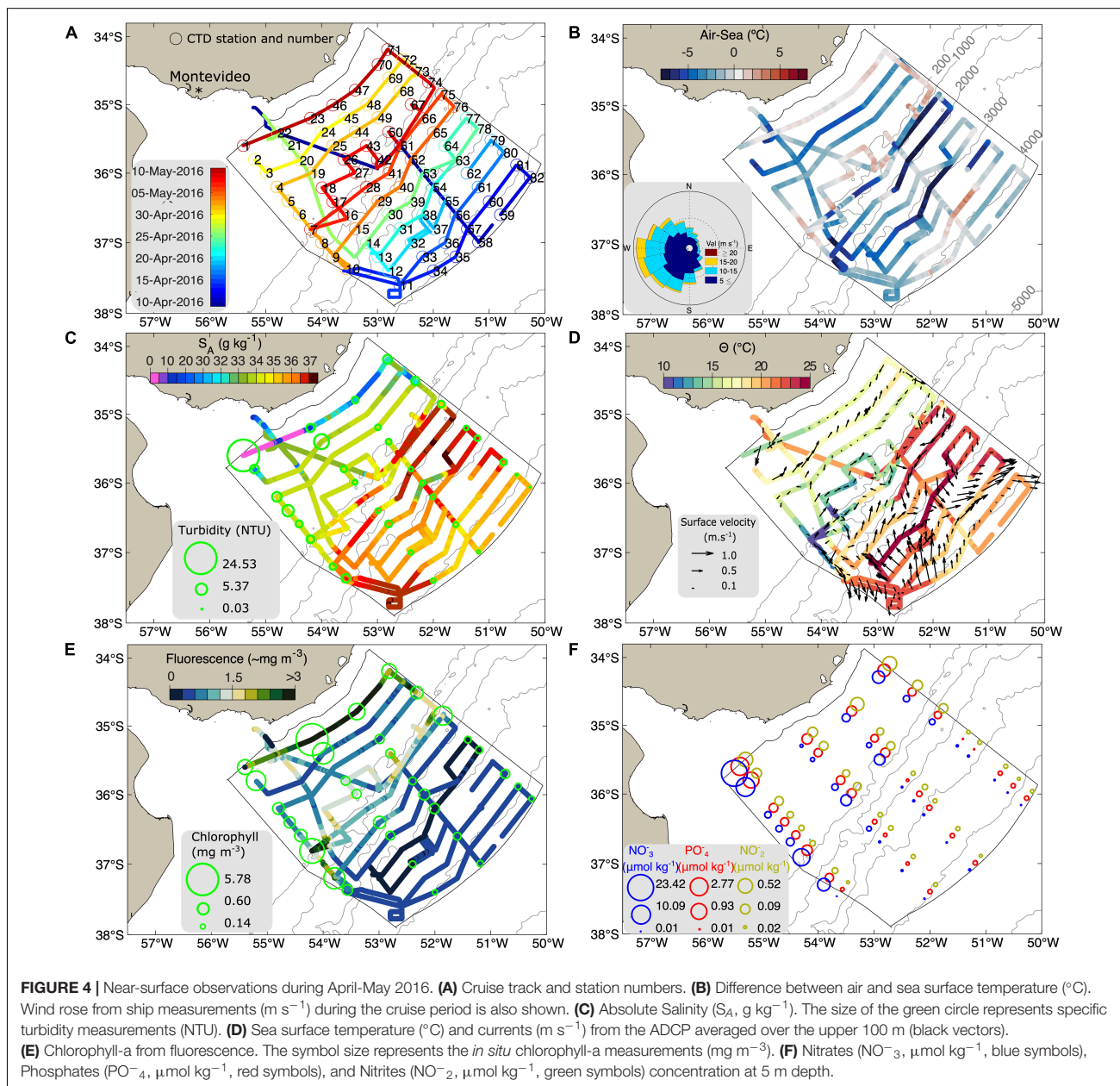
In agreement with satellite geostrophic observations, observed upper-ocean currents (averaged over the upper 100 m) displayed two clearly different regimes in the shelf and deep ocean (Figures 1, 4D). Despite the stations over the shelf being occupied over a period of nearly 1 month, northeastward surface velocities prevailed in this region, while velocities over the deep ocean were higher and with different directions due to mesoscale eddies and the retroflection of the major currents. The BC appeared as a southward flow in the northern half of the Uruguayan EEZ over the 2,000 m isobath with $\Theta > 23^\circ\text{C}$ and $S_A > 36 \text{ g kg}^{-1}$, respectively, and very low chlorophyll-a and nutrient concentration. A retroflection of the BC, usually referred to as “overshoot,” was observed at about [36.5°S, 52°W] between the 3,000 and 4,000 m isobaths (Figure 4D).

Below the surface, the full-depth CTD profiles showed three different water masses on the shelf and seven water masses in the deep ocean (see Table 2 for acronyms and mean properties). From the coast to the 50 m isobath (about 80–100 km), the study area was mostly filled with RDPPW. With $S_A < 33.65 \text{ g kg}^{-1}$, it is the most nutrient-rich and high-chlorophyll-a water mass. SASW prevailed toward the outer shelf, narrowing considerably toward the north as the shelf also narrows as it tends to be replaced by STSW. A very small fraction of the shelf was occupied with STSW which was mainly found in the outermost stations in the northern part of the shelf (Figure 5A). The observed transition between SASW and STSW agrees with the location of the Subtropical Shelf Front determined from historical data (Piola et al., 2000).

The deep ocean exhibited TW and SACW in the upper layers. The data display evidence of intrusions of SASW and STSW at several vertical levels within the relatively warm and salty TW and SACW. Large amplitude thermohaline intrusions observed in this region are ubiquitous of the confluence region (e.g., Piola and Georgi, 1982; Bianchi et al., 1993; Orúe-Echevarría et al., 2021), and are indicative of intense isopycnal mixing between the adjacent water masses with contrasting thermohaline properties (Figure 5B). Water masses found at deeper depths were those characteristics of the region: UCDW, NADW, LCDW, and AABW, respectively (Maamaatuaiahutapu et al., 1992, 1994; Provost et al., 1995; Valla et al., 2018; Table 2 and Figure 5B).

Surface Water Export

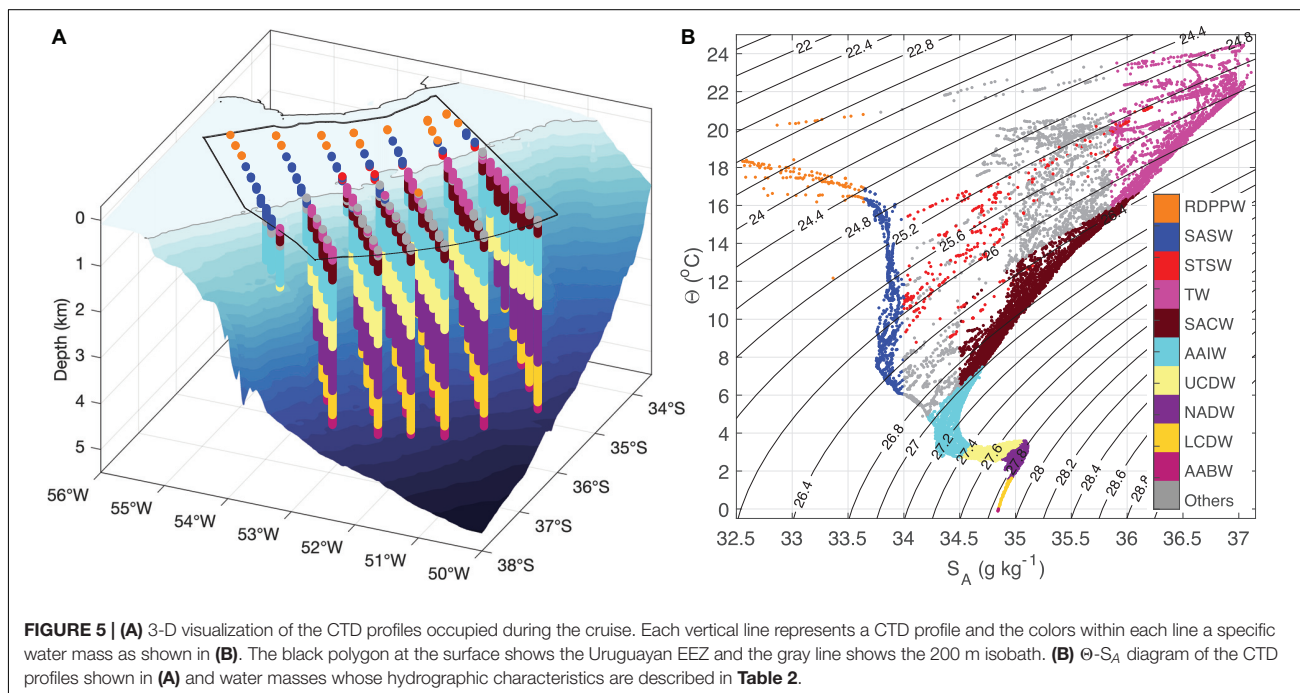
In this subsection we describe the evidence suggesting the export of shelf waters to the adjacent open ocean and discuss the processes involved. A well-known process exporting surface shelf water consists of brackish RDPPW and mixtures of shelf waters being advected offshore by the mesoscale activity of the BC. These have been detected by satellite SSS observations (Guerrero et al., 2014) and in numerical simulations (Matano et al., 2014). Export of low-salinity shelf waters is also apparent in hydrographic observations from the BC and near the confluence (Gordon, 1989; Provost et al., 1996; Piola et al., 2008; Berden et al., 2020). The high-resolution UEEZ observations reported here provide valuable information from the region of detachment of shelf



waters. We identified an export event during the first half of the cruise, although only the initial part of the low salinity plume detaching from the shelf was detected in satellite SSS (**Supplementary Figure 3C**), suggesting that the coarse satellite observations cannot properly resolve it. Nevertheless, satellite chlorophyll-a provides useful information about the spatial structure of the export due to the contrasting values between shelf and the open ocean waters (such as during 24 April at 36°S 52.5°W , **Figure 6**). The high chlorophyll-a filament consisted of a brackish water filament detached from the shelf along the BC retroflection (**Figure 6A**). The TSG measurements across the filament and 2 CTD profiles occupied that day display the 3-D

structure of the low salinity RDPPW filament. The filament was 70 km wide and 20 m deep according to the TSG and the CTD profiles inside the filament, respectively (**Figures 6B,C**). Within the 70 km wide filament and the ADCP measurements in the upper 60 m, which better represent the filament, the mean across-slope velocity was 0.30 m s^{-1} (**Figures 6B,C**), and the off-shore estimated transport 0.42 Sv .

The northern edge of the filament showed very sharp gradients. In 20 km, S_A decreased from 36.45 to 32.34 g kg^{-1} , temperature from 23.75 to 20.1°C , and fluorescence increased from 0.2 to 0.4 mg m^{-3} . Also, very close to the front, a local maximum of 0.7 m s^{-1} in the across-slope velocity was observed



(**Figure 6C**). The southern side of the filament showed a less intense fluorescence gradient, probably because the region north of the filament was occupied by oligotrophic BC water, while cold-core ($< 19.5^\circ\text{C}$), high-fluorescence ($> 0.35 \text{ mg m}^{-3}$) eddy C1 was located south of the filament. The CTD profile occupied within the filament showed that the brackish water extended downward to about 20 m depth, characterized by RDPPW properties ($S_A < 33.65 \text{ g kg}^{-1}$; **Figure 6D**) and high fluorescence ($> 0.45 \text{ mg m}^{-3}$). It is remarkable also that the vertically integrated fluorescence in the upper 140 m was higher in the CTD profile outside the filament, but the peak was below 40 m of depth and it was not apparent in satellite observations (**Figure 6B**).

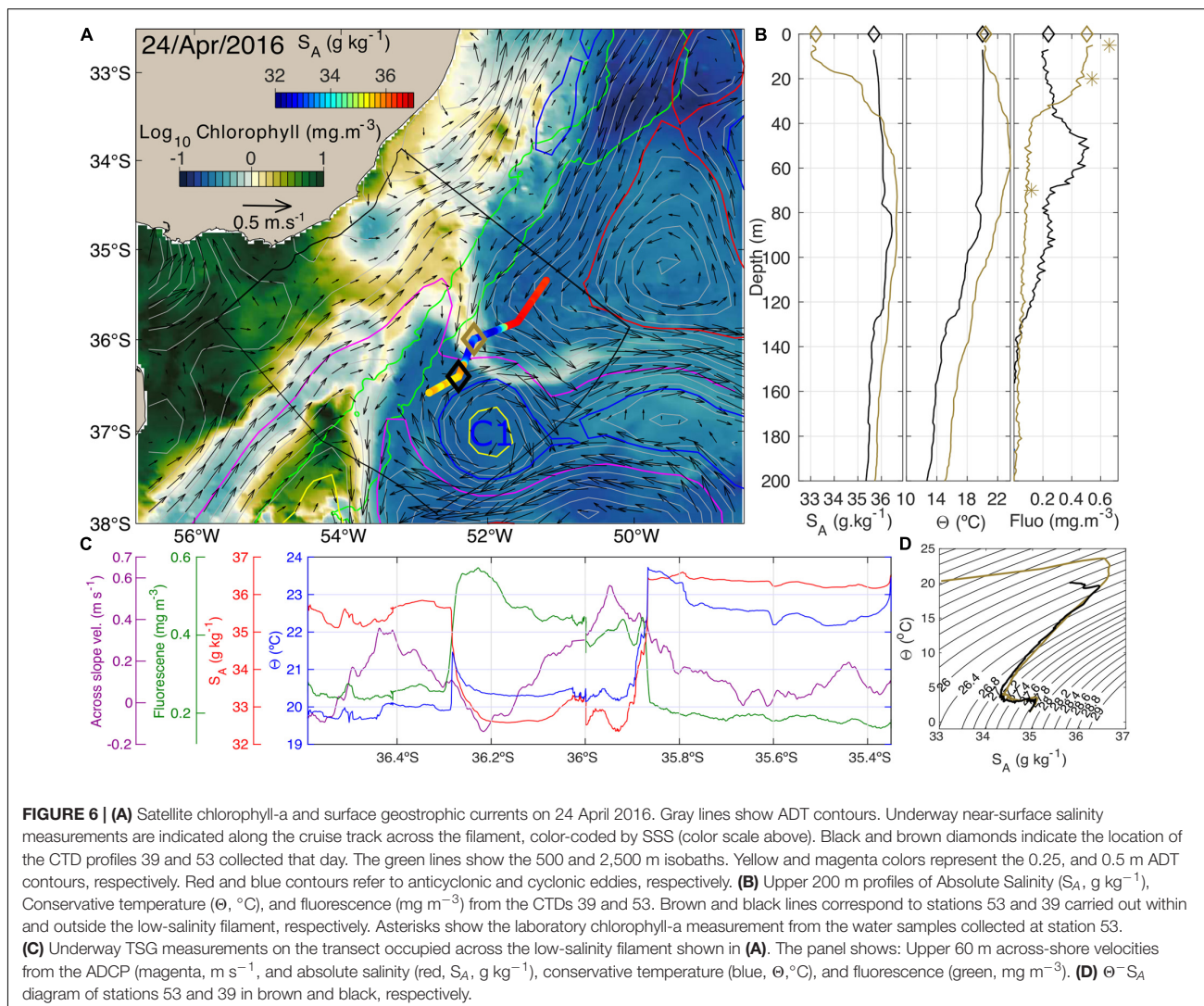
Subsurface Water Export

The *in situ* data also showed evidence of subsurface shelf-water export over the slope located at the BMC during the second half of the cruise. The gridded absolute salinity field from CTD profiles averaged between 40 and 120 m depth shows a low salinity tongue of SASW ($S_A < 34 \text{ g kg}^{-1}$; $< 12^\circ\text{C}$) being exported offshore up to the outer slope, approximately over the 2,000 m isobath (**Figure 7A**). Most of the CTD profiles over the slope were occupied within the first week of May 2016. Hence, the altimetry map of 3 May might be taken as representative of the regional circulation during that week (**Figure 7B**). The SASW tongue was located between the BMC and the BC separation from the shelf (yellow and magenta contours in **Figure 7B**, respectively), with geostrophic velocities oriented perpendicular to the slope toward the open ocean. The Θ - S_A diagram of that section shows a clear transition from subantarctic waters within the MC to subtropical waters from the BC (**Figure 7C**). Three CTD profiles showed the presence of SASW. The freshest SASW

variety was observed at the BMC (station 40 at $36.2^\circ\text{S } 52.6^\circ\text{W}$), with a homogeneous layer of 33.76 g kg^{-1} found between 70 and 130 m of depth (**Figures 7C,F**). The next CTD profile to the south showed evidence of SASW located between 160 and 230 m of depth. Here, SASW properties showed evidence of mixing with saltier waters with a relative maximum of 34.45 g kg^{-1} at 200 m of depth. Finally, the third profile with SASW was located in the southernmost CTD profile (station 9), which displayed a Θ - S_A structure typical from the MC over the slope (**Figures 7B,C**).

We next constructed an along-slope section over the main core of the WBCs, occupied during the period 3–5 May, when eddy C1 was merging with the MC. We did so from continuous ADCP velocity measurements and seven CTD profiles occupied along the 285 km section (stations 9, 15, 29, 40, 53, 65, and 76 from south to north, respectively; **Figures 7D–G**). The CTD profile containing the homogeneous layer of SASW at the BMC (station 40) was separated from the two closest stations by about 40 km. Therefore, we assumed that the horizontal extension of this layer was 40 km, half the distance between the two closest stations and approximately the extension of the low salinity surface signature from the TSG, with an uncertainty of 40 km. The mean across-slope velocity measured from the ADCP within the representative 40 km of the CTD station and the 70–130 m depth containing the homogenous SASW layer was 0.38 m s^{-1} . Hence, our estimate of the offshore export of SASW at the BMC is $0.91 \pm 0.91 \text{ Sv}$.

An across-slope CTD transect allowed us to identify and track the core of the SASW from the shelf to the deep adjacent ocean, although it must be interpreted with caution because the transect is a collection of non-synoptic data. The profiles showing the



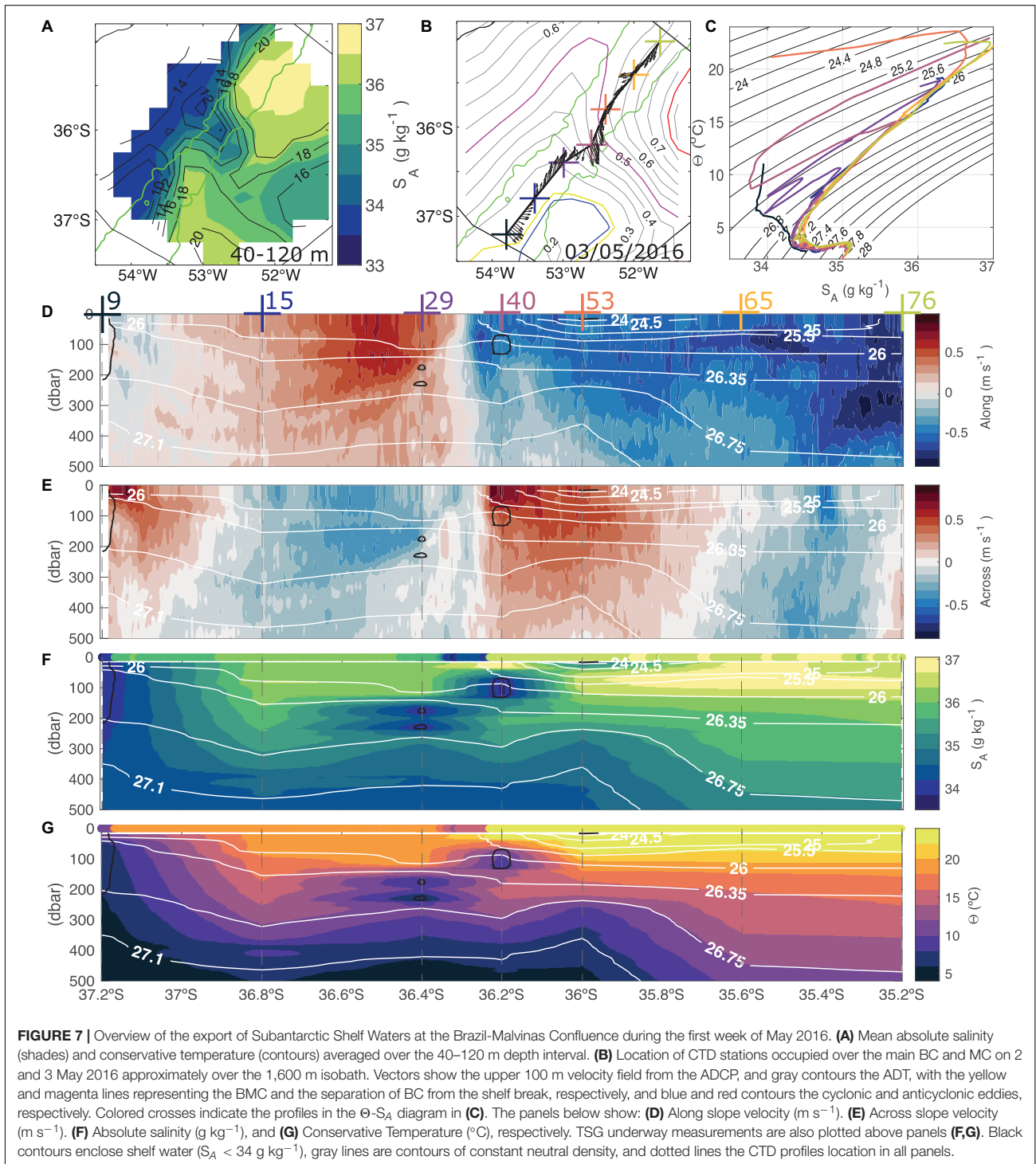
layer of SASW immediately outside the shelf were conducted on 4 and 6 May 2016. The reconstructed transect shows a 60 m thick layer of SASW (Θ between 6–12 $^{\circ}\text{C}$ and S_A 33.75–34 g kg^{-1}) flowing below the $\gamma = 25.7 \text{ kg m}^{-3}$ isopycnal. This vein of SASW left the surface at the shelf break where it subducted, reaching 130 m of depth at the 2,300 m isobath (**Figure 8A**). The exported SASW might have reached deeper levels, but this cannot be assessed with the cruise data as the following offshore CTD profiles along this transect were collected 10 days earlier (**Figures 8A,B**).

In this case, no low salinity signature was identified in satellite SSS (**Supplementary Figure 3D**). Chlorophyll-a showed a relative maximum at the same location where the SASW offshore export is apparent in the observations. However, the signal was very weak and might have also been locally generated instead of being advected (**Supplementary Video 1**). On the other hand, geostrophic currents derived from satellite altimetry show a high correlation and the lowest root mean square

error (RMSE) with ADCP measurements at a depth of 110 m ($p < 0.01$; R^2 0.82 and 0.35; RMSE 0.25 and 0.23 m s^{-1} , for along and across slope velocities, respectively; **Supplementary Figure 4**). Therefore, although satellite observations cannot directly detect the subsurface export of SASW, satellite altimetry might be used as an indicator of where and when such export events take place.

Shelf Waters Detection From Argo Floats and Satellite Observations

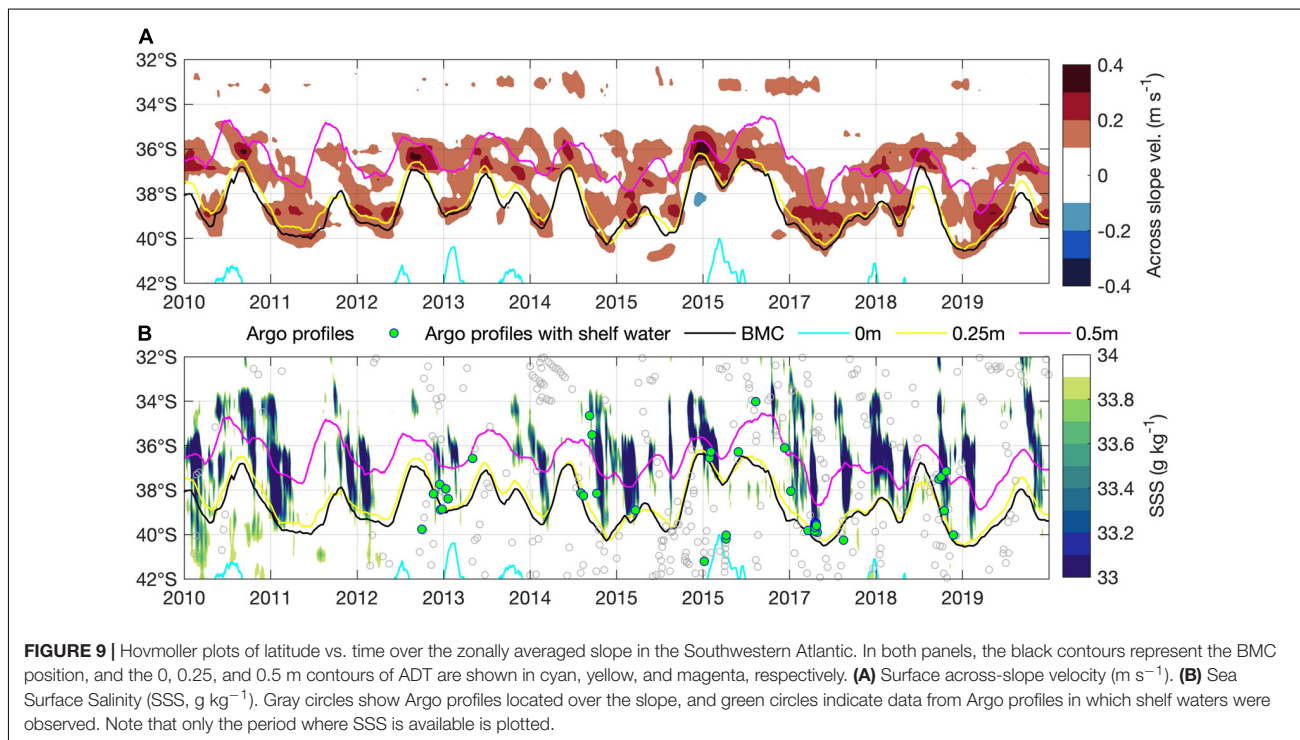
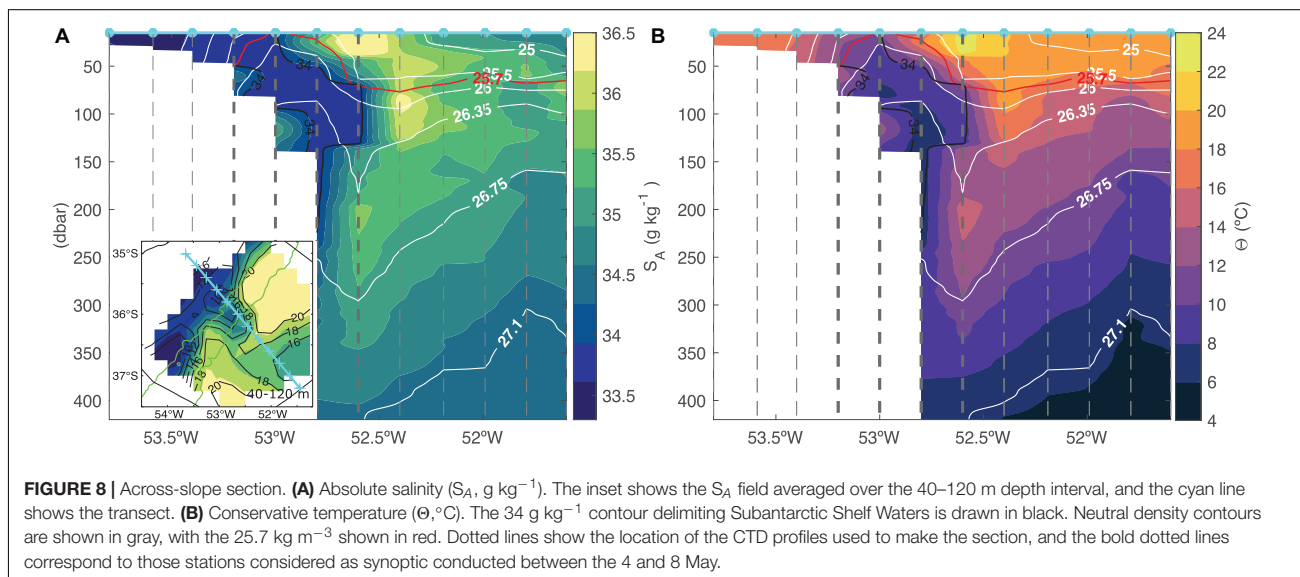
In this section, we explore the frequency of RDPPW and SASW over the slope and their relationship with altimetry using long-term Argo floats and satellite observations. The Hovmöller diagram constructed from satellite geostrophic currents and SSS in the zonally averaged slope shows that most of the observed across-slope positive (offshore) velocities occur between the BMC and the separation of the BC from the shelf break,



following the described seasonal migration of the BMC (see black and magenta contours in **Figures 9A,B**). It is also remarkable that a local maximum in across-slope velocity ($0.3\text{--}0.4 \text{ m s}^{-1}$) is observed when the BMC reaches its extreme highest and lowest latitude. Also, across-slope velocities

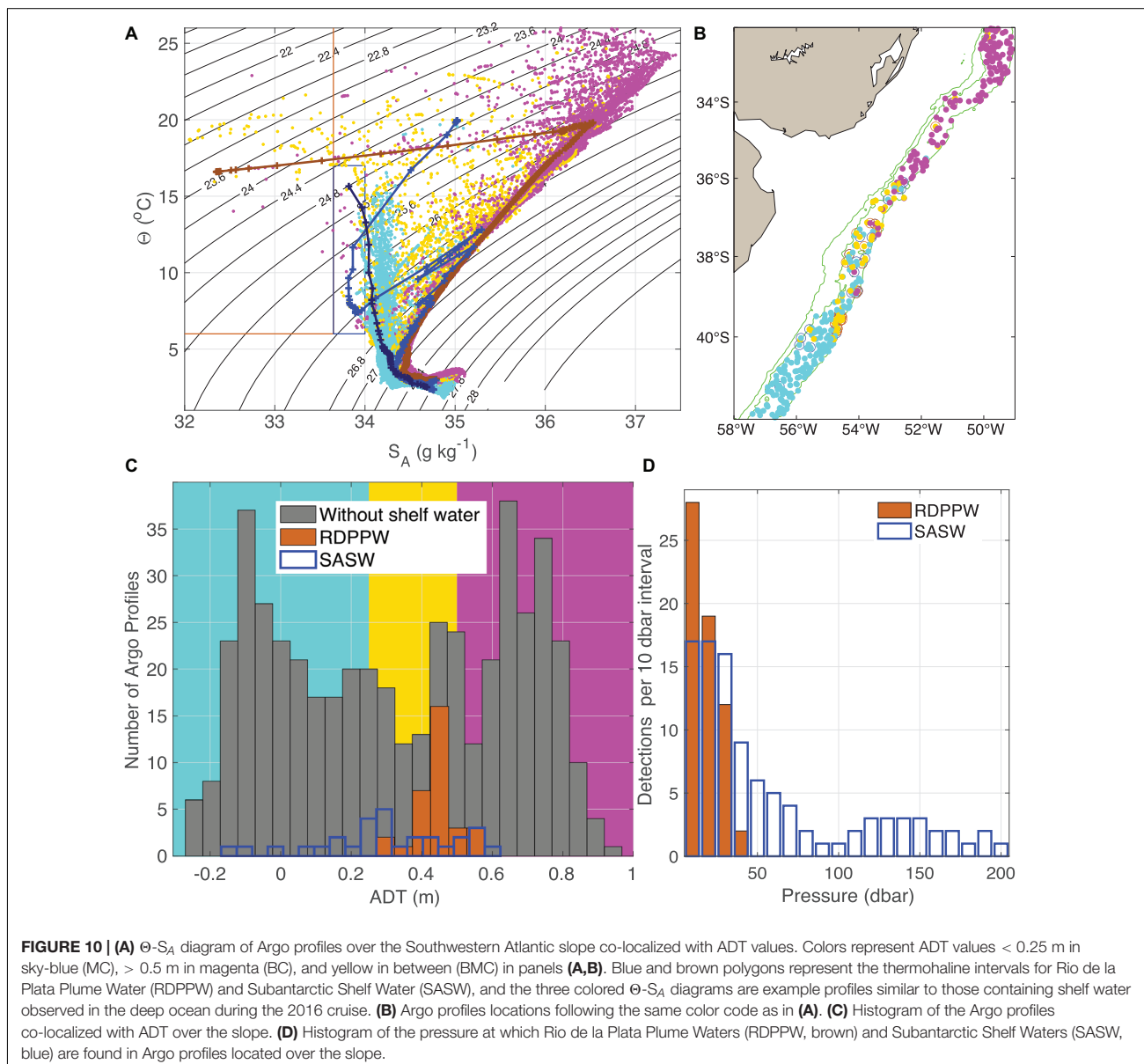
higher than 0.1 m s^{-1} are observed during winter north of the separation of the BC from the shelf break at about 33°S (**Figure 9A**).

Satellite SSS with shelf water characteristics ($S_A < 34 \text{ g kg}^{-1}$) are observed over the slope north of the BMC in most of the



cases. They display a clear seasonal cycle, mostly determined by the southward extension of the BMC, reaching higher latitudes at the end of the summer (**Figure 9B**). From the 431 Argo profiles located between the 1,000 and 2,500 m isobaths and from 32 to 42°S over the southwestern Atlantic slope, 59 (12%) contained shelf waters, while 32 (7%) contained exclusively RDPPW. Most of the profiles containing shelf waters were located north or at the BMC, in particular between the BMC and the separation of BC from the shelf-break (Yellow and

magenta contours in **Figure 9B**, respectively). The shallowest salinity observations from the 427 Argo profiles were significantly correlated with satellite SSS ($p < 0.01$; $R^2 = 0.64$). Co-localized Satellite SSS measurements showed less variance than *in situ* observations, as expected from its coarse space-time resolution. Nevertheless, the RMSE was 0.78 g kg^{-1} , which might be an acceptable value to identify RDPPW, yet too large to correctly single out SASW. While shelf water ($S_A < 34 \text{ g kg}^{-1}$) was detected in the shallowest measurement (1–10 m) of 54 of



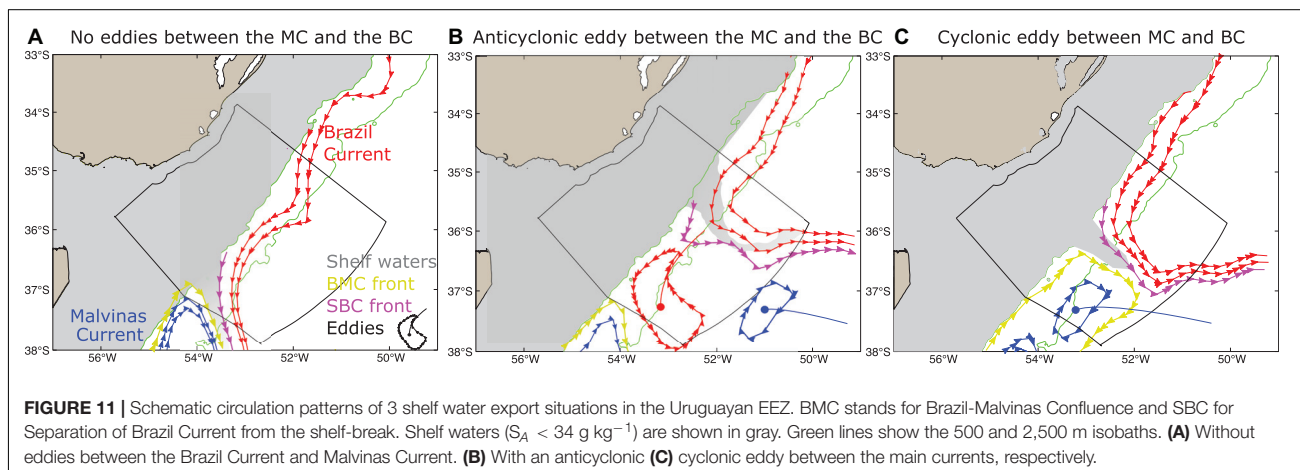
the 427 Argo profiles, the corresponding co-localized satellite SSS detected 58.

Argo profiles in the slope co-localized with ADT show values ranging between -0.25 and 0.96 m, with remarkable differences in the Θ - S_A signature depending on which side of the fronts the floats were localized (Figures 10A,B). Figure 10A also shows three Θ - S_A diagrams from Argo floats containing shelf waters similar to CTD stations occupied during the 2016 cruise (station 53 in Figure 6D and stations 9 and 40 in Figure 7C). The histogram in Figure 10C displays the number of Argo profiles as a function of ADT. The maximum frequencies are observed in the -0.1 to -0.05 m and 0.6–0.65 m intervals. Argo profiles containing SASW spread over a wide range of ADTs (-0.15 and 0.6 m), while the profiles containing exclusively RDPPW are restricted to the 0.25 and 0.6 m range, thus falling between

the BMC and the separation of the BC from the shelf break. In particular, ADT ranges between 0.35 and 0.45 m contain the majority of Argo profiles with RDPPW, with 23 out of 38 profiles (~60%) within these two class intervals (Figure 10C). Inspection of the vertical distribution of shelf waters in the Argo profiles, both RDPPW and SASW are most frequently observed in the upper ocean interval (10–20 dbar). However, while RDPPW is exclusively restricted to the upper 40 dbar, these data show that SASW can reach depths of 200 dbar (Figure 10D).

SUMMARY AND CONCLUSION

The hydrographic cruise that took place in April–May 2016 in the Uruguayan EEZ provided an unprecedented dataset to



investigate local water masses, ocean dynamics, and cross-shelf exchanges at the Brazil Malvinas Confluence. Despite the survey covering a relatively small area, our study shows that it is characterized by a highly variable and dynamic environment. Water properties can fluctuate from below 0°C to over 25°C in conservative temperature and from almost freshwater to over 37 g kg^{-1} in absolute salinity. The region hosts intense western boundary currents and mesoscale activity developing offshore, displaying large oceanic space-time variability at all scales (from synoptic, to interannual and interdecadal) driving cross-shore exchanges.

The first half of 2016 was an anomalous period in the southwestern Atlantic in terms of atmospheric and oceanic circulation. It was characterized by intense southwesterly winds, negative SST anomalies, and large Rio de la Plata discharges. By extending the Brazil Malvinas Confluence latitudinal position index of Lumpkin and Garzoli (2011), we showed that the confluence was located anomalously north during the first half of 2016, occupying the Uruguayan EEZ when the *in situ* survey was conducted.

In this work, we focused on cross-shelf exchanges as they have important consequences for carbon export, water masses transformations, and marine biodiversity. Previous studies provide evidence that, regionally, shelf water export is closely related to the confluence position (e.g., Matano et al., 2014; Berden et al., 2020; Orúe-Echevarría et al., 2021; **Figure 11A**). This control is somehow expected since the Brazil and Malvinas currents generate a barotropic pressure gradient that extends into the shelf controlling the outer shelf circulation (Palma et al., 2008; Matano et al., 2010). Our analyses provide evidence of the 3-D structure and evolution of two different kinds of shelf water export associated with the BMC dynamics: one related to Rio de la Plata waters that remain confined to the surface layers; the other involves SASWs that subducts under the subtropical thermocline while crossing the slope. To understand the dynamical setting associated with these processes and to assess their significance in time we used a combination of different observations that include the cruise hydrographic data, Argo profiles, satellite maps of SSS,

SST, ADT, and chlorophyll-a, and a recently developed eddy detection algorithm.

A near-surface export of shelf water consisted of a thin off-shelf layer of Rio de la Plata waters following the path of the retroflexion of the Brazil Current after an anticyclonic eddy shedding that dissipated after 10 days due to strong winds that mixed the stratified plume (**Figure 11B**). In addition, the hydrographic observations reveal a subsurface export of SASW. In this case, the driving mechanism also appears to be associated with mesoscale dynamics triggered by the merging of a cyclonic eddy with the Malvinas Current at the confluence with Brazil Current (**Figure 11C**). This generated intense off-shelf velocities at the shelf break. Evidence of subsurface export of shelf waters based on hydrographic and lowered ADCP observations near the BMC has been recently reported by Berden et al. (2020, their Figures 4C, 8E). The novelty of this study relies on the availability of closely spaced along-slope sections which reveal the detailed structure of the cross-shelf fluxes. Combining these *in situ* and satellite observations we reconstruct the 3-D field, quantify the export, and associate mesoscale ocean dynamics as the driving mechanism.

Using numerical simulations, Matano et al. (2014) showed that a time-averaged convergence of volume of about 1.21 Sv in the along-shore flow of SASWs (1.15 Sv) and STSW (0.038 Sv) and the inflow of Rio de la Plata waters (0.024 Sv) between 34 and 38°S must be exported offshore. The 1.21 Sv could hardly be achieved by the exported low salinity RdLP plumes, but the sum of both surface and subsurface export as observed in this work is closer to. In addition, Franco et al. (2018) using numerical simulations showed that released neutrally buoyant particles equally distributed in the vertical at 38°S over the shelf were exported all along the shelf-break between the retroflexion of the Malvinas Current and the Subtropical Shelf Front at about 32°S . Most of the neutrally buoyant particles were exported at the BMC, in particular within the 50–200 m layers. They also showed that as SASW was exported, it rapidly became saltier. The intense mixing observed over the slope together with the fact that the difference between SASWs and the surrounding ocean waters can be less than 0.2 g kg^{-1} , makes it difficult to detect this water mass based

only on salinity differences with the surrounding waters, as the shelf water freshwater signature rapidly fades as shown by Franco et al. (2018).

By using Argo profiles located within the southwestern Atlantic slope, we provide evidence of the presence of Rio de la Plata waters and SASWs between the separation of the Brazil Current from the shelf-break and the confluence and at the same depths as observed during the 2016 cruise. At specific values of absolute dynamic topography of 0.35–0.45 m, we found shelf waters over the slope in more than half of the Argo profiles, further suggesting the export of shelf waters at this location is relatively frequent. Also, by inspecting Argo profiles together with satellite surface salinity we show that SASWs is often found over the slope, especially within the shallow branch of the Malvinas Current. Because of the similarity between SASWs and surrounding waters thermohaline properties and the intense mixing taking place over the slope, detection of shelf waters within this current is challenging. Nonetheless, by combining *in situ* water velocity measurements and concomitant satellite altimetry observations we found evidence of SASWs along the BMC. In contrast, Rio de la Plata waters are more easily detectable in the open ocean due to their low salinity characteristics.

We also provided evidence that, although satellite surface salinity reveals shelf water exports (Guerrero et al., 2014), the coarse resolution of satellite data limits the ability to detect the fine structure and temporal evolution of the exported waters. This suggests that several export events might not be properly captured by satellite surface salinity. Chlorophyll-a, which has higher resolution especially under clear sky conditions, could be a complementary tool to detect these freshwater export events, but need to be contrasted with other salinity observations, as high chlorophyll-a filaments could be associated with several other processes not related to shelf-waters. Combination of different observations in the future (e.g., satellite Chlorophyll-a and salinity observations) could provide more insights on detecting and characterizing shelf water export events.

Another useful approximation to study shelf water export processes are high-resolution numerical models, as they reproduce the shelf-water export, especially when the confluence and the separation of the Brazil Current from the shelf break are along the same front (Berden et al., 2020; Orúe-Echevarría et al., 2021), but probably also to better simulate the impact of mesoscale eddies, like those observed during the 2016 cruise (Figure 11). Recent numerical simulations highlight the role of along-shelf winds in modulating the magnitude of along-shelf transports and the resulting shelf-open ocean exchanges (Berden et al., in press). In agreement with our findings, the numerical models indicate that a majority of the cross-shore flow occurs close to the confluence. Our retrospective analysis indicates seasonal fluctuations of the export location between 35.5 and 40°S which are modulated by displacements of the confluence, and also suggest a secondary export route near 33°S. This latter export location is also apparent in ocean reanalyses (Berden et al., in press). One of the several advantages of studying cross-shelf exchanges with numerical models is the

ability to be able to track the water being exported (Franco et al., 2018; Combes et al., 2021).

Finally, our analyses suggest that geostrophic currents derived from satellite altimetry are a robust indicator for the regional dynamics and a useful tool to track cross-shore water export events. By providing relatively accurate steric height estimates, satellite altimetry shows a high correlation with absolute velocities at 100 m of depth. Hence, satellite altimetry seems to be more useful than satellite surface salinity to identify subsurface shelf water export events. As altimetry is relatively accurate in identifying the location of the confluence (ADT contour 0.25 m over the slope) and the separation of Brazil Current from the shelf-break (ADT contour 0.5 m), across-slope velocity maxima confined between the 0.25 and 0.5 m ADT contours over the shelf break might be a good indicator for subsurface shelf water export occurrences. However, satellite altimetry does not resolve smaller scales than the largest mesoscale. Hence, several filaments of a few tens of km and small eddy-like structures near the BMC (diameter about 50 km) such as the merging of eddy C1 with the MC are not well-resolved as suggested by Ferrari et al. (2017). In addition, intense (> 1Sv) wind-driven high frequency (1–3 days) cross-shelf exchanges were detected by Berden et al. (in press) from high-resolution reanalyses not properly resolved by altimetry.

In conclusion, *in situ* hydrographic and ADCP observations combined with long-term satellite observations, an eddy detection algorithm, and Argo float profiles allowed us to identify and characterize the 3-D structure and evolution of surface and subsurface shelf water export to the adjacent deep ocean. The two types of shelf water export pathways may contribute to balancing the mass convergence associated with along-shore flows. Future oceanographic surveys covering the entire width of the continental slope and achieving high-resolution synoptic along-slope sections at the BMC might help to better constrain the structure of subsurface shelf water export.

DATA AVAILABILITY STATEMENT

The full processed data necessary to reproduce the reported finding is available at <https://doi.org/10.17882/86206>. Raw TSG and meteorological underway measurements are available at <http://data.utm.csic.es/viewer/?vessel=sdg&cruise=20160408&dataset=tss>. Raw CTD and ADCP data is available for research under the previous authorization of the Uruguayan national oil company (<https://www.ancap.com.uy>). ADT and chlorophyll-a data were downloaded from <http://marine.copernicus.eu/>, SST from <https://psl.noaa.gov/>, SSS from <https://catalogue.ceda.ac.uk/uuid/fad2e982a59d44788eda09e3c67ed7d5> and eddy tracking from https://vesg.ipsl.upmc.fr/thredds/catalog/IPSLFS/rlaxe/catalog.html?dataset=DatasetScanIPSLFS/rlaxe/Database_South_Atl.zip.

AUTHOR CONTRIBUTIONS

GM processed the hydrographic data and made the transport calculations, and prepared the manuscript with contributions

from all co-authors. All authors participated in the scientific interpretation of the results.

FUNDING

This work was supported by the European Union's Horizon 2020 research and innovation program under grant agreements no. 817578 (TRIATLAS), the TOEddies CNES-TOSCA research grant. We also acknowledge the mesoscale calculation server CICLAD (<http://ciclad-web.ipsl.jussieu.fr>) dedicated to Institut Pierre Simon Laplace modeling effort for technical and computational support. GM received funding from bourse ANII-Campus France (POS_CFRA_2017_1_146868). AP acknowledges the support from the Inter-American Institute for Global Change Research/CONICET (Argentina) grant RD3347.

REFERENCES

- Amante, C., and Eakins, B. W. (2009). *ETOPO1 1 Arc-Minute Global Relief Model: Procedures, Data Sources and Analysis*. NOAA Technical Memorandum NESDIS NGDC-24. Washington, DC: NOAA, doi: 10.7289/V5C8276M
- Argo (2021). *Argo Float Data and Metadata From Global Data Assembly Centre (Argo Gdac)*. France: SEANOE doi: 10.17882/42182
- Arruda, W. Z., and da Silveira, I. C. A. (2019). Dipole-induced Central Water extrusions south of Abrolhos Bank (Brazil, 20.5°S). *Continental Shelf Res.* 188:976. doi: 10.1016/j.csr.2019.103976
- Artana, C., Provost, C., Lellouche, J. M., Rio, M. H., Ferrari, R., and Sennechael, N. (2019). The Malvinas Current at the Confluence with the Brazil Current: Inferences from 25 years of Mercator Ocean reanalysis. *J. Geophys. Res.: Oceans* 124, 7178–7200. doi: 10.1029/2019JC015289
- Barré, N., Provost, C., Renault, A., and Sennéchaël, N. (2011). Fronts, meanders and eddies in Drake Passage during the ANT-XXIII/3 cruise in January–February 2006: A satellite perspective. *Top. Stud. Oceanogr.* 58, 2533–2554. doi: 10.1016/j.dsr2.2011.01.003
- Barreiro, M. (2010). Influence of ENSO and the South Atlantic Ocean on climate predictability over Southeastern South America. *Clim. Dyn.* 35, 1493–1508. doi: 10.1007/s00382-009-0666-9
- Berden, G., Charo, M., Möller, O. O. Jr., and Piola, A. R. (2020). Circulation and Hydrography in the Western South Atlantic Shelf and Export to the Deep Adjacent Ocean: 30° S to 40° S. *J. Geophys. Res. Oceans* 125:e2020JC016500.
- Berden, G., Piola, A. R., and Palma, E. D. (in press). *Cross-Shelf Exchange in the South Western Atlantic shelf: Climatology and extreme events*. *Front. Mar. Sci.* doi: 10.3389/fmars.2022.855183
- Bianchi, A. A., Giulivi, C. F., and Piola, A. R. (1993). Mixing in the Brazil-Malvinas confluence. *Oceanogr. Res. Papers* 40, 1345–1358.
- Bodnariuk, N., Simionato, C. G., Saraceno, M., Osman, M., and Diaz, L. B. (2021). Interannual variability of the Latitude of Separation of the Brazil Current: Teleconnections and Oceanic Rossby Waves Propagation. *J. Geophys. Res. Oceans* 126:e2021JC017557. doi: 10.1029/2021JC017557
- Borús, J. (2017). *Evaluación de Caudales Diarios Descargados por los Grandes Ríos del Sistema del Plata al Río de la Plata*. Argentina: Dirección de Sistemas de Información y Alerta Hidrológico Instituto Nacional del Agua.
- Borús, J., UriburuQuirno, M., and Calvo, D. (2017). *Evaluación de Caudales Mensuales Descargados por los Grandes ríos del Sistema del Plata al Estuario del Río de la Plata*. Ezeiza: Alerta Hidrológico-Instituto Nacional del Agua y el Ambiente.
- Boutin, J., Reul, N., Köhler, J., Martin, A. C., Catany, R., Guimbard, S., et al. (2021). Satellite-based Time-Series of Sea Surface Salinity designed for Ocean and Climate Studies. *ESSOAr* 1–47. doi: 10.1002/essoar.10507337.1

ACKNOWLEDGMENTS

We deeply acknowledge all the people behind the cruise planning and sampling processing, especially those on board RV Sarmiento de Gamboa, as well as all the open access datasets. GM acknowledges Uruguayan law No. 18.381 (exp No. 2018/14000/020893) and Phillip Miller for the very useful discussions. We also acknowledge William Sadvige, Tamaryn Morris, and Anna Rubio for their constructive comments and suggestions that greatly improved the manuscript.

SUPPLEMENTARY MATERIAL

The Supplementary Material for this article can be found online at: <https://www.frontiersin.org/articles/10.3389/fmars.2022.857594/full#supplementary-material>

- Capet, A., Mason, E., Rossi, V., Troupin, C., Faugère, Y., Pujol, I., et al. (2014). Implications of refined altimetry on estimates of mesoscale activity and eddy-driven offshore transport in the Eastern Boundary Upwelling Systems. *Geophys. Res. Lett.* 41, 7602–7610. doi: 10.1002/2014GL061770
- Carreto, J. I., Montoya, N. G., Benavides, H. R., Guerrero, R., and Carignan, M. O. (2003). Characterization of spring phytoplankton communities in the Río de La Plata maritime front using pigment signatures and cell microscopy. *Marine Biol.* 143, 1013–1027. doi: 10.1007/s00227-003-1147-z
- Chaigneau, A., Le Texier, M., Eldin, G., Grados, C., and Pizarro, O. (2011). Vertical structure of mesoscale eddies in the eastern South Pacific Ocean: A composite analysis from altimetry and Argo profiling floats. *J. Geophys. Res.* 116:C11025. doi: 10.1029/2011JC007134
- Chelton, D. B., Schlax, M. G., Witter, D. L., and Richman, J. G. (1990). Geosat altimeter observations of the surface circulation of the Southern Ocean. *J. Geophys. Res.* 95, 17877–17903. doi: 10.1029/JC095iC10p17877
- Chin, T. M., Vazquez-Cuervo, J., and Armstrong, E. M. (2017). A multi-scale high-resolution analysis of global sea surface temperature. *Remote Sens. Environ.* 200, 154–169. doi: 10.1016/j.rse.2017.07.029
- Combes, V., Matano, R. P., and Palma, E. D. (2021). Circulation and cross-shelf exchanges in the northern shelf region of the southwestern Atlantic: Kinematics. *J. Geophys. Res.* 126:e2020JC016959. doi: 10.1029/2020JC016959
- Fang, M., and Zhang, J. (2015). Basin-scale features of global sea level trends revealed by altimeter data from 1993 to 2013. *J. Oceanogr.* 71, 297–310. doi: 10.1007/s10872-015-0289-1
- Ferrari, R., Artana, C., Saraceno, M., Piola, A. R., and Provost, C. (2017). Satellite altimetry and current-meter velocities in the Malvinas current at 41°S: Comparisons and modes of variations. *J. Geophys. Res. Oceans* 122, 9572–9590. doi: 10.1002/2017jc013340
- Framiñan, M. B., Etala, M. P., Acha, E. M., Guerrero, R. A., Lasta, C. A., and Brown, O. B. (1999). “Physical characteristics and processes of the Río de la Plata estuary,” in *Estuaries of South America* (Heidelberg: Springer), 161–194. doi: 10.1007/978-3-642-60131-6_8
- Franco, B. C., Palma, E. D., Combes, V., Acha, E. M., and Saraceno, M. (2018). Modeling the offshore export of Subantarctic Shelf Waters from the Patagonian shelf. *J. Geophys. Res.* 123, 4491–4502. doi: 10.1029/2018JC013824
- Franco, B. C., Palma, E. D., Combes, V., and Lasta, M. L. (2017). Physical processes controlling passive larval transport at the Patagonian Shelf Break Front. *J. Sea Res.* 124, 17–25. doi: 10.1016/j.seares.2017.04.012
- Garnesson, P., Mangin, A., Fanton, d'Andon, O., Demaria, J., and Bretagnon, M. (2019). The CMEMS GlobColour chlorophyll a product based on satellite observation: multi-sensor merging and flagging strategies. *Ocean Sci.* 15, 819–830. doi: 10.5194/os-15-819-2019

- Goni, G. J., Bringas, F., and DiNezio, P. N. (2011). Observed low frequency variability of the Brazil Current front. *J. Geophys. Res.* 116:198. doi: 10.1029/2011JC007198
- Gordon, A. L. (1989). Brazil-Malvinas Confluence—1984. *Deep Sea Res. Part A. Oceanogr. Res. Papers* 36, 359–384. doi: 10.1016/0198-0149(89)90042-3
- Grasshoff, K., Kremling, K., and Ehrhardt, M. (eds) (2009). *Methods of Seawater Analysis*. New Jersey, NJ: John Wiley & Sons.
- Grimm, A. M., Barros, V. R., and Doyle, M. E. (2000). Climate variability in southern South America associated with El Niño and La Niña events. *J. Clim.* 13, 35–58. doi: 10.1175/1520-04422000013
- Guerrero, R. A., Piola, A. R., Fenco, H., Matano, R. P., Combes, V., Chao, Y., et al. (2014). The salinity signature of the cross-shelf exchanges in the Southwestern Atlantic Ocean: Satellite observations. *J. Geophys. Res. Oceans* 119, 7794–7810. doi: 10.1002/2014JC010113
- Hersbach, H., Bell, B., Berrisford, P., Hirahara, S., Horányi, A., Muñoz-Sabater, J., et al. (2020). The ERA5 global reanalysis. *Q. J. Roy. Meteorol. Soc.* 146, 1999–2049. doi: 10.1002/qj.3803
- Ismail, M. F. A., and Ribbe, J. (2019). On the cross-shelf exchange driven by frontal eddies along a western boundary current during austral winter 2007. *Estuarine* 227:106314. doi: 10.1016/j.ecss.2019.106314
- Kruk, C., Martínez, A., Nogueira, L., Alonso, C., and Calliari, D. (2015). Morphological traits variability reflects light limitation of phytoplankton production in a highly productive subtropical estuary (Río de la Plata South America). *Mar. Biol.* 162, 331–341. doi: 10.1007/s00227-014-2568-6
- Lago, L. S., Saraceno, M., Piola, A. R., and Ruiz-Etcheverry, L. A. (2021). Volume Transport Variability on the Northern Argentine Continental Shelf from In Situ and Satellite Altimetry Data. *J. Geophys. Res.* 126:e2020JC016813. doi: 10.1029/2020JC016813
- Laxenaire, R., Speich, S., Blanck, B., Chaigneau, A., Pegliasco, C., and Stegner, A. (2018). Anticyclonic eddies connecting the western boundaries of Indian and Atlantic oceans. *J. Geophys. Res.* 123, 7651–7677. doi: 10.1029/2018JC014270
- Laxenaire, R., Speich, S., and Stegner, A. (2019). Evolution of the Thermohaline Structure of One Agulhas Ring Reconstructed from Satellite Altimetry and Argo Floats. *J. Geophys. Res.* 124, 8969–9003. doi: 10.1029/2018JC014426
- Laxenaire, R., Speich, S., and Stegner, A. (2020). Agulhas Ring Heat Content and Transport in the South Atlantic Estimated by Combining Satellite Altimetry and Argo Profiling Floats Data. *J. Geophys. Res.* 125:e2019JC015511. doi: 10.1029/2019JC015511
- Le Bot, P., Kermabon, C., Lherminier, P., and Gaillard, F. (2011). *CASCADE V6. 1: Logiciel de Validation et de Visualisation des Mesures ADCP de Coque. OPS/LPO 11-01*. Available online at: <https://archimer.ifremer.fr/doc/00342/45285/> (accessed January 27, 2021).
- Lumpkin, R., and Garzoli, S. (2011). Interannual to decadal changes in the western South Atlantic's surface circulation. *J. Geophys. Res.* 116:C01014. doi: 10.1029/2010JC006285
- Maamaatuaiahutapu, K., Garçon, V. C., Provost, C., Boulahdid, M., and Bianchi, A. A. (1994). Spring and winter water mass composition in the Brazil-Malvinas Confluence. *J. Mar. Res.* 52, 397–426. doi: 10.1357/0022240943077064
- Maamaatuaiahutapu, K., Garçon, V. C., Provost, C., Boulahdid, M., and Osiroff, A. P. (1992). Brazil-Malvinas confluence: Water mass composition. *J. Geophys. Res.* 97, 9493–9505. doi: 10.1029/92JC00484
- Maciél, F. P., Santoro, P. E., and Pedocchi, F. (2021). Spatio-temporal dynamics of the Río de la Plata turbidity front; combining remote sensing with in-situ measurements and numerical modeling. *Cont. Shelf Res.* 213:104301. doi: 10.1016/j.csr.2020.104301
- Malan, N., Archer, M., Roughan, M., Cetina-Heredia, P., Hemming, M., Rocha, C., et al. (2020). Eddy-driven cross-shelf transport in the East Australian Current separation zone. *J. Geophys. Res.* 125:e2019JC015613. doi: 10.1029/2019JC015613
- Martínez, A., and Ortega, L. (2015). Delimitation of domains in the external Río de la Plata estuary, involving phytoplanktonic and hydrographic variables. *Braz. J. Oceanogr.* 63, 217–227. doi: 10.1590/s1679-87592015086106303
- Matano, R. P., Combes, V., Piola, A. R., Guerrero, R., Palma, E. D., Strub, P. T., et al. (2014). The salinity signature of the cross-shelf exchanges in the Southwestern Atlantic Ocean: Numerical simulations. *J. Geophys. Res.* 119, 7949–7968. doi: 10.1002/2014JC010116
- Matano, R. P., Palma, E. D., and Piola, A. R. (2010). The influence of the Brazil and Malvinas Currents on the Southwestern Atlantic Shelf circulation. *Ocean Sci.* 6, 983–995. doi: 10.5194/os-6-983-2010
- McDougall, T. J., and Barker, P. M. (2011). *Getting Started with TEOS-10 and the Gibbs Seawater (GSW) Oceanographic Toolbox Version 3.06.12*. SCOR/IAPSO WG127.
- Orúe-Echevarría, D., Pelegrí, J. L., Alonso-González, I. J., Benítez-Barrios, V. M., Emelianov, M., García-Olivares, A., et al. (2021). A view of the Brazil-Malvinas confluence, March 2015. *Deep Sea Res. Part I Oceanogr. Res. Papers* 172: 103533.
- Palma, E. D., Matano, R. P., and Piola, A. R. (2008). A numerical study of the Southwestern Atlantic Shelf circulation: Stratified ocean response to local and offshore forcing. *J. Geophys. Res. Oceans* 109, 1–17. doi: 10.1029/2007JC004720
- Pegliasco, C., Chaigneau, A., and Morrow, R. (2015). Main eddy vertical structures observed in the four major Eastern Boundary Upwelling Systems. *J. Geophys. Res. Oceans* 120, 6008–6033. doi: 10.1002/2015JC010950
- Piola, A. R., Campos, E. J., Möller, O. O. Jr., Charo, M., and Martínez, C. (2000). Subtropical shelf front off eastern South America. *J. Geophys. Res. Oceans* 105, 6565–6578. doi: 10.1029/1999JC000300
- Piola, A. R., and Georgi, D. T. (1982). Circumpolar properties of Antarctic intermediate water and Subantarctic Mode Water. *Deep Sea Res. Part A. Oceanogr. Res. Papers* 29, 687–711. doi: 10.1016/0198-0149(82)90002-4
- Piola, A. R., Matano, R. P., Palma, E. D., Möller, O. O. Jr., and Campos, E. J. (2005). The influence of the Plata River discharge on the western South Atlantic shelf. *Geophys. Res. Lett.* 32, 1–4. doi: 10.1029/2004GL021638
- Piola, A. R., Möller, O. O. Jr., Guerrero, R. A., and Campos, E. J. (2008). Variability of the subtropical shelf front off eastern South America: winter 2003 and summer 2004. *Cont. Shelf Res.* 28, 1639–1648. doi: 10.1016/j.csr.2008.03.013
- Piola, A. R., Palma, E. D., Bianchi, A. A., Castro, B. M., Dottori, M., Guerrero, R. A., et al. (2018). Physical oceanography of the SW Atlantic Shelf: a review. *Plankton Ecol. South. Atlantic* 2018, 37–56. doi: 10.1007/978-3-319-77869-3_2
- Proença, L. A., Schramm, M. A., Alves, T. P., and Piola, A. R. (2017). “The extraordinary 2016 autumn DSP outbreak in Santa Catarina, Southern Brazil, explained by large-scale oceanographic processes,” in *Marine and Fresh-Water Harmful Algae. Proceedings of the 17th International Conference on Harmful Algae*, eds L. A. O. Proença and G. M. Hallegraeff (Washington, DC: International Society for the Study of Harmful Algae)
- Provost, C., Gana, S., Garçon, V., Maamaatuaiahutapu, K., and England, M. (1995). Hydrographic conditions in the Brazil-Malvinas Confluence during austral summer 1990. *J. Geophys. Res.* 100, 10655–10678. doi: 10.1029/94JC02864
- Provost, C., Garçon, V., and Falcon, L. M. (1996). Hydrographic conditions in the surface layers over the slope-open ocean transition area near the Brazil-Malvinas confluence during austral summer 1990. *Cont. Shelf Res.* 16, 215–235.
- Pujol, M.-I., Faugère, Y., Taburet, G., Dupuy, S., Pelloquin, C., Ablain, M., et al. (2016). DUACS DT2014: the new multi-mission altimeter data set reprocessed over 20 years. *Ocean Sci.* 12, 1067–1090. doi: 10.5194/os-12-1067-2016
- Reynolds, R. W., Smith, T. M., Liu, C., Chelton, D. B., Casey, K. S., and Schlax, M. G. (2007). Daily high-resolution-blended analyses for sea surface temperature. *J. Clim.* 20, 5473–5496. doi: 10.1175/2007JCLI1824.1
- Roughan, M., Cetina-Heredia, P., Ribbat, N., and Suthers, I. M. (2022). Shelf Transport Pathways Adjacent to the East Australian Current Reveal Sources of Productivity for Coastal Reefs. *Front. Mar. Sci.* 8:789687.
- Roughan, M., Macdonald, H. S., Baird, M. E., and Glasby, T. M. (2011). Modelling coastal connectivity in a Western Boundary Current: Seasonal and inter-annual variability. *Deep Sea Res. Part II* 58, 628–644. doi: 10.1016/j.dsr2.2010.06.004
- Ruiz-Etcheverry, L. A., and Saraceno, M. (2020). Sea Level Trend and Fronts in the South Atlantic Ocean. *Geosciences* 10:218. doi: 10.3390/geosciences10060218
- Schiermeier, Q. (2015). Hunting the Godzilla El Niño. *Nat. News* 526:490.
- Valla, D., Piola, A. R., Meinen, C. S., and Campos, E. (2018). Strong mixing and recirculation in the northwestern Argentine Basin. *Oceans* 123, 4624–4648.
- Vivier, F., and Provost, C. (1999). Volume transport of the Malvinas Current: Can the flow be monitored by TOPEX/POSEIDON? *Oceans* 104, 21105–21122. doi: 10.1029/1999JC000056
- Yentsch, C. S., and Menzel, D. W. (1963). A method for the determination of phytoplankton chlorophyll and phaeophytin by fluorescence. *Deep*

Sea Res. Oceanogr. Abstracts 10, 221–231. doi: 10.1016/0011-7471(63)90358-9

Conflict of Interest: The authors declare that the research was conducted in the absence of any commercial or financial relationships that could be construed as a potential conflict of interest.

Publisher's Note: All claims expressed in this article are solely those of the authors and do not necessarily represent those of their affiliated organizations, or those of the publisher, the editors and the reviewers. Any product that may be evaluated in

this article, or claim that may be made by its manufacturer, is not guaranteed or endorsed by the publisher.

Copyright © 2022 Manta, Speich, Barreiro, Trinchin, de Mello, Laxenaire and Piola. This is an open-access article distributed under the terms of the Creative Commons Attribution License (CC BY). The use, distribution or reproduction in other forums is permitted, provided the original author(s) and the copyright owner(s) are credited and that the original publication in this journal is cited, in accordance with accepted academic practice. No use, distribution or reproduction is permitted which does not comply with these terms.

Chapter 4

The South Atlantic Dipole From Multichannel Singular Spectrum Analysis

In this chapter, we address the coupled ocean-atmosphere variability of the South Atlantic basin. This has been carried out in the attempt to disentangle from the observed scales of variability in the data we have analyzed so far the ones inherent to coupled ocean-atmosphere modes of variability and those internal to the ocean dynamics. Previous studies have revealed distinct climate variability modes due to air-sea interaction in the tropical Atlantic and North Atlantic regions. Analysis of the linkage between the Northeast Brazilian rainfall anomalies and sea surface temperature (SST) suggests a pattern of SST anomalies with opposite signs north and south of the Intertropical Convergence Zone (Hastenrath et al., 1977; Cabos et al., 2019). In addition, the equatorial Atlantic shows a zonal mode, which has been sometimes labeled as Atlantic Niño (Zebiak, 1993). In the North Atlantic, the North Atlantic Oscillation stands out as the dominant mode of short-range climate variability in the north Atlantic-European region, exerting a dominant influence from weeks to decades. It is characterized by a dipole-like structure with a north-south orientation in the sea level pressure (SLP) anomaly field over the Northern Atlantic Ocean (Van Loon et al., 1978; Hurrell et al., 2003). Although it is considered mostly an atmospheric oscillation, it also drives an out-of-phase relationship in surface temperature between Greenland and northern Europe (Marshall et al., 2001 and references therein). In the South Atlantic, published studies suggest that the dominant mode of coupled variability connecting SLP and SST is the South Atlantic Subtropical Dipole (Venegas et al., 1997; Sterl et al., 2003; Morioka et al., 2011; Haarsma et al., 2005; Santis et al., 2020). However, there have been some different characterizations of this mode of variability and its spatio-temporal scales and evolution are still under debate. For example, the role of the Southern Annular Mode and El Niño in its dynamics is not yet entirely clear. In this chapter, we discuss the coupled ocean-atmosphere variability modes in the South Atlantic using the Multichannel Singular Spectrum analysis applied to SST and SLP fields. The existing framework has been further developed and provided as an open-access tool for the scientific community. The results obtained provide a more in-depth characterization of the coupled basin-scale ocean-atmosphere variability. From these results, a manuscript is being prepared to submit to an international journal. In this chapter, we detail the analyses carried out and the results obtained.

1 Abstract

Finding and explaining oscillatory modes of the climate system contributes to its predictability. Multivariate Singular Spectrum Analysis (M-SSA) enables the identification of spatio-temporal modes from multidimensional time series, for instance, a nonlinear trend, oscillatory modes, noise, and chaotic components. We applied M-SSA to the South Atlantic sea surface temperature (SST) and mean sea level pressure (SLP) fields for the 72-year time period of ERA5 reanalysis (1950–2021), and identified an increasing trend in SST and interannual oscillations. The leading oscillatory mode is characterized by a period of 12.8 years. It is observed both in the individual variables and the coupled analysis and depicts a basinwide southwest-northeast dipole. This mode is very likely linked to the South Atlantic Dipole previously described in the literature, albeit with fewer details related to its periodicity. Another mode of variability isolated by the M-SSA is a significant 5.3-year period oscillation also with a dipolar structure, but it seems to be more related to the ocean subtropical gyre circulation and ENSO in the Pacific. With the trend, the decadal and interannual oscillation we were able to reproduce almost 40% of the total interannual variability of SST, SLP, and the coupled variables. These results contribute to characterizing the spatio-temporal evolution of the SST and SLP variability in the South Atlantic, in particular related to the South Atlantic Dipole.

2 Introduction

Finding and explaining oscillatory modes of the climate system contributes to its predictability. Multivariate Singular Spectrum Analysis (M-SSA) allows identifying spatio-temporal oscillatory modes from multidimensional time series (Plaut et al., 1994; Ghil et al., 2002), being efficient and robust even in extracting dynamics from short, noisy time series (Ghil et al., 2002). M-SSA separates time series into a nonlinear trend, oscillatory modes, noise, and chaotic components (Ghil et al., 1991), with the extracted low-frequency modes better corresponding to the predictable modes of the climate system than those extracted by regular spatial EOFs (Vautard et al., 1996; Bach et al., 2021). M-SSA has been applied in many climatic analyses, such as characterizing interannual variability of the North Atlantic Ocean sea temperature and wind stress (Groth et al., 2017), the Madden–Julian Oscillation (Lau et al., 2011), macroeconomic response to climatic variability (Garnot et al., 2018), among others.

In the subtropical South Atlantic the low-frequency dominant mode of coupled variability connecting sea level pressure (SLP) and sea surface temperature (SST) is the South Atlantic Subtropical Dipole (SASD; Venegas et al., 1997; Sterl et al., 2003; Morioka

et al., 2011; Haarsma et al., 2005). This southwest–northeast oriented dipole influences the variability of precipitation events in southeastern South America and Western Africa (Muza et al., 2009; Zhou et al., 1998; Carvalho et al., 2002; Chou et al., 2001; Nnamchi et al., 2011a), cyclogenesis (Bombardi et al., 2014), and the position and intensity of the South Atlantic Convergence Zone (Barreiro et al., 2002; Barreiro et al., 2004; Barreiro et al., 2005; Zhou et al., 1998; Chaves et al., 2004; Bombardi, 2013; Robertson et al., 2000), being a key component for the understanding of the climate predictability of the basin. The mechanism of the establishment of the dipole event is attributed to intrinsic atmospheric variability, but it has been also linked to the remote effect of the Pacific ENSO events producing the Pacific–South America wave train affecting both the intensity and position of the South Atlantic subtropical high, triggering SASD events (Barreiro et al., 2004; Rodrigues et al., 2015; Morioka et al., 2014).

There have been different characterizations of the dipolar SST variability in the South Atlantic. Studies that have focused their attention on austral summer have usually observed and defined the South Atlantic Subtropical Dipole (SASD) which is stronger during austral summer and restricted to higher latitudes, while those interested in austral winter have usually observed and defined the South Atlantic Ocean Dipole (SAOD), which covers a broader area and peaks in austral winter (Nnamchi et al., 2011b; Nnamchi et al., 2011a; Nnamchi et al., 2016; Nnamchi et al., 2017). Nevertheless, both are thought to be the same mode of variability originating from differences in the seasonal position of the St. Helena subtropical anticyclone (Nnamchi et al., 2017). There are still some open questions about this dipole, in particular concerning its spatiotemporal variability and the role of air-sea coupling. We will address these issues using the M-SSA analysis, a technique especially well designed to analyze and describe oscillatory behavior in the climate system. Moron et al., 1998 analyzed South Atlantic SST variability and trends using bivariate SSA. They found significant interdecadal oscillations, with a spectral peak around 13–14 years, which appeared to be correlated to a corresponding North Atlantic interdecadal mode. They also found a 4–5 year oscillatory mode. However, due to the use of only two channels, they did not carry out a detailed spatial study, and they did not analyze the atmospheric fields.

The objective of this chapter is to characterize the spatiotemporal evolution of the South Atlantic Dipole using the M-SSA technique.

3 Data and Methods

3.1 Data

We used ERA5 reanalysis (Hersbach et al., 2020) annual means with a horizontal resolution of 0.25° for the variables SST, SLP and 10-meter winds (U and V) and heat fluxes combining the reanalysis period from 1979 to 2021 with the backward extension 1950-1978, resulting in a 72 years-long time series for the South Atlantic ($10\text{--}50^\circ\text{S}$ $63^\circ\text{W}\text{--}20^\circ\text{E}$). We gridded into 1° average to filter the mesoscale variability and to make computational analysis faster. For SLP, winds, and heat fluxes, we removed the data values over land. The ERA5 SST fields come from the HadISST2 and OSTIA products (Hersbach et al., 2020). Although ERA5 is an uncoupled reanalysis (i.e., the model is run with prescribed SSTs), the atmospheric fields are expected to contain information about coupled interactions due to their being introduced in the data assimilation through the impact of observations (Ruiz-Barradas et al., 2017).

To focus on interannual variability, we used annual means ($N=72$ years) of standardized anomalies, which were then multiplied by the standard deviation before plotting in order to recover the units. Before the M-SSA analysis, we first projected the dataset onto a subset of spatial EOFs (S-EOFs) by means of a conventional principal component (PC) analysis. This compression of the dataset into PCs is meant to reduce the computational costs of the M-SSA analysis. Groth et al., 2017, in Appendix B, show that the M-SSA analysis on PCs is mathematically equivalent to that on the full gridded dataset when all the PCs are retained.

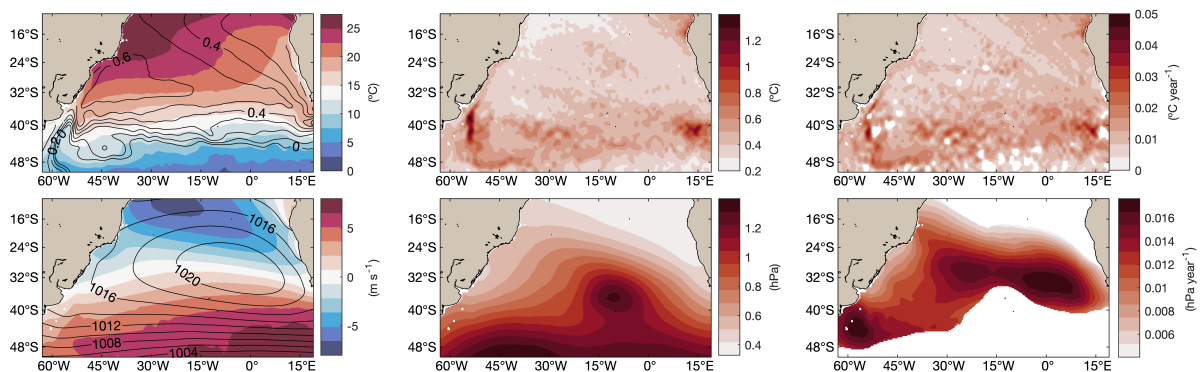


Figure 4.1: Climatological properties of surface fields in the South Atlantic. a) Mean SST and sea level (m) in shades and contours, respectively. b) Mean zonal wind and SLP (hPa) in shades and contours, respectively. Interannual standard deviation of c) SST and d) SLP. Linear trend for e) SST and f) SLP. Only significant grid points are plotted (T-test 5%).

3.2 Multichannel Singular Spectrum Analysis (M-SSA)

The M-SSA method diagonalizes the lag-covariance matrix to obtain a set of orthogonal eigenvectors and the corresponding eigenvalues. The eigenvectors are also referred to as space-time empirical orthogonal functions (ST-EOFs), while the eigenvalues provide information about the variance that is captured by the ST-EOF. The oscillatory behavior is reflected in pairs of ST-EOFs with similar eigenvalues and fundamental frequencies (Vautard et al., 1989; Plaut et al., 1994).

We used a window length of $M=14$ years for the M-SSA, which represents between one-fourth and one-fifth of the time series, a common length used for this type of analysis. With the annual averaging, the Nyquist frequency is 0.5 years⁻¹. Thus, we do not expect to be able to resolve oscillations with periods of about 2 years, such as the quasi-biennial mode, which has previously been found in the South Atlantic (Moron et al., 1998). We performed the M-SSA analysis for the SST and SLP separately and then together in order to understand the similarities and differences between them and isolate the role of air-sea interaction in the dynamics. Phase composite analyses were performed using the method of Moron et al., 1998.

Sensitivity tests were performed to determine the robustness of the results: (i) we compared the results obtained using annual means versus those found using a Chebyshev filter for frequencies $f > 0.5$ cycles per year with a Chebyshev type-I low-pass filter from which we then took all July values; (ii) the size of the window was varied from 14 to $N/4$; (iii) several different grid sizes were used and, given our interest in basin scale dynamics and that results were not sensitive to resolution, we finally settled for 1.5° ; (iv) we also changed the region considered by expanding/contracting by 5° on each north and south of the domain. Finally, we performed the M-SSA analysis for the SST and SLP separately and then together, in order to understand the similarities and differences between them and isolate the role of air-sea interaction in the dynamics.

3.3 Monte Carlo M-SSA

We use Monte Carlo M-SSA (Allen et al., 1996; Groth et al., 2015) to test the statistical significance of the obtained modes. To do so, we simulated 1000 repetitions and used the Procrustes algorithm to construct the confidence intervals for the eigenvalues (Groth et al., 2015; Groth et al., 2017).

4 Results

The PCs describe the variability modes, usually in pairs, except for the first mode which describes the trend. The analysis performed separately for SST and SLP shows in both cases a significant trend followed by two oscillatory modes with a fundamental frequency of 12.8 years (PCs 2-3). A trend is observed both for SST and SLP, explaining 22.0% and 12.1% of the variance, respectively (Fig.4.2). The 12.8 years mode explains more variance in SLP than in SST: 14.2% and 10.1%, respectively (Fig.4.2). In addition, the M-SSA shows that the SST field presents another oscillatory mode with a period of 5.3 years which explains 7.6% of the variance (PCs 5-6, left column Fig.4.2). Finally, the M-SSA applied to the coupled SST and SLP fields also show a trend, and 12.8-year and 5.3-year oscillations, this case explaining less variance, 14.1%, 13.2%, and 6.6%, respectively. The only pair of modes statistically significant are the 5.3-year oscillation for SST and coupled (shown in red in Fig.4.2).

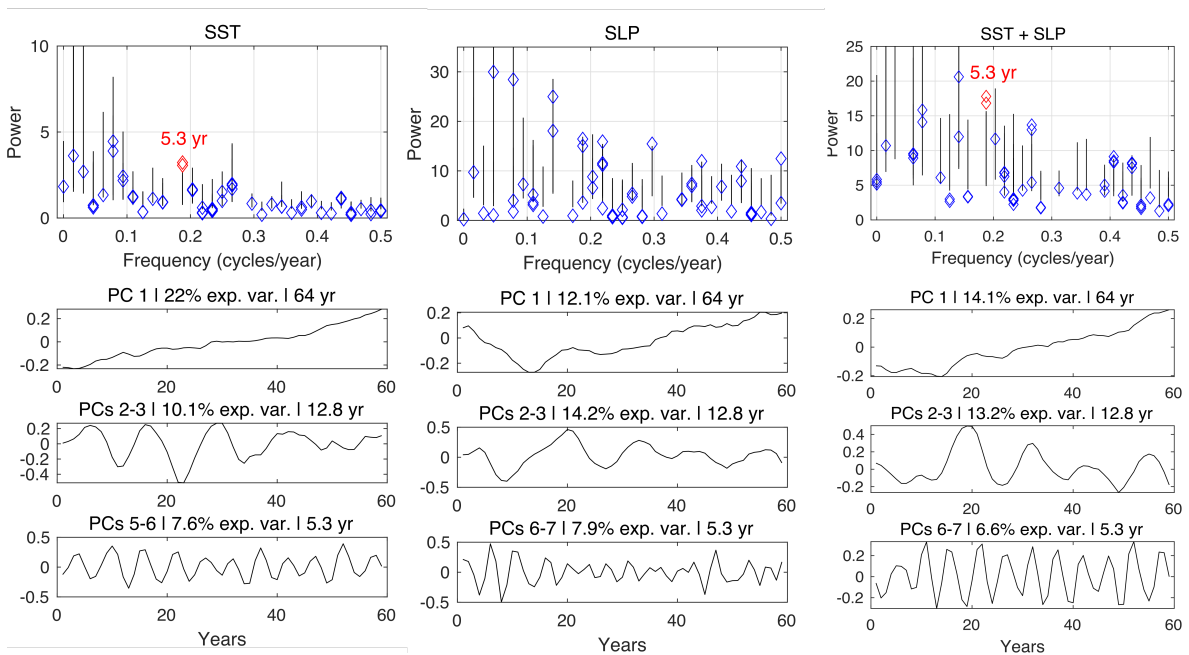


Figure 4.2: Montecarlo analysis and leading principal components (PCs) associated with the M-SSA of SST, SLP, and coupled SST and SLP. The upper rows show the power of each PC as a function of its frequency plotted as diamonds. The black line shows the confidence intervals. The significant mode with a periodicity of 5.3 years is plotted in red. The rows below show the trend (PC1), and the 12.8 and 5.3 yr modes explain the majority of the variance (shown as % in the title of each panel). The length of the PCs is equal to the length of the time series minus the window length.

Fig.4.3 shows an example of the resulting reconstructed time series for a random grid-point using the above mentioned modes. About 40% of the interannual variability can

be explained by the near linear trend, a near decadal oscillation (12.8 years) and an interannual oscillation (5.3 and 3.4 years for SST and SLP, respectively).

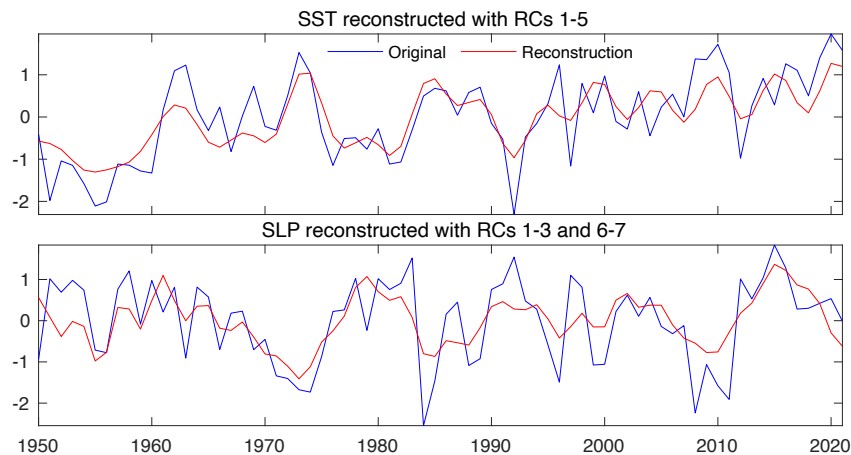


Figure 4.3: Example of original time series and reconstructed timeseries from 5 reconstructed components (trend, decadal and interannual modes explained in the text) for a random grid point for SST (above) and SLP (below).

4.1 Spatiotemporal evolution of the oscillatory modes

Both SST and SLP fields show a 12.8-year oscillation mode with a SW-NE dipole structure with a predominance of the meridional axis over the zonal axis (Figs. 4.4 and 4.5). The axis of the SST dipole closely follows the 0 mean Uwind, so that SST anomalies develop to the north and south of about 32°S depicting a standing pattern. The dipole shows maximum amplitude in the southwestern and tropical Atlantic regions, and thus the most prominent zonal differences are observed in the SST mode south of 30°S (Fig.4.4). Both SST and SLP fields show a 12.8-year oscillatory mode with a SW-NE dipolar structure with a predominance of the meridional axis over the zonal axis (Figs. 4.4 and 4.5). The dipole shows maximum amplitude in the southwestern and tropical Atlantic regions, and thus the most prominent zonal differences are observed in the SST mode south of 33°S (Fig. 4.4). The decadal mode resulting from the M-SSA of the SLP field is shown in Fig. 4.5, and the SLP anomalies are seen to oscillate in sign and intensity with S-N movements.

As mentioned before, the M-SSA applied to both SST and SLP fields also recovers a 12.8-year oscillatory mode (Figures 4.6 and 4.7), with similar anomalies as those found in the analysis of individual fields. There are, however, some differences such as that the

SST pattern tends to be more concentrated to the north of 40°S and that the tropical pole seems weaker than in the mode recovered by applying M-SSA only to the SST field.

The single 5.3-year SST mode has similarities and differences with respect to the 12.8-year mode. It has also a dipole structure, but it is less symmetric. During many phases, one pole is restricted near the western boundary of the basin, within the recirculation area of the subtropical gyre, and the anomalies instead of behaving as a standing oscillation as for the 12.8 years dipole mode, tend to follow an anticlockwise propagation (Fig.4.8).

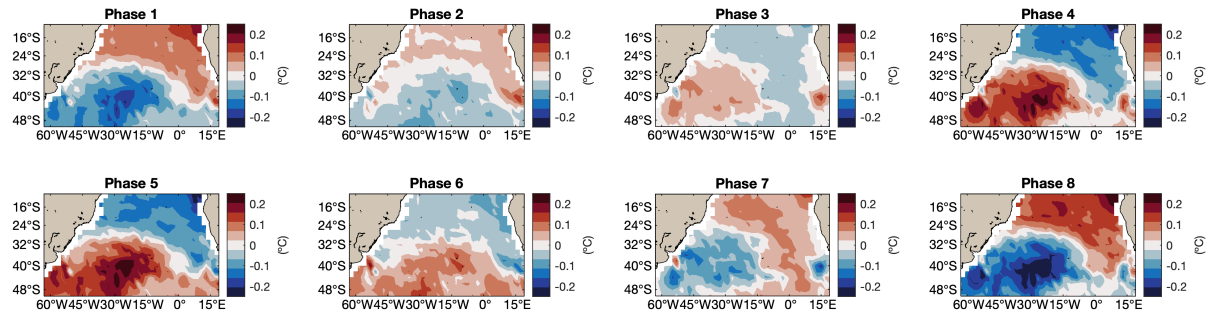


Figure 4.4: 12.8-year oscillatory mode of SST.

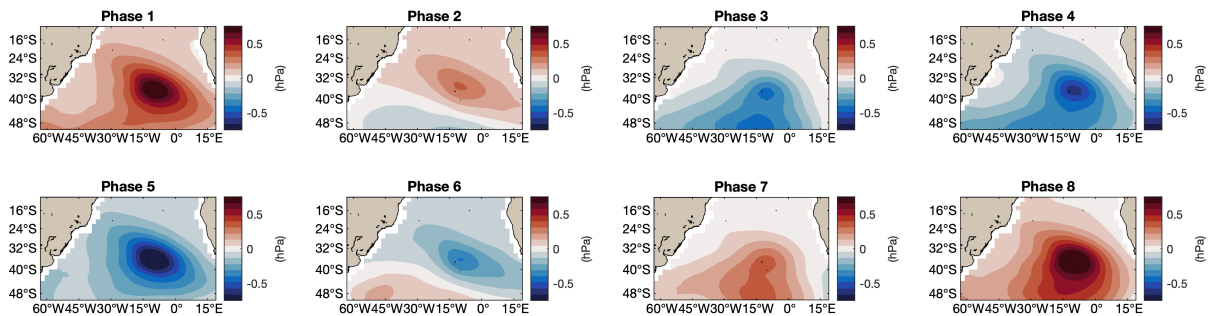


Figure 4.5: 12.8-year oscillatory mode of SLP.

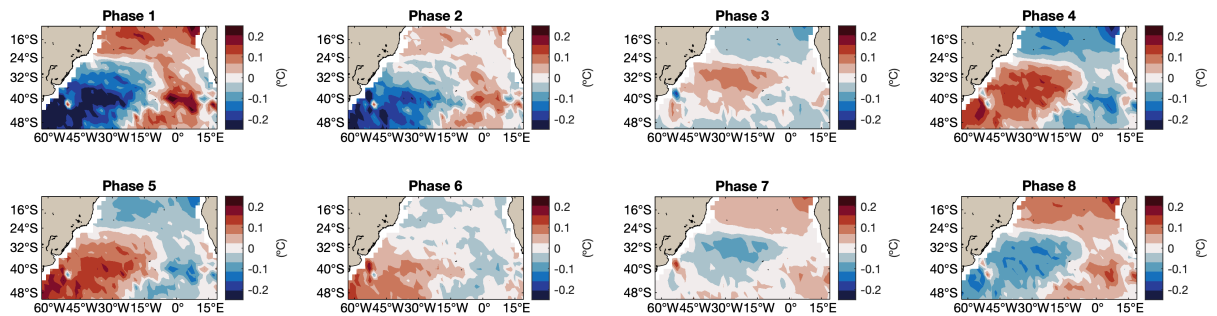


Figure 4.6: 12.8-year coupled oscillatory mode of SST.

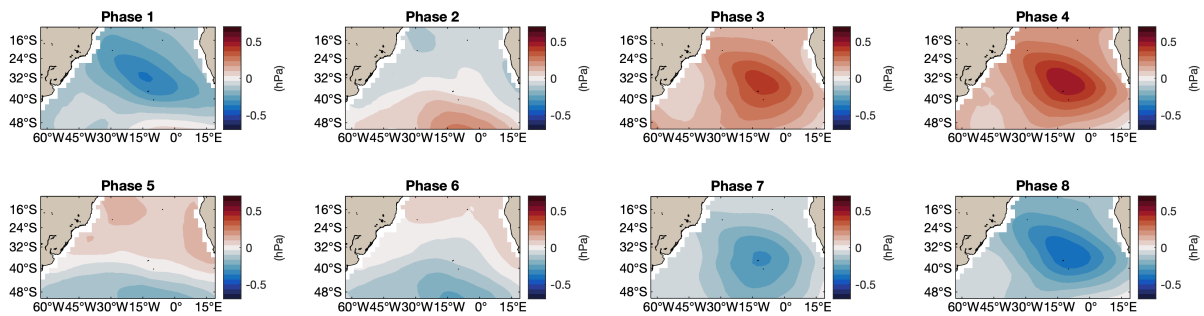


Figure 4.7: 12.8-year coupled oscillatory mode of SLP.

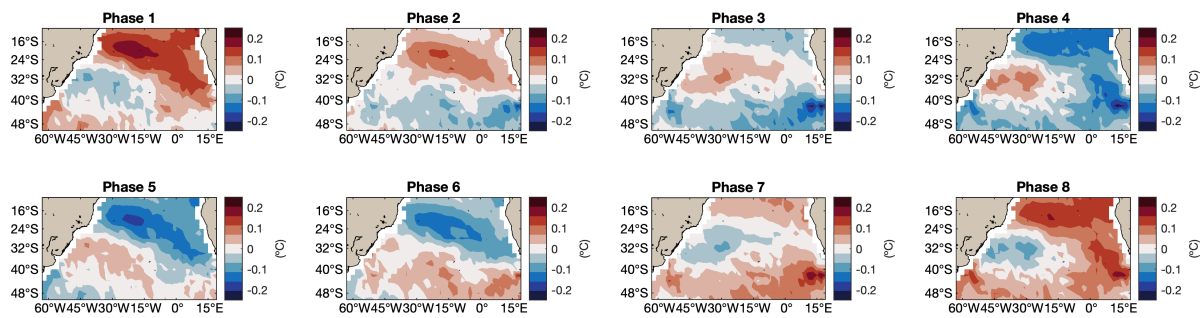


Figure 4.8: 5.3-year coupled oscillatory mode of SST.

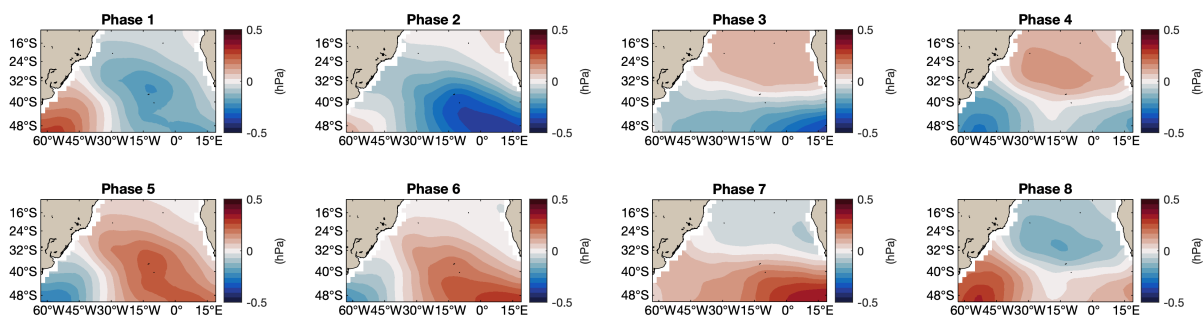


Figure 4.9: 5.3-year coupled oscillatory mode of SLP.

The spatial structure of SST associated with the coupled 5.3-year mode is very similar to the 5.3-year single mode of SST (Fig.4.8 and Fig.4.9). The spatial structure of SLP associated with the coupled 5.3-year mode has spatial differences and it is not a monopole like the 12.8-year mode. It has a dipole structure with N-S orientation in most of the phases, with the 0 value near 40°S (Fig.4.10).

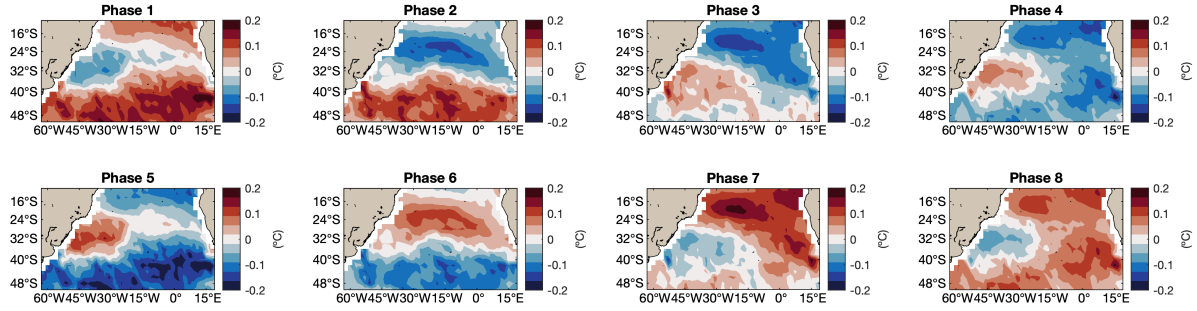


Figure 4.10: 5.3-year oscillatory mode of SST.

The composite of SST for the entire world associated with the 5.3-year oscillation of SST shows SST anomalies in the Tropical Pacific associated with EL Niño during phases 4 and 5 and with La Niña during phases 1 and 8, respectively (Fig.4.11).

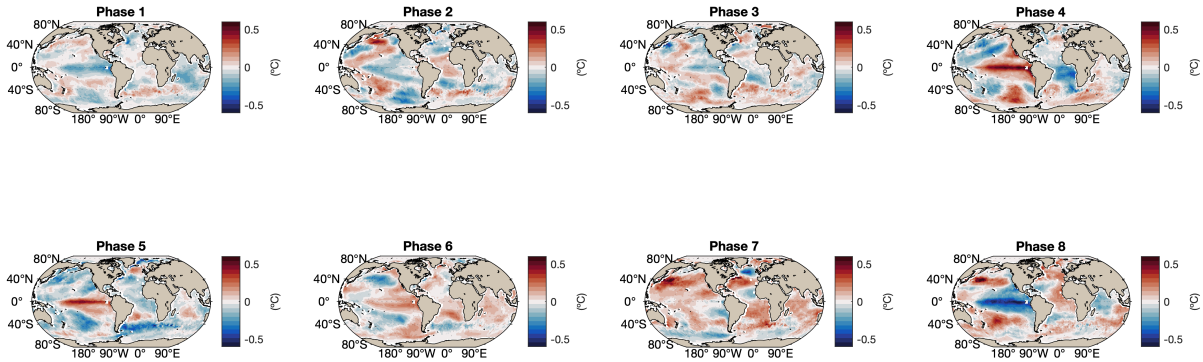


Figure 4.11: Composite of SST anomalies associated with the 5.3-year oscillatory mode of SST.

5 Summary and conclusion

We have used an advanced spectral method, the Multivariate Singular Spectrum analysis (M-SSA), applied to the ERA5 reanalysis to describe interannual-to-decadal oscillations in the south Atlantic basin. We identified an increasing nearly linear trend in both SST and SLP, being more prominent and explaining more variance in the SST field. We then identified a dominant oscillation of 12.8 years both in the individual variables and the coupled analysis. This mode is very likely linked to the South Atlantic Dipole

described in the literature albeit with fewer details, which has been related to climate anomalies in neighboring continents such as precipitations over South America, and is therefore of economical relevance. For example, the phase of the dipole with negative SST anomalies over the tropics and positive SST anomalies over the extratropics is associated with increased precipitation during the rainy season over eastern Brazil (Bombardi et al., 2011).

The other mode of variability isolated by the M-SSA in SST is characterized by a 5.3-year period and a similar spatial pattern as the South Atlantic Dipole, but it has no homologous SLP mode. Also, the spatial structure suggests it may be related to the ocean subtropical gyre circulation and therefore with internal oceanic variability. If so, it will modulate the position of the Brazil-Malvinas Confluence on interannual time scales. For the case of SLP, a 3.4-year oscillation was also described. This mode not only displays meridional but also zonal variations of the anomalies of SLP rotating counterclockwise. If this mode is related to the 4-year oscillation reported by Venegas et al., 1997 is yet to be determined.

In conclusion, with the trend, a decadal and an interannual oscillation, we were able to reproduce about 40% of the interannual variability of SST, SLP, and the coupled variables in the South Atlantic. These results contribute to characterizing the spatio-temporal evolution of the variability modes, including the South Atlantic Dipole. A better understanding of the physical mechanisms responsible for the observed oscillations will contribute to an improved understanding and predicting capabilities.

Chapter 5

General conclusions and perspectives

In this thesis, we have investigated different aspects of the oceanic circulation in the South Atlantic from the large scale to mesoscale dynamics, using mostly observations but also reanalysis. These studies have provided original insights. Each of the three topics addressed in this PhD work has involved the application of different methods of analysis and very diverse datasets. In particular, the work carried out provides the hydrographic analyses of two oceanographic cruises not yet investigated. The validated and calibrated datasets and scripts to reproduce the results have been made available in open access. For the oceanographic cruise in the Uruguayan economic exclusive zone, data was processed from the raw files (e.g. binaries from the Ship ADCP). The processed data are now available at the Sea scientific open data publication repository (<https://doi.org/10.17882/86206>).

Besides from the new processed datasets generated from oceanographic cruises, we have taken advantage of the expansion of the South Atlantic observing system to better infer the context of the hydrographic cruises into a time-varying ocean circulation framework. In particular, the important deployment of Argo profiling floats has increased spectacularly the spatio-temporal sampling of hydrographic properties in the upper 2000 m of the basin. Nowadays it is therefore possible to combine upper ocean 2-D sampling varying in time of the ocean surface from satellite observations with vertical profiles, and approach a 3-D characterization of the ocean state. This thesis tried to take advantage of this increased observing capability to gather an enhanced knowledge in the South Atlantic AMOC estimates and variability (discussed in Chapter 2) as well as in an attempt to describe the complex interaction between two western boundary currents along and across the South American continental slope (Chapter 3). We also used the recently released ERA5 reanalysis (1979 to 2021) with its associated experimental product (1950-1978), accounting for 72 years of data to study large scale coupled variability in the South Atlantic (Chapter 4).

The main scientific contributions of this thesis are described below separated by chapters.

Regarding the large-scale circulation and the AMOC, we provided the first description of the water mass structure, currents and meridional volume, heat, and freshwater transports across 34.5°S in the South Atlantic Ocean. At 34.5°S we identify and quantify an upper (15.64 ± 1.39 Sv) and an abyssal overturning cell (2.4 ± 1.6 Sv). The latter consists of the northward flow of relatively recently formed AABW confined to the western basin. Across the section, a net meridional heat transport of 0.27 ± 0.10 PW is observed when prescribing the geostrophic approximation and 0.26 PW from direct velocity observations (corrected for the mass imbalance over the section). These heat transport estimates are lower than previously reported (0.5 PW, Dong et al., 2015) and could be explained by the relatively low intensity of the upper overturning cell during the cruise compared with the mean reported from moorings (Kersale et al., 2020) and the anomalous predominance of cold-core eddies along the section. In comparisons with neighboring transbasin sections, applying the same analysis methods, we find that the AMOC volume and heat transport increased toward the equator (0.65 PW at 30°S and 1.08 PW at 24°S), in agreement with previous results. The decrease in strength of the upper overturning cell is, among other phenomena, associated with the intensification of the warm Brazil Current flowing southward between 24°S and 34.5°S during the same period of time, and, to a minor extent, to a decrease in the mesoscale activity, leading to a weakening of the AMOC with increasing latitude (from 24.47 Sv at 24°S to 15.18 Sv at 34.5°S).

From the 34.5°S section we identified the existence of more recently ventilated water masses on the western side of the basin and older waters in the east. The major differences in oxygen and thermohaline composition were observed within the AAIW, NADW, and LCDW layers. AAIW is directly injected from the Brazil-Malvinas Confluence region in the west while in the east is supplied mostly from the Indian Ocean and therefore is saltier, warmer and less oxygenated. NADW flows southward and reaches 34.5°S along both boundaries. Because of the indirect path, the eastern NADW branch is less salty and less oxygenated. LCDW is warmer and saltier in the eastern part of the section and also the transport changes sign across the basin, flowing northward in the western part and southward in the eastern part.

Mesoscale eddies, which have been identified as coherent structures, also transport water mass properties that originate on the eastern side of the basin, from the Indian Ocean

(mostly central and subtropical mode waters) and, on the western side, subantarctic waters originating from the Pacific that undergoes to some lateral mixing and ventilation near the Brazil-Malvinas confluence. During the SAMBA GO-SHIP cruise in January 2017 along 34.5°S, our estimates show that eddies have a limited impact on the upper overturning cell. However, they largely influence the heat transport which almost doubles when the eddies (predominantly cold-core eddies) are removed from the estimate.

Due to the relevance of the western margin of the South Atlantic imposed by the Brazil and Malvinas currents and the derived high mesoscale eddy activity, we then focus on the confluence region of these two currents, processing and analyzing different types of data.

To do so, we processed and analyzed new in-situ hydrographic and ADCP measurements and combined them with long-term satellite observations, an eddy detection algorithm, and Argo float profiles allowed us to identify and characterize the Brazil-Malvinas Confluence dynamics. In particular, we have been able to describe the 3-D structure and evolution of surface and subsurface shelf water export to the adjacent deep ocean. We did so by using data from an hydrographic cruise that took place in April-May 2016 in the Uruguayan EEZ, which provided an unprecedented dataset to investigate local water masses, ocean dynamics, and cross-shelf exchanges at the Brazil-Malvinas Confluence. Despite the survey covering a relatively small area, our study shows that it is a highly variable environment, hosting large Rio de la Plata discharges and a complex interaction between two colliding western boundary currents and mesoscale activity developing offshore.

By extending the Brazil-Malvinas Confluence latitudinal position index of Lumpkin et al., 2011, besides from confirming the seasonal cycle and southward displacement over the last 27 years of about 1°, we showed that the confluence was located anomalously north during the first half of 2016, occupying the Uruguayan EEZ when the in-situ survey was conducted. We found two events of shelf-water export during the cruise, which are known to have important consequences for carbon export, water masses transformations, and marine biodiversity.

In particular, our analyses provide evidence of the 3-D structure and evolution of two different kinds of shelf water export associated with the Brazil-Malvinas Confluence dynamics: one related to Rio de la Plata waters that remains confined to the upper 20-40 meters; the other involves Subantarctic Shelf Waters that subducts under the subtropical

thermocline while crossing the continental slope. The surface export of shelf water observed during the hydrographic cruise consisted of a thin off-shelf layer of Rio de la Plata waters following the path of the Brazil Current retroflexion after an anticyclonic eddy was shed from the current. The subsurface export of Subantarctic Shelf Water appears to be associated with mesoscale dynamics triggered by the merging of a cyclonic eddy with the Malvinas Current at the Brazil-Malvinas Confluence.

By using Argo profiles located within the southwestern Atlantic slope, we provide evidence of the presence of Rio de la Plata waters and Subantarctic Shelf Waters between the separation of the Brazil Current from the shelf-break and the confluence. These shelf water export events are all located at the same depths as observed during the 2016 cruise. Moreover, for specific values of absolute dynamic topography that define the Brazil-Malvinas Confluence Front and the separation of the Brazil Current from the shelf (ranging from 0.25 to 0.5 m) shelf waters are found over the slope in a large proportion of the Argo profiles, suggesting that the export of these waters at the Confluence is relatively frequent and mostly taking place at specific values of absolute dynamic topography. Analyses of Argo profiles and satellite sea surface salinity, show that Subantarctic Shelf Waters are often found over the slope within the shallow branch of the Malvinas Current. Because of the similarity in thermohaline properties between Subantarctic Shelf Waters and surrounding waters and the intense mixing taking place in the area, the detection of shelf waters within the Malvinas current is challenging. Nonetheless, by combining in-situ water velocity measurements, waters properties and concomitant satellite altimetry observations we found evidence of Subantarctic Shelf Waters along the Brazil-Malvinas Confluence. In contrast, Rio de la Plata waters are more easily discernible in the open ocean due to their unique low salinity and low-density characteristics.

We also provided evidence that, although satellite surface salinity reveals shelf water exports (Guerrero et al., 2014), the coarse resolution of satellite data limits the ability to detect the fine structure and temporal evolution of the exported waters. This suggests that several export events might not be properly captured by these remotely sensed data. Chlorophyll-a, which has higher resolution especially under clear sky conditions, could be a complementary tool to discern such freshwater export events, but it needs to be contrasted with other salinity observations, as high chlorophyll-a filaments might be associated with several other processes not related to shelf-waters. Nonetheless, the combination of different observations (eg. satellite Chlorophyll-a and salinity observations) might be combined to gain more insights into the mechanisms of shelf water export.

Finally, our analyses suggest that geostrophic currents derived from satellite altimetry are a robust indicator for the regional dynamics and a useful tool to track cross-shore water export events. By providing relatively accurate steric height estimates, satellite altimetry shows a high correlation with absolute velocities at 100m of depth. Hence, satellite altimetry seems to be more useful than satellite surface salinity to identify subsurface shelf water export events. As altimetry is relatively accurate in identifying the location of the confluence (ADT contour 0.25 m over the slope) and the separation of Brazil Current from the shelf-break (ADT contour 0.5 m), across-slope velocity maxima confined between the 0.25 and 0.5 m ADT contours over the shelf break might be a good indicator for subsurface shelf water export occurrences.

In Chapters 2 and 3 we have analyzed large-scale and regional-scale South Atlantic processes that are highly variable. Some of the observed variability is due to the internal ocean dynamics like the overturning circulation and mesoscale eddies. However, a portion of the observed variability is forced externally. To disentangle the internal variability in the time series we have tried to assess the coupled modes of variability of the ocean and atmosphere at the basin scale. This has been achieved by carrying out a multivariate analysis of the upper ocean and lower atmosphere time series that we discuss in Chapter 4 of this manuscript.

By applying the Multi-channel Singular Spectrum Analysis to the time series of ERA5 reanalysis of sea surface temperature and sea level pressure, we provided evidence of interannual and decadal oscillations in the South Atlantic. We found a dominant oscillation of 12.8 years both in the individual variables and the coupled analysis. This mode is very likely linked to the South Atlantic Dipole described in the literature albeit with fewer details, and has several implications for climate, like precipitations over southeast South America, and therefore economical relevance. For example, the phase of the dipole with negative SST anomalies over the tropics and positive SST anomalies over the extratropics are associated with increased precipitation during the rainy season over eastern Brazil (Bombardi et al., 2011).

The other mode of variability isolated by the M-SSA in SST is characterized by a 5.3-year period and a similar spatial pattern as the South Atlantic Dipole, but it has no homologous SLP mode. The spatial structure suggests it is more related to the ocean subtropical gyre circulation and probably responds to oceanic internal variability. For the case of SLP, a 3.4-year oscillation was also described. This mode not only displays meridional but also zonal variations of the SLP.

In conclusion, in Chapter 4 we were able to reproduce about 40% of the interannual variability of SST, SLP, and the coupled variables in the South Atlantic with the trend, a decadal and an interannual oscillation obtained from the reconstructed components of the Multivariate Singular Spectral Analysis. These results contribute to characterizing the spatio-temporal evolution of the variability modes in the South Atlantic, including the highly relevant for climate and economy South Atlantic Dipole. A better understanding the physical mechanisms responsible for the observed oscillations including the role of the ocean as a forcing mechanism will contribute to an improved understanding and predicting capabilities.

1 Perspectives

The main short-term perspective of this thesis is to finalize and submit the manuscript of Chapter 4, which shows M-SSA as a promising tool to provide an enhanced description of the South Atlantic Dipole, the role of air-sea coupling in its dynamics, and distinguish it from other modes of variability. Applying also the M-SSA taking into account the different seasons could contribute to the discussion of the behaviour of this dipole throughout the year. In particular, a memory effect of the ocean restoring the anomalies from one winter to the other through the fossilized mixed layer depth has been postulated as a possible driver of the South Atlantic Dipole (Santis et al., 2020). In addition to that, some open questions from Chapters 2 and 3 remain to be answered in the near future such as the ones described in the paragraphs below.

From Chapter 2, the understanding of the abyssal circulation in the eastern South Atlantic, in terms of both, the origin of the water masses and the details of the circulation, seems to be a very relevant scientific question. It is indeed a very active research topic (e.g. Kersalé et al., 2019; Kersale et al., 2020), that is not yet resolved despite a decade of moorings measurements.

During January 2017, an important subantartic intrusion at 8°E was observed (Manta et al., 2021). It consisted of relatively fresh and highly oxygenated water characterized by an ADT below 0.4 m associated with a cyclonic eddy. This eddy was not a time-coherent structure, and TOEddies revealed successive merging and splitting associated with this structure. This region is part of the route undertaken by Agulhas Rings across the Cape Basin that encompasses this area. Moreover, here waters from the South Atlantic, Indian and the Southern Ocean converge in a turbulent regime, where eddies and currents in the form of jets strongly interact. These processes might provide the routes of meridional

exchanges between subtropical and subpolar waters. A higher spatio-temporal sampling of this kind of process would provide more details on the processes involved and on the meridional transports of properties.

In Chapter 3 we have investigated small-scale events in the very turbulent region of the Brazil-Malvinas Confluence. This study has in particular provided the evidence of subsurface export of shelf waters, a process that is documented in high-resolution ocean numerical simulations but very rarely observed. To detail and quantify one of such events, we made use of observations undertaken during an oceanographic cruise that was planned with not such an objective. As a consequence, the suite of the observations achieved was not optimal in terms of synopsicity and spatial detail. We think that to gather a better understanding, mapping and quantification of cross-shelf exchanges, that seem to happen at the submesoscale (i.e., scales smaller than 50 km), dedicated cruises should be organized by sampling the area with sections parallel to the slope and by implementing TSG, ADCP but also underway CTD continuously profiling the upper 200-500 m measurements (with instruments such as the Moving Vessel Profilers, Seasoar, uCTD/Rapid cast). Also, the description and quantitative assessment of the impact of the different types of shelf-water export from a biogeochemical perspective are relevant scientific questions.

One specific question that remains open in our investigation concerns the cyclonic eddy that is often positioned between the Brazil and Malvinas Currents. This eddy is detected from satellite altimetry maps by TOEddies. During the cruise, one of such eddies was sampled by the SADCPC which provided a description of the vertical structure of the eddy that was consistent with that produced by satellite altimetry. This type of eddies is often observed where the slope widens, at the Ewing terrace, between the 200 and 2000 m isobath. It is shed by the Malvinas Current whenever the current weakens and retracts southward. This eddy seems to play an important role in the cross-shelf exchanges and probably has also a significant impact on fisheries. Unfortunately, this eddy structure is not fully resolved by the actual altimetric products, but it might be in the near future, after the launch of the SWOT satellite in November 2022. The NASA_CNES SWOT satellite will provide instantaneous 2D fields and improve effectively the ADT resolution to solve eddies as small as these ones (Morrow et al., 2019).



General Bibliography

- Abdalla, Saleh, Abdolnabi Abdeh Kolahchi, Michaël Ablain, Susheel Adusumilli, Suchandra Aich Bhowmick, Eva Alou-Font, et al. (2021). “Altimetry for the future: Building on 25 years of progress”. *Advances in Space Research* 68.2, pp. 319–363 (cit. on pp. 9, 11).
- Allen, M and L Smith (1996). “Monte Carlo SSA: Detecting irregular oscillations in the presence of colored noise”. *Journal of climate* 9.12, pp. 3373–3404 (cit. on p. 69).
- Bach, Eviatar, Safa Mote, V Krishnamurthy, A Surjalal Sharma, Michael Ghil, and Eugenia Kalnay (2021). “Ensemble Oscillation Correction (EnOC): Leveraging oscillatory modes to improve forecasts of chaotic systems”. *Journal of Climate* 34.14, pp. 5673–5686 (cit. on p. 66).
- Barreiro, Marcelo, Ping Chang, and Ramalingam Saravanan (2002). “Variability of the South Atlantic convergence zone simulated by an atmospheric general circulation model”. *Journal of Climate* 15.7, pp. 745–763 (cit. on p. 67).
- (2005). “Simulated precipitation response to SST forcing and potential predictability in the region of the South Atlantic convergence zone”. *Climate dynamics* 24.1, pp. 105–114 (cit. on p. 67).
- Barreiro, Marcelo, Alessandra Giannini, Ping Chang, and Ramalingam Saravanan (2004). “On the role of the South Atlantic atmospheric circulation in tropical Atlantic variability”. *Earth’s Climate: The Ocean-Atmosphere Interaction, Geophys. Monogr* 147, pp. 143–156 (cit. on pp. 6, 67).
- Bombardi, Rodrigo J and Leila Carvalho (2011). “The South Atlantic dipole and variations in the characteristics of the South American Monsoon in the WCRP-CMIP3 multi-model simulations”. *Climate Dynamics* 36.11, pp. 2091–2102 (cit. on pp. 75, 80).
- Bombardi, Rodrigo J, Leila Carvalho, Charles Jones, and Michelle S Reboita (2014). “Precipitation over eastern South America and the South Atlantic Sea surface temperature during neutral ENSO periods”. *Climate Dynamics* 42.5, pp. 1553–1568 (cit. on p. 67).
- Bombardi, Rodrigo Jose (2013). *The South Atlantic Coupled Variability and the South Atlantic Convergence Zone* (cit. on p. 67).
- Brett, Annie, Jim Leape, Mark Abbott, Hide Sakaguchi, Ling Cao, Kevin Chand, et al. (2020). *Ocean data need a sea change to help navigate the warming world* (cit. on pp. 12, 13).
- Bryden, Harry L, Hannah R Longworth, and Stuart A Cunningham (2005). “Slowing of the Atlantic meridional overturning circulation at 25 N”. *Nature* 438.7068, pp. 655–657 (cit. on p. 14).
- Buckley, Martha W and John Marshall (2016). “Observations, inferences, and mechanisms of the Atlantic Meridional Overturning Circulation: A review”. *Reviews of Geophysics* 54.1, pp. 5–63 (cit. on p. 3).
- Cabos, William, Alba de la Vara, and Shunya Koseki (2019). “Tropical Atlantic variability: Observations and modeling”. *Atmosphere* 10.9, p. 502 (cit. on p. 65).
- Carvalho, Leila MV, Charles Jones, and Brant Liebmann (2002). “Extreme precipitation events in southeastern South America and large-scale convective patterns in the South Atlantic convergence zone”. *Journal of Climate* 15.17, pp. 2377–2394 (cit. on p. 67).
- Chai, Fei, Kenneth S Johnson, Hervé Claustre, Xiaogang Xing, Yuntao Wang, Emmanuel Boss, et al. (2020). “Monitoring ocean biogeochemistry with autonomous platforms”. *Nature Reviews Earth & Environment* 1.6, pp. 315–326 (cit. on p. 13).

- Chaigneau, Alexis, Arnaud Gizolme, and Carmen Grados (2008). “Mesoscale eddies off Peru in altimeter records: Identification algorithms and eddy spatio-temporal patterns”. *Progress in Oceanography* 79.2-4, pp. 106–119 (cit. on p. 11).
- Chaigneau, Alexis, Marie Le Texier, Gérard Eldin, Carmen Grados, and Oscar Pizarro (2011). “Vertical structure of mesoscale eddies in the eastern South Pacific Ocean: A composite analysis from altimetry and Argo profiling floats”. *Journal of Geophysical Research: Oceans* 116.C11 (cit. on p. 11).
- Chaves, Rosane Rodrigues and Paulo Nobre (2004). “Interactions between sea surface temperature over the South Atlantic Ocean and the South Atlantic Convergence Zone”. *Geophysical Research Letters* 31.3 (cit. on p. 67).
- Chelton, Dudley B, Michael G Schlax, and Roger M Samelson (2011). “Global observations of nonlinear mesoscale eddies”. *Progress in oceanography* 91.2, pp. 167–216 (cit. on pp. 8, 9, 11).
- Chelton, Dudley B, Michael G Schlax, Roger M Samelson, and Roland A de Szoeke (2007). “Global observations of large oceanic eddies”. *Geophysical Research Letters* 34.15 (cit. on p. 9).
- Chelton, Dudley B, Michael G Schlax, Donna L Witter, and James G Richman (1990). “Geosat altimeter observations of the surface circulation of the Southern Ocean”. *Journal of Geophysical Research: Oceans* 95.C10, pp. 17877–17903 (cit. on p. 8).
- Chidichimo, MP, AR Piola, CS Meinen, RC Perez, EJD Campos, S Dong, et al. (2021). “Brazil Current Volume Transport Variability During 2009–2015 From a Long-Term Moored Array at 34.5° S”. *Journal of Geophysical Research: Oceans* 126.5, e2020JC017146 (cit. on p. 13).
- Chou, Chia and J David Neelin (2001). “Mechanisms limiting the southward extent of the South American summer monsoon”. *Geophysical research letters* 28.12, pp. 2433–2436 (cit. on p. 67).
- Collins, Curtis A and Robert H Heimiller (1989). “The POLYMODE program” (cit. on p. 9).
- Cornec, Marin, Rémi Laxenaire, Sabrina Speich, and Hervé Claustre (2021). “Impact of mesoscale eddies on deep chlorophyll maxima”. *Geophysical research letters* 48.15, e2021GL093470 (cit. on pp. 9, 12).
- Czaja, Arnaud and John Marshall (2006). “The partitioning of poleward heat transport between the atmosphere and ocean”. *Journal of the atmospheric sciences* 63.5, pp. 1498–1511 (cit. on p. 2).
- Dong, Shenfu, Gustavo Goni, and Francis Bringas (2015). “Temporal variability of the South Atlantic meridional overturning circulation between 20 S and 35 S”. *Geophysical Research Letters* 42.18, pp. 7655–7662 (cit. on pp. 4, 77).
- Ferrari, Raffaele and David Ferreira (2011). “What processes drive the ocean heat transport?” *Ocean Modelling* 38.3-4, pp. 171–186 (cit. on p. 2).
- Frajka-Williams, Eleanor, Isabelle J Ansorge, Johanna Baehr, Harry L Bryden, Maria Paz Chidichimo, Stuart A Cunningham, et al. (2019). “Atlantic meridional overturning circulation: Observed transport and variability”. *Frontiers in Marine Science*, p. 260 (cit. on pp. 4, 14).
- Friedlingstein, Pierre, Matthew W Jones, Michael O’Sullivan, Robbie M Andrew, Dorothee CE Bakker, Judith Hauck, et al. (2021). “Global carbon budget 2021”. *Earth System Science Data Discussions*, pp. 1–191 (cit. on p. 2).
- Fuglister, FREDERICK C and LV Worthington (1951). “Some results of a multiple ship survey of the Gulf Stream”. *Tellus* 3.1, pp. 1–14 (cit. on p. 9).
- Ganopolski, Andrey and Stefan Rahmstorf (2001). “Rapid changes of glacial climate simulated in a coupled climate model”. *Nature* 409.6817, pp. 153–158 (cit. on p. 3).
- Garnot, Vivien Sainte Fare, Andreas Groth, and Michael Ghil (2018). “Coupled climate-economic modes in the Sahel’s interannual variability”. *Ecological economics* 153, pp. 111–123 (cit. on p. 66).
- Garzoli, Silvia L, Molly O Baringer, Shenfu Dong, Renellys C Perez, and Qi Yao (2013). “South Atlantic meridional fluxes”. *Deep Sea Research Part I: Oceanographic Research Papers* 71, pp. 21–32 (cit. on pp. 3, 4).
- Gentemann, CL, Joel P Scott, Piero LF Mazzini, Cassia Pianca, Santha Akella, Peter J Minnett, et al. (2020). “Saildrone: adaptively sampling the marine environment”. *Bulletin of the American Meteorological Society* 101.6, E744–E762 (cit. on p. 13).

General Bibliography

- Ghil, M, MR Allen, MD Dettinger, K Ide, D Kondrashov, ME Mann, et al. (2002). “Advanced spectral methods for climatic time series”. *Reviews of geophysics* 40.1, pp. 3–1 (cit. on p. 66).
- Ghil, M and R Vautard (1991). “Interdecadal oscillations and the warming trend in global temperature time series”. *Nature* 350.6316, pp. 324–327 (cit. on p. 66).
- Gordon, Arnold L (1986). “Interocean exchange of thermocline water”. *Journal of Geophysical Research: Oceans* 91.C4, pp. 5037–5046 (cit. on p. 7).
- Grist, Jeremy P and Simon A Josey (2003). “Inverse analysis adjustment of the SOC air–sea flux climatology using ocean heat transport constraints”. *Journal of Climate* 16.20, pp. 3274–3295 (cit. on p. 2).
- Groth, Andreas, Yizhak Feliks, Dmitri Kondrashov, and Michael Ghil (2017). “Interannual variability in the North Atlantic ocean’s temperature field and its association with the wind stress forcing”. *Journal of Climate* 30.7, pp. 2655–2678 (cit. on pp. 66, 68, 69).
- Groth, Andreas and Michael Ghil (2015). “Monte Carlo singular spectrum analysis (SSA) revisited: Detecting oscillator clusters in multivariate datasets”. *Journal of Climate* 28.19, pp. 7873–7893 (cit. on p. 69).
- Guerrero, Raul A, Alberto R Piola, Harold Fenco, Ricardo P Matano, Vincent Combes, Yi Chao, et al. (2014). “The salinity signature of the cross-shelf exchanges in the S outhwestern A tlantic O cean: Satellite observations”. *Journal of Geophysical Research: Oceans* 119.11, pp. 7794–7810 (cit. on pp. 8, 79).
- Haarsma, Reindert J, Edmo JD Campos, Wilco Hazeleger, Camiel Severijns, Alberto R Piola, and Franco Molteni (2005). “Dominant modes of variability in the South Atlantic: A study with a hierarchy of ocean–atmosphere models”. *Journal of climate* 18.11, pp. 1719–1735 (cit. on pp. 65, 67).
- Hastenrath, Stefan and Leon Heller (1977). “Dynamics of climatic hazards in northeast Brazil”. *Quarterly Journal of the Royal Meteorological Society* 103.435, pp. 77–92 (cit. on p. 65).
- Hernandez, Fabrice, Pierre-Yves Le Traon, and Rosemary Morrow (1995). “Mapping mesoscale variability of the Azores Current using TOPEX/POSEIDON and ERS 1 altimetry, together with hydrographic and Lagrangian measurements”. *Journal of Geophysical Research: Oceans* 100.C12, pp. 24995–25006 (cit. on p. 9).
- Hersbach, Hans, Bill Bell, Paul Berrisford, Shoji Hirahara, András Horányi, Joaquín Muñoz-Sabater, et al. (2020). “The ERA5 global reanalysis”. *Quarterly Journal of the Royal Meteorological Society* 146.730, pp. 1999–2049 (cit. on p. 68).
- Hurrell, James W, Yochanan Kushnir, Geir Ottersen, and Martin Visbeck (2003). “An overview of the North Atlantic oscillation”. *Geophysical Monograph-American Geophysical Union* 134, pp. 1–36 (cit. on p. 65).
- Ioannou, Artemis (2019). “Dynamical evolution of intense mesoscale Ierapetra eddies in connection with orographic wind forcing”. PhD thesis. Sorbonne université (cit. on p. 9).
- Jayne, Steven R and Jochem Marotzke (2002). “The oceanic eddy heat transport”. *Journal of Physical Oceanography* 32.12, pp. 3328–3345 (cit. on p. 2).
- Jayne, Steven R, Dean Roemmich, Nathalie Zilberman, Stephen C Riser, Kenneth S Johnson, Gregory C Johnson, et al. (2017). “The Argo program: present and future”. *Oceanography* 30.2, pp. 18–28 (cit. on p. 12).
- Kersale, Marion, Christopher S Meinen, Renellys C Perez, Matthieu Le Henaff, Daniel Valla, Tarron Lamont, et al. (2020). “Highly variable upper and abyssal overturning cells in the South Atlantic”. *Science advances* 6.32, eaba7573 (cit. on pp. 4, 13, 77, 81).
- Kersalé, Marion, Christopher S Meinen, Renellys C Perez, AR Piola, S Speich, EJD Campos, et al. (2021). “Multi-Year Estimates of Daily Heat Transport by the Atlantic Meridional Overturning Circulation at 34.5° S”. *Journal of Geophysical Research: Oceans* 126.5, e2020JC016947 (cit. on pp. 4, 14, 15).
- Kersalé, Marion, Renellys C Perez, Sabrina Speich, Christopher S Meinen, Tarron Lamont, Matthieu Le Hénaff, et al. (2019). “Shallow and deep eastern boundary currents in the South Atlantic at 34.5 S: Mean structure and variability”. *Journal of Geophysical Research: Oceans* 124.3, pp. 1634–1659 (cit. on p. 81).

- Khatiwala, Samar, Toste Tanhua, S Mikaloff Fletcher, Markus Gerber, Scott C Doney, Heather D Graven, et al. (2013). “Global ocean storage of anthropogenic carbon”. *Biogeosciences* 10.4, pp. 2169–2191 (cit. on p. 2).
- Lago, Loreley Selene, Martin Saraceno, Alberto Ricardo Piola, and Laura Agustina Ruiz-Etcheverry (2021). “Volume transport variability on the northern argentine continental shelf from in situ and satellite altimetry data”. *Journal of Geophysical Research: Oceans* 126.2, e2020JC016813 (cit. on p. 6).
- Lau, William K-M and Duane E Waliser (2011). *Intraseasonal variability in the atmosphere-ocean climate system*. Springer Science & Business Media (cit. on p. 66).
- Laxenaire, R, S Speich, Bruno Blanke, Alexis Chaigneau, C Pegliasco, and A Stegner (2018). “Anticyclonic eddies connecting the western boundaries of Indian and Atlantic Oceans”. *Journal of Geophysical Research: Oceans* 123.11, pp. 7651–7677 (cit. on p. 11).
- Laxenaire, R, S Speich, and A Stegner (2020). “Agulhas ring heat content and transport in the South Atlantic estimated by combining satellite altimetry and Argo profiling floats data”. *Journal of Geophysical Research: Oceans* 125.9, e2019JC015511 (cit. on pp. 11, 12).
- Laxenaire, Rémi, Sabrina Speich, and Alexandre Stegner (2019). “Evolution of the thermohaline structure of one Agulhas ring reconstructed from satellite altimetry and Argo floats”. *Journal of Geophysical Research: Oceans* 124.12, pp. 8969–9003 (cit. on pp. 11, 12).
- Levitus, Sydney, John I Antonov, Tim P Boyer, Olga K Baranova, Hernan Eduardo Garcia, Ricardo Alejandro Locarnini, et al. (2012). “World ocean heat content and thermosteric sea level change (0–2000 m), 1955–2010”. *Geophysical Research Letters* 39.10 (cit. on p. 2).
- Lumpkin, Rick and Silvia Garzoli (2011). “Interannual to decadal changes in the western South Atlantic’s surface circulation”. *Journal of Geophysical Research: Oceans* 116.C1 (cit. on p. 78).
- Lumpkin, Rick and Kevin Speer (2007). “Global ocean meridional overturning”. *Journal of Physical Oceanography* 37.10, pp. 2550–2562 (cit. on p. 3).
- Manta, G, S Speich, Johannes Karstensen, Rebecca Hummels, M Kersalé, R Laxenaire, et al. (2021). “The South Atlantic Meridional Overturning Circulation and Mesoscale Eddies in the First GO-SHIP Section at 34.5° S”. *Journal of Geophysical Research: Oceans* 126.2, e2020JC016962 (cit. on pp. 16, 81).
- Manta, Gaston, Sabrina Speich, Marcelo Barreiro, Romina Trinchin, Camila de Mello, Rémi Laxenaire, et al. (2022). “Shelf Water Export at the Brazil-Malvinas Confluence Evidenced From Combined in situ and Satellite Observations”. *Frontiers in Marine Science* 9 (cit. on p. 16).
- Marshall, John, Yochanan Kushnir, David Battisti, Ping Chang, Arnaud Czaja, Robert Dickson, et al. (2001). “North Atlantic climate variability: phenomena, impacts and mechanisms”. *International Journal of Climatology: A Journal of the Royal Meteorological Society* 21.15, pp. 1863–1898 (cit. on p. 65).
- McDonagh, Elaine L, Karen J Heywood, and Michael P Meredith (1999). “On the structure, paths, and fluxes associated with Agulhas rings”. *Journal of Geophysical Research: Oceans* 104.C9, pp. 21007–21020 (cit. on p. 7).
- McDougall, Trevor J and Raffaele Ferrari (2017). “Abyssal upwelling and downwelling driven by near-boundary mixing”. *Journal of Physical Oceanography* 47.2, pp. 261–283 (cit. on p. 3).
- McMahon, Clive Reginald, Fabien Roquet, Sophie Baudel, Mathieu Belbeoch, Sophie Bestley, Clint Blight, et al. (2021). “Animal Borne Ocean Sensors—AniBOS—an essential component of the Global Ocean Observing System (GOOS)”. *Frontiers in Marine Science*, p. 1625 (cit. on p. 12).
- McWilliams, James C (2019). “A survey of submesoscale currents”. *Geoscience Letters* 6.1, pp. 1–15 (cit. on p. 8).
- Meinen, Christopher S, Sabrina Speich, Renellys C Perez, Shenfu Dong, Alberto R Piola, Silvia L Garzoli, et al. (2013). “Temporal variability of the meridional overturning circulation at 34.5 S: Results from two pilot boundary arrays in the South Atlantic”. *Journal of Geophysical Research: Oceans* 118.12, pp. 6461–6478 (cit. on p. 14).

General Bibliography

- Meinen, Christopher S, Sabrina Speich, Alberto R Piola, Isabelle Ansorge, Edmo Campos, Marion Kersalé, et al. (2018). “Meridional overturning circulation transport variability at 34.5 S during 2009–2017: Baroclinic and barotropic flows and the dueling influence of the boundaries”. *Geophysical Research Letters* 45.9, pp. 4180–4188 (cit. on pp. 13, 14).
- Menemenlis, Dimitris, Ichiro Fukumori, and Tong Lee (2005). “Using Green’s functions to calibrate an ocean general circulation model”. *Monthly weather review* 133.5, pp. 1224–1240 (cit. on p. 15).
- Morioka, Yushi, Sébastien Masson, Pascal Terray, Chloé Prodhomme, Swadhin K Behera, and Yukio Masumoto (2014). “Role of tropical SST variability on the formation of subtropical dipoles”. *Journal of climate* 27.12, pp. 4486–4507 (cit. on p. 67).
- Morioka, Yushi, Tomoki Tozuka, and Toshio Yamagata (2011). “On the growth and decay of the subtropical dipole mode in the South Atlantic”. *Journal of Climate* 24.21, pp. 5538–5554 (cit. on pp. 65, 66).
- Moron, Vincent, R Vautard, and M Ghil (1998). “Trends, interdecadal and interannual oscillations in global sea-surface temperatures”. *Climate Dynamics* 14.7, pp. 545–569 (cit. on pp. 67, 69).
- Morrow, Rosemary, Lee-Lueng Fu, Fabrice Ardhuin, Mounir Benkiran, Bertrand Chapron, Emmanuel Cosme, et al. (2019). “Global observations of fine-scale ocean surface topography with the Surface Water and Ocean Topography (SWOT) mission”. *Frontiers in Marine Science* 6, p. 232 (cit. on pp. 10, 82).
- Muza, Michel N, Leila MV Carvalho, Charles Jones, and Brant Liebmann (2009). “Intraseasonal and interannual variability of extreme dry and wet events over southeastern South America and the subtropical Atlantic during austral summer”. *Journal of Climate* 22.7, pp. 1682–1699 (cit. on p. 67).
- Nnamchi, Hyacinth C, Fred Kucharski, Noel S Keenlyside, and Riccardo Farneti (2017). “Analogous seasonal evolution of the South Atlantic SST dipole indices”. *Atmospheric Science Letters* 18.10, pp. 396–402 (cit. on p. 67).
- Nnamchi, Hyacinth C and Jianping Li (2011a). “Influence of the South Atlantic Ocean dipole on West African summer precipitation”. *Journal of Climate* 24.4, pp. 1184–1197 (cit. on p. 67).
- Nnamchi, Hyacinth C, Jianping Li, and Raymond NC Anyadike (2011b). “Does a dipole mode really exist in the South Atlantic Ocean?” *Journal of Geophysical Research: Atmospheres* 116.D15 (cit. on p. 67).
- Nnamchi, Hyacinth C, Jianping Li, Fred Kucharski, In-Sik Kang, Noel S Keenlyside, Ping Chang, et al. (2016). “An equatorial–extratropical dipole structure of the Atlantic Niño”. *Journal of Climate* 29.20, pp. 7295–7311 (cit. on p. 67).
- Olson, Donald B, Guillermo P Podesta, Robert H Evans, and Otis B Brown (1988). “Temporal variations in the separation of Brazil and Malvinas Currents”. *Deep Sea Research Part A. Oceanographic Research Papers* 35.12, pp. 1971–1990 (cit. on pp. 7–10).
- Pegliasco, Cori, Alexis Chaigneau, and Rosemary Morrow (2015). “Main eddy vertical structures observed in the four major Eastern Boundary Upwelling Systems”. *Journal of Geophysical Research: Oceans* 120.9, pp. 6008–6033 (cit. on p. 11).
- Peterson, Larry C, Gerald H Haug, Konrad A Hughen, and Ursula Rohl (2000). “Rapid changes in the hydrologic cycle of the tropical Atlantic during the last glacial”. *Science* 290.5498, pp. 1947–1951 (cit. on p. 3).
- Peterson, Ray G and Lothar Stramma (1991). “Upper-level circulation in the South Atlantic Ocean”. *Progress in oceanography* 26.1, pp. 1–73 (cit. on pp. 5, 7).
- Plaut, Guy and Robert Vautard (1994). “Spells of low-frequency oscillations and weather regimes in the Northern Hemisphere”. *Journal of the atmospheric sciences* 51.2, pp. 210–236 (cit. on pp. 66, 69).
- Robertson, Andrew W and Carlos R Mechoso (2000). “Interannual and interdecadal variability of the South Atlantic convergence zone”. *Monthly weather review* 128.8, pp. 2947–2957 (cit. on p. 67).
- Rodrigues, Regina R, Edmo JD Campos, and Reindert Haarsma (2015). “The impact of ENSO on the South Atlantic subtropical dipole mode”. *Journal of Climate* 28.7, pp. 2691–2705 (cit. on pp. 6, 67).

- Roemmich, Dean, Matthew H Alford, Hervé Claustre, Kenneth Johnson, Brian King, James Moum, et al. (2019). “On the future of Argo: A global, full-depth, multi-disciplinary array”. *Frontiers in Marine Science* 6, p. 439 (cit. on p. 12).
- Rudnick, Daniel L, Katherine D Zaba, Robert E Todd, and Russ E Davis (2017). “A climatology of the California Current System from a network of underwater gliders”. *Progress in Oceanography* 154, pp. 64–106 (cit. on p. 12).
- Rühs, Siren, Franziska U Schwarzkopf, Sabrina Speich, and Arne Biastoch (2019). “Cold vs. warm water route–sources for the upper limb of the Atlantic Meridional Overturning Circulation revisited in a high-resolution ocean model”. *Ocean Science* 15.3, pp. 489–512 (cit. on p. 7).
- Ruiz-Barradas, Alfredo, Eugenia Kalnay, Malaquías Peña, Amir E BozorgMagham, and Safa Motesharrei (2017). “Finding the driver of local ocean–atmosphere coupling in reanalyses and CMIP5 climate models”. *Climate Dynamics* 48.7, pp. 2153–2172 (cit. on p. 68).
- Santis, Wladimir, Paola Castellanos, and Edmo Campos (2020). “Memory effect of the Southern Atlantic subtropical dipole”. *Journal of Climate* 33.17, pp. 7679–7696 (cit. on pp. 65, 81).
- Smethie Jr, William M, Rana A Fine, Alfred Putzka, and E Peter Jones (2000). “Tracing the flow of North Atlantic Deep Water using chlorofluorocarbons”. *Journal of Geophysical Research: Oceans* 105.C6, pp. 14297–14323 (cit. on p. 7).
- Speich, Sabrina, Bruno Blanke, and Gurvan Madec (2001). “Warm and cold water routes of an OGCM thermohaline conveyor belt”. *Geophysical research letters* 28.2, pp. 311–314 (cit. on p. 7).
- Srokosz, MA and HL Bryden (2015). “Observing the Atlantic Meridional Overturning Circulation yields a decade of inevitable surprises”. *Science* 348.6241, p. 1255575 (cit. on pp. 3, 13).
- Stammer, Detlef (1997). “Global characteristics of ocean variability estimated from regional TOPEX/POSEIDON altimeter measurements”. *Journal of Physical Oceanography* 27.8, pp. 1743–1769 (cit. on p. 8).
- Stammer, Detlef and Anny Cazenave (2017). *Satellite altimetry over oceans and land surfaces*. CRC press (cit. on pp. 9, 10).
- Sterl, Andreas and Wilco Hazeleger (2003). “Coupled variability and air-sea interaction in the South Atlantic Ocean”. *Climate Dynamics* 21.7, pp. 559–571 (cit. on pp. 65, 66).
- Stewart, Robert H (2008). *Introduction to physical oceanography*. Robert H. Stewart (cit. on p. 10).
- Stott, Lowell, Christopher Poulsen, Steve Lund, and Robert Thunell (2002). “Super ENSO and global climate oscillations at millennial time scales”. *science* 297.5579, pp. 222–226 (cit. on p. 3).
- Talley, Lynne D (2003). “Shallow, intermediate, and deep overturning components of the global heat budget”. *Journal of Physical oceanography* 33.3, pp. 530–560 (cit. on pp. 2, 3).
- (2011). *Descriptive physical oceanography: an introduction*. Academic press (cit. on pp. 2, 7).
- (2013). “Closure of the global overturning circulation through the Indian, Pacific, and Southern Oceans: Schematics and transports”. *Oceanography* 26.1, pp. 80–97 (cit. on p. 3).
- Trenberth, Kevin E and David P Stepaniak (2003). “Seamless poleward atmospheric energy transports and implications for the Hadley circulation”. *Journal of Climate* 16.22, pp. 3706–3722 (cit. on p. 2).
- Van Loon, Harry and Jeffery C Rogers (1978). “The seesaw in winter temperatures between Greenland and northern Europe. Part I: General description”. *Monthly Weather Review* 106.3, pp. 296–310 (cit. on p. 65).
- Vautard, Robert and Michael Ghil (1989). “Singular spectrum analysis in nonlinear dynamics, with applications to paleoclimatic time series”. *Physica D: Nonlinear Phenomena* 35.3, pp. 395–424 (cit. on p. 69).
- Vautard, Robert, Carlos Pires, and Guy Plaut (1996). “Long-range atmospheric predictability using space–time principal components”. *Monthly weather review* 124.2, pp. 288–307 (cit. on p. 66).
- Vellinga, Michael and Richard A Wood (2002). “Global climatic impacts of a collapse of the Atlantic thermohaline circulation”. *Climatic change* 54.3, pp. 251–267 (cit. on p. 14).
- Venegas, SA, LA Mysak, and DN Straub (1997). “Atmosphere–ocean coupled variability in the South Atlantic”. *Journal of Climate* 10.11, pp. 2904–2920 (cit. on pp. 6, 65, 66, 75).

General Bibliography

- Von Schuckmann, Karina, Lijing Cheng, Matthew D Palmer, James Hansen, Caterina Tassone, Valentin Aich, et al. (2020). “Heat stored in the Earth system: where does the energy go?” *Earth System Science Data* 12.3, pp. 2013–2041 (cit. on p. 2).
- Wong, Annie PS, Susan E Wijffels, Stephen C Riser, Sylvie Pouliquen, Shigeki Hosoda, Dean Roemmich, et al. (2020). “Argo data 1999–2019: two million temperature-salinity profiles and subsurface velocity observations from a global array of profiling floats”. *Frontiers in Marine Science*, p. 700 (cit. on p. 12).
- Wunsch, Carl (1999). “Where do ocean eddy heat fluxes matter?” *Journal of Geophysical Research: Oceans* 104.C6, pp. 13235–13249 (cit. on pp. 2, 8).
- (2005). “The total meridional heat flux and its oceanic and atmospheric partition”. *Journal of climate* 18.21, pp. 4374–4380 (cit. on p. 2).
- Zebiak, Stephen E (1993). “Air–sea interaction in the equatorial Atlantic region”. *Journal of Climate* 6.8, pp. 1567–1586 (cit. on p. 65).
- Zhou, Jiayu and KM Lau (1998). “Does a monsoon climate exist over South America?” *Journal of climate* 11.5, pp. 1020–1040 (cit. on p. 67).

Appendix 1: Supplementary figures for Chapter 2

The South Atlantic Meridional Overturning Circulation and Mesoscale Eddies in the First GO-SHIP Section at 34.5°S

G. Manta^{1,2}, S. Speich¹, J. Karstensen³, R. Hummels³, M. Kersalé^{4,5}, R. Laxenaire⁶, A. Piola^{7,8}, M. P. Chidichimo^{7,9,10}, O. T. Sato¹¹, L. Cotrim da Cunha¹², I. Ansorge¹³, T. Lamont^{13,14,15}, M.A. van den Berg¹⁴, U. Schuster¹⁶, T. Tanhua³, R. Kerr¹⁷, R. Guerrero¹⁸, E. Campos^{11,19}, and C. S. Meinen⁵

¹ Laboratoire de Météorologie Dynamique, LMD-IPSL, UMR 8539, Ecole Polytechnique, ENS, CNRS, Paris, France

² Departamento de Ciencias de la Atmósfera, Facultad de Ciencias, Universidad de la República, Montevideo, Uruguay

³ GEOMAR Helmholtz Centre for Ocean Research Kiel, Kiel, Germany

⁴ Cooperative Institute for Marine and Atmospheric Studies, University of Miami, Miami, USA

⁵ NOAA Atlantic Oceanographic and Meteorological Laboratory, Miami, USA

⁶ Center for Ocean-Atmospheric Prediction Studies, Florida State University, Tallahassee, Florida, USA

⁷ Departamento de Oceanografía, Servicio de Hidrografía Naval (SHN), Buenos Aires, Argentina

⁸ Departamento de Ciencias de la Atmósfera y los Océanos, Universidad de Buenos Aires, Argentina

⁹ Consejo Nacional de Investigaciones Científicas y Técnicas, Buenos Aires, Argentina

¹⁰ Instituto Franco-Argentino sobre Estudios de Clima y sus Impactos, CNRS-CONICET-UBA, Buenos Aires, Argentina

¹¹ Oceanographic Institute, University of São Paulo, São Paulo, Brazil

¹² Faculdade de Oceanografia, BrOA, Universidade do Estado do Rio de Janeiro, Rio de Janeiro, Brazil

¹³ Oceanography Department, University of Cape Town, Cape Town, South Africa

¹⁴ Oceans & Coasts Research Branch, Department of Environment, Forestry and Fisheries, Cape Town, South Africa

¹⁵ Bayworld Centre for Research and Education, Constantia, Cape Town, South Africa

¹⁶ College of Life and Environmental Sciences, University of Exeter, Exeter, UK

¹⁷ Laboratório de Estudos dos Oceanos e Clima, Instituto de Oceanografia, Universidade Federal do Rio Grande – FURG, Rio Grande, RS, Brazil

¹⁸ Departamento de Ciencias Marinas, Facultad de Ciencias Exactas y Naturales, Universidad Nacional de Mar del Plata, Argentina

¹⁹ Gulf Environments Research Institute, American University of Sharjah, Sharjah, United Arab Emirates

The South Atlantic Meridional Overturning Circulation and Mesoscale Eddies in the First GO-SHIP Section at 34.5°S

G. Manta^{1,2}, S. Speich¹, J. Karstensen³, R. Hummels³, M. Kersalé^{4,5}, R. Laxenaire⁶, A. Piola^{7,8}, M. P. Chidichimo^{7,9,10}, O. T. Sato¹¹, L. Cotrim da Cunha¹², I. Ansorge¹³, T. Lamont^{13,14,15}, M.A. van den Berg¹⁴, U. Schuster¹⁶, T. Tanhua³, R. Kerr¹⁷, R. Guerrero¹⁸, E. Campos^{11,19}, and C. S. Meinen⁵

¹ Laboratoire de Météorologie Dynamique, LMD-IPSL, UMR 8539, Ecole Polytechnique, ENS, CNRS, Paris, France

² Departamento de Ciencias de la Atmósfera, Facultad de Ciencias, Universidad de la República, Montevideo, Uruguay

³ GEOMAR Helmholtz Centre for Ocean Research Kiel, Kiel, Germany

⁴ Cooperative Institute for Marine and Atmospheric Studies, University of Miami, Miami, USA

⁵ NOAA Atlantic Oceanographic and Meteorological Laboratory, Miami, USA

⁶ Center for Ocean-Atmospheric Prediction Studies, Florida State University, Tallahassee, Florida, USA

⁷ Departamento de Oceanografía, Servicio de Hidrografía Naval (SHN), Buenos Aires, Argentina

⁸ Departamento de Ciencias de la Atmósfera y los Océanos, Universidad de Buenos Aires, Argentina

⁹ Consejo Nacional de Investigaciones Científicas y Técnicas, Buenos Aires, Argentina

¹⁰ Instituto Franco-Argentino sobre Estudios de Clima y sus Impactos, CNRS-CONICET-UBA, Buenos Aires, Argentina

¹¹ Oceanographic Institute, University of São Paulo, São Paulo, Brazil

¹² Faculdade de Oceanografia, BrOA, Universidade do Estado do Rio de Janeiro, Rio de Janeiro, Brazil

¹³ Oceanography Department, University of Cape Town, Cape Town, South Africa

¹⁴ Oceans & Coasts Research Branch, Department of Environment, Forestry and Fisheries, Cape Town, South Africa

¹⁵ Bayworld Centre for Research and Education, Constantia, Cape Town, South Africa

¹⁶ College of Life and Environmental Sciences, University of Exeter, Exeter, UK

¹⁷ Laboratório de Estudos dos Oceanos e Clima, Instituto de Oceanografia, Universidade Federal do Rio Grande – FURG, Rio Grande, RS, Brazil

¹⁸ Departamento de Ciencias Marinas, Facultad de Ciencias Exactas y Naturales, Universidad Nacional de Mar del Plata, Argentina

¹⁹ Gulf Environments Research Institute, American University of Sharjah, Sharjah, United Arab Emirates

Contents of this file

Figures S1 to S9

Table S1

Introduction

This supporting information provides 9 additional figures and 1 table about the data gridding (S1), results and differences of using potential temperature and practical salinity instead of conservative temperature and absolute salinity (S2 and S4), the complete trajectories of mesoscales eddies crossed during the cruise (S3), differences in properties between the western and eastern part of the section (S5 and S6), estimates from moorings during the month of the cruise (S7), Ekman transport timeseries (S8), and hydrographic properties of CTD profiles done close to the center of eddies (S9).

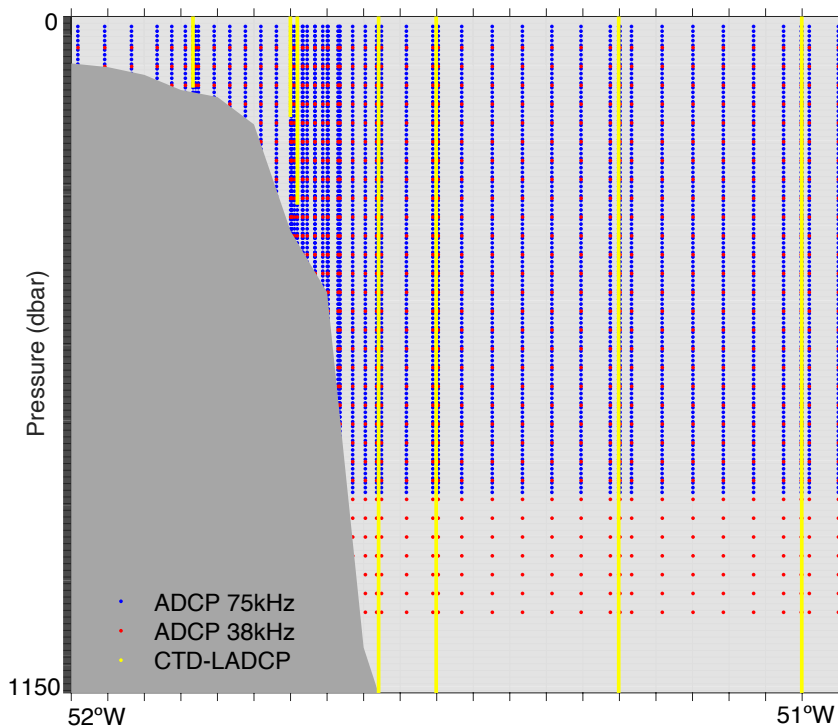


Figure S1. Schematic figure showing the data gridding in the upper 1150 dbar in the western boundary. Grey cells correspond to the grid and colored dots to each observation used in the linear interpolation. Blue and red dots correspond to the 75 and 38 kHz SADCPC underway measurements with an averaged measurement every 10 minutes, with the respective bin spacing, while CTD measurements are in yellow. The underway measured bathymetry, also averaged every 10 minutes, is plotted as a grey mask. The 75 KHz SADCPC sampled the water column down to 800m with 4 m bins and the 38kHz SADCPC sampled every 8m bins down to 1600m, although we only used the 0-1000 m data because of the quality of the lower quality of deeper data.

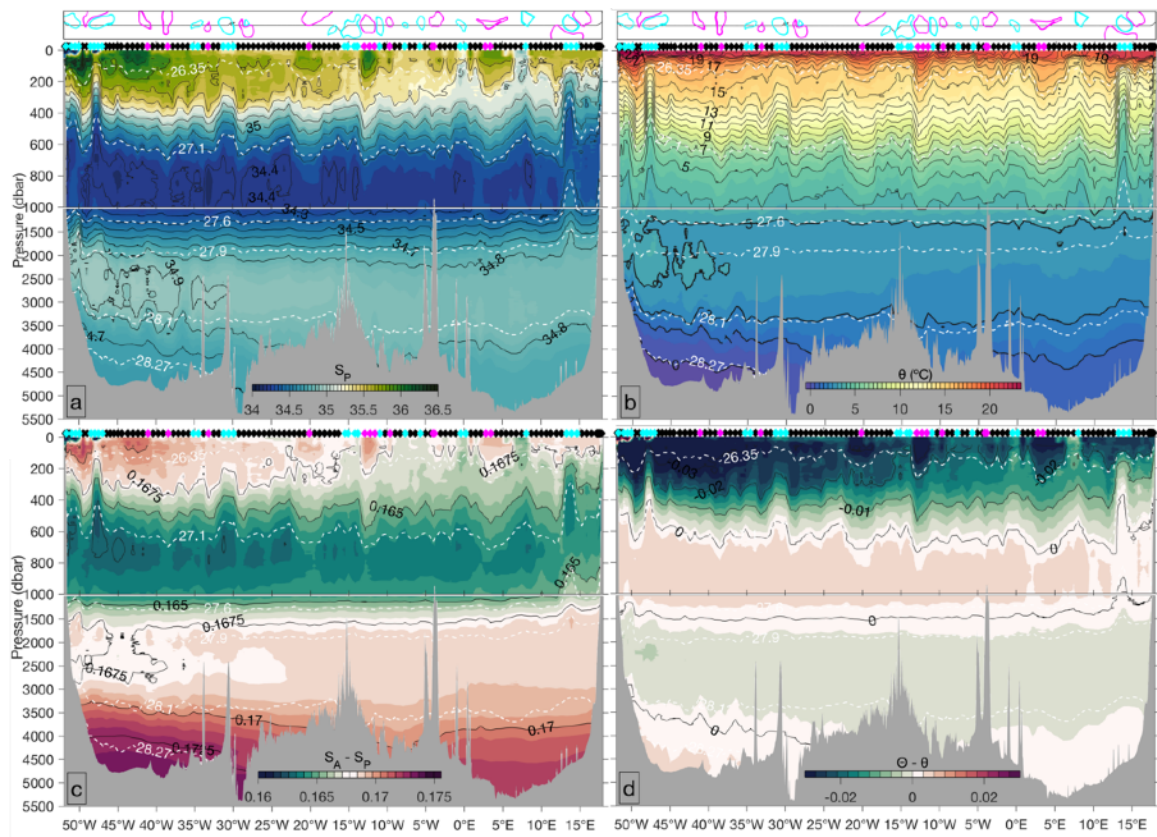


Figure S2. Oceanic section along 34.5°S in the South Atlantic during January 2017. a) Practical Salinity, b) Potential temperature (°C), c) Difference between Absolute salinity and practical salinity and d) Difference between conservative temperature and potential temperature for the MSM60 cruise.

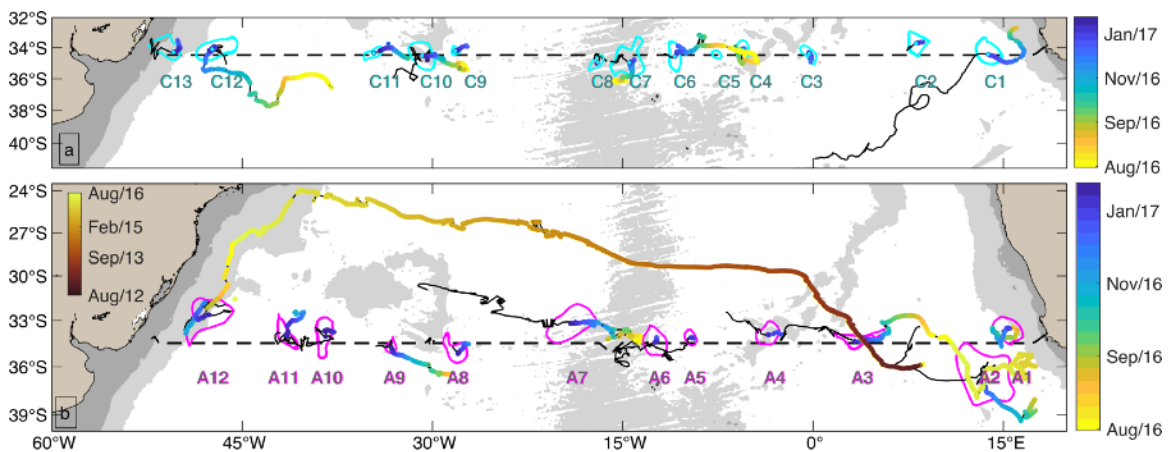


Figure S3. Lifetime trajectories of the mesoscale eddies crossed during MSM60 in January 2017. a) Cyclonic mesoscale eddies. The outermost contour at the day each eddy was crossed by the ship track is colored in cyan and the trajectory of the centroid in colors indicates the date. Continuous black lines indicate the eddy trajectory after being sampled by the cruise. In each panel, the dotted black line shows the cruise track and the gray shading represents water depths

less than 200 and 3500 m in the ETOPO2 data set (Smith & Sandwell, 1997). b) Same as a), but for anticyclonic mesoscale eddies with its outermost contour colored in magenta. An extra color scale was added for the long-lived Agulhas rings A3 and A12.

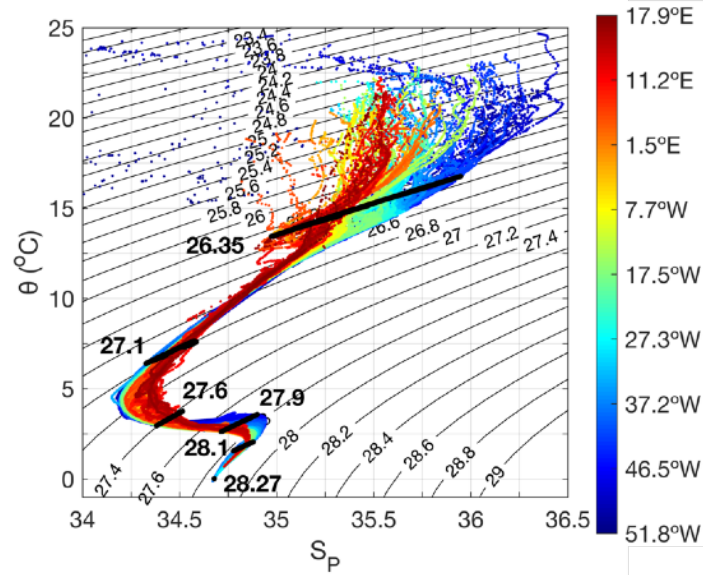


Figure S4. θ - S_p diagram from CTD profiles of MSM60 cruise across 34.5°S in the South Atlantic.

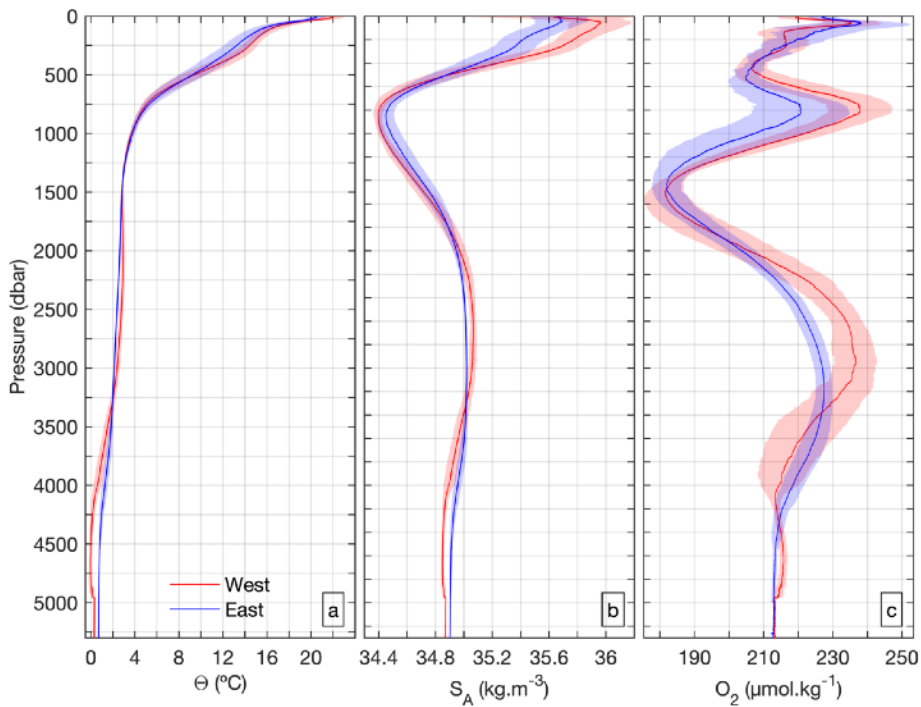


Figure S5. Mean profiles (lines) and standard deviation (shaded) west and east of the Mid-Atlantic Ridge in the South Atlantic at 34.5°S during January 2017 of: a) Conservative temperature (θ , °C), b) Absolute Salinity, (S_A , g kg^{-1}) and c) Dissolved Oxygen (O_2 , $\mu\text{mol kg}^{-1}$).

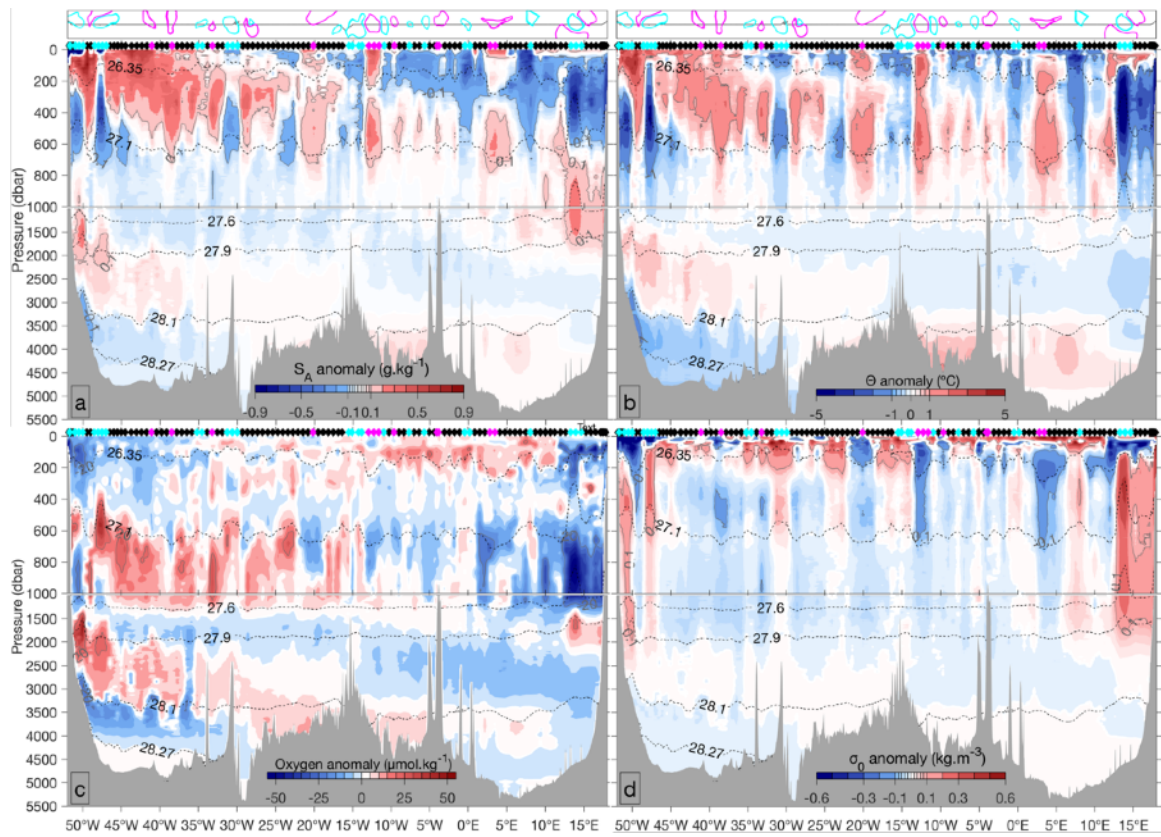


Figure S6. Anomalies relative to the zonal average of the section at 34.5°S in the South Atlantic. The upper 1000 dbars are vertically stretched. a) Absolute salinity (S_A , g kg^{-1}), b) Conservative temperature (Θ , $^{\circ}\text{C}$), c) Dissolved oxygen concentration ($\mu\text{mol kg}^{-1}$) and d) Potential density (σ_0 , kg m^{-3}). Neutral density layers (γ^n , kg m^{-3}) bounding each water mass are shown in black.

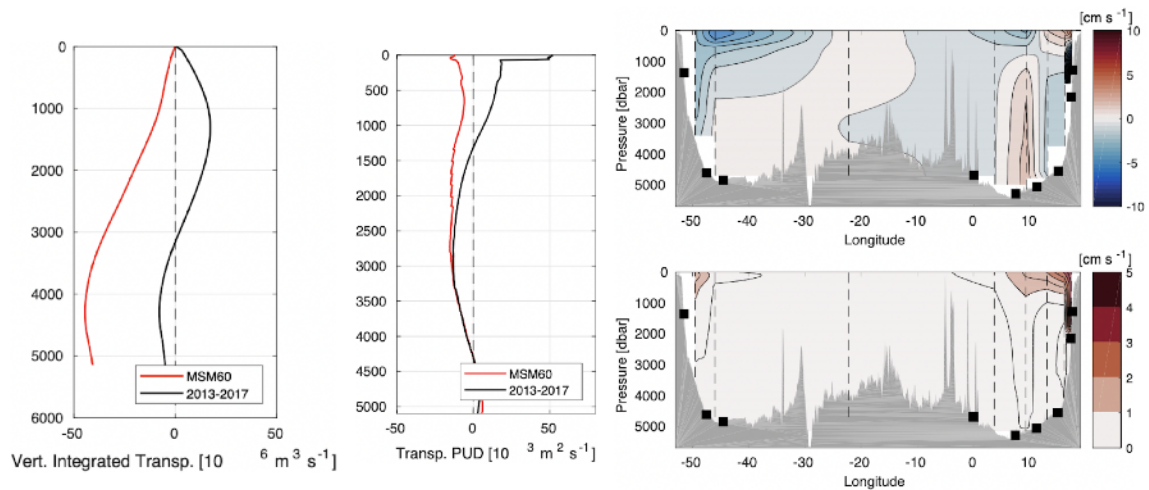


Figure S7. Cumulative transport, transport, and velocities (mean and standard deviation) from PIESs during January 2017. Black squares show the PIESs locations. See Kersalé et al., (2020) for methods.

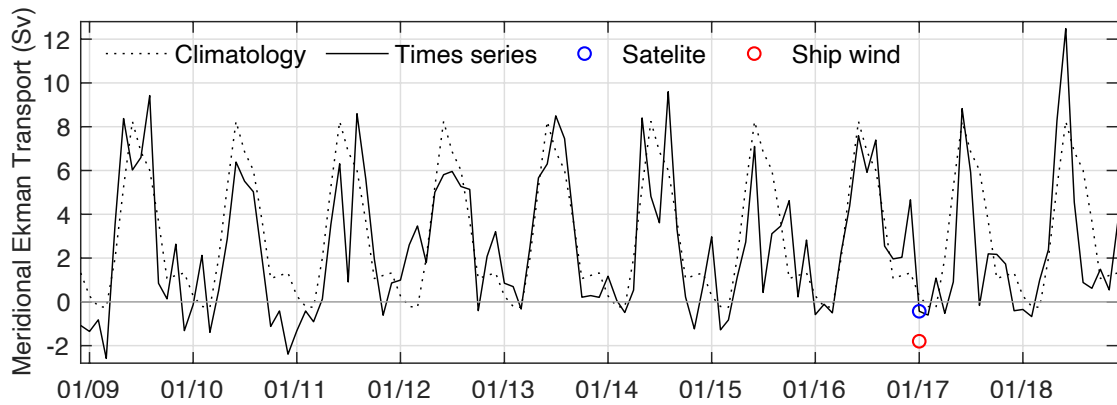


Figure S8. Monthly Ekman transport averaged zonally along 34.5°S in the South Atlantic. The black and dashed line shows the time series and the climatology from satellite wind stress. 6 hourly data for the period 1992-2018 were used to build the climatology. The blue circle is the value of the same data set at the time of the MSM60 cruise. The red circle is the calculated Ekman transport from MSM60 wind ship measurements.

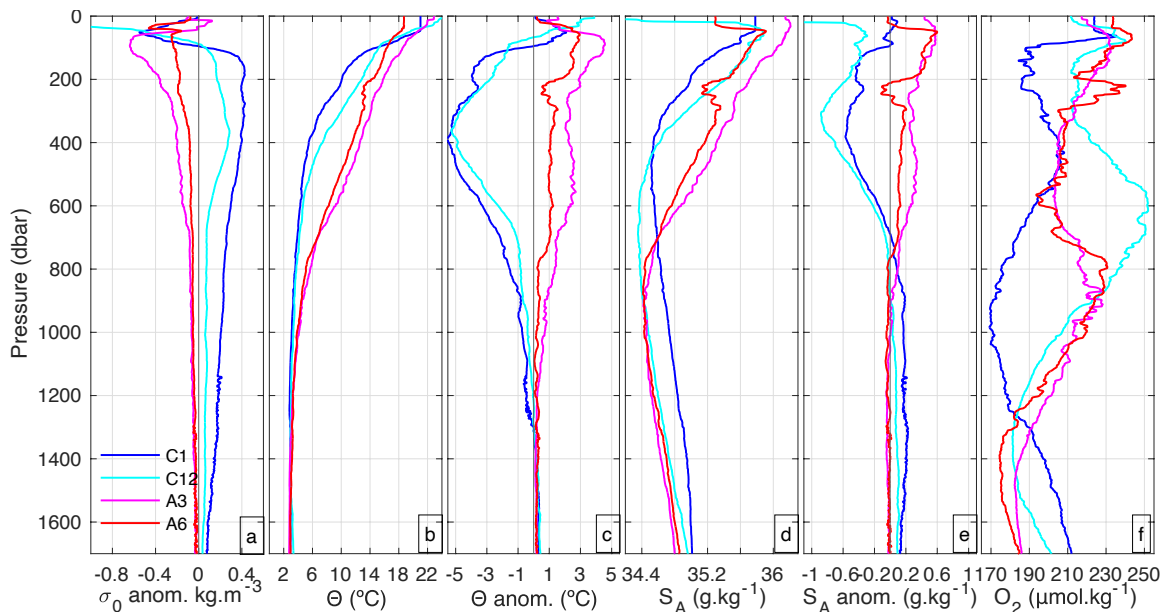


Figure S9. CTD profiles carried out close to the center of mesoscale eddies crossed during the MSM60 in January 2017. Anomalies were calculated relative to summer climatological non-eddy Argo profiles. a) Potential density anomaly (kg m^{-3}), b) Conservative temperature (Θ , $^{\circ}\text{C}$), c) Conservative temperature anomaly ($^{\circ}\text{C}$), d) Absolute salinity (S_A , g kg^{-1}), e) Absolute salinity anomaly (g kg^{-1}) and f) Dissolved oxygen concentration (O_2 , $\mu\text{mol kg}^{-1}$).

Table S1. Water mass properties (mean and standard deviation) at 34.5°S in the Atlantic Ocean in the west and the east. They were separated exactly by half in terms of distance at 17°W in the Mid Atlantic Ridge.

| Water Mass | Θ (°C) | S_A (g kg ⁻¹) | S_P (psu) | O_2 (μmol kg ⁻¹) |
|------------|---------------|-----------------------------|--------------|--------------------------------|
| W-SW | 18.67 ± 2.25 | 35.89 ± 0.31 | 35.72 ± 0.31 | 225.15 ± 11.87 |
| E-SW | 17.22 ± 2.12 | 35.63 ± 0.17 | 35.46 ± 0.17 | 230.51 ± 11.94 |
| W-SACW | 12.08 ± 2.70 | 35.32 ± 0.42 | 35.15 ± 0.42 | 212.20 ± 7.02 |
| E-SACW | 11.15 ± 2.16 | 35.11 ± 0.27 | 34.95 ± 0.26 | 210.44 ± 8.02 |
| W-AAIW | 4.23 ± 1.02 | 34.45 ± 0.06 | 34.29 ± 0.06 | 222.13 ± 15.79 |
| E-AAIW | 4.47 ± 1.09 | 34.50 ± 0.07 | 34.34 ± 0.06 | 210.75 ± 14.22 |
| W-UCDW | 2.89 ± 0.17 | 34.77 ± 0.12 | 34.60 ± 0.12 | 186.55 ± 6.98 |
| E-UCDW | 2.87 ± 0.16 | 34.76 ± 0.09 | 34.59 ± 0.09 | 184.47 ± 5.68 |
| W-NADW | 2.63 ± 0.34 | 35.04 ± 0.04 | 34.87 ± 0.04 | 228.03 ± 11.93 |
| E-NADW | 2.32 ± 0.25 | 35.00 ± 0.03 | 34.83 ± 0.03 | 218.97 ± 9.86 |
| W-LCDW | 0.95 ± 0.59 | 34.92 ± 0.06 | 34.75 ± 0.06 | 217.59 ± 8.30 |
| E-LCDW | 1.19 ± 0.42 | 34.95 ± 0.04 | 34.78 ± 0.04 | 217.64 ± 4.88 |
| AABW | -0.07 ± 0.04 | 34.85 ± 0.00 | 34.67 ± 0.00 | 215.85 ± 0.57 |

Contents of this file

Figures S1 to S9

Table S1

Introduction

This supporting information provides 9 additional figures and 1 table about the data gridding (S1), results and differences of using potential temperature and practical salinity instead of conservative temperature and absolute salinity (S2 and S4), the complete trajectories of mesoscales eddies crossed during the cruise (S3), differences in properties between the western and eastern part of the section (S5 and S6), estimates from moorings during the month of the cruise (S7), Ekman transport timeseries (S8), and hydrographic properties of CTD profiles done close to the center of eddies (S9).

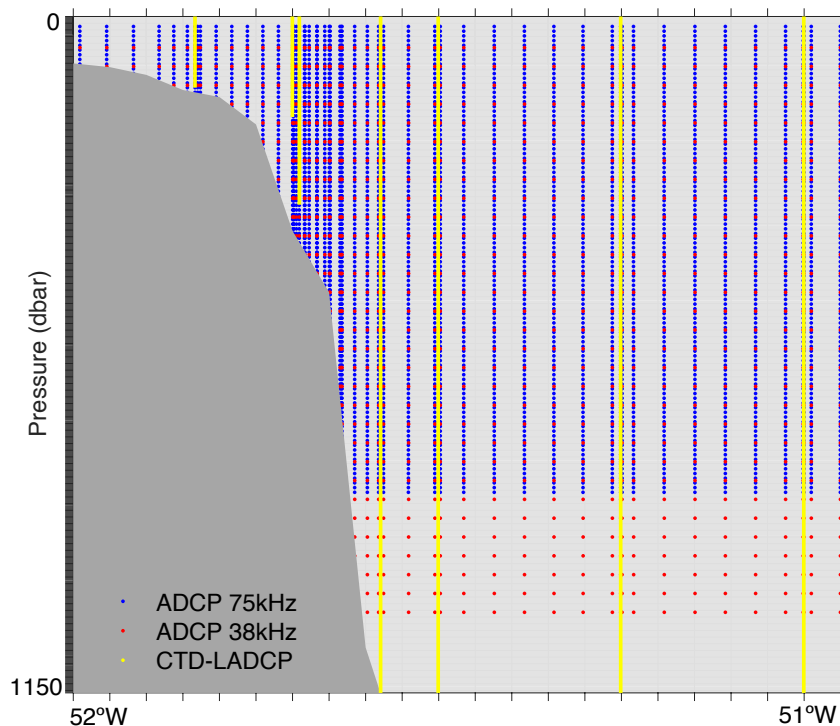


Figure S1. Schematic figure showing the data gridding in the upper 1150 dbar in the western boundary. Grey cells correspond to the grid and colored dots to each observation used in the linear interpolation. Blue and red dots correspond to the 75 and 38 kHz SADCPC underway measurements with an averaged measurement every 10 minutes, with the respective bin spacing, while CTD measurements are in yellow. The underway measured bathymetry, also averaged every 10 minutes, is plotted as a grey mask. The 75 KHz SADCPC sampled the water column down to 800m with 4 m bins and the 38kHz SADCPC sampled every 8m bins down to 1600m, although we only used the 0-1000 m data because of the quality of the lower quality of deeper data.

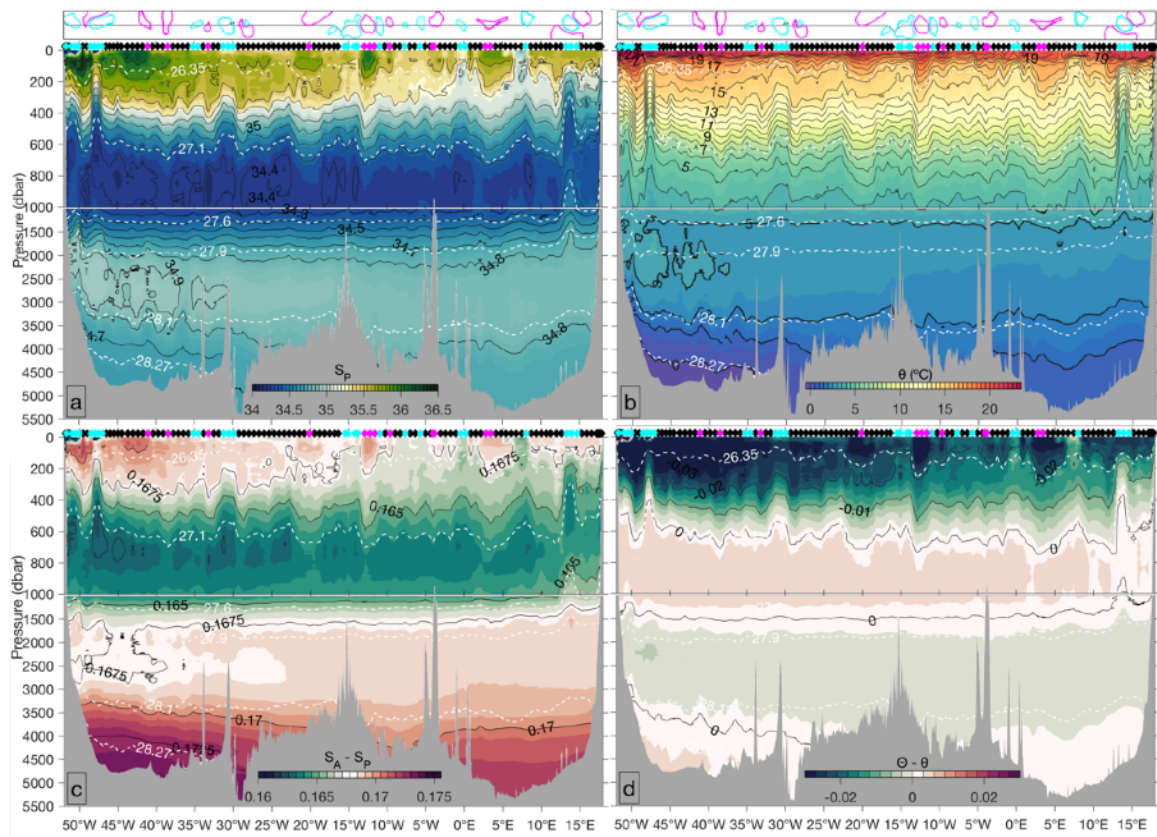


Figure S2. Oceanic section along 34.5°S in the South Atlantic during January 2017. a) Practical Salinity, b) Potential temperature (°C), c) Difference between Absolute salinity and practical salinity and d) Difference between conservative temperature and potential temperature for the MSM60 cruise.

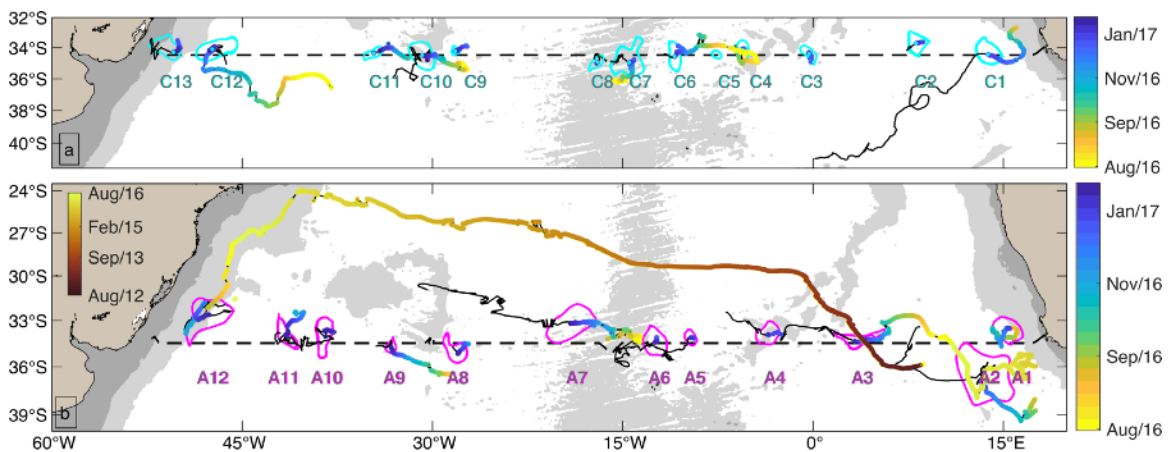


Figure S3. Lifetime trajectories of the mesoscale eddies crossed during MSM60 in January 2017. a) Cyclonic mesoscale eddies. The outermost contour at the day each eddy was crossed by the ship track is colored in cyan and the trajectory of the centroid in colors indicates the date. Continuous black lines indicate the eddy trajectory after being sampled by the cruise. In each panel, the dotted black line shows the cruise track and the gray shading represents water depths

less than 200 and 3500 m in the ETOPO2 data set (Smith & Sandwell, 1997). b) Same as a), but for anticyclonic mesoscale eddies with its outermost contour colored in magenta. An extra color scale was added for the long-lived Agulhas rings A3 and A12.

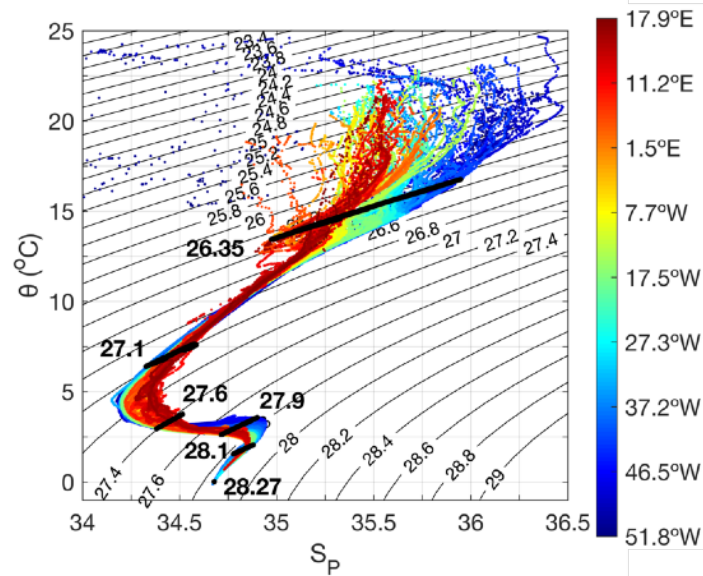


Figure S4. θ - S_p diagram from CTD profiles of MSM60 cruise across 34.5°S in the South Atlantic.

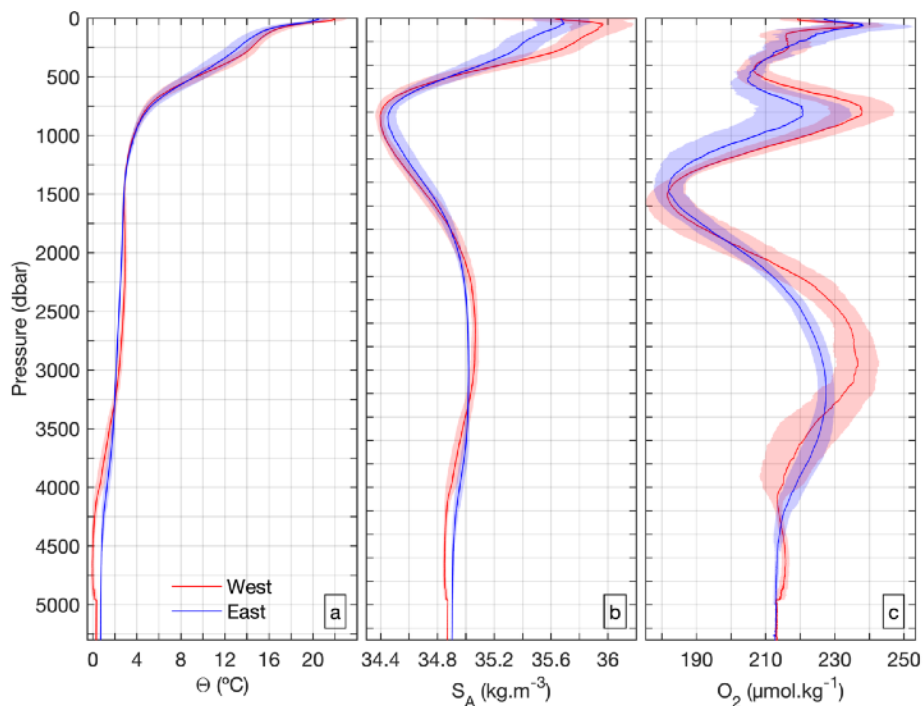


Figure S5. Mean profiles (lines) and standard deviation (shaded) west and east of the Mid-Atlantic Ridge in the South Atlantic at 34.5°S during January 2017 of: a) Conservative temperature (θ , °C), b) Absolute Salinity, (S_A , g kg^{-1}) and c) Dissolved Oxygen (O_2 , $\mu\text{mol kg}^{-1}$).

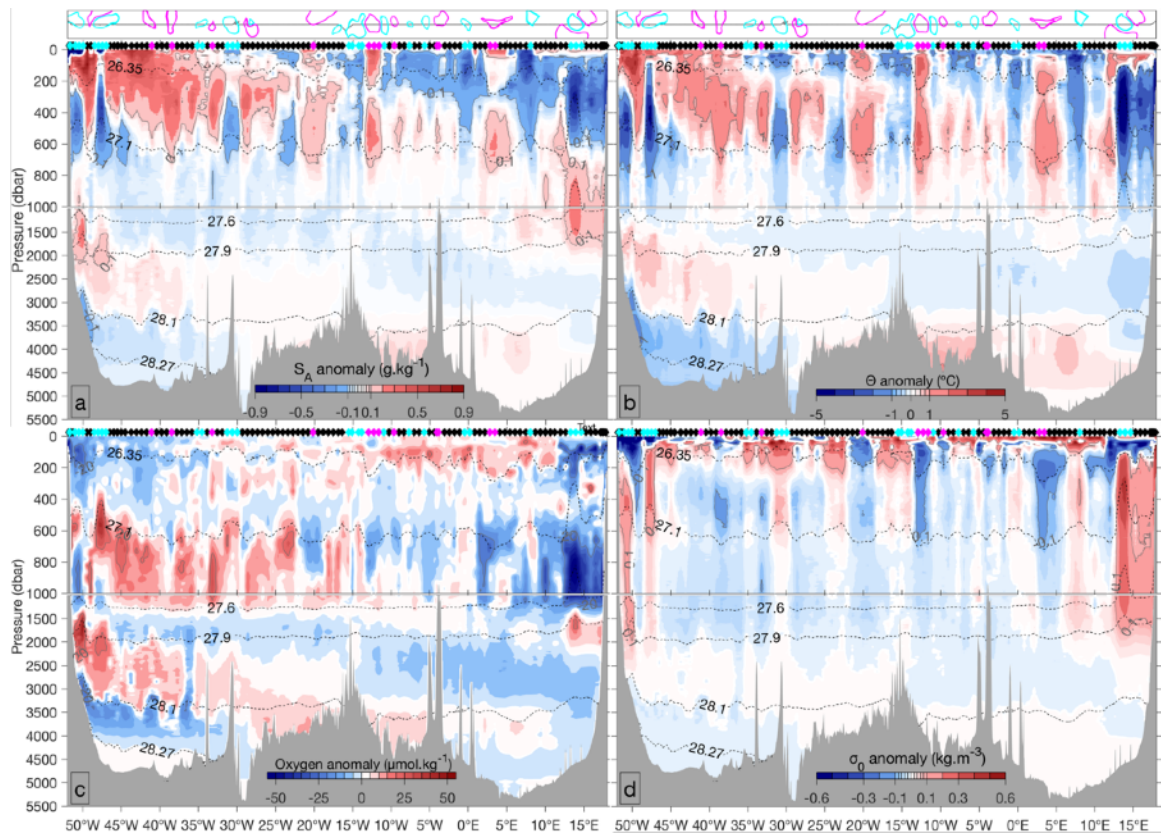


Figure S6. Anomalies relative to the zonal average of the section at 34.5°S in the South Atlantic. The upper 1000 dbars are vertically stretched. a) Absolute salinity (S_A , g kg^{-1}), b) Conservative temperature (Θ , $^{\circ}\text{C}$), c) Dissolved oxygen concentration ($\mu\text{mol kg}^{-1}$) and d) Potential density (σ_0 , kg m^{-3}). Neutral density layers (γ^n , kg m^{-3}) bounding each water mass are shown in black.

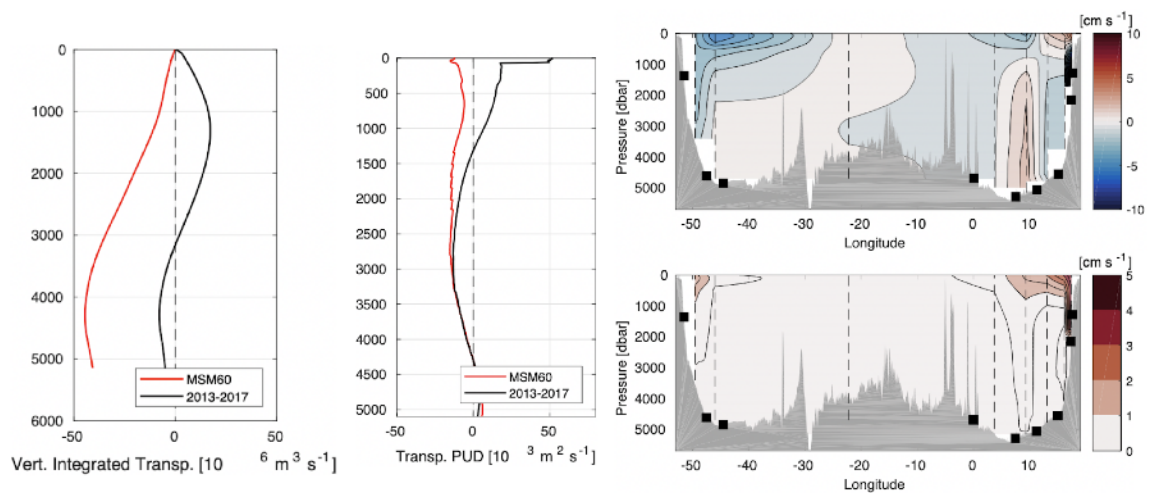


Figure S7. Cumulative transport, transport, and velocities (mean and standard deviation) from PIESs during January 2017. Black squares show the PIESs locations. See Kersalé et al., (2020) for methods.

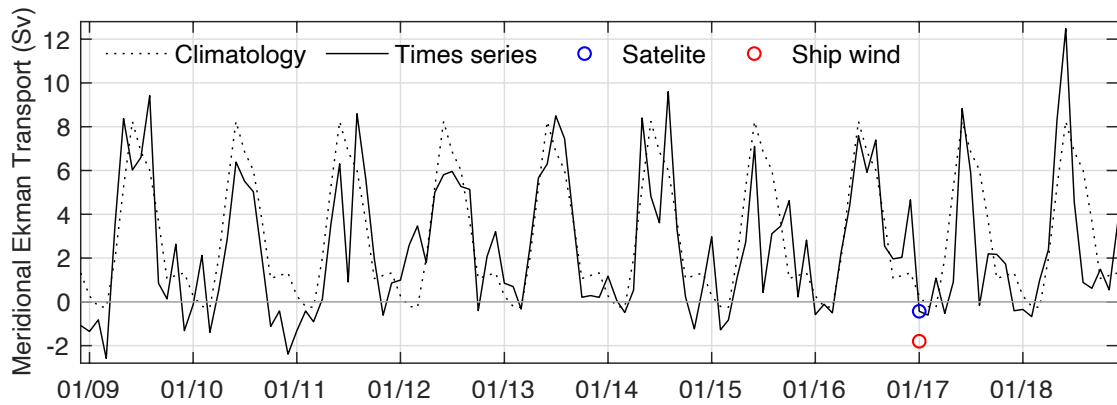


Figure S8. Monthly Ekman transport averaged zonally along 34.5°S in the South Atlantic. The black and dashed line shows the time series and the climatology from satellite wind stress. 6 hourly data for the period 1992-2018 were used to build the climatology. The blue circle is the value of the same data set at the time of the MSM60 cruise. The red circle is the calculated Ekman transport from MSM60 wind ship measurements.

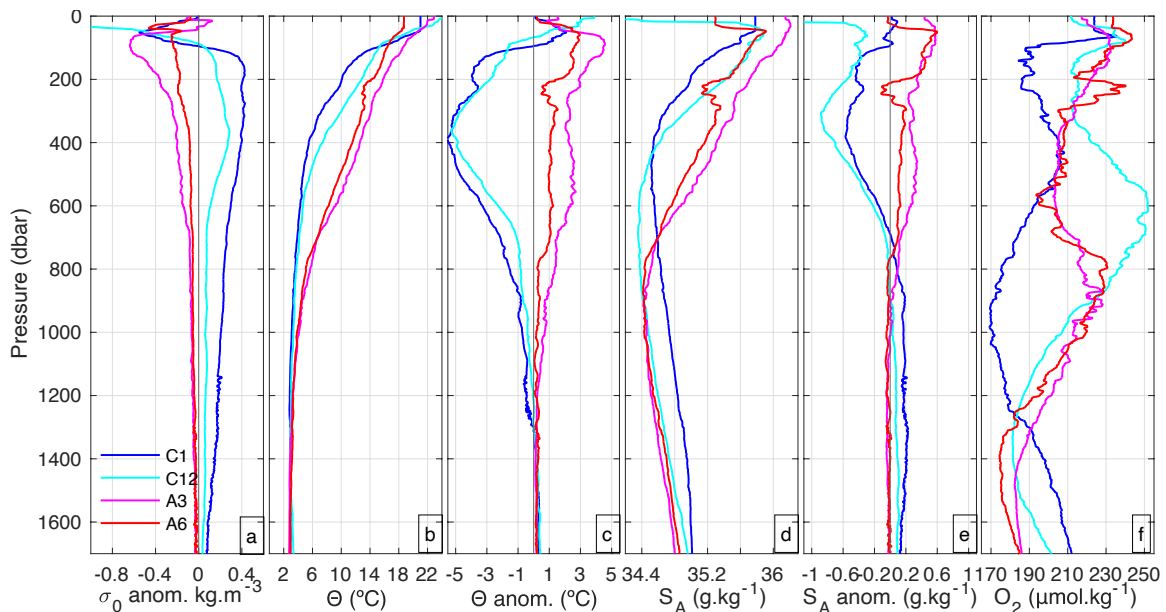


Figure S9. CTD profiles carried out close to the center of mesoscale eddies crossed during the MSM60 in January 2017. Anomalies were calculated relative to summer climatological non-eddy Argo profiles. a) Potential density anomaly (kg m^{-3}), b) Conservative temperature (Θ , $^{\circ}\text{C}$), c) Conservative temperature anomaly ($^{\circ}\text{C}$), d) Absolute salinity (S_A , g kg^{-1}), e) Absolute salinity anomaly (g kg^{-1}) and f) Dissolved oxygen concentration (O_2 , $\mu\text{mol kg}^{-1}$).

Table S1. Water mass properties (mean and standard deviation) at 34.5°S in the Atlantic Ocean in the west and the east. They were separated exactly by half in terms of distance at 17°W in the Mid Atlantic Ridge.

| Water Mass | Θ (°C) | S_A (g kg ⁻¹) | S_P (psu) | O_2 (μmol kg ⁻¹) |
|------------|---------------|-----------------------------|--------------|--------------------------------|
| W-SW | 18.67 ± 2.25 | 35.89 ± 0.31 | 35.72 ± 0.31 | 225.15 ± 11.87 |
| E-SW | 17.22 ± 2.12 | 35.63 ± 0.17 | 35.46 ± 0.17 | 230.51 ± 11.94 |
| W-SACW | 12.08 ± 2.70 | 35.32 ± 0.42 | 35.15 ± 0.42 | 212.20 ± 7.02 |
| E-SACW | 11.15 ± 2.16 | 35.11 ± 0.27 | 34.95 ± 0.26 | 210.44 ± 8.02 |
| W-AAIW | 4.23 ± 1.02 | 34.45 ± 0.06 | 34.29 ± 0.06 | 222.13 ± 15.79 |
| E-AAIW | 4.47 ± 1.09 | 34.50 ± 0.07 | 34.34 ± 0.06 | 210.75 ± 14.22 |
| W-UCDW | 2.89 ± 0.17 | 34.77 ± 0.12 | 34.60 ± 0.12 | 186.55 ± 6.98 |
| E-UCDW | 2.87 ± 0.16 | 34.76 ± 0.09 | 34.59 ± 0.09 | 184.47 ± 5.68 |
| W-NADW | 2.63 ± 0.34 | 35.04 ± 0.04 | 34.87 ± 0.04 | 228.03 ± 11.93 |
| E-NADW | 2.32 ± 0.25 | 35.00 ± 0.03 | 34.83 ± 0.03 | 218.97 ± 9.86 |
| W-LCDW | 0.95 ± 0.59 | 34.92 ± 0.06 | 34.75 ± 0.06 | 217.59 ± 8.30 |
| E-LCDW | 1.19 ± 0.42 | 34.95 ± 0.04 | 34.78 ± 0.04 | 217.64 ± 4.88 |
| AABW | -0.07 ± 0.04 | 34.85 ± 0.00 | 34.67 ± 0.00 | 215.85 ± 0.57 |

Appendix 2: Supplementary figures for Chapter 3

[Supplementary Video S1](#). Animation during the period of the cruise. Shade colors show satellite chlorophyll-a values, while light gray show ADT contours. Black vectors represent surface geostrophic currents. Gray contours show Absolute Dynamic Topography, with the yellow and magenta lines representing the BMC and the separation of BC from the shelf break over the slope, respectively. Cyan contour represents the main retroflection of Malvinas Current. Red and blue contours show Anticyclonic and Cyclonic eddies, respectively. Magenta bold lines represent the cruise track for each day, and cyan crosses and numbers indicate the CTD stations.

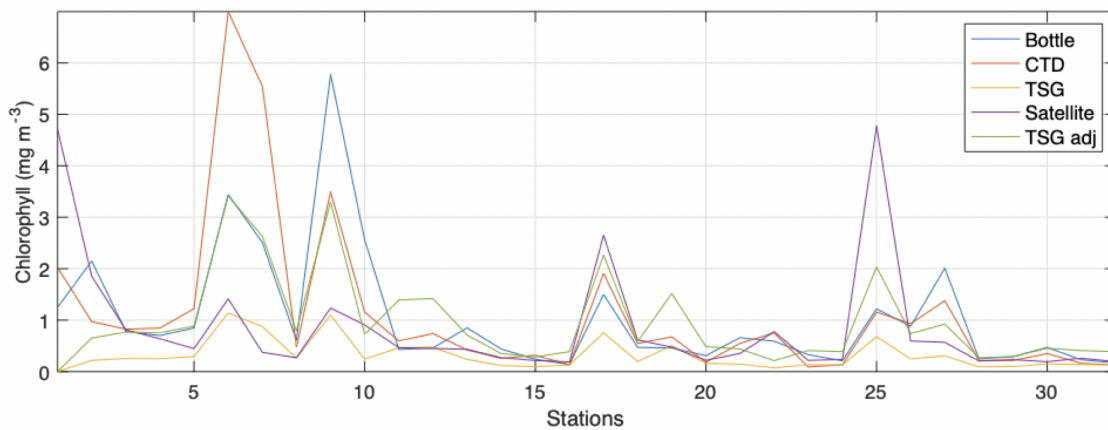


Figure 7.1: 32 simultaneous sampling points of chlorophyll-a at near-surface from the CTD rosette (Bottle), Fluorescence sensor from the CTD (CTD), Termosalinograph (TSG) fluorescence raw (TSG) and adjusted (TSG adj), and satellite measurements.

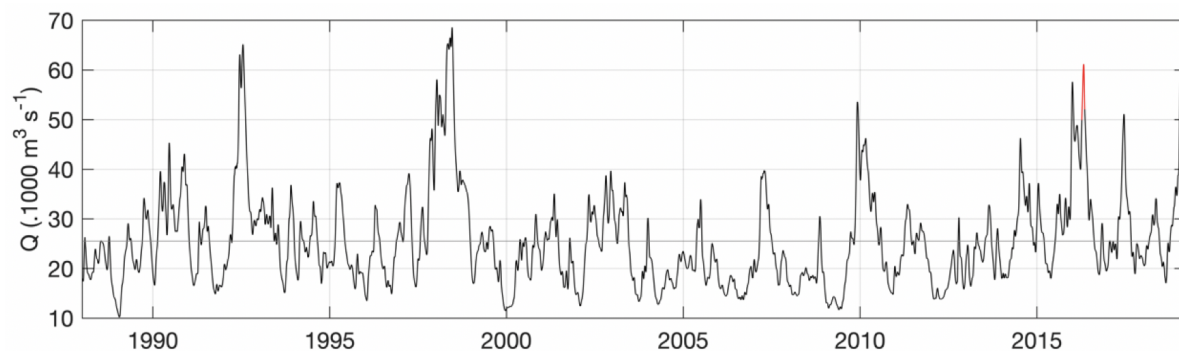


Figure 7.2: Time series of the Rio de la Plata discharges. The period of the cruise is shown in red, and the mean discharges by the gray line.

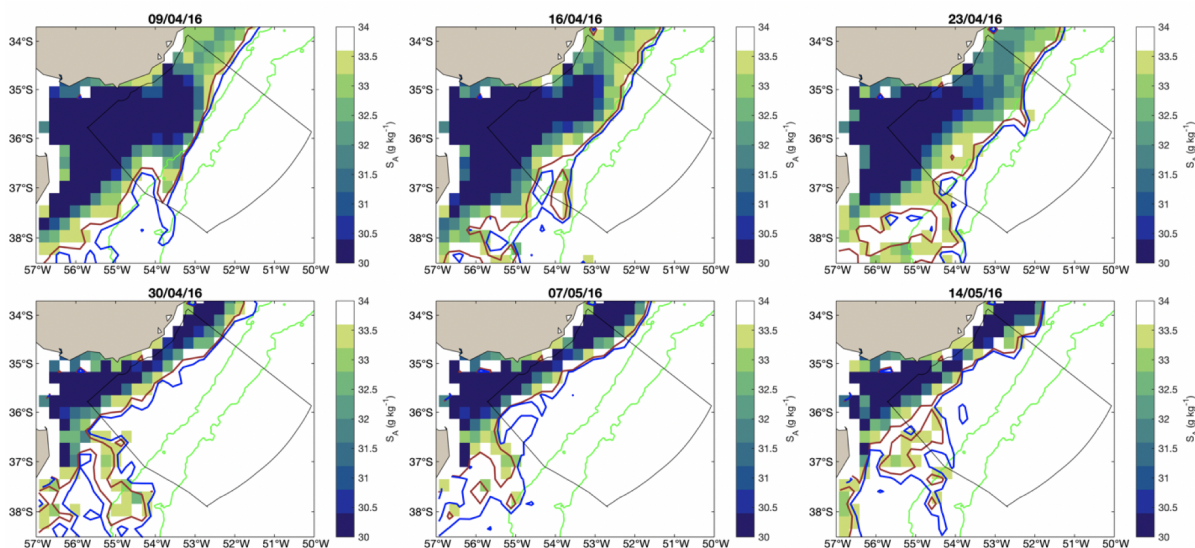


Figure 7.3: Weekly surface salinity fields during April and May 2016 in the Uruguayan Economic Exclusive Zone (black polygon). In green, are shown the 500 and 2500 m isobaths. The brown and blue contours correspond to Rio de la Plata Plume Waters and Subantarctic Shelf Waters, respectively.

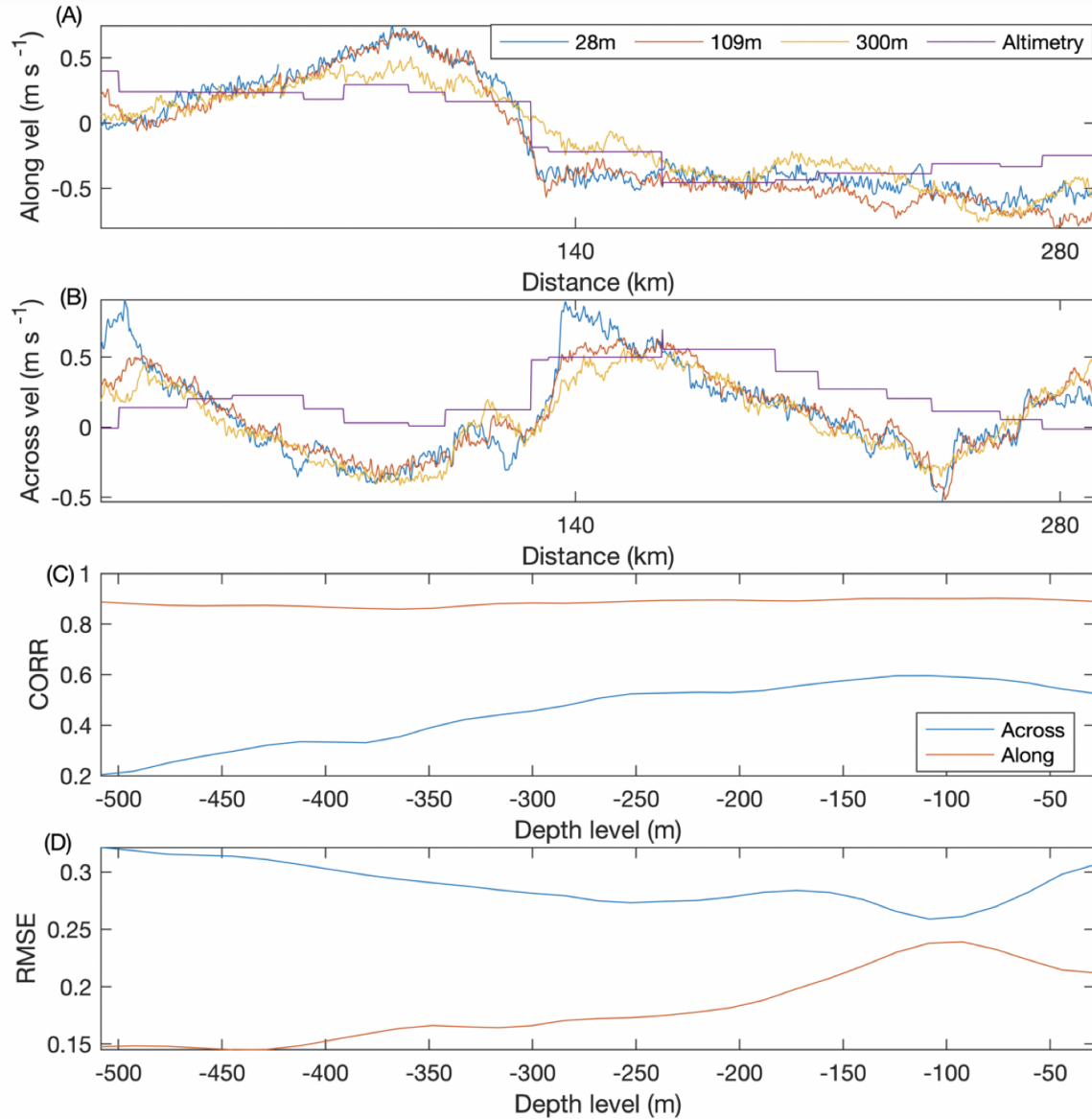


Figure 7.4: Comparison between altimetry measurements and Ship ADCP along the transect of Brazil-Malvinas Confluence. The comparison was made by interpolating the altimetry into the SADCPC quasi-continuous measurements. The upper panels show the measurements along and across-slope, while the lower panels show the Pearson correlation coefficient (CORR) and the Root Mean Square Error (RMSE) for each bin depth of the Ship ADCP with respect to Altimetry.

ABSTRACT

The ocean, like the atmosphere, is a key component of the climate system redistributing heat from lower to higher latitudes. Also, it has absorbed the majority of the anthropogenic heat through its large heat capacity. The Atlantic Meridional Overturning Circulation (AMOC) is the main mechanism in how the ocean redistributes heat and other properties across this basin. The AMOC has historically received special attention in its northern basin due to its large contribution to the global circulation and influence over the climate in Europe and North America. Over the last decade, the efforts to observe the global ocean and in particular the South Atlantic have increased, as this basin has the unique characteristic to export heat to the northern hemisphere across the equator and it connects the AMOC with the other ocean basins. This Ph.D. thesis aims to understand new insights from the South Atlantic Ocean circulation from a physical oceanography perspective, using the exponentially growing number of observations provided by the deployment of Argo floats, ship-based hydrography, and satellite observations. The study uses different new analyses applied to the ocean and to a recently released atmospheric reanalysis. The Ph.D. work has focused on three different aspects of the South Atlantic Circulation. In the first part, it has aimed to assess the meridional volume, freshwater, and heat (MHT) transports at 34.5°S in the South Atlantic in the first GO-SHIP hydrographic transect at this latitude that took place in January 2017. An upper and an abyssal overturning cell are identified with a strength of 15.64 ± 1.39 Sv and 2.4 ± 1.6 Sv, respectively. The net northward MHT is 0.27 ± 0.10 PW, increasing by 0.12 PW when we remove the observed mesoscale eddies with a climatology derived from the Argo floats data set. We attribute this change to an anomalous predominance of cold-core eddies during the cruise period. The zonal changes in water masses properties and velocity denote the imprint of exchange pathways with both the Southern and the Indian oceans. During the second part of the Ph.D., the analysis focused on the Brazil-Malvinas Confluence, which is the region where opposing and intense western boundary currents, major contributors of the AMOC, meet along the Southwestern Atlantic slope. Based on shipborne observations combined with satellite data and an eddy tracking algorithm, we analyze the cross-shelf exchanges during May 2016. Two types of shelf water export were observed triggered by mesoscale dynamics: one was the export of shallow Rio de la Plata Plume waters driven off-shelf by the retroflexion of the Brazil Current. An additional type of off-shelf transport consisted of a subsurface layer of Subantarctic Shelf Waters that subducted at the Confluence. We show that geostrophic currents derived from satellite altimetry over the slope can be useful to track this subsurface off-shelf export as they are significantly correlated with absolute velocity measurements at this depth. Moreover, Argo temperature and salinity profiles show evidence of these two types of shelf water export, suggesting this is a relatively frequent phenomenon. The last part of the study consisted of studying the natural coupled variability of ocean and atmosphere by applying the Multivariate Singular Spectrum Analysis (MSSA) to the ERA5 dataset. We identified prominent interannual oscillations of 12.8 and 5.3 year periods, characterized by a basinwide southwest-northeast anticlockwise propagation pattern. The novelty of these results relies on that MSSA allows characterizing the spatio-temporal evolution of the variability mode. The results of the Ph.D. work have been summarized in three papers prepared for international A-rated scientific journals. Two of them have already been published.

KEYWORDS

Heat transport, mesoscale eddies, shelf water export, coupled variability

RÉSUMÉ

L'océan, comme l'atmosphère, est un élément clé du système climatique qui redistribue la chaleur des basses vers les hautes latitudes. Il a également absorbé la majorité de la chaleur anthropique grâce à sa grande capacité thermique. La circulation méridienne de retournement de l'Atlantique (AMOC) est le principal mécanisme par lequel l'océan redistribue la chaleur et d'autres propriétés dans ce bassin. Historiquement, l'AMOC a fait l'objet d'une attention particulière dans son bassin nord en raison de sa grande contribution à la circulation mondiale et de son influence sur le climat en Europe et en Amérique du Nord. Au cours de la dernière décennie, les efforts d'observation de l'océan global et en particulier de l'Atlantique Sud ont augmenté, car ce bassin a la caractéristique unique d'exporter de la chaleur vers l'hémisphère Nord à travers l'équateur et connecte l'AMOC avec les autres bassins océaniques. Ce doctorat vise à améliorer la compréhension de la circulation dans l'océan Atlantique Sud du point de vue de l'océanographie physique, en utilisant le nombre croissant d'observations fournies par les flotteurs Argo, des mesures hydrographiques et des observations satellitaires. Le travail s'est concentré sur trois aspects différents de la circulation de l'Atlantique Sud. Dans la première partie, il s'agissait d'évaluer les transports méridiens de volume, d'eau douce et de chaleur (MHT) à 34.5°S dans l'Atlantique Sud lors du premier transect hydrographique GO-SHIP à cette latitude, en janvier 2017. Une cellule de retournement supérieure et une cellule de retournement abyssale sont identifiées avec une force de 15.64 ± 1.39 Sv et 2.4 ± 1.6 Sv, respectivement. La MHT nette vers le nord-est de 0.27 ± 0.10 PW, augmentant de 0.12 PW lorsque nous retirons les tourbillons de méso-échelle observés avec une climatologie dérivée de l'ensemble de données des flotteurs Argo. Nous attribuons cette différence à une prédominance anormale des tourbillons de cœur froid pendant la période de la campagne. Au cours de la deuxième partie du doctorat, l'analyse s'est concentrée sur la confluence Brésil-Malouines, qui est la région où des courants de bord ouest opposés et intenses, contributeurs majeurs du AMOC, se rencontrent et génèrent l'une des régions les plus énergétiques de l'océan mondial. Sur la base d'observations embarquées combinées à des données satellitaires et à un algorithme de suivi des tourbillons, nous analysons les échanges trans-plateau au cours du mois de mai 2016. Deux types d'exportation d'eau du plateau ont été observés, déclenchés par la dynamique de méso-échelle: l'exportation des eaux peu profondes du panache du Rio de la Plata, entraînées hors du plateau par la réflexion du courant du Brésil, et le transport vers le large d'une couche d'eaux du plateau subantarctique situé sous la surface, qui s'est subductée à la confluence. Nous montrons que les courants géostrophiques dérivés de l'altimétrie par satellite au-dessus du talus peuvent être utiles pour suivre cette exportation hors plateau en subsurface. De plus, les profils de température et de salinité Argo montrent des preuves de ces deux types d'exportation d'eau du plateau, suggérant qu'il s'agit d'un phénomène relativement fréquent. La dernière partie de l'étude a consisté à étudier la variabilité naturelle couplée de l'océan et de l'atmosphère en appliquant l'analyse multivariée du spectre singulier (MSSA) au jeu de données ERA5. Nous avons identifié des oscillations interannuelles importantes de périodes de 12 et 5 ans, caractérisées par un modèle de propagation sud-ouest-nord-est dans le sens inverse des aiguilles d'une montre. La nouveauté de ces résultats repose sur le fait que la méthode MSSA permet de caractériser l'évolution spatio-temporelle du mode de variabilité. Les résultats de ces travaux ont été résumés dans trois articles préparés pour des revues scientifiques internationales de rang A, dont deux d'entre eux ont déjà été publiés.

MOTS CLÉS

Transport de chaleur, tourbillons à méso-échelle, exportation de l'eau du plateau, variabilité couplée